Paracoccus denitrificans as a model system for studying the mechanism of respiratory complex I

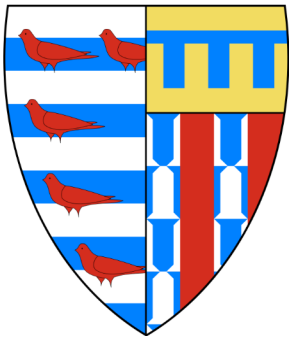

Owen D. Jarman

MRC Mitochondrial Biology Unit, University of Cambridge,

Pembroke College

March 2022

This thesis is submitted for the degree of Doctor of Philosophy

Declaration

This thesis is the result of my own work and includes nothing which is the outcome of work done in collaboration except as declared in the Preface and specified in the text.

I further state that no substantial part of my thesis has already been submitted, or, is being concurrently submitted for any such degree, diploma or other qualification at the University of Cambridge or any other University or similar institution except as declared in the Preface and specified in the text.

It does not exceed the prescribed word limit for the relevant Degree Committee

Owen D. Jarman
March 2022

The work presented in this thesis has been published in the following papers:

Jarman, O.D., Biner, O. and Hirst, J. (2021) Regulation of ATP hydrolysis by the ε subunit, ζ subunit and Mg-ADP in the ATP synthase of *Paracoccus denitrificans*, *Biochimica et Biophysica Acta - Bioenergetics*, **1862**, 148355.

Jarman, O.D., Biner, O., Wright, J.J. and Hirst, J. (2021) *Paracoccus denitrificans*: a genetically tractable model system for studying respiratory complex I, *Scientific Reports*, **11**, 10143.

Acknowledgements

First I would like to thank Prof Judy Hirst for providing me with the incredible opportunity to work in her lab. Her continual enthusiasm and expert knowledge has provided me with great motivation and help during my PhD. The rigorous and high quality science, to which she holds herself to, is something I aspire to replicate in my future scientific endeavours.

There are many members of the Hirst lab, past and present, I would like to thank for their support, friendship and advice over the years. First, I am grateful for the help of Dr Jamie Blaza in the first few months of my PhD, introducing me to bacterial genetics, kinetic assays, and working with *P. denitrificans*. Also to Dr Hannah Bridges for her help setting me up in the lab. Furthermore, I would like to thank Dr Justin Fedor for his help troubleshooting all aspects of my project, while always being available for friendly discussions.

It has been a joy to work alongside others in the lab during various stages of my PhD, including Dr Olivier Biner and Dr Daniel Grba. I am also grateful to Dr John Wright for reading this thesis and his useful advice.

I'd like to thank Dr Mike Harbour, Dr Shujing Ding and Dr Ian Fearnley for performing mass spectrometry experiments for me and I would also like to thank Dr Zhan Yin for making grids and setting up my Cryo-EM data collection together with Dr Dima Chirgadze. I am extremely grateful for my discussions with Dr Rita Monson, whose expertise in bacterial genetics was important for progressing the *P. denitrificans* mutagenesis work.

A huge thank you goes to the friendly Hadstock Silver Band, who have provided a welcome break of relaxed music-making each week.

Finally, and most important to me, my family. Their constant love and support means so much, and I appreciate everything they have done for me over the years.

Abstract

Respiratory complex I (NADH:ubiquinone oxidoreductase) is a crucial metabolic enzyme that couples the free energy released from NADH oxidation and ubiquinone reduction to the translocation of four protons across an energy-transducing membrane, contributing to the proton motive force used to synthesise ATP. Although structural knowledge of complex I is now extensive, the mechanisms by which it captures the redox energy for proton translocation, and the mechanisms and pathways of the proton pumps, remain elusive. In this thesis, the α-proteobacterium *Paracoccus denitrificans* is developed and presented as a powerful model system for understanding mitochondrial complex I, combining interrogative biophysical and structural characterisation with the potential for mutagenesis in every subunit. First, aiming to establish conditions for studying the thermodynamic reversibility of *P. denitrificans* complex I, activation of ATP hydrolysis by the unidirectional F_1F_O-ATP synthase of *P. denitrificans* was investigated by the deletion of potential inhibitory subunits and treatment with potential chemical activators. While no conditions were found in which ATP hydrolysis could be sufficiently activated to drive complex I in reverse, insights were gained into the regulatory mechanism of *P. denitrificans* ATP synthase and the inhibitory role of Mg-ADP.

Next, a strain of *P. denitrificans* containing an alternative NADH dehydrogenase, a bypass enzyme, was generated to facilitate the creation of deleterious complex I variants. In addition, a purification tag was engineered onto complex I, enabling its rapid purification. The isolated complex I was thoroughly characterised and its reconstitution into proteoliposomes was optimised, expanding the toolkit available for the study of complex I variants. The structure of the enzyme was also partially resolved by cryo-EM. The well-resolved map of the hydrophilic domain revealed a novel supernumerary subunit and demonstrated that *P. denitrificans* complex I exists entirely in the so-called 'active' state. However, due to conformational heterogeneity, the cryo-EM map was poorly resolved in the membrane domain, preventing detailed structural modelling of the complete enzyme.

Finally, single point variants in the Nqo13 (ND4) subunit of complex I were generated to investigate: (1) key residues in the energy propagation pathway; (2) coordination to the lateral helix of Nqo12 (ND5); and (3) a potential hydration channel controlled by a gating mechanism. Comprehensive characterisation of the variants revealed insights into all three components of the mechanism. Furthermore, no variants were identified that pump fewer than four protons per NADH oxidised, emphasising the tight coupling between ubiquinone reduction and proton translocation, which is conserved even when the rate of catalysis is compromised.

Abbreviations

In addition to the abbreviations below, standard chemical symbols and SI units are used throughout. Any non-standard abbreviations not stated here are mentioned in the text.

ACMA	9-amino-6-chloro-2-methoxyacridine
ADP	Adenosine diphosphate
ADP-ribose	Adenosine diphosphate ribose
AOX	Alternative oxidase
Ap5A	Diadenosine pentaphosphate
$APAD^+$	3-acetylpyridine adenine dinucleotide
ATP	Adenosine triphosphate
BCA	Bicinchoninic acid
Bis-Tris	Bis(2-hydroxyethyl)amino-tris(hydroxymethyl)methane
BN-PAGE	Blue native-polyacrylamide gel electrophoresis
Bovine	*Bos taurus*
BSA	Bovine serum albumin
CHAPS	3-[(3-cholamidopropyl) dimethylammonio]-1-propanesulphonate
CDL	Cardiolipin
CTF	Contrast transfer function
Cryo-EM	Cryogenic electron microscopy
Cyt *c*	Cytochrome *c*
DAP	Diaminopimelic acid
DDM	*n*-dodecyl β-D-maltoside
DMSO	Dimethyl sulfoxide
DNA	Deoxyribonucleic acid
dNADH	Reduced nicotinamide hypoxanthine dinucleotide
dNTPs	Deoxyribonucleoside triphosphate

DOPC	1,2-dioleoyl-sn-glycero-3-phosphocholine
DOPE	1,2-dioleoyl-sn-glycero-3-phosphoethanolamine
DOPG	1,2-dioleoyl-sn-glycero-3-phospho-(1'-rac-glycerol)
DQ	Decylubiquinone
EDTA	Ethylenediaminetetraacetic acid
EPR	Electron paramagnetic resonance
ETC	Electron transfer chain
FAD	Flavin adenine dinucleotide
FET	Forward electron transfer
FES	Iron-sulfur
FMN	Flavin mononucleotide
FSC	Fourier shell correlation
FumC	Fumarate hydratase
H_2O_2	Hydrogen peroxide
HEPES	(4-(2-hydroxyethyl)-1-piperazineethanesulphonic acid)
HRP	Horseradish peroxidase
IBM	Inner boundary membrane
IC_{50}	Half-maximal inhibitory concentration
Kan^R	Kanamycin resistance
IMM	Inner mitochondrial membrane
IMS	Intermembrane space
LC	Liquid chromatography
LDAO	Lauryldimethylamine N-oxide
LHON	Leber's hereditary optic neuropathy
LMNG	Lauryl maltose neopentyl glycol
MaeB	Oxaloacetate decarboxylating malic enzyme
MALDI	Matrix-assisted laser desorption/ionisation

MES	2-(*N*-morpholino)ethanesulphonic acid
MM	Mitochondrial matrix
MOPS	3-(*N*-morpholino)propanesulphonic acid
MS	Mass spectrometry
mtDNA	Mitochondrial DNA
NAD^+	Nicotinamide adenine dinucleotide
NADH	Reduced nicotinamide adenine dinucleotide
$NADP^+$	Nicotinamide adenine dinucleotide phosphate
NADPH	Reduced nicotinamide adenine dinucleotide phosphate
NanoDSF	Nano differential scanning fluorimetry
NBT	nitroblue tetrazolium
NDH-2	Alternative NADH dehydrogenase
OD_{600}	Optical density at 600 nm
OG	Octyl-glucoside
OMM	Outer mitochondrial membrane
PAGE	Poly-acrylamide gel electrophoresis
PCR	Polymerase chain reaction
Pd-CI	*Paracoccus denitrificans* complex I
P_i	Inorganic phosphate
PL	Proteoliposome
PMSF	Phenylmethanesulphonylfluoride
Q	Ubiquinone
Q_1	Isoprenylubiquinone
Q_{10}	Coenzyme Q-decaisoprenylubiquinone
QH_2	Ubiquinol
RET	Reverse electron transfer
ROS	Reactive oxygen species

RPM	Rotations per minute
SBP	Sub-bacterial particles
SDS	Sodium dodecyl sulphate
SMP	Sub-mitochondrial particle
SOC	Super optimal broth with catabolite repression
SOD	Superoxide dismutase
TCA cycle	Tricarboxylic acid cycle
TOF	Time of flight
Tris	Tris(hydroxymethyl)aminomethane
X-gal	5-bromo-4-chloro-3-indolyl-β-D-galactopyranoside
Δp	Proton motive force
ΔpH	Proton potential difference
ΔΨ	Charge potential difference

Table of contents

1. Introduction

To support life on Earth, energy is required. Without energy, Nature would be unable to perform fundamental complex cellular reactions, such as metabolism, DNA replication, signalling, protein synthesis and protein transport. The thermodynamic laws of the Universe state that all reactions can only occur if they increase the entropy (the disorder) of the Universe, ultimately leading to endpoints where only disorder exists and no meaningful work can be performed. All life exists in an open system where, to create order and higher complexity, it consumes available energy and materials from the environment, observing the laws of thermodynamics. Organisms use either light energy or redox-driven reactions to generate chemical disequilibria, which in turn drive complex cellular metabolism and essential life-sustaining function. The processes by which cells generate and harness this potential energy, the bioenergetics of the cell, are essential to life.

In biological systems, light and chemical energy is harnessed to generate electrochemical gradients across energy-transducing membranes. These include the inner mitochondrial membrane, the thylakoid membrane in chloroplasts and cyanobacteria, and the plasma membrane in prokaryotes. The electrochemical gradients generated across these energy-transducing membranes can be harnessed to synthesise ATP, the cellular energy currency, from ADP and P_i. This is the basis of the chemiosmotic theory proposed by Mitchell (1961). While ATP molecules themselves cannot 'do work', ATP synthesis is powered to produce a high [ATP]/[ADP] ratio in the cell, which can be used to drive metabolism by releasing the energy trapped in this chemical disequilibrium through ATP hydrolysis.

The chemiosmotic theory proposed by Mitchell has two fundamental components (Mitchell, 1961). First, an energy-transducing membrane is required that is impermeable to ions. Second, distinct ion pumps must be present, one to generate an electrochemical gradient across the membrane and the other to consume or harness this gradient: for example, to drive ATP synthesis. In the cell, these components form the enzymes of the respiratory chain, or electron transport chain (ETC), and of oxidative phosphorylation.

In mitochondria, protons are pumped/translocated across the membrane to establish a proton motive force (Δp). The Δp is composed of the potential created by the difference in H^+ ion concentration between the two sides of the membrane (ΔpH) and the difference in electrical or

membrane potential ($\Delta\Psi$) created by the charge separation across the membranes. Δp is defined in terms of both of these components by **Equation 1.1**.

$$\Delta\mathrm{p} = \Delta\Psi - \frac{RT\Delta\mathrm{pH}}{F}$$

or, at 25 ˚C:

$$\Delta\mathrm{p} = \Delta\Psi - (59\ \mathrm{mV})\Delta\mathrm{pH}$$

Equation 1.1. The proton motive force (Δp) described as a combination of $\Delta\Psi$ and ΔpH. *F* is the Faraday constant (9.65×10^{-2} kJ mol^{-1} mV^{-1}), *R* is the molar gas constant (8.31 J mol^{-1} K^{-1}) and *T* is the temperature (K). At 25 ˚C, the equation can be simplified further, with the Δp expressed in mV.

The respiratory chain regenerates Δp through redox reactions (reduction–oxidation reactions of enzymes and nutrients, respectively) and ATP is synthesised in response (phosphorylation reaction). Together 'oxidative phosphorylation' powers the cell. The enzymes that catalyse oxidative phosphorylation and their mechanisms are explored in this thesis.

1.1. Mitochondria

In non-photosynthetic eukaryotic cells, oxidative phosphorylation occurs in mitochondria. Mitochondria are double-membrane organelles possessing an outer mitochondrial membrane (OMM), which is a freely permeable (to small molecules) membrane containing porins/voltage-depended anion channels (VDACs), and an inner mitochondrial membrane (IMM), which is impermeable to ions and metabolites. The IMM adopts a highly invaginated morphology, forming cristae, in which the respiratory chain enzymes are localised. The space between the IMM and OMM is called the intermembrane space (IMS), equivalent to the periplasm of prokaryotes. Where the IMM follows the OMM it is called the inner boundary membrane (IBM), and this is where many import and export proteins and machineries, for both metabolites and proteins, are predominantly located. Proteins are imported into the mitochondria via the TIM and TOM complexes (translocases of the inner and outer membrane, respectively), and metabolites and ions are exchanged across the membranes through exclusive mitochondrial transporters and channels (Bauer et al., 2000; Kunji, 2004). In particular, the adenine nucleotide translocase (ANT) is crucial for oxidative phosphorylation, exchanging ADP in the cytosol for ATP in the mitochondrial matrix (Ruprecht and Kunji, 2020).

1.1.1. Roles of mitochondria

Mitochondria not only supply energy to the cell, but also are a hub for metabolism. Pathways linked to mitochondria include the tricarboxylic acid cycle (TCA), β oxidation of fatty acids and the urea cycle. In addition, mitochondria have many other roles in the cell, which are summarised in **Figure 1.1**. They are the workshop for iron–sulfur (FeS) cluster and haem biogenesis (Lill and Stehling, 2013) and play a part in calcium homeostasis and localised signalling, which can regulate mitochondrial metabolism, ATP synthesis and many physiological functions (Giorgi et al., 2018). Furthermore, the release of cytochrome *c* from the IMS into the cell cytosol is a key initiator for apoptosis, by promoting the activation of caspase-9 (Wang and Youle, 2009). Mitochondria have also been seen to activate hypoxic gene expression by the production of reactive oxygen species (ROS), which act as redox signalling molecules (Chandel, 2014).

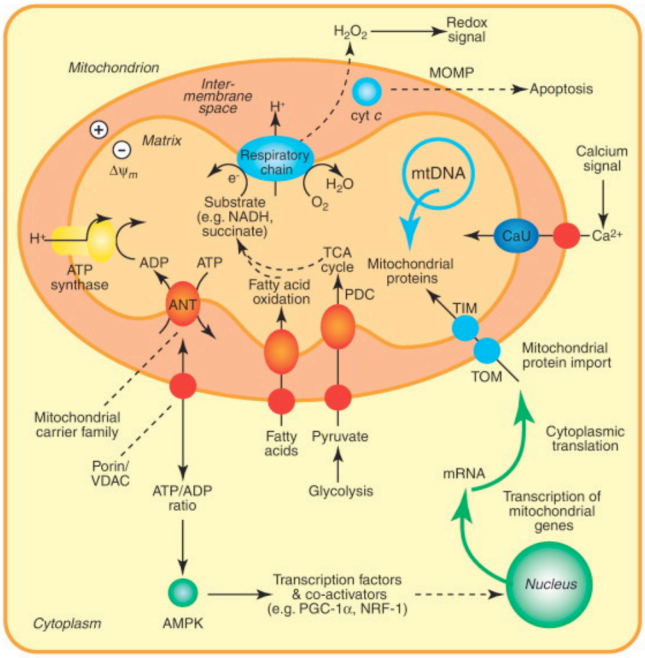

Figure 1.1. Functions and roles of the mitochondrion. ATP is produced by oxidative phosphorylation with glycolytic substrates like pyruvate transported into the mitochondrial matrix via porins and the pyruvate translocase located in the OMM and IMM, respectively. Fatty acid oxidation also provides substrates for oxidative phosphorylation. Nuclear-encoded proteins are imported into the mitochondria via TIM and TOM complexes. The cell can respond to a low cytosolic ATP/ADP ratio by activation of AMP-dependent kinase (AMPK), which in turn can affect protein transcription in the nucleus. ROS production by the respiratory chain can act as redox signalling molecules to the cell, and the release of cytochrome *c* can induce apoptosis when the outer membrane becomes permeabilised. Import of calcium through the calcium uniporter also provides regulation to the cell and mitochondrial functions. Figure taken from Smith et al. 2012.

1.1.2. Mitochondrial origins

A distinct feature of mitochondria is that they contain their own DNA, which in the case of humans, encodes 13 mitochondrial proteins, 22 transfer RNAs and two ribosomal RNAs in a small, circularised chromosome (16,569 base pairs (bp) in human mitochondrial DNA) (Taanman, 1999). Multiple copies of this mitochondrial (mt) DNA can be found within one mitochondrion. Interestingly, the encoded proteins are all hydrophobic, membrane-bound subunits of the respiratory chain enzymes. mtDNA is thus most likely to be an evolutionary leftover from the creation of mitochondria in an endosymbiotic event that led to the formation of eukaryotic cells. Endosymbiotic theory suggests that eukaryotic cells formed when a microbe engulfed or assimilated another prokaryotic cell (Margulis, 1967) to remove competition for resources or as a consequence of their close localisation. Over time, many functions of the assimilated prokaryotic cell were taken over by the host cell, or lost as the cell lost autonomy, eventually leading to the cells becoming co-dependent on one another. The protomitochondria have been suggested to originate from the assimilation of an α-proteobacterium. Remnants of such an event can be seen in existing eukaryotic cells, including the presence of cardiolipins and porins in the IMM and OMM, respectively, which are otherwise only found in bacterial cell membranes (Mileykovskaya and Dowhan, 2009; Zeth and Thein, 2010), and the existence of circularised mtDNA.

1.2. The respiratory complexes of oxidative phosphorylation

1.2.1. Overview

Oxidative phosphorylation encompasses five membrane-bound, multi-subunit enzyme complexes, four of which form the mitochondrial respiratory chain, or ETC (**Figure 1.2**). Electrons can enter the respiratory chain through the oxidation of NADH at NADH:ubiquinone oxidoreductase (complex I; CI) and oxidation of succinate at succinate:ubiquinone oxidoreductase (complex II; CII). Both these complexes transfer two electrons to the electron acceptor ubiquinone (Q), a hydrophobic, membrane-constrained molecule, thus reducing it to ubiquinol. Other routes for supplying electrons to the respiratory chain by ubiquinone reduction include the electron-transferring-flavoprotein (ETF) dehydrogenase and *s*,*n*-glycerophosphate dehydrogenase. The ubiquinol is subsequently re-oxidised to ubiquinone at ubiquinone:cytochrome *c* oxidoreductase (complex III; CIII). In two, single-electron transfer steps, the single subunit protein cytochrome *c* (cyt *c*), which is found in the IMS, transfers electrons to the terminal complex, cytochrome *c* oxidase (complex IV; CIV). At complex IV, electrons are finally transferred to reduce oxygen. The full reduction of oxygen to water requires four electrons (two reducing equivalents of NADH or succinate). The overall transduction of electrons from NADH or succinate to oxygen is energetically favourable, with

a redox potential energy difference (ΔE) of –1.14 or –0.8 V, respectively. The energy is captured by the enzyme complexes to pump or translocate protons across the IMM, establishing a Δp, where the mitochondrial matrix has a relative deficiency of protons (ΔpH) and the IMS is relatively positively charged ($\Delta \Psi$). Per NADH oxidised, 10 protons are pumped or translocated across the IMM. Fewer protons, 6, contribute to the Δp via succinate oxidation. The Δp of respiration is predominantly consumed by the final enzyme complex of oxidative phosphorylation, ATP synthase (complex V; CV), to synthesise ATP in a rotary mechanism. In the mitochondrial ATP synthase, 8 protons are consumed per 3 ATP molecules synthesised (2.67 protons per ATP).

This thesis focuses on complex I and how its mechanism can be studied. Here, an overview of the other complexes involved in oxidative phosphorylation will be discussed first before considering complex I in more detail. Properties of the ATP synthase will also be discussed in more detail in Chapter 3.

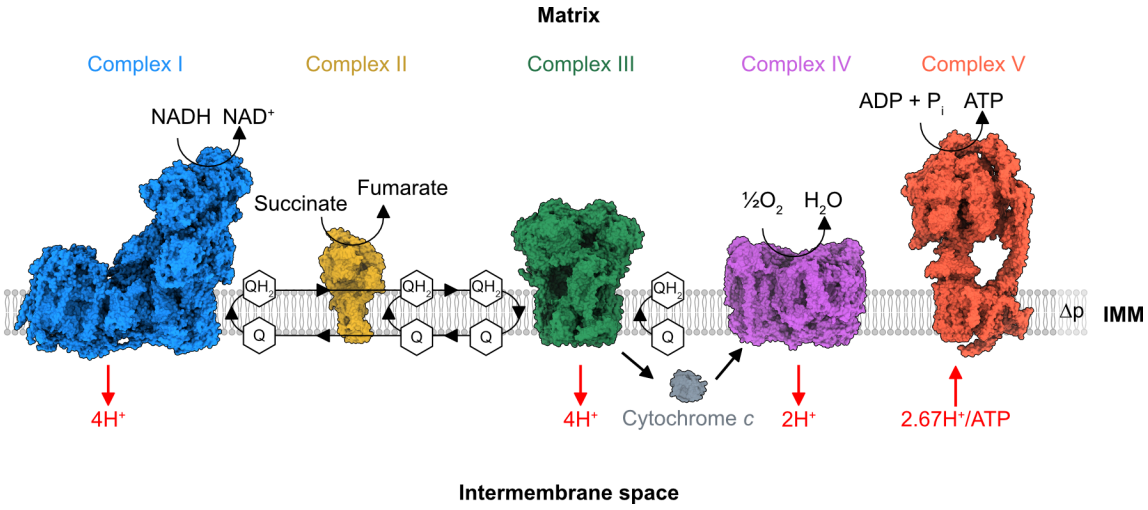

Figure 1.2. Complexes of oxidative phosphorylation on the inner mitochondrial membrane. Complexes I–V and cytochrome *c* are shown. The oxidoreduction of the ubiquinone pool at each enzyme is shown. The numbers of protons that each complex releases to the IMS per two electrons (the number of protons translocated) are shown in red. Contributions to the Δp by protons, such as those required to protonate oxygen to water, are not shown. The number of protons consumed by complex V to generate one molecule of ATP in the mammalian mitochondrial enzyme is also shown in red.

1.2.2. Succinate:ubiquinone oxidoreductase (complex II)

Succinate:ubiquinone oxidoreductase (complex II) links the TCA cycle to the ETC by coupling the oxidation of succinate to fumarate with the reduction of ubiquinone. It is the only membrane-bound enzyme of the TCA cycle. The structure of the mammalian mitochondrial complex II from porcine heart is shown in **Figure 1.3** (Sun et al., 2005). The complex consists

of four separate subunits, two in the hydrophilic domain (SdhA and SdhB) and two in the membrane domain (SdhC and SdhD). Complex II is the only ETC complex for which all subunits are encoded by the nuclear DNA. During enzyme turnover succinate is oxidised to fumarate at the flavin dinucleotide (FAD) cofactor in the SdhA subunit, or flavin dinucleotide-binding protein (FP) (Cecchini, 2003). Two electrons are then transferred in a stepwise manner down a chain of three FeS clusters ([2Fe-2S], [4Fe-4S] and [3Fe-4S]), which are present in the iron–sulfur-binding protein (ISP), or SdhB. Electrons are finally passed onto ubiquinone bound in the membrane domain, reducing it to ubiquinol. Importantly, all electron transfer steps are within ~14 Å of each other, which allows sufficiently fast electron transfer via electron tunnelling, leading to unimpeded catalytic turnover (Moser et al., 2006). Interestingly, complex II possesses a low-potential cytochrome *b* haem (–185 mV) bound in the SdhC and SdhD subunits, which does not appear to take part in the catalytic mechanism (Kim et al., 2012). During ubiquinone reduction, complex II does not contribute to the Δp across the IMM. Like most ETC complexes, complex II catalysis is reversible.

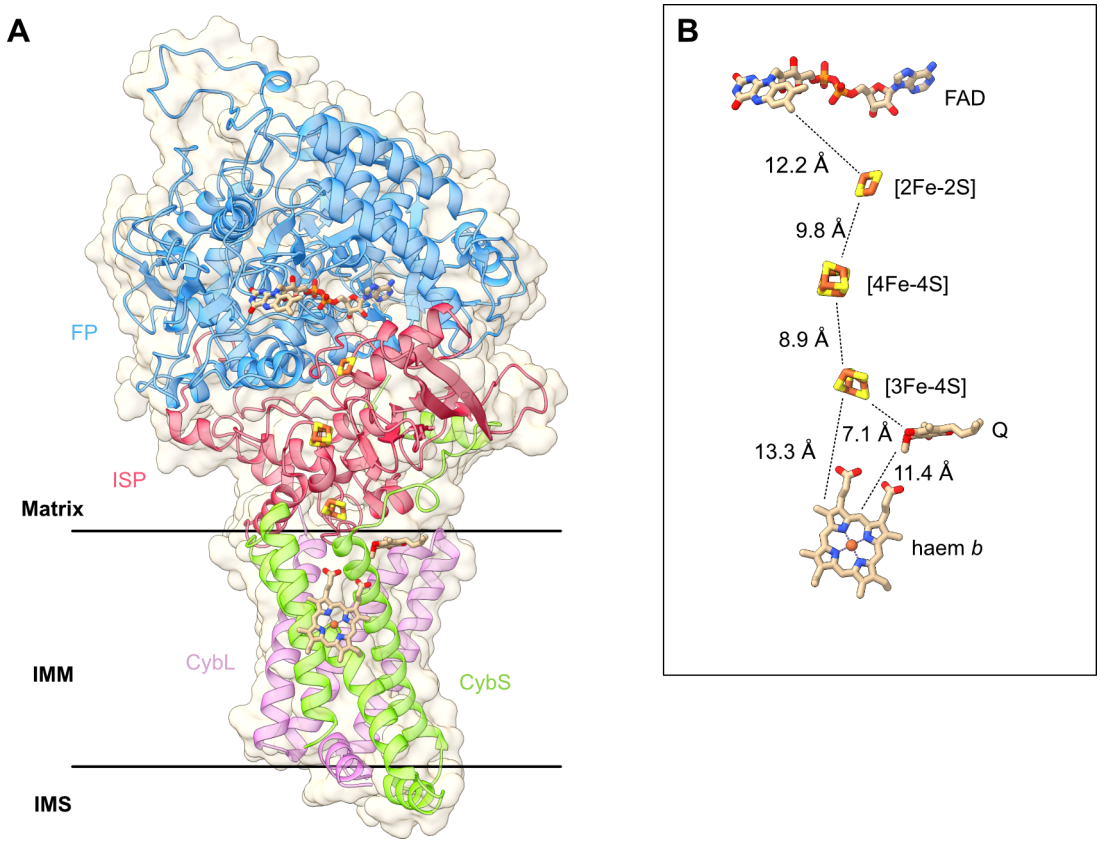

Figure 1.3. Structure of complex II from porcine heart (Sun et al., 2005). (A) The four subunits are shown. The flavin dinucleotide-binding subunit (FP/SdhA) and the FeS-binding subunit (ISP/SdhB) form the hydrophilic domain. The two remaining subunits form the membrane domain and are the site for quinone and cytochrome *b* haem binding (CybL/SdhC and CybS/SdhD). (B) Electron transfer chain to ubiquinone (Q) in complex II. The distances between cofactors and prosthetic groups are highlighted.

1.2.3. Ubiquinone:cytochrome *c* oxidoreductase (complex III)

The next component of the ETC is ubiquinone:cytochrome *c* oxidoreductase (complex III, cytochrome bc_1 complex). Complex III takes ubiquinol and extracts two electrons to reduce cytochrome *c* in two, one-electron steps. During this process, complex III contributes two protons to the Δp, not by direct proton pumping but by protonation and deprotonation events of ubiquinone in a modified Q cycle. The structure of the functional homodimer of complex III from human cells is shown in **Figure 1.4** (Guo et al., 2017). The mammalian enzyme possesses 11 subunits and contains a 2Fe-2S cluster, named the Rieske cluster, which has a characteristic coordination to two His and two Cys residues and is contained within the Rieske protein. The enzyme also possesses high ($E_{m,7}$ = 100 mV) and low ($E_{m,7}$ = –30 mV) potential haem cofactors (b_H and b_L, respectively) and two ubiquinone/ubiquinol-binding sites, one near the matrix side of the protein (Q_i) and the other closer to the IMS (Q_o). The basic principles for the enzyme mechanism are shown in **Figure 1.4**. Ubiquinol binds to the Q_o site and electrons are bifurcated; one electron is transferred to the Rieske cluster ($E_{m,7}$ = 250 mV) and the other to the b_L haem (Sarewicz et al., 2021). The electron received by the Rieske cluster is passed onto a cyt c_1 haem, by movement of the Rieske protein, which subsequently reduces cyt *c*. The single electron on the b_L haem is transferred to the b_H haem and reduces a single ubiquinone molecule bound in the Q_i site, forming a semi-ubiquinone intermediate. The cycle fully repeats for a second time, oxidising a second ubiquinol molecule and further reducing the unstable semi-ubiquinone intermediate to ubiquinol. Consequently, two ubiquinol molecules are oxidised and one ubiquinone is reduced, leading to an overall reaction where one ubiquinol molecule is oxidised and a net two protons are added to the Δp as a result of the deprotonation and protonation events of the ubiquinol cycle (Sarewicz et al., 2021). Complex III catalysis is thermodynamically reversible.

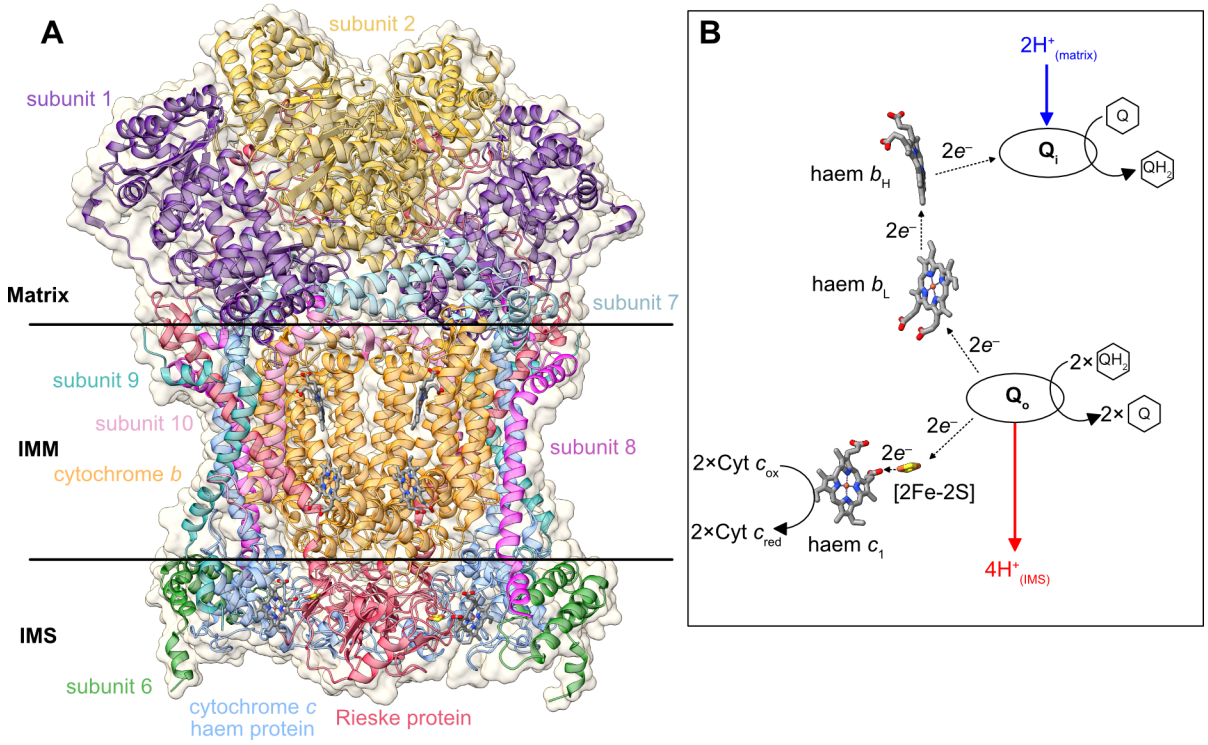

Figure 1.4. Structure of complex III from human cells (Guo et al., 2017). (A) Architecture of the homodimer of complex III. Subunits are colour coded with their labels. (B) Depiction of the cofactors and prosthetic groups in a complex III monomer, and the pathway of electrons during ubiquinol oxidation. Two protons are taken up from the matrix to protonate one ubiquinone (blue arrow) and four protons are released into the IMS on the oxidation of two ubiquinol molecules (red arrow). Electrons are bifurcated from the Q_o site, as highlighted by the arrows showing electron flow.

1.2.4. Cytochrome *c* oxidase (complex IV)

Cytochrome *c* oxidase (complex IV) is the final energy-transducing enzyme complex in the mammalian mitochondrial respiratory chain. More specifically, complex IV is an aa_3-type oxidase, the only terminal oxidase present in mammalian mitochondria. Other organisms possess different types of terminal oxidases with different haem groups, but aa_3 oxidases are the major terminal oxidase found in species containing complex III and cyt *c*. Catalytically, complex IV receives electrons from cyt *c* in four, single-electron transfer steps (four cyt *c* enzymes) and uses these electrons to reduce oxygen to two molecules of water. Two electrons are extracted from cyt *c* on the IMS face to reduce $½O_2$ and two protons are taken from the matrix side to protonate it to water, automatically generating a Δp. In addition, per $½O_2$ reduced, complex IV pumps two protons across the IMM, contributing to the Δp (Wikström, 1977). The enzyme reaction is irreversible, which helps drive the reduction of oxygen and respiration. Mammalian complex IV consists of 13 subunits, with the catalytic core formed by three 'core' subunits encoded by the mitochondrial DNA (**Figure 1.5A**). A summary of the cofactors and reaction mechanism of complex IV are depicted in **Figure 1.5B**. All electron

transfer reactions are single-electron steps, but are repeated for the four cyt *c* donors. Cyt *c* (reduced by complex III) in the IMS transfers an electron to a dinuclear Cu_A centre bound in the subunit COX2. The electron is then transferred to an *a*-type haem group and subsequently to an a_3-type haem coordinated to a copper atom (Cu_B). Molecular oxygen coordinates this site, from which it accepts four electrons to fully reduce it to water, with the uptake of four protons from the matrix to protonate the two nascent water molecules. For each single-electron reduction of oxygen, a single proton is pumped by complex IV across the IMM. The mechanism and pathways by which the protons are pumped and travel to protonate reduced oxygen are not fully understood, but there are three proposed channels, the H-, K- and D-channels (**Figure 1.5C**) (Rich and Maréchal, 2013). The D-channel has been suggested as the route for the translocated protons, and for at least some of the protons for oxygen protonation. However, a more recently described H-channel has also been suggested to translocate protons in vertebrates (Kamiya et al., 2007). A proton import channel has been proposed for the K-channel (Iwata et al., 1995). Uncertainty remains about the role of each proposed channel and these are still contested issues. Interestingly, mutations in complex IV have been created in the D-channel in bacteria and the H-channel in mammalian complex IV, in which proton pumping is abolished despite normal rates for oxygen reduction and electron transfer (Pfitzner et al., 2000; Shimokata et al., 2007; Zhu et al., 2010). These 'uncoupling' mutations are important factors to consider when describing the proton pathways.

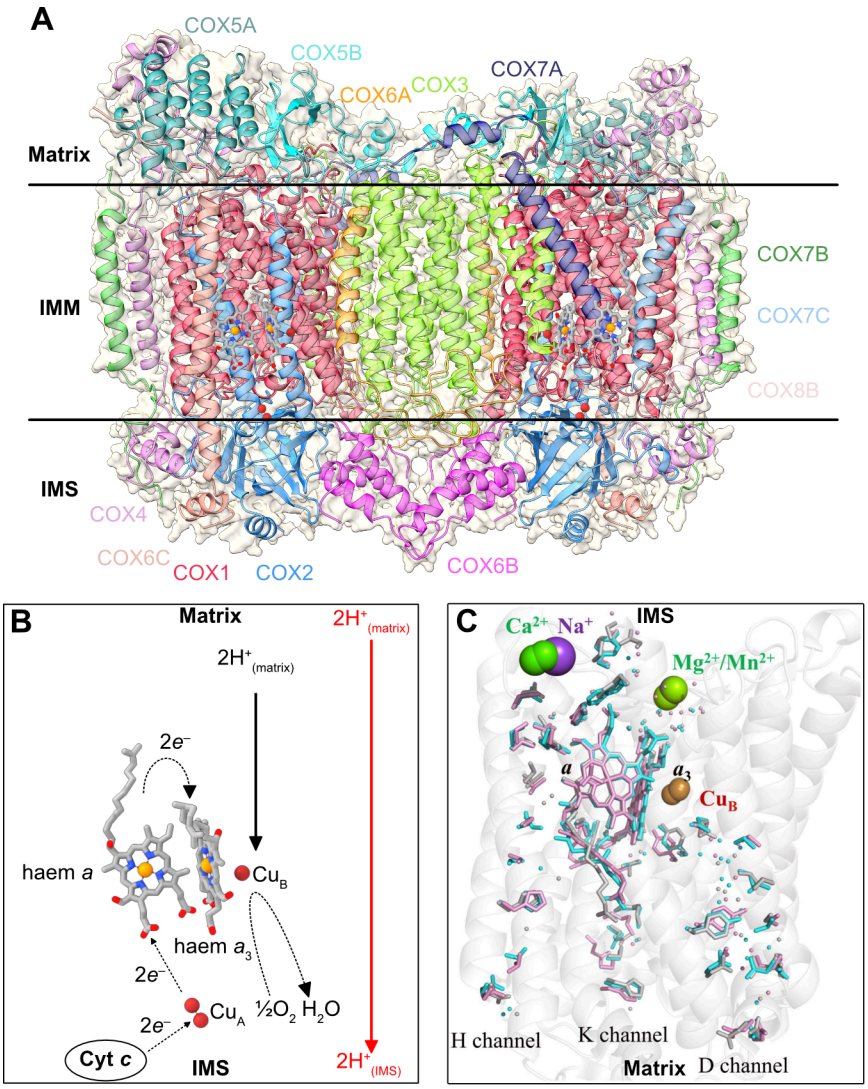

Figure 1.5. Structure and reaction scheme of complex IV from bovine heart (Tsukihara et al., 1996). (A) Structure of the functional homodimer of mammalian complex IV from bovine heart (PDB: 1OOC). Subunits are colour coded with their labels. (B) Overview of the cofactors in complex IV and the overall reaction scheme/pathway. Pumped protons per two electrons are shown in red. (C) Proposed proton channels in complex IV. Note, the enzyme is shown in the opposite orientation to panels A and B, with the IMS and matrix at the top and bottom respectively. The H-, K- and D-channels are highlighted in three superimposed structures from bovine heart, *Paracoccus denitrificans* and *Rhodobacter sphaeroides*. The figure in panel C was taken directly from Rich and Maréchal, 2013.

1.2.5. F_1F_O-ATP synthase

F_1F_O-ATP synthase (complex V) harnesses the Δp generated by respiration in a rotary mechanism to drive ATP synthesis from ADP and P_i. All F_1F_O-ATP synthases contain two functional domains, the soluble F_1 domain and the membrane-intrinsic F_O domain (**Figure 1.6A**). The F_1 domain contains three alternating α and β subunits arranged in a circular structure, which is connected to the F_O domain by a central stalk made up of the γ, δ and ε subunits. The F_O domain contains the *a* subunit and a ring of *c* subunits, which vary in

stoichiometry between species ($c_{8–17}$). In mammalian mitochondrial ATP synthase, the *c*-ring possesses 8 subunits (Watt et al., 2010), but different numbers of *c* subunits are found in other organisms. The yeast enzyme possesses 10 subunits (Symersky et al., 2012) and the bacterial enzyme possesses a range of numbers of *c* subunits ($c_{9\text{-}17}$) (Kühlbrandt, 2019). The F_1 and F_O domains are also connected via a peripheral stalk, which acts as a stator, preventing the α and β subunits rotating during turning of the central stalk (**Figure 1.6A**).

To synthesise ATP, ∆p is consumed to drive a rotary mechanism. Protons enter a half channel in the *a* subunit, from where they are able to protonate key aspartate or glutamate residues near the centre of the *c*-ring subunits. The protonation of these residues drives rotation of the *c*-ring, as the neutralised charges move in the direction of the more hydrophobic environment of the lipid belt (**Figure 1.6B**). This repeats for each *c*-ring subunit. The residues are subsequently deprotonated as they reach another half channel in the *a* subunit. Unidirectional rotation is enforced by the direction of the ∆p and its magnitude. The rotation of the *c*-ring in turn drives the rotation of the central stalk. As the γ subunit revolves around its axis, it induces conformational changes in the immobile α and β subunits with which it interacts. These conformational changes lead to the synthesis of ATP, as shown in **Figure 1.6C**. Catalytic and non-catalytic nucleotide-binding sites are located in the β and α subunits, respectively. The catalytic sites in the β subunit are found either with ATP bound (β_{TP}), with ADP and P_i bound (β_{DP}), or empty (β_E). During ATP synthesis, rotation of the γ subunit in the clockwise direction (looking down onto F_1 from the matrix) causes the β subunit-binding sites to cycle from empty to the ADP + P_i bound state, followed by the final ATP-bound states as ATP is synthesised (Abrahams et al., 1994). The functions of the non-catalytic sites in the α subunits are ambiguous, but it has been suggested that binding of nucleotides at these sites can regulate ATP synthase activity (Jault et al., 1995; Milgrom and Cross, 1993). For every 360˚ rotation of the *c*-ring, three molecules of ATP are synthesised. Differences in the number of *c* subunits between species leads to altered H^+/ATP stoichiometries. In bovine mitochondria, the 8 subunit *c*-ring yields a stoichiometry of 2.67, but in organisms such as *Paracoccus denitrificans*, which possesses a 12 subunit *c*-ring, the stoichiometry is higher, at 4 (Morales-Ríos et al., 2015; Spikes et al., 2020). The reason for these different stoichiometries is unclear, but it is possible that this is an adaptation to optimal growth conditions or to the physiological environment (Kühlbrandt, 2019).

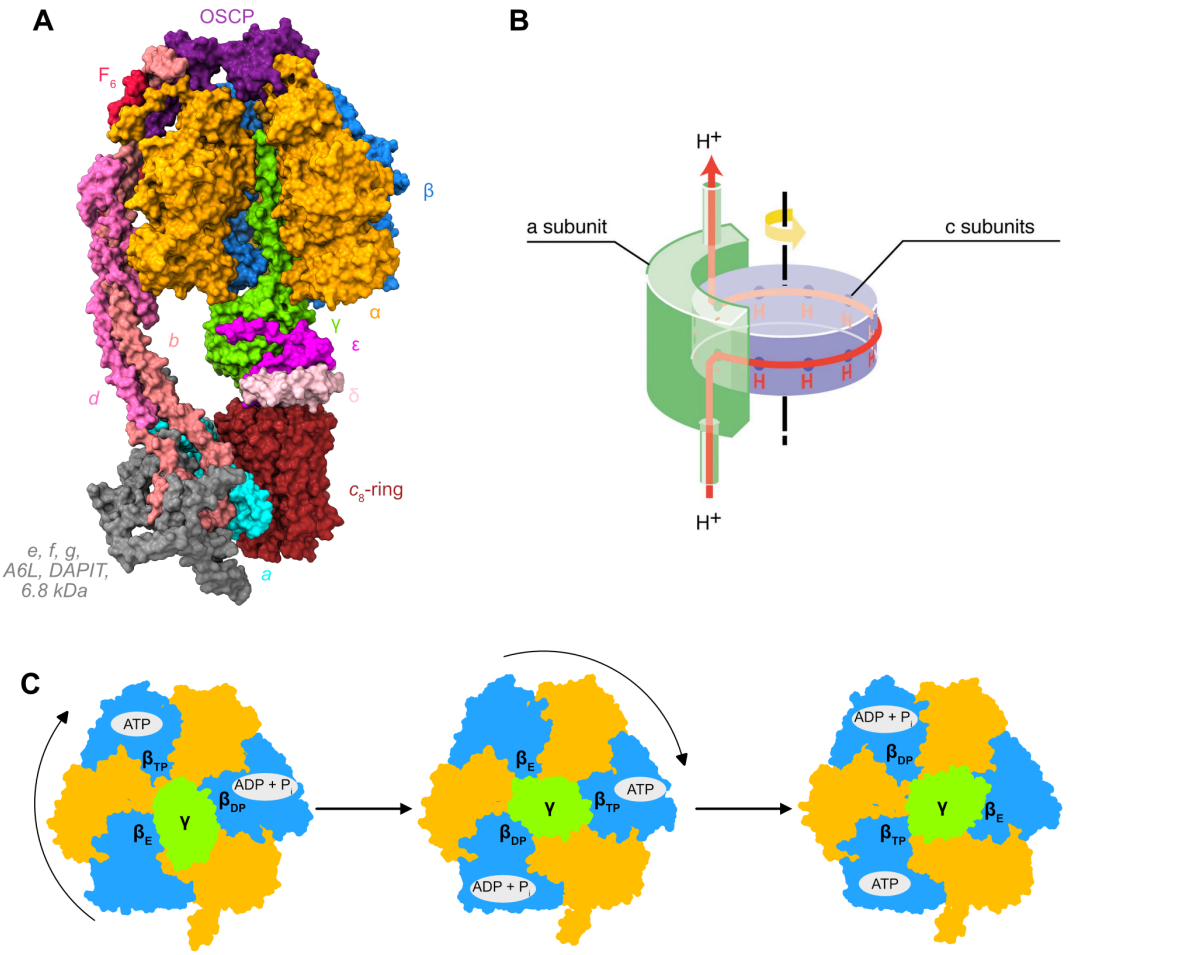

Figure 1.6. Structure and mechanism of ATP synthase. (A) Structure of bovine ATP synthase monomer (PDB: 6ZPO) (Spikes et al., 2020). One of the front β subunits is removed so the central stalk can be viewed. Subunits are colour coded with their labels. Additional membrane-bound subunits in the mammalian enzyme are shown in grey. (B) Cartoon model for the mechanism of proton transfer inducing *c*-ring rotation in ATP synthase. This figure was taken directly from Walker (2013). (C) Rotary mechanism for the synthesis of ATP shown looking from the matrix side onto the F_1 domain. Rotation of the γ subunit induces conformational changes at the αβ subunit interface. The catalytic nucleotide-binding sites in β subunits are shown in three different conformations: ATP bound (β_{TP}), ADP and P_i bound (β_{DP}), and empty (β_E). The figure was generated using PDB files 6YYO, 6ZR1 and 6Z1U of the bovine ATP synthase F_1 domain resolved in three different states (different angle of the γ subunit) (Spikes et al., 2020).

The mitochondrial ATP synthase is fully reversible—it can instead hydrolyse ATP and pump protons across the IMM to establish a Δp when the Δp is depleted, for example, during lack of oxygen where respiration is halted. However, it is not always favourable to hydrolyse ATP, as this will deplete the ATP pool in the cell. Hence, mitochondria and other organisms have evolved regulatory mechanisms to inhibit the reverse ATP hydrolysis reaction. In mammalian mitochondria, an inhibitory protein, IF_1, inserts itself at the αβγ interface during a near full turn of the enzyme, preventing further rotation in the anticlockwise hydrolysis direction (Gledhill et al., 2007). Other inhibitory mechanisms have been proposed for other organisms in place of

IF_1 (Krah et al., 2018; Morales-Ríos et al., 2010; Zarco-Zavala et al., 2018). These mechanisms will be discussed in more detail in Chapter 3 where the mechanism of inhibition for the bacterial ATP synthase from *Paracoccus denitrificans* is explored.

1.3. Complex I

The main entry point for electrons into the respiratory chain is via NADH oxidation at complex I. Complex I catalyses the oxidation of NADH at a flavin mononucleotide (FMN) site and transfers electrons in one-electron steps down a chain of seven FeS clusters to the terminal FeS cluster, labelled N2. Two electrons are transferred sequentially to ubiquinone, reducing it to ubiquinol. Somehow, during this electron transfer process, the energy is captured and coupled to the translocation of four protons across the IMM, contributing to the Δp (Jones et al., 2017). Complex I is a crucial metabolic enzyme that helps sustain metabolism by regenerating the NAD^+ pool in the mitochondrial matrix from oxidation of NADH predominantly generated from the TCA cycle and β-oxidation of fatty acids. Complex I is also a key site of ROS generation in the cell (Kussmaul and Hirst, 2006; Pryde and Hirst, 2011), and is the origin of a wide range of neuromuscular and metabolic disorders (Fassone and Rahman, 2012; Fiedorczuk and Sazanov, 2018). Its dysfunction has been associated with ~30% of all mitochondria-linked diseases (Mimaki et al., 2012) and it is a target for drug treatments such as anti-hyperglycaemic biguanides (Bridges et al., 2016). Conditions such as Leber's hereditary optic neuropathy (LHON), which leads to degeneration of the heart and eyes, are associated with specific mutations in complex I (Ylikallio and Suomalainen, 2012). Much is known about the NADH oxidation and electron transfer reaction in complex I, but the mechanism to capture the energy required for proton pumping, as well as the proton-pumping mechanism itself, are outstanding questions in complex I research. Understanding the basic mechanism of complex I is crucial for understanding its dysfunction in mitochondria-linked diseases and disorders, and how they may be treated. A detailed look into the structure and known/proposed mechanistic features of complex I will be presented here.

1.3.1. Architecture of complex I

Respiratory complex I forms a distinct 'L' shape with two major domains: the peripheral arm, containing the FMN, FeS clusters and part of the Q-binding site, and the membrane arm, which forms the remainder of the Q-binding site and the proton-pumping modules (**Figure 1.7**). In its most minimal form, as found in bacterial species, complex I is composed of 14 conserved catalytic 'core' subunits. Seven of these subunits form the hydrophilic domain and the remaining seven form the hydrophobic domain, which is encoded by the mtDNA. In the

mammalian mitochondrial enzyme, these 14 core subunits are supplemented with up to 31 'supernumerary' subunits, which are generally not considered to be involved in the enzyme mechanism but may play other roles, such as in stabilising the enzyme, in complex assembly and enzyme regulation (Hirst, 2011; Padavannil et al., 2022). This makes mitochondrial complex I around 1 MDa in size, the largest of the respiratory complexes. The number of supernumerary subunits differs between those species that contain them, with the yeast enzyme from *Yarrowia lipolytica* possessing 29 supernumerary subunits (Kmita and Zickermann, 2013; Morgner et al., 2008). In some bacterial species, such as in α-proteobacteria, relatively few supernumerary subunits have been observed (Baradaran et al., 2013; Kolata and Efremov, 2021; Yip et al., 2011). The core subunits are highlighted in **Figure 1.7**.

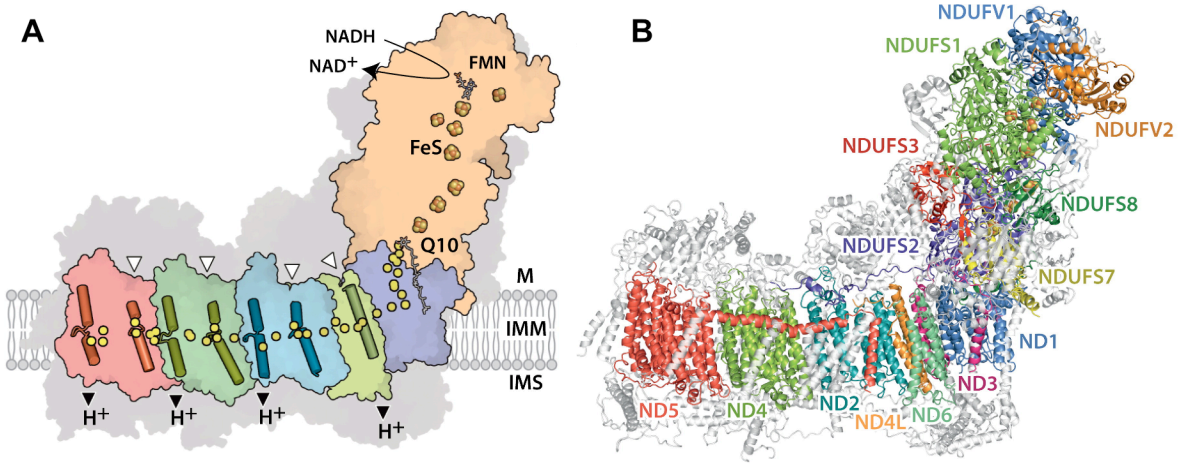

Figure 1.7. Overall architecture of complex I. (A) Schematic of mammalian complex I from mouse (PDB: 6G2J) highlighting key features of the structure. The structure is coloured according to key features; the hydrophilic domain in orange and the three antiporter-like subunits in blue (ND2), green (ND4) and red (ND5), commonly considered as separate proton-pumping modules. A putative fourth proton pump is shown in purple (ND1, ND3) or light green (ND4L, ND6). Oxidation at the flavin mononucleotide (FMN) site is shown with a chain of seven FeS clusters that connect the FMN site to the ubiquinone-binding site. A fourth FeS cluster, to the right of the FMN (in the figure), is considered not to participate in electron transfer (Barker et al., 2007). Proton import and export is shown by white and black triangles, respectively. Discontinuous helices in the antiporter subunits are shown and key conserved charge residues connecting the Q-site to proton pumping are shown as yellow circles. (B) Subunit composition of mitochondrial complex I from mouse heart. The 14 core subunits are highlighted, and the 31 supernumerary subunits are coloured in grey. Figure taken from Agip et al. (2019).

The nomenclature for complex I subunits is different depending on the organism from which the complex I originates. Shown in **Table 1.1** is the standard nomenclature for various key species discussed in this thesis. Throughout this thesis the nomenclature used will be that of both the human (*Homo sapiens)* and *Paracoccus denitrificans* enzymes.

Table 1.1. Complex I subunit nomenclature across various species.

Domain	*Bos taurus*	*H. sapiens*	*Yarrowia lipolytica*	*P. denitrificans*	*E. coli*
Hydrophilic arm	75 kDa	NDUFS1	NUAM	Nqo3	NuoG
	51 kDa	NDUFV1	NUBM	Nqo1	NuoF
	49 kDa	NDUFS2	NUCM	Nqo4	NuoD
	30 kDa	NDUFS3	NUGM	Nqo5	NuoC
	24 kDa	NDUFV2	NUHM	Nqo2	NuoE
	PSST	NDUFS7	NUKM	Nqo6	NuoB
	TYKY	NDUFS8	NUIM	Nqo9	NuoI
Hydrophobic arm	ND1	ND1	NU1M	Nqo8	NuoH
	ND2	ND2	NU2M	Nqo14	NuoN
	ND3	ND3	NU3M	Nqo7	NuoA
	ND4	ND4	NU4M	Nqo13	NuoM
	ND4L	ND4L	NULM	Nqo11	NuoK
	ND5	ND5	NU5M	Nqo12	NuoL
	ND6	ND6	NU6M	Nqo10	NuoJ
Supernumerary subunits	10 kDa	NDUFV3			
	13 kDa	NDUFS6	NUMM	PdNUMM	
	15 kDa	NDUFS5	NIPM		
	18 kDa	NDUFS4	NUYM	PdNUYM	
	39 kDa	NDUFA9	NUEM		
	42 kDa	NDUFA10			
	ACP	NDUFAB1α	ACPM		
	ACP	NDUFAB1β			
	AGGG	NDUFB2			
	ASHI	NDUFB8	NIAM		
	B8	NDUFA2	NI8M		
	B9	NDUFA3	NI9M		
	B12	NDUFB3	NB2M		
	B13	NDUFA5	NUFM		
	B14	NDUFA6	NB4M		
	B14.5a	NDUFA7	NUZM		
	B14.5b	NDUFC2	NEBM		
	B14.7	NDUFA11	NUJM		
	B15	NDUFB4	NB5M		
	B16.6	NDUFA13	NB6M		
	B17	NDUFB6	NUUM		
	B17.2	NDUFA12	N7BM	PdN7BM	
	B18	NDUFB7	NB8M		
	B22	NDUFB9	NI2M		
	ESSS	NDUFB11	NESM		
	KFYI	NDUFCI			
	MNLL	NDUFB11			
	MWFE	NDUFA1	NIMM		
	PGIV	NDUFA8	NUPM		
	PDSW	NDUFB10	NIDM		
	SGDH	NDUFB5	NUNM		
			NUXM		
			ST1		

In the mitochondria, the respiratory chain enzymes are known to form respiratory supercomplexes, which are higher order structures where complexes I, III and IV are associated together. The mitochondrial 'respirasome' is generally considered to be made up of a CI_1:$CIII_2$:CIV_1 ratio of complexes, although other stoichiometries exist, such as non-complex I-containing assemblies and even larger 'megacomplexes' containing CI_2:$CIII_2$:CIV_2 (Gu et al., 2016; Guo et al., 2017; Letts et al., 2016; Milenkovic et al., 2017). Shown in **Figure 1.8** is the architecture of the CI_1:$CIII_2$:CIV_1 supercomplex from *Sus scrofa* (pig) at 5.4 Å (Letts et al., 2016). It is unclear what role supercomplexes play in the mitochondria, but using flux control analysis and mutant yeast strains lacking supercomplexes, it has been suggested that supercomplexes channel ubiquinone and cyt *c* between complexes, providing kinetic advantages to the enzyme by preventing diffusion of the substrates to other enzymes (Berndtsson et al., 2020; Bianchi et al., 2004). However, other studies have provided evidence against quinone channelling, based on the quinone pool still being accessible for other enzymes (Blaza et al., 2014; Fedor and Hirst, 2018). Other possibilities for the purpose of supercomplexes include roles to regulate the respiratory chain, decrease ROS production or stabilise/help assemble the respiratory complexes (Milenkovic et al., 2017). Alternatively, they may just be a product of the protein-rich IMM, forming more ordered structures to prevent unwanted aggregation (Blaza et al., 2014).

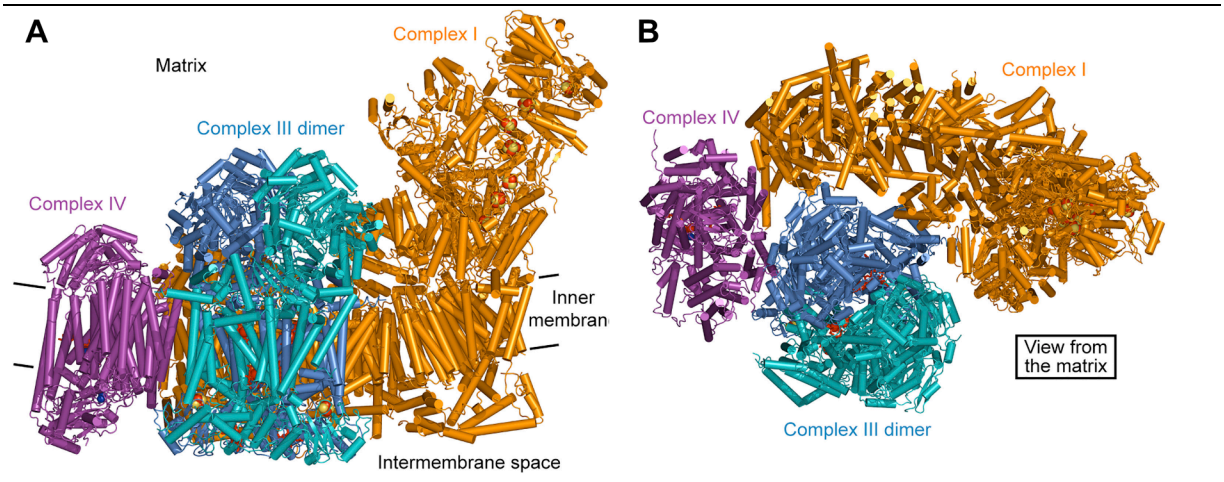

Figure 1.8. Architecture of the CI_1:$CIII_2$:CIV_1 supercomplex from porcine mitochondria from two different viewpoints. Complex I is shown in orange, complex III dimers in blue and cyan and complex IV in purple. (A) Side-on view of the supercomplex along the plane of the membrane. (B) Top-down matrix view of the supercomplex. Figure adapted from Milenkovic et al. (2017).

1.3.2. Flavin site reaction and FeS clusters

The mechanisms of NADH oxidation and intramolecular electron transfer in complex I are the most well-understood elements of complex I turnover. NADH first coordinates to the non-covalently bound FMN factor, as shown in **Figure 1.9A**. The NADH and FMN are positioned such that they facilitate hydride transfer from the C4 of the nicotinamide ring to position N5 of the flavin, oxidising the NADH (Berrisford and Sazanov, 2009). NADH oxidation is reversible, as the reduction potential of NAD^+ is only slightly higher than that of flavin (–340 mV and –380 mV, respectively, at pH 7.5), which has a lower reduction potential than free flavin because the oxidised FMN is bound more strongly than the reduced form (Hirst, 2013). The rate of NADH oxidation in bovine complex I is >15,000 s^{-1}, which is an order of magnitude faster than NADH:ubiquinone oxidoreduction, and so it is not rate limiting to complex I turnover (Birrell et al., 2009). In the *Escherichia coli* enzyme, turnover of one NADH and the subsequent dissociation of NAD^+ occurred within 1 ms, as measured by ultrafast freeze-quenching (Verkhovskaya et al., 2008).

After reduction of the flavin site, electrons pass down a chain of seven FeS clusters to the terminal FeS cluster, N2. The positions of the FeS clusters in the bacterial complex I structure from *Thermus thermophilus* are shown in **Figure 1.9B**. The electron transfer down this chain is not considered rate limiting to catalysis as all clusters are within 14 Å of each other allowing for rapid electron tunnelling (Baradaran et al., 2013; Page et al., 1999). The [2Fe-2S] cluster 'upstream' of the FMN (N1b) is not involved in the intramolecular electron transfer and its role is unclear. In the mitochondrial enzyme it may play a role in stabilising the structure around FMN or it may be an evolutionary relic (Barker et al., 2007; Hirst, 2013). However, in *E. coli* complex I, this cluster is reduced, consistent with its high reduction potential, and it has been proposed that its role is to scavenge electron radicals from the flavin site before the formation of hydrogen peroxide and other highly reactive species (Verkhovskaya et al., 2008). The reduction potential pathway for each cluster and component is shown in **Figure 1.9C**, as determined by electron paramagnetic resonance (EPR) spectroscopy of the bovine enzyme and from estimated values in clusters not detected in EPR analyses. The profile shows alternating reduction potentials from NADH to ubiquinone, which is a common profile for proteins that contain multiple sequential cofactors. This allows for rapid electron transfer between clusters compared to when two low-potential clusters are adjacent to each other (Page et al., 1999; Roessler et al., 2010). The alternating profile may be a result of the electrostatic interactions between adjacent clusters in which the favourable reduction of one cluster makes it less favourable to reduce a neighbouring cluster (Bridges et al., 2012).

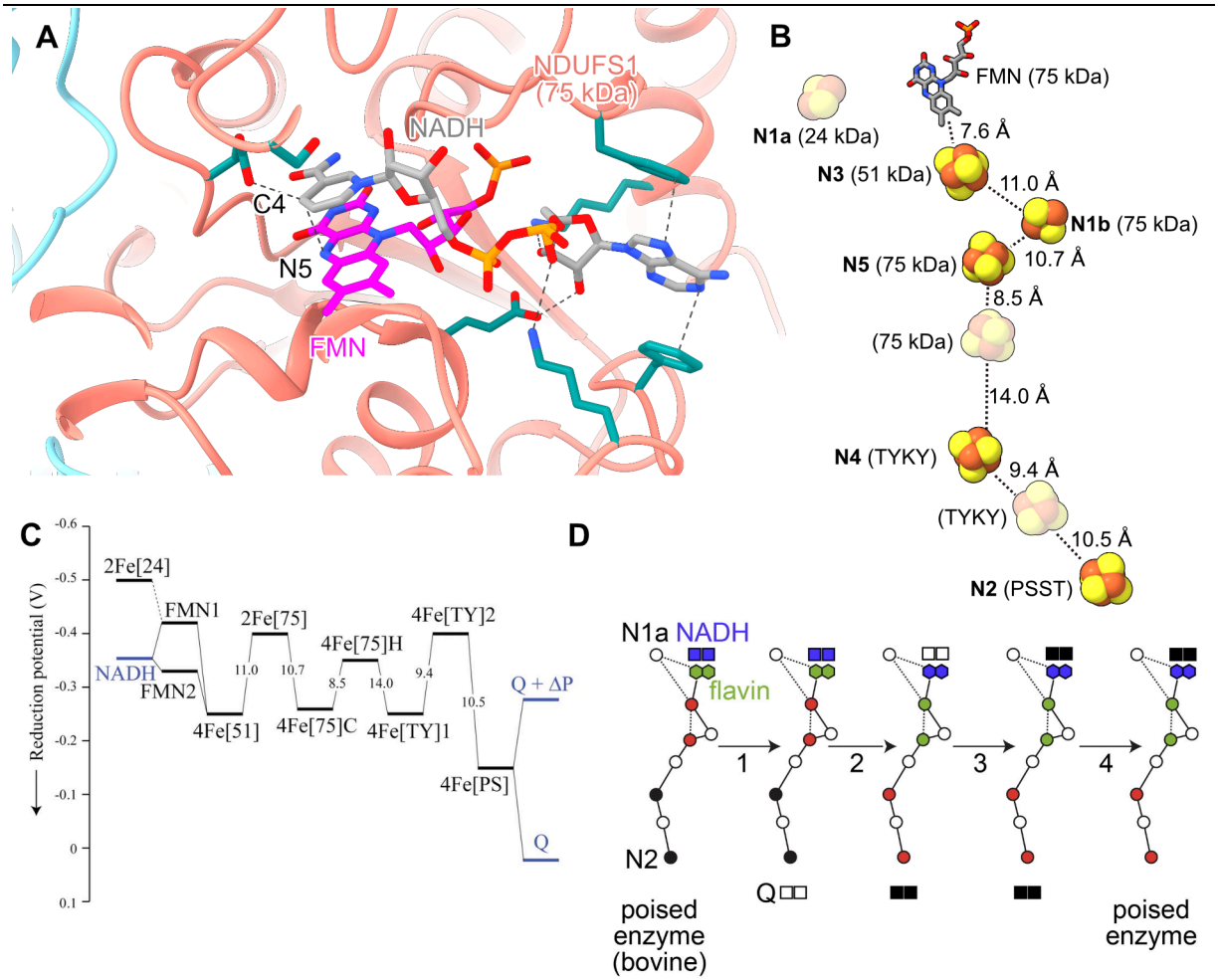

Figure 1.9. NADH binding and intramolecular electron transfer wire of FeS clusters in complex I. (A) NADH binding to FMN in ovine complex I (PDB: 6ZKC). Hydride transfer occurs between the C4 of the nicotinamide ring to position N5 of the flavin. (B) Chain of FeS clusters in *T. thermophilus* (PDB: 4HEA). Distances between clusters are labelled. Transparent FeS clusters do not contribute to the EPR spectrum of the NADH-reduced mitochondrial enzyme. The names of EPR-active clusters (across all species) are shown in bold and the subunit in which each cluster is found is labelled in the bovine nomenclature to match panel C. Figure adapted from Bridges et al. (2012). (C) Reduction potentials for each cluster along the electron transfer wire as measured experimentally or estimated (Bridges et al., 2012). The profile shows alternating potentials as the electrons travel from NADH to ubiquinone. FMN1 and FMN2 are the different potentials for each one-electron reduction step of the FMN site. The potential for ubiquinone is shown by the presence/absence of a Δp. Figure taken from Hirst (2010). (D) Scheme for the delivery of electrons from NADH to ubiquinone (Q) in the bovine enzyme. Electrons occupy alternate clusters. The colours represent pairs of electrons moving along the chain. The enzyme is poised with electrons ready for Q binding. Figure taken from Hirst and Roessler, 2016.

The N2 cluster, as well as other clusters in the chain, can be considered as 'pre-loaded' or 'poised' with single electrons, meaning they are ready to pass electrons onto ubiquinone (De Vries et al., 2015; Verkhovskaya et al., 2008). A proposed scheme for electron transfer from NADH to ubiquinone is shown in **Figure 1.9D**. Upon quinone binding, electrons pre-loaded in the FeS chain are transferred to reduce ubiquinone to ubiquinol. In doing so, electrons refill the FeS chain by stripping electron from the NADH bound to FMN, which is driven by the high

reduction potential of the N2 cluster acting as an electron sink. A new NADH molecule binds, and the enzyme is ready for further Q reduction after exit of the reduced ubiquinol. The entire intramolecular electron transfer between FeS clusters occurs within 100 µs, close to the rate expected for electron tunnelling, suggesting that the reaction is not slowed by additional processes, such as coupling reactions to proton translocation (De Vries et al., 2015; Verkhovskaya et al., 2008). It is likely that the coupling of the energy from NADH oxidation to proton pumping is further downstream from this intramolecular electron transfer, possibly occurring during ubiquinone reduction and ubiquinone entry/exit.

1.3.3. Quinone-binding site

The electron acceptor in human mitochondrial complex I is ubiquinone-10 (Q_{10}). Structurally, Q_{10} possesses a benzoquinone head group with two adjacent methoxy groups and one methyl group attached to the ring. In addition, a chain of 10 isoprenoid groups makes up the Q_{10} tail, conferring extreme hydrophobicity, which limits its localisation to the membrane plane. Different organisms have different native ubiquinone electron acceptors in the membrane, with different isoprenoid chain lengths. Human, bovine and *P. denitrificans* complex I all use Q_{10}, but mouse complex I and the yeast *Yarrowia lipolytica* uses ubiquinone-9 (John and Whatley, 1977; Lass et al., 1997; Olgun et al., 2003). In *E. coli*, ubiquinone-8 is used, with the capacity to switch to menaquinone-8 under anaerobic conditions (Castro et al., 2016; Olgun et al., 2003).

In mitochondrial complex I, ubiquinone enters the enzyme from the IMM though a long binding channel made up of the NDUFS2, NDUFS7, ND1 and ND3 subunits, to position the redox-active head group within 10–12 Å of the terminal N2 cluster located in NDUFS7. Despite being a very hydrophobic molecule, this channel extends above the plane of the membrane to coordinate to a conserved tyrosine and histidine pair in NDUFS2 (**Figure 1.10A+B**) (Baradaran et al., 2013). Halfway down the mostly hydrophobic Q-channel is a cluster of conserved charge residues that form a hydrophilic region (**Figure 1.10B**). These residues form the start of the E-channel, a chain of conserved charge residues that connect the ubiquinone channel to the proton-pumping machinery. This location has been shown to be a key second site for inhibitor binding to complex I, such as rotenone and possibly piericidin A (the first site is at the top of the Q-channel) (Bridges et al., 2020; Kampjut and Sazanov, 2020). Using complex I reconstituted into proteoliposomes, the effect of different isoprenoid chain lengths has been investigated, showing that catalysis was faster and the K_M for ubiquinone was reduced when the number of isoprenoid units reached and surpassed the number necessary to interact with this hydrophilic pocket. Interestingly, shorter chain ubiquinone analogues still elicit the same

proton-pumping stoichiometry, so energy coupling is probably linked with the movement/reactivity of the redox head group instead (Galkin et al., 1999; Jones et al., 2017). Shuttling of the ubiquinone head group between the two sites during catalysis may be key for energy coupling, and some studies have even proposed a second reactive Q-binding site further away from N2, but this remains unclear without further evidence (Haapanen et al., 2019; Parey et al., 2019).

Ubiquinone is sequentially reduced by one-electron reduction steps, meaning a semiquinone will form during turnover before full reduction to ubiquinol. Whether this semiquinone is sufficiently stable and long lived in complex I to play an important role in the energy-coupling mechanism is unclear. Semiquinone signals have been attributed to complex I during turnover in sub-mitochondrial particles (SMPs) (Magnitsky et al., 2002; Yano et al., 2005) and proteoliposomes (Narayanan et al., 2015), but their assignment has so far been ambiguous, with difficulties deconvoluting EPR signals from semiquinone formation in other respiratory enzymes (Wright et al., 2020) and the absence of semiquinone UV-visible absorbance signals suggesting that any semiquinone present is, at best, a short-lived intermediate (Hirst and Roessler, 2016; Verkhovsky et al., 2012).

The complete reduction of ubiquinone to ubiquinol also requires two protonation events. When these events occur during turnover, the source and channels for the protons for protonation is of key importance to the mechanism and energy coupling. Various proton channels for ubiquinol anion protonation have been suggested based on the presence of water molecules as shown by high-resolution structures and mutagenesis studies. A chain of waters in the NDUFS2 subunit from *Y. lipolytica* were conserved with the structurally homologous subunit from the NiFe hydrogenase from *Desulfovibrio vulgaris*, which suggested a potential channel (Grba and Hirst, 2020). An alternative pathway has been suggested in the ND4L subunit, taking protons from the matrix face and transporting them to the Q-site via conserved charged residues (Kampjut and Sazanov, 2020). In addition, residues in the supernumerary subunit NDUFA6 in *Y. lipolytica* have been shown to be essential for complex I turnover, potentially providing a proton import channel for Q protonation (Galemou Yoga et al., 2020). Finally, a study using UV-visible spectroscopy proposed a QH^- anion intermediate that was suggested to play a key role in the coupling of Q reduction to proton translocation. This led to the suggestion of a coupling mechanism based on this intermediate, where protonation to QH_2, potentially via one of the above-suggested channels, is followed by a single deprotonation event that delivers a proton to the proton-pumping machinery. The QH^- anion is then displaced to lower down in the Q-site, from which it is then re-protonated via the E-channel linked to the proton-pumping machinery (Nuber, et al., 2021). In this case, the movement of the QH^- anion

provides the energy for proton translocation. Overall, further studies are required to elucidate Q protonation pathways and the quinone species involved in each step of the mechanism, which are fundamental for unlocking how the energy from Q reduction is captured for proton translocation.

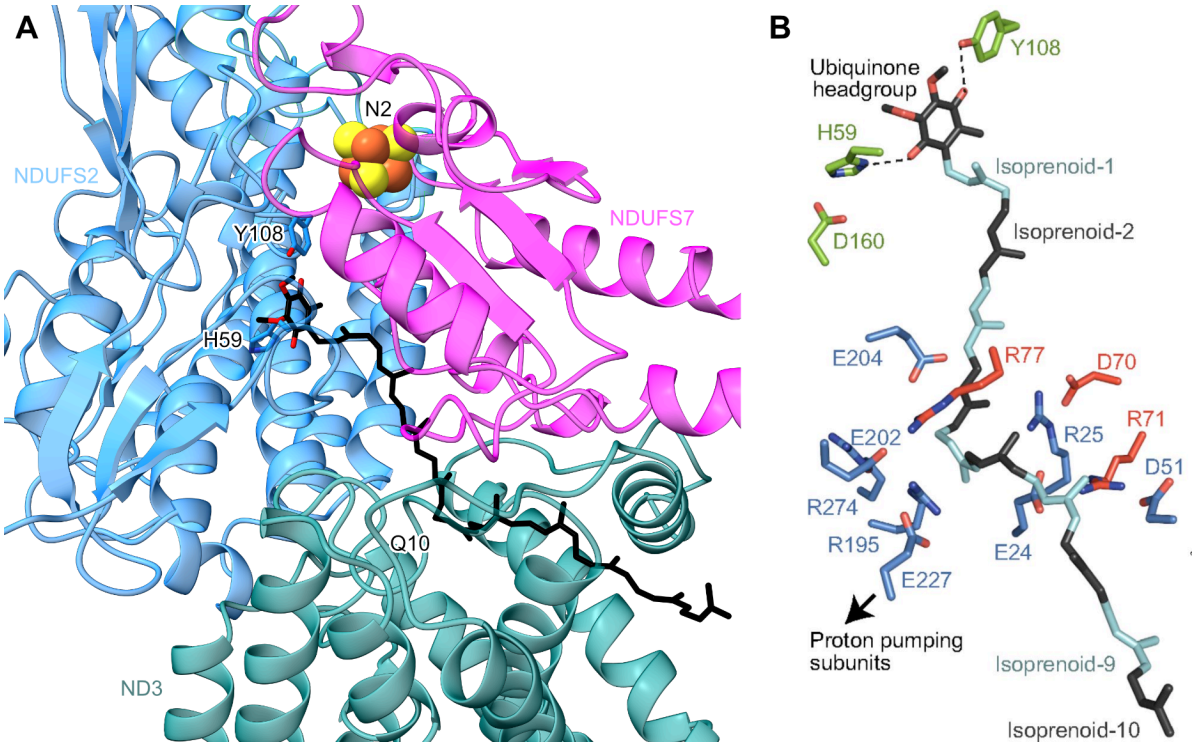

Figure 1.10. Q-binding site in complex I. (A) Ubiquinone-10 docked into complex I from mouse (PDB: 6ZR2). The Q_{10} docking was simulated by the relaxing of atomistic molecular dynamics when Q_{10} was placed in the channel of the bovine enzyme in the same state (Fedor et al., 2017). (B) Coordination of Q_{10} to H59 and Y108 in NDUFS2. Key residues surrounding the Q-channel are highlighted. A 'kink' in the Q_{10} isoprenoid chain occurs roughly halfway down in the locality of a cluster of conserved charge residues in NDUFS7 (red) and ND1 (blue). Figure taken from Fedor et al. 2017.

1.3.4. Membrane domain

The membrane domain of complex I contains the proton-translocation machinery. Complex I pumps four protons across the IMM and the pathways/channels for these pumps are not completely clear (Jones et al., 2017). Of the core subunits, three of the subunits (ND2, ND4 and ND5) are antiporter-like subunits, related to other antiporters found in membrane-bound NiFe hydrogenases (MBH), membrane-bound sulfane sulfur reductases (MBS) and multiple resistance and pH (Mrp) complexes (Yu et al., 2021). In complex I, each of these subunits possess a pair of half channels with two discontinuous transmembrane helices (TMH7 and TMH12) (**Figure 1.11A**). While three of the proton channels are likely to be in the three antiporter subunits, complex I pumps four protons per cycle (Efremov and Sazanov, 2011; Jones et al., 2017). The location of the fourth proton channel is less well defined, but hydration

simulations in the *Thermus thermophilus* complex I structure have highlighted potential water channels that may open and close during turnover (Di Luca et al., 2017) (**Figure 1.11B**). These simulations highlighted a major water channel, and potential site of proton translocation, in the region of the ND1, ND4L and ND6 subunits of complex I, as predicted by structural analysis (Baradaran et al., 2013; Di Luca et al., 2017). Alternatively, recent cryo-EM studies have suggested it is also possible that all four protons are ejected at the ND5 subunit (but imported in various channels) based on resolved water molecules in ND5 and hydration simulations (Kampjut and Sazanov, 2020; Parey et al., 2021). Investigating these proton channels and how the enzyme controls and synchronises proton pumping remain key questions.

Connecting the Q-binding site to the proton-pumping machinery is an E-channel, made up of conserved charge residues and water molecules, which are probably important in coupling the energy from electron transfer to proton pumping. In the central axis of the membrane domain, a chain of key conserved charge residues also exists, with pairs of glutamate and lysine residues in the ND2, ND4 and ND5 subunits considered crucial in energy and charge propagation (**Figure 1.11A+C**) (Sato et al., 2014). Another key feature of the membrane domain is the lateral, transverse α-helix of the terminal ND5 subunit, which spans the membrane. Previous theories have suggested the transverse helix may act as a piston to drive proton translocation, coupling and synchronising the pumps with each other (Efremov et al., 2010). However, mutations and crosslinking studies in the lateral helix have argued against this, and the helix may be more important structurally by clamping the membrane domain. Despite this, other conformational changes in the lateral helix involved with proton pumping cannot yet be discounted (Belevich et al., 2011; Steimle et al., 2012; Zhu and Vik, 2015). Further details of studies investigating proton pumping and energy transduction in the membrane domain will be discussed in Chapter 6.

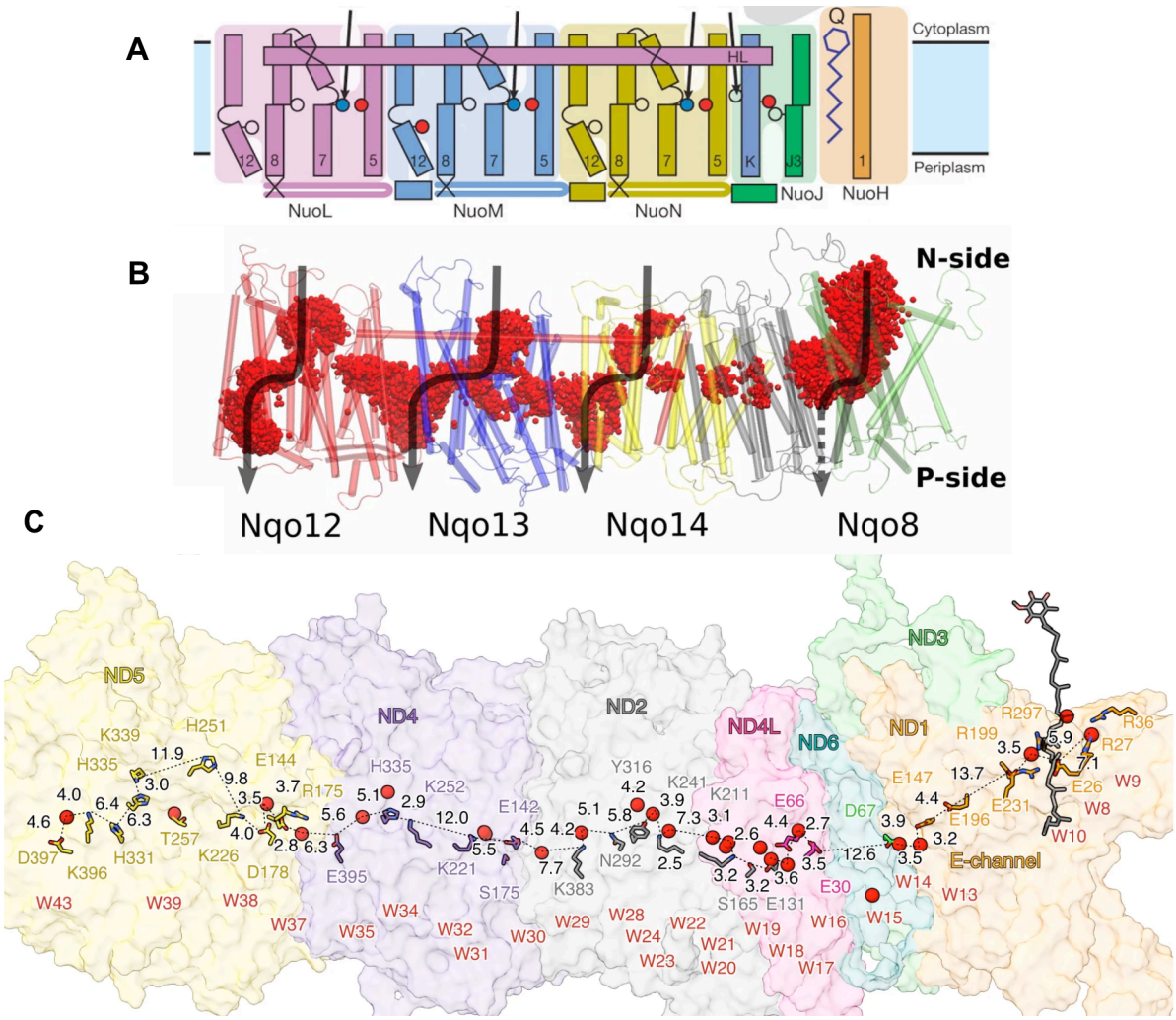

Figure 1.11. Membrane domain of complex I. (A) Cartoon depiction of membrane domain of complex I from *E. coli*. The lateral transverse helix spans the membrane domain and two discontinuous transmembrane helices (TMH7 and 12) are seen in each of the three antiporter subunits forming two half channels. Also shown on the figure are key lysine and glutamate residues represented by circles. Figure adapted from Efremov and Sazanov (2011). (B) Potential water channels in complex I membrane domain from *T. thermophilus* as predicted from seven independent hydration simulations. Four potential channels for protons are highlighted by black arrows. Figure taken from Di Luca et al. (2017). (C) Key conserved charge residues and water molecules that span the central axis of the membrane domain, as identified in the complex I structure from *Y. lipolytica*. The residues and waters form a chain connecting the Q-site to the proton-pumping machinery (the E-channel) and enable charge propagation to the terminal antiporter-like subunit ND5. Figure taken from Grba and Hirst (2020).

1.3.5. Reverse electron transfer in complex I

In standard conditions, complex I operates in the forward reaction, oxidising NADH, reducing ubiquinone and pumping four protons from the mitochondrial matrix to the intermembrane space. This forward reaction is known as forward electron transfer (FET). However, complex I is a thermodynamically efficient catalyst, meaning that it is able to maintain a dynamic equilibrium and that minimal energy is lost in the coupling of electron transfer to the translocation of four protons. In the mitochondrion, complex I operates close to thermodynamic equilibrium, and so under certain conditions it is possible for the system to switch to favour the 'reverse' reaction or reverse electron transfer (RET) (Chance and Hollunger, 1960; Pryde and Hirst, 2011). The RET reaction, instead of generating a Δp, harnesses the energy stored in the Δp to drive electrons from ubiquinol onto the N2 terminal cluster and along the chain of FeS clusters, to reduce the flavin site. Molecules of NAD^+ or oxygen can then access the site and be reduced. This RET reaction becomes thermodynamically favourable when the Q-pool is highly reduced and in the presence of a high Δp (Robb et al., 2018).

Importantly, during RET the electrons on the fully reduced flavin, waiting for NAD^+ to bind, can be easily picked up by oxygen, resulting in a significant production of mitochondrial ROS, in particular, superoxide ($O_2^{\bullet-}$) (Kussmaul and Hirst, 2006; Pryde and Hirst, 2011). In the FET reaction this is less likely to happen because the FMN site is blocked by NADH coordination and electrons on the reduced flavin are rapidly transferred down the chain of FeS clusters to reduce ubiquinone at the hydrophilic/hydrophobic interface, a much less exposed site for oxygen. The production of ROS during RET is both medically and physiologically important. ROS are important signalling molecules in the cell, having roles in the stimulation of muscle differentiation and oxygen sensing (Fernández-Agüera et al., 2015; Lee et al., 2011; Onukwufor et al., 2019). Medically, complex I RET is important due to its role in ischaemia–reperfusion injury (Chouchani et al., 2016). Ischaemia occurs when the blood supply to an organ is reduced or blocked, such as during a heart attack or stroke, depriving the cells of the oxygen required for mitochondrial respiration. During this event, the Δp generated from respiration collapses and metabolites, such as succinate, build up (Chouchani et al., 2016). During reperfusion, when the oxygen supply is re-established, the metabolite build up leads to a reduced Q-pool through succinate oxidation at complex II. Coupled with the return of a Δp generated by respiration, or by the proton-pumping ATP hydrolysis reaction at ATP synthase, the conditions thermodynamically favour RET and this results in a burst of ROS, mainly in the form of superoxide, at complex I (Chouchani et al., 2016; Pryde and Hirst, 2011), which can then lead to damage of the surrounding tissue. Inhibiting the RET reaction and slowing down the reactivation of complex I has potential for developing therapeutics to treat or prevent events such as ischemia–reperfusion injury (Galkin and Moncada, 2017; Niatsetskaya et al., 2012).

1.3.6. Active/deactive transition of mammalian complex I

Mammalian complex I has been observed to rest in two distinct states, termed the ‘active’ and ‘deactive’ states, which have been identified both biochemically and structurally (Agip et al., 2018; Blaza et al., 2018; Kotlyar and Vinogradov, 1990). The enzyme can transition between these two states (the active/deactive (A/D) transition), with the deactive state considered to be a profound resting state that forms slowly in the absence of substrates. In the presence of both NADH and ubiquinone, the enzyme can be reactivated to form the active state, a state that is considered ‘ready-to-go’ and can quickly start catalysing (Agip et al., 2018; Blaza et al., 2018; Kotlyar and Vinogradov, 1990). A feature of the deactive/active transition is the observation of a distinct lag phase in the NADH oxidation traces in SMPs or membranes, as complex I slowly reactivates in the presence of substrates, an effect that is enhanced in the presence of divalent cations and an elevated pH (Blaza et al., 2018; Gorenkova et al., 2013; Kotlyar and Vinogradov, 1990; Kotlyar et al., 1992) (**Figure 1.12A**). Interestingly, the deactive state is unable to catalyse the RET reaction unless it is first reactivated in the presence of NADH (Kotlyar and Vinogradov, 1990). The A/D transition is conceivably a physiologically relevant mechanism in mitochondria for limiting oxidative damage due to ROS production at complex I, which can occur when conditions favour RET, such as in ischaemia–reperfusion injury; although, this has not been confirmed. Interestingly, a single point mutation in the ND6 subunit of mouse complex I has been shown to facilitate rapid conversion to the deactive state, protecting against cardiac ischaemia–reperfusion injury in vivo without affecting the FET reaction (Yin et al., 2021).

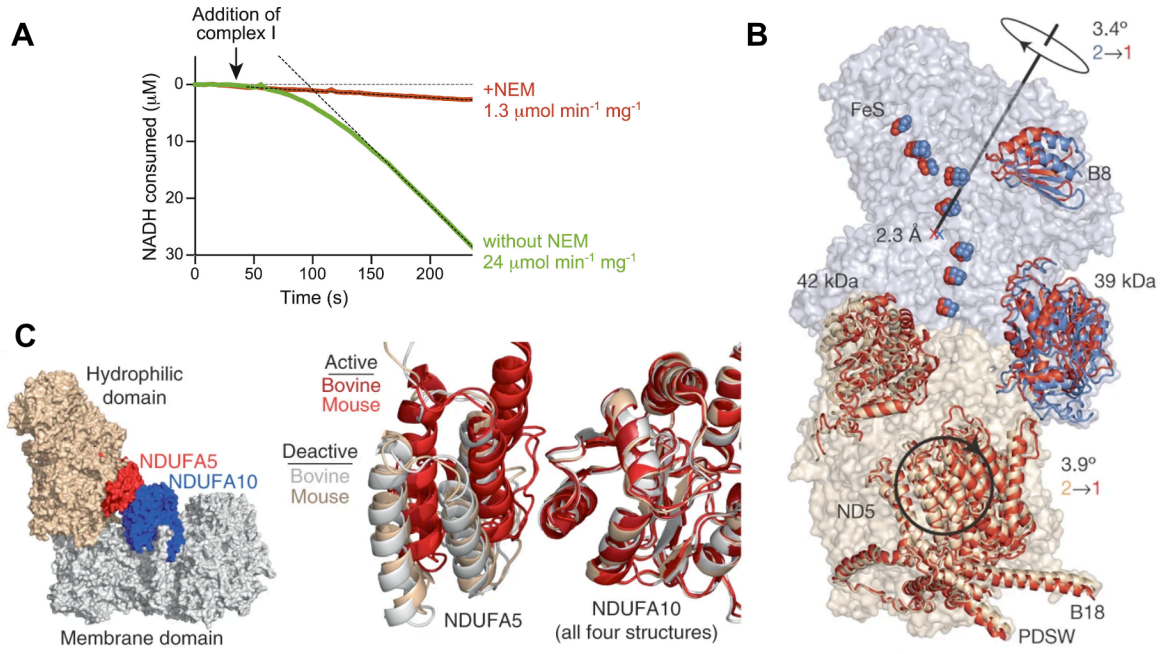

Figure 1.12. Large-scale structural changes of the A/D states. (A) Complex I, which has first been deactivated by heating, is shown catalysing NADH with/without treatment with the derivatising agent NEM. Incubation of the pre-deactivated sample with NEM prevented catalytic turnover (red line), locking the enzyme in the deactive state. Samples slowly reactivated to maximum turnover rates when not treated with NEM (green line). Figure taken from Blaza et al. (2018). (B) Overall twisting of the hydrophilic domain relative to the membrane domain in bovine complex I. The active state is shown in blue and wheat, and the deactive state in red. Figure taken from Zhu et al. (2016). (C) Shifting of the contact site between the NDUFA5 and NDUFA10 supernumerary subunits in the active and deactive states. The NDUFA10 subunits were superimposed and the NDUFA5 subunits from the bovine and mouse deactive and active states were compared. The active state is shown in red and deactive states in wheat and grey. Figure taken from Agip et al. (2018).

One of the features that is often used to define the active and deactive states is the difference in behaviour when treated with thiolating/alkylating reagents, the most common of which is *N*-ethylmaleimide (NEM), which can covalently modify solvent-exposed cysteine residues in proteins. In the active state, NEM does not affect the enzyme; however, in the deactive state modification by NEM locks the enzyme into the deactive state, preventing it from being reactivated by NADH/ubiquinone addition (**Figure 1.12A**) (Blaza et al., 2018; Galkin et al., 2008; Gavrikova et al., 1999). Structurally, the active and deactive states have been assigned to two distinct classes, which were resolved in cryo-EM analysis of the 'as-prepared' bovine enzyme (Zhu et al., 2016). These two classes presented an overall twisting/bending in the structure of the hydrophilic domain relative to the membrane domain, as shown in **Figure 1.12B+C**. High-resolution cryo-EM maps of mouse complex I were subsequently resolved, showing that mouse complex I existed predominantly in the active state and could relax into the deactive state on heating the mitochondria to 37 ˚C (Agip et al., 2018). This work revealed

more localised features that were distinct between the two states (**Figure 1.13**). Of note is the TMH1-2 loop of ND3, which is disordered in the deactive state but is well defined in the active state, and which is the site of the Cys39 residue (mouse) that can be derivatised by thiolating/alkylating reagents in the deactive state, where this Cys is solvent exposed (**Figure 1.13A)**. Disordered loops in the Q-site are a general feature of the deactive state, with the TMH5-6 loop of ND1 and the β1-β2 loop of NDUFS2, which harbour critical ubiquinone-binding residues, also being disordered. Another feature of the deactive state is that TM3 of ND6 forms a π-bulge instead of a normal α-helical structure. This has the effect of rotating bulky tyrosine and phenylalanine residues around the helix (**Figure 1.13B**). In the clinically relevant point mutant ND6-P25L, it was seen that substitution of the proline for leucine altered the rotation route of these residues, effectively favouring the deactive state conformation (Yin et al., 2021).

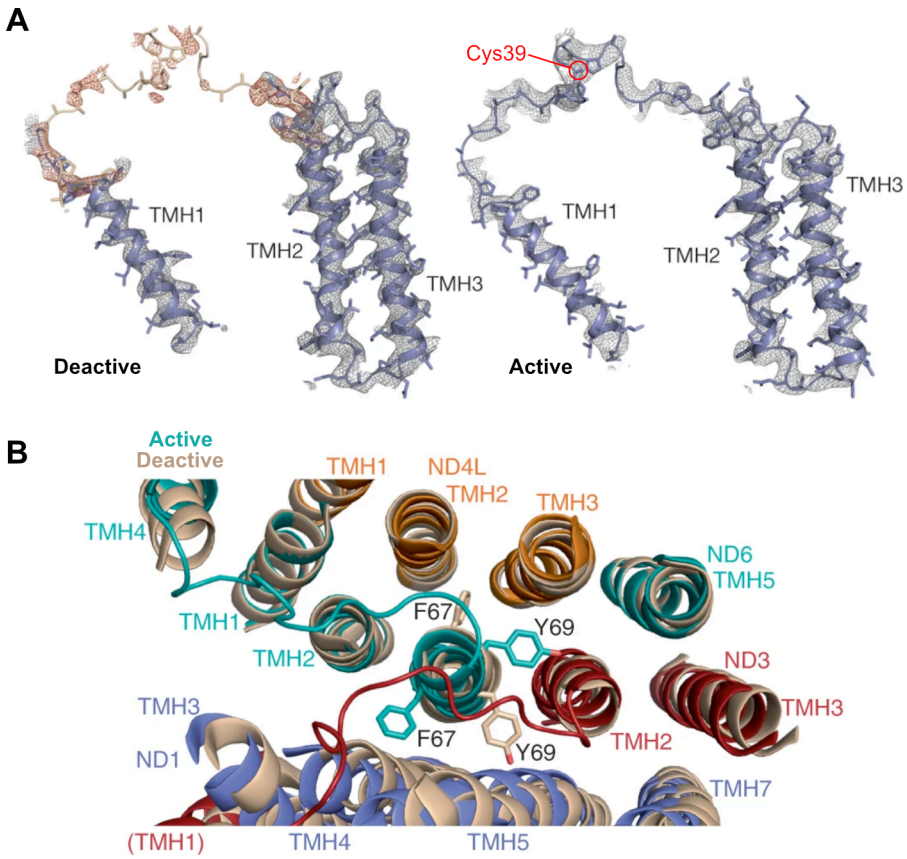

Figure 1.13. Highlighted structural differences in the active and deactive states. (A) Cryo-EM electron density for the TMH1-2 loop of ND3 in the active and deactive states of mouse complex I. The map is shown in mesh and with the modelled protein in cartoon. The loop is disordered in the deactive state. The site of alkylation (Cys39) is highlighted in the active model. Figure adapted from Zhu et al. (2016). (B) Comparison of the positions of residues F67 and Y69 in the TMH3 of ND6 in the active and deactive states of mouse complex I. The deactive subunits are shown all in wheat and the active state is coloured by subunit. Figure adapted from Agip et al. (2018).

1.3.7. Proposed mechanisms for complex I catalysis

Over the last decade various alternatives for the energy-coupling mechanism of complex I have been proposed, including different proton import and export channels for proton pumping. Most of these mechanisms have been based on detailed structural information and comparison between different enzyme states observed in 'as-prepared' samples, as well as in apparent catalytic intermediates identified under turnover-like conditions. Presented below are three different mechanisms that have recently been proposed, which highlight the uncertainty still involved when discussing complex I mechanism.

All the proposed mechanisms couple the energy from ubiquinone reduction to proton pumping via residues in the E-channel and along the central axis of the membrane domain. In particular glutamate and lysine ion pairs are essential to the charge propagation (Sato et al., 2014). One putative mechanism, based on computational simulations of the complex I structure, describes a forward and backward electrostatic pulse through the membrane domain, which drives proton translocation and further Q reduction (**Figure 1.14A**) (Kaila, 2018; Mühlbauer et al., 2020). On Q reduction, proton uptake from the ND1 subunit may be triggered by conformational changes and the ubiquinol may move down the Q-channel to a second binding site, propagating charge into the membrane domain via the E-channel. During the forward electrostatic pulse, the Glu-Lys ion pairs in the antiporter-like subunits (ND2, ND4, ND5) are opened, establishing inter-subunit contacts between the antiporter-like subunits, which favours the hydration of the half channels within each subunit. After reaching the terminal ND5 subunit, a proton in the ND5 subunits is pumped to the IMS and a proton is subsequently taken up from the mitochondrial matrix. The half channel is then closed by the re-establishment of the ion-pair coordination within the same subunit, which destabilises the adjacent ND4 subunit, causing it to eject its proton to the IMS followed by proton uptake from the matrix. This backward electrostatic pulse continues back to the Q-site, causing each proton-pumping module to first release a proton and then import a proton from the mitochondrial matrix before closing the half channels. The transport of protons along a chain of conserved charge residues is also integral to the mechanism of one of the most simple and well-understood proton pumps, bacteriorhodopsin, found in archaea. Bacteriorhodopsin contains a retinal cofactor, which undergoes an isomerisation reaction upon absorption of a photon, introducing strain into the enzyme. The rest of the enzyme responds by undergoing a sequence of conformational changes, altering the pK_a values of conserved acidic and basic side chains in the core of the protein, leading to the translocation of a proton to the extracellular face of the protein (Lanyi and Schobert, 2004). Thus, protonation and conformational changes of Glu-Lys ion pairs in complex I are probably also essential to the enzyme mechanism, possibly initiated by the movement of side chains in the Q-site in response to the reduction and/or movement of the Q

head group, as described above. A more detailed description of these ion pairs is discussed in Chapter 6.

An alternative mechanism based on high-resolution structural information of the mammalian enzyme showed minor conformational changes during turnover of NADH and the soluble ubiquinone analogue, decylubiquinone, supporting an electrostatic-driven proton-pumping mechanism, which was suggested to proceed in two forward waves (not one forward and one back) (**Figure 1.14B**) (Kampjut and Sazanov, 2020). Movement of the Glu-Lys ion pairs was not observed in the structures and thus only protonation events between these residues were considered sufficient to drive proton pumping. The ND4 subunit has an asymmetry with the ND2 and ND5 subunits, where the central lysine residue on TMH12 (in ND2 and ND5) is replaced by a glutamate instead. This may be important for the mechanism. Two states of complex I were observed in the structural information, termed as the open and closed states, which were considered intermediates of the catalytic cycle. On Q binding and reduction, the Q is protonated from Glu residues in the ND4L subunits, creating a negative charge in this subunit. This is balanced by an adjacent Glu on TMH5 in ND2 being protonated from its Lys partner. This then initiates a sequence of protonation and re-protonation events along the chain of charge residues, causing protons to be ejected to the IMS in ND4 but imported from the mitochondrial matrix (MM) in ND2 and ND5, due to the asymmetry of ND4. In the second electrostatic wave, ubiquinol diffuses down to a lower binding site in the Q-channel, inducing conformational changes in the Q-site. Protons imported into the ND2 subunit are used to re-protonate the Glu residues in ND4L. This is followed by proton pumping in the ND4L, ND2 and ND5 modules due to further protonation and deprotonation events along the chain of charge. This mechanism does not exclude a situation where all protons are pumped via ND5 rather than at individual pumps, as the protons are able to transfer along the central axis between subunits sufficiently well.

Until recently, the prevailing theory was that protons are pumped one by one by each individual antiporter subunit. However, the putative mechanism just discussed does not overlook that protons could instead be ejected only at ND5, based on cryo-EM structures showing only well resolved water molecules in the proposed exit channel of ND5 but not in the exit channels of the other antiporter subunits. Although, it is worth noting that more transient, but functionally important water molecules are not always observed in structures, even at high resolutions, such as in complex IV (Kaila et al., 2010). Nonetheless, another recent mechanistic proposal, based on cryo-EM structures of *Y. lipolytica* complex, has also supported the proposal that protons are ejected only at ND5 (Parey et al., 2021), but through a different sequence of events (**Figure 1.14C**). Two separate electron/proton transfer events were proposed, initiated by each

individual one-electron transfer to ubiquinone, implying that a semiquinone is a key intermediate in the mechanism. A proton channel identified in the ND1 subunit was proposed to connect the MM to the E-channel, transporting protons to a proton-loading site (PLS). The proton is imported after the one-electron reduction of ubiquinone induces conformational changes in ND1, and the proton enters to balance the charge on the semiquinone/anionic ubiquinone intermediate. In addition, a separate proton pathway in the ND3 and NDUFS2 subunit could provide a route for the protons required to protonate the semiquinone/anionic ubiquinone, which would also be controlled by the ND1 subunit loop movements. By neutralising the ubiquinone intermediate, the proton in the PLS is then released into the E-channel, and eventually ejected into the IMS at the ND5 subunit. The process would be repeated for the second electron reduction of ubiquinone, and so two of the four protons pumped by complex I enter the E-channel from the PLS. The remaining two protons are anticipated to be imported at two of the three antiporter subunits and ejected at ND5. This proposal suggested that during a single turnover event, only two of the three antiporter subunits are importing a proton from the MM, and they alternate between successive turnover events. Overall, this proposal resembles the mechanism of complex IV, where simply put, a proton from a Glu residue in the D-channel is transferred into a ‘trap’ site (a proton loading site), which electrostatically lowers the energy required to transfer an electron to oxygen but is itself blocked from protonating the reduced oxygen (Rich, 2017). After protonation of the reduced oxygen by import of protons through alternative channels, balancing the charges, this ‘trapped’ proton is no longer needed to maintain electroneutrality and is released into the IMS. It is thus tempting to propose that complex I also shares somewhat similar mechanistic features with the proton pumping mechanism of complex IV.

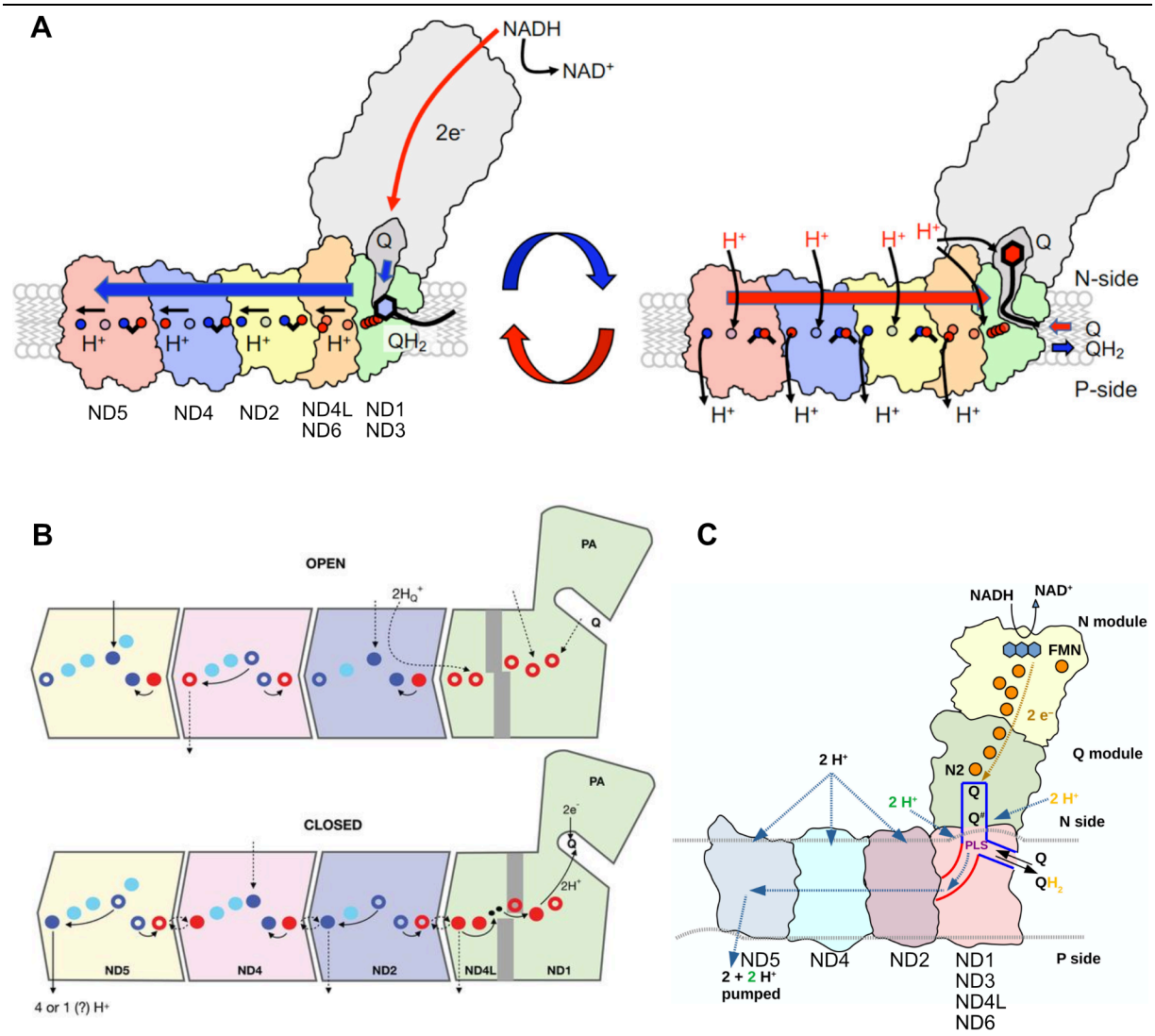

Figure 1.14. Examples of three putative mechanisms for complex I energy coupling and proton pumping. (A) Mechanism based on a forward and backward electrostatic pulse. Glu-Lys ion pairs are represented by red and blue circles. Movement of the reduced ubiquinone induces a forward electrostatic wave (blue arrow), which opens half channels for hydration. The backward electrostatic wave (red arrow) results in successive proton ejection and import events at each antiporter subunit and ND4L/ND6 (orange). Figure adapted from Mühlbauer et al. (2020). (B) Mechanism based on two forward electrostatic-driven waves. Two enzyme states are shown and the arrows demonstrate the transfer of charge/protons required to switch between the two states. Glutamate, lysine and histidine residues are shown by red, blue and cyan circles, respectively. Residues are either charged (full circle) or neutral (open circle). Protons are either ejected at each antiporter and ND4L, or all through ND5. Figure taken from Kampjut and Sazanov, 2020. (C) Two-state stabilisation change mechanism. Successive electron transfer events to ubiquinone are stabilised by import of protons to a proton-loading site (PLS) from the MM (green protons). These protons are then released to the E-channel when the ubiquinone intermediate is protonated via a second import channel from the MM (yellow protons). All protons are pumped at ND5. Figure adapted from Parey et al. (2021).

Recently, complex I–like respiratory complexes have also been structurally resolved, which have highlighted important features conserved during evolution that may be critical to the coupling and proton pumping mechanism of complex I (Schuller et al., 2018; Steiner and Sazanov, 2020; Yu et al., 2018). Along with complex I, membrane-bound NiFe hydrogenases (MBH) and membrane-bound sulfane sulfur reductases (MBS) are considered to have evolved from multiple resistance and pH (Mrp) complexes, which catalyse Na^+/H^+ antiporter activity. While MBH and MBS have retained the Na^+/H^+ antiporter activity, respiratory complex I (as well as the related photosynthetic complex I, which catalyses ferredoxin oxidation and plastoquinone reduction) have evolved to only pump protons without Na^+ translocation. Interestingly, some features are preserved between the complexes, despite differences in electron acceptors/donors and assembly of the different enzyme modules (Parey et al., 2020; Yu et al., 2021). First, the antiporter subunits all possess two half channels and contain a chain of conserved charge residues that form a hydrophilic axis along the membrane domain, highlighting the importance of these residues during complex I catalysis and in proton translocation. In addition, key loops in the ND1, ND3 and NDUFS2 subunits of complex I, considered important for sensing ubiquinone reduction and inducing conformational changes, are structurally conserved with MBH and MBS despite little sequence conservation between them. Finally, it is also worth noting that the lateral helix is universally conserved between the complexes, although it differs in length, and so it is probably a crucial element either structurally or perhaps even mechanistically. Altogether, features of these complex I–like respiratory complexes suggest a coupling mechanism is probably conserved between them yet the mechanism of complex I energy coupling and proton pumping still remains elusive and all the proposed mechanisms are speculative. Further investigations are required that complement structural studies with detailed functional investigations of key residues and proposed proton pathways.

1.4. Models for respiratory complex I

To study the mechanism of respiratory complex I, a model system is required that can combine mutagenesis with detailed structural and biophysical characterisation, all in the one model system. Developing a model that encompass all three strategies would be highly beneficial for efforts to understand the underlying mechanism of complex I catalysis and eventually how pathogenetic mutations can cause phenotypes. Particular attention is now being focused on the membrane domain and how the energy coupling drives proton translocation. The following section describes the various model organisms that have been used to study complex I and their main benefits and limitations. A potential new model organism is then described.

1.4.1. Mammalian models

To date, the mammalian enzyme from bovine (*Bos taurus)* and ovine (*Ovis aries*) mitochondria have been a key focus for both structural and biochemical studies of complex I. The first near-complete cryo-EM models were built in 2016 and, since then, higher resolution structures have been resolved, providing the bases for a range of mechanistic proposals (Blaza et al., 2018; Chung et al., 2022; Fiedorczuk et al., 2016; Kampjut et al., 2020; Zhu et al., 2016). In addition, mouse (*Mus musculus*) complex I cryo-EM structures have offered significant insight into the active and deactive states, complex I inhibitor-binding modes and the effect of clinically relevant mutations (Agip et al., 2018; Bridges et al., 2020; Chung et al., 2021; Yin et al., 2021).

Biochemically, bovine material has been studied extensively in the form of mammalian SMPs. These are outward-facing vesicle systems that contain the whole, membrane-bound respiratory chain in the native inner mitochondrial membrane, and can be prepared by 'pinching' off the cristae of isolated mitochondria by sonication. SMP membranes are well coupled and the ETC active sites are exposed to the external buffer, allowing assessment of the complexes by addition of substrates to the external buffer. The fact that they can sustain a Δp across the membrane allows various informative functional characterisations in the presence of a Δp. Key examples of studies performed in the SMP system are investigations of the ROS-generating RET reaction, complex I reversibility (Pryde and Hirst, 2011), assigning possible semiquinone species to complex I (Magnitsky et al., 2002; Yano et al., 2005), assessment of the deactive/active transition (Kotlyar and Vinogradov, 1990), evaluating small-molecule inhibitors and probes of complex I (Chung et al., 2021; Sekiguchi et al., 2009) and assessing possible substrate channelling in mitochondrial supercomplexes (Fedor and Hirst, 2018). Additionally, SMPs have been used to accurately determine the complex I proton-pumping stoichiometry (four protons per NADH oxidised), a key mechanistic feature of the enzyme (Fedor and Hirst, 2018; Jones et al., 2017). This assay system will be discussed in more detail in Chapter 6.

Aside from SMPs, the purified bovine enzyme has also been successfully reconstituted into liposomes containing Q_{10} or other insoluble quinone analogues, which has allowed complex I to be studied in a well-defined lipid membrane in the presence of its physiological substrate but without the complications of other proteins present in the membrane. This system has been used to assess quinone kinetics (Fedor et al., 2017; Uno et al., 2020), complex I lipid requirements (Biner et al., 2020) and modes of inhibition from inhibitors and small molecules (Bridges et al., 2020; Chung et al., 2021).

The major drawback to using the mammalian model is the feasibility of performing mutagenesis of key residues of interest. Generating mutations in key functional residues and pathogenic mutations is a typical way to reveal mechanistic information. To some extent, mouse models allow for some genetic manipulation in nuclear genes, yet it is not simple or ethical to generate and to screen a wide range of mutations, especially if they are pathogenic, and mouse mutagenesis is a time-consuming and expensive process. In addition, the amount of material obtained from mouse models is not adequate for much more than basic characterisation and structures of the purified enzyme, and one cannot prepare usable quantities of SMPs.

1.4.2. Yeast models

Another common model for studying complex I is mitochondrial complex I from the yeast fungus *Yarrowia lipolytica*. This model system has advantages over mammalian model systems as the cells can be easily grown in the laboratory and mutations can be generated in the nuclear-encoded hydrophilic domain of the enzyme (but not in the mitochondria-encoded hydrophobic core subunits). To generate these mutations, the alternative NADH dehydrogenase (NDH-2), present in *Y. lipolytica* but not in mammalian mitochondria, is redirected from the IMS face to the mitochondrial matrix face of the IMM, allowing for the essential regeneration of NAD^+ when complex I catalysis is compromised during mutagenesis (Kerscher et al. 2001, 2002). Like the bovine enzyme, there are established purification protocols for *Y. lipolytica* complex I and the enzyme has also been shown to be amenable to structural work, with current published structures at a resolution of 2.7 Å and ~2.1 Å (Grba et al., 2020; Kashani-Poor et al., 2001; Kerscher et al., 2002; Parey et al., 2021). Functionally, *Y. lipolytica* has certain limitations. While protocols have been developed to study wild-type and complex I variants in membranes, in the isolated form and in proteoliposomes it has proved difficult to generate SMPs from *Y. lipolytica* cells because of the tough cell wall, and, typically, yields are suboptimal. Critically, *Y. lipolytica* SMPs have not demonstrated Δp-linked capabilities (Lin et al., 2008). Currently, this means that measuring proton stoichiometry by the quantitative methods detailed in Chapter 6 is not feasible, limiting its use in studying all aspects of complex I catalysis. In the past, proton pumping in *Y. lipolytica* has instead been studied in proteoliposomes, using semi-quantitative pH/Ψ dyes, which is a less robust system (Cabrera-Orefice et al., 2018; Dröse et al., 2011). Finally, it is worth mentioning that, as a disease model, *Y. lipolytica* is not ideal because mutations that have been shown to be pathogenic in mammalian complex I are not pathogenic (or not expressed) in yeast (Varghese et al., 2015).

1.4.3. Bacterial models

Bacterial model systems offer the only alternative in which mutations can be made in any complex I subunit, as all the encoding genes are easily accessible in the genomic DNA. In addition, it is easier to grow bacterial cells when compared to *Y. lipolytica*, which can take multiple days to grow. The biggest advantage of bacterial models for complex I studies is the ability to generate mutations in the core hydrophobic subunits associated with proton pumping and part of the E-channel, inaccessible in model species which contain mitochondria. While the first intact complex I structure was solved from *T. thermophilus*, this model has not been utilised widely beyond structural work, which is probably due to the difficulty in growing cells at 70 °C and the challenge of biophysical experiments at elevated temperatures (Baradaran et al., 2013; Gutiérrez-Fernández et al., 2020). To date, most mutational studies have been carried out in the *E. coli* enzyme, such as by Yagi and co-workers, who have performed extensive mutational studies of key residues for every hydrophobic core subunit (Sato et al., 2014). However, these studies were performed and interpreted prior to the significant structural insights now available. More recent mutagenesis studies using the *E. coli* model have begun to evaluate their data with respect to structural data and computational simulations (Mühlbauer et al., 2020; Nuber, Schimpf, et al., 2021), but the suitability of *E. coli* as a model system for the mitochondrial enzyme remains in question. It uses menaquinone or ubiquinone-8 as a terminal electron acceptor rather than ubiquinone-10 (used in human) and it also has a lower sequence homology with the human enzyme than other species (**Table 1.2**) (Castro et al., 2016; Yip et al., 2011). The redox potential difference between NADH and ubiquinone or menaquinone (in the Q binding site) is 420 mV and 240 mV, respectively, which results in a significant reduction in the energy available for proton translocation in the *E. coli* enzyme when using menaquinone (Gamiz-Hernandez et al., 2017). This emphasises the caution that should be exercised when extending the established mammalian complex I $H^+/2e^-$ proton-pumping stoichiometry to other organisms that have not been well characterised in this regard (Castro et al., 2016; Jones et al., 2017). Although *E. coli* complex I can be studied in proteoliposomes and in its purified isolated form, inverted membrane vesicles (the equivalent to SMPs) from *E. coli* cells result in poorly coupled vesicles, meaning RET and suitable quantitative proton-pumping measurements have not been successfully carried out (Jones et al., 2017). Furthermore, *E. coli* lacks complex III and an aa_3-type cytochrome *c* oxidase (complex IV) and thus cannot form respirasome-like supercomplexes (Anraku and Gennis, 1987). Currently there is also limited quality structural data on the *E. coli* enzyme, with separate structures of the peripheral (Schimpf et al., 2022) and membrane arm (Efremov and Sazanov, 2011) reported. The full, intact enzyme has recently been reported but in an uncoupled conformation with poor resolution in the membrane domain (Kolata and Efremov, 2021).

Table 1.2. Sequence comparison between species for all 14 core subunits of complex I. The sequence identity and similarity (in parentheses) are shown with respect to the human complex. Table adapted from Yip et al. (2011).

Domain	Subunit	Identity (similarity) /%			
		B. taurus	***P. denitrificans***	***T. thermophilus***	***E. coli***
Peripheral arm	NDUFV1/Nqo1	97 (99)	64 (77)	43 (57)	38 (56)
	NDUFV2/Nqo2	96 (98)	36 (52)	33 (54)	34 (56)
	NDUFS1/Nqo3	97 (99)	52 (64)	23 (39)	16 (29)
	NDUFS2/Nqo4	95 (99)	59 (77)	44 (64)	27 (42)
	NDUFS3/Nqo5	89 (94)	51 (66)	25 (38)	8 (15)
	NDUFS7/Nqo6	86 (91)	69 (81)	47 (67)	36 (51)
	NDUFS8/Nqo9	93 (95)	72 (82)	31 (43)	29 (41)
Membrane arm	ND3/Nqo7	74 (83)	28 (50)	21 (41)	22 (41)
	ND1/Nqo8	78 (88)	35 (54)	35 (51)	35 (56)
	ND6/Nqo10	62 (75)	17 (33)	15 (31)	17 (36)
	ND4L/Nqo11	73 (90)	24 (49)	23 (42)	19 (46)
	ND5/Nqo12	69 (81)	28 (41)	31 (46)	28 (45)
	ND4/Nqo13	74 (85)	26 (47)	24 (40)	26 (44)
	ND2/Nqo14	63 (81)	14 (29)	19 (31)	16 (32)

1.4.4. *Paracoccus denitrificans* as a model

The α-proteobacterium *P. denitrificans* appears to offer great potential as a bacterial model system for elucidating the mechanism of complex I, and its development as a genetically tractable model system for complex I is the focus of this thesis. The general features of *P. denitrificans* and its suitability as a model system for studying complex I catalysis are discussed here, followed by an assessment of the current limitations of the model.

P. denitrificans is a Gram-negative, soil bacterium, which is well adapted for aerobic and anaerobic growth on a variety of carbon sources (Baker et al., 1998). While mitochondria operate in a constant environment, bacteria must adapt their ETC to their environment to continue respiring. Hence, *P. denitrificans* possesses three different aerobic routes for passing electrons to oxygen (Van Spanning et al., 1991). The first route mirrors the mitochondrial respiratory chain—*P. denitrificans* possesses the same complexes as the canonical mitochondrional respiratory chain, including an aa_3-type oxidase (John and Whatley, 1975). Electrons from complex III can be transported to complex IV via two different types of cytochrome *c*, cyt c_{550}, which operates in the periplasm, or cyt c_{552}, a membrane-bound cyt *c*. When *P. denitrificans* is grown on carbon sources, such as methanol or methylamine, different cytochromes are expressed, such as c_{551i} and cyt c_{553i} (Van Spanning et al., 1991). Alternative

routes for electrons to oxygen exist in *P. denitrificans*, as it can also express ba_3- and cbb_3-type oxidases in addition to complex IV (aa_3-type oxidase) (De Gier et al., 1994). The cbb_3-type oxidase has a high affinity for oxygen and is expressed predominantly in low oxygen conditions (De Gier et al., 1996). The ba_3-type quinol oxidase is expressed over a wider range of oxygen concentrations and oxidises ubiquinol directly, not via complex III and cyt *c*. Due to its high K_M for ubiquinol, the enzyme becomes active only when the Q-pool is highly reduced (Otten et al., 1999). While the ba_3-type oxidase is considered to pump protons, there have been conflicting reports as to whether the cbb_3-type oxidase is a proton pump, depending on the buffer used (Raitio and Wikström, 1994; Van Spanning et al., 1995). It has been reported that low amounts of both cbb_3- and ba_3-type oxidases are expressed in aerobic growth conditions (Stroh et al., 2004). In addition to aerobic respiration, *P. denitrificans* can use hydrogen as an electron donor, or nitrate as a terminal electron acceptor, instead of oxygen (Baker et al., 1998).

P. denitrificans is perhaps one of the most relevant bacterial models for complex I with respect to the mammalian enzyme. *P. denitrificans* has been proposed to be a close descendant of the protoendosymbiont that went onto become what is now the mitochondrion (John and Whatley, 1975), as suggested by endosymbiotic theory. Consequently, the complex I from *P. denitrificans* is more like its mammalian counterpart compared with other bacterial species, as shown by its sequence similarity with the human enzyme, particularly in the hydrophilic domain (**Table 1.2**). The ETC of *P. denitrificans* is also similar to its mammalian counterpart, as described above, containing all the central components (complexes I–IV), as well as using ubiquinone-10 as the electron acceptor, the same as in the human enzyme (Castro et al., 2016; John and Whatley, 1975). Finally, the *P. denitrificans* complex I also possesses a subset of supernumerary subunits, which are present in the mammalian enzyme, as well as existing as part of a respiratory supercomplex, like the mammalian mitochondrial enzyme (Stroh et al., 2004; Yip et al., 2011). Importantly, *P. denitrificans* also facilitates in-depth characterisation of complex I variants in well-coupled sub-bacterial particles (SBPs), which can be generated from *P. denitrificans* cells by osmolysis of the bacterial cytoplasmic membrane (Burnell et al., 1975). This supports the measurement of fundamental biochemical and biophysical data in complex I variants, which previously could only be measured in SMPs from the wild-type mammalian enzyme. Of note, SBPs have been used to show that *P. denitrificans* can undergo RET (Kotlyar and Borovok, 2002; Kotlyar et al., 1998) and have allowed the proton-pumping stoichiometry of *P. denitrificans* complex I to be measured, and shown to be four, the same as for the mammalian enzyme (Jones et al., 2017). Quantitative methods like this are often lacking in previous studies of *E. coli* variants and will be useful for probing the catalytic mechanism.

Overall, *P. denitrificans* offers great potential to be used as a single model to combine mutagenesis, structural and functional characterisation. Unfortunately, there are a few limitations that, so far, have prevented *P. denitrificans* being employed routinely in this regard. One is that complex I is essential to *P. denitrificans*, so deleterious mutations cannot currently be made without killing the cell, impeding their further study. Second, there is no robust purification procedure for the enzyme, which has hindered structural studies and functional characterisation of the isolated enzyme. A final limitation is that the ATP synthase of *P. denitrificans* is unable to hydrolyse ATP and generate a Δp independent of respiration, a requirement for studying complex I reversibility by modulation of the Q-pool redox state independent of Δp (Pryde and Hirst, 2011), which would be an invaluable tool for studying complex I variants.

In this thesis, attempts to address these current limitations are described with the aim to develop *P. denitrificans* as a complete bacterial model for complex I. The work in Chapter 3 discusses attempts to activate ATP hydrolysis in the *P. denitrificans* ATP synthase, to pave the way for future RET and enzyme reversibility studies of complex I variants in SBPs. In Chapter 4 a protocol for the purification of the *P. denitrificans* enzyme is developed and a strain created that is suitable for complex I mutagenesis. The purified enzyme is fully characterised and is also optimised for proteoliposome studies. Chapter 5 discusses attempts to solve the *P. denitrificans* complex I structure by cryo-EM, and Chapter 6 combines the methodology and systems established in the previous chapters to ask questions about the proton-pumping and energy-transduction mechanism in complex I. More specifically, mutations in the ND4 (Nqo13) subunit of *P. denitrificans* complex I are generated, characterised and evaluated with regard to the mechanism of energy transduction.

2. Materials and Methods

2.1. Bacterial strains, plasmids and growth media

Table 2.1. Table of bacterial strains used in this thesis.

Strain	Species	Details	References/Source
NEB® 5-α	*E. coli*	*fhu*A2, Δ(*arg*F-*lac*Z)U169, *pho*A, *gln*V44, Φ80Δ(*lac*Z)M15, *gyr*A96, *rec*A1, *rel*A1, *end*A1, *thi*-1, *hsd*R17	New England BioLabs
BL21 (DE3)	*E. coli*	F^-, *ompT*, *gal*, *dcm*, $hsdS_B$ (r_B^-, m_B^-), (DE3)	New England BioLabs
MFD*pir*	*E. coli*	*E. coli* MG1655, RP4-2-Tc::[ΔMu1::*aac(3)*IV, Δ*aphA*, Δ*nic35*-ΔMu2::*zeo*], Δ*dapA*::(*erm-pir*), Δ*recA*	(Ferrières et al., 2010)
Pd1222	*P. denitrificans*	*rif*^{R}, s*pc*^{R}, enhanced conjugation frequencies, m^+	(De Vries et al., 1989)
ΔHy	*P. denitrificans*	*Pd1222,* Δ*Hydrogenase*	(Jones et al., 2017)
Δζ	*P. denitrificans*	Δ*Hydrogenase,* Δζ	(Varghese et al., 2018)
$\varepsilon^{\Delta 110}$	*P. denitrificans*	Δ*Hydrogenase,* $\varepsilon^{\Delta 110\text{-}148}$	This work
$\varepsilon^{\Delta 88}$	*P. denitrificans*	Δ*Hydrogenase,* $\varepsilon^{\Delta 88\text{-}148}$	This work
$\Delta\zeta\varepsilon^{\Delta 110}$	*P. denitrificans*	Δ*Hydrogenase,* Δζ, $\varepsilon^{\Delta 110\text{-}148}$	This work
$\Delta\zeta\varepsilon^{\Delta 88}$	*P. denitrificans*	Δ*Hydrogenase,* Δζ, $\varepsilon^{\Delta 88\text{-}148}$	This work
Pd-Nqo5^{His6}	*P. denitrificans*	Δ*Hydrogenase*, *nqo5*^{His6}	This work
Pd-Nqo13^{E141Q}	*P. denitrificans*	*Pd*-Nqo5^{His6}, *nqo13*^{E141Q}	This work
Pd-Nqo13^{K232Q}	*P. denitrificans*	*Pd*-Nqo5^{His6}, *nqo13*^{K232Q}	This work
Pd-Nqo13^{K263Q}	*P. denitrificans*	*Pd*-Nqo5^{His6}, *nqo13*^{K263Q}	This work
Pd-Nqo13^{E405Q}	*P. denitrificans*	*Pd*-Nqo5^{His6}, *nqo13*^{E405Q}	This work
Pd-Nqo13^{H239Q}	*P. denitrificans*	*Pd*-Nqo5^{His6}, *nqo13*^{H239Q}	This work
Pd-Nqo13^{Y315F}	*P. denitrificans*	*Pd*-Nqo5^{His6}, *nqo13*^{Y315F}	This work
Pd-Nqo13^{L242A}	*P. denitrificans*	*Pd*-Nqo5^{His6}, *nqo13*^{L242A}	This work
Pd-Nqo13^{W241F}	*P. denitrificans*	*Pd*-Nqo5^{His6}, *nqo13*^{W241F}	This work
Pd-Nqo13^{A314L}	*P. denitrificans*	*Pd*-Nqo5^{His6}, *nqo13*^{A314L}	This work
Pd-Nqo13^{H246F}	*P. denitrificans*	*Pd*-Nqo5^{His6}, *nqo13*^{H246F}	This work
Pd-Nqo13^{H320L}	*P. denitrificans*	*Pd*-Nqo5^{His6}, *nqo13*^{H320L}	This work

Pd-Nqo13^{H346Q}	*P. denitrificans*	*Pd*-Nqo5^{His6}, *nqo13^{H346Q}*	This work
Pd-Nqo13^{R367H}	*P. denitrificans*	*Pd*-Nqo5^{His6}, *nqo13^{R367H}*	This work
Pd-Nqo12^{D648N}	*P. denitrificans*	*Pd*-Nqo5^{His6}, *nqo13^{D648N}*	This work

Table 2.2. Table of plasmids used in this thesis.

Plasmids	Details	Reference/Source
pRVS1	*amp*^{R}, *sm*^{R}, *Tn5p*, *lacZ*, ColE1-like *oriV*	(Van Spanning et al., 1991)
pQF	IncP *oriV*; ColE1 *oriV*; RP4 *oriT*; *Tc*^{R}, *cym*^{R*}, P_{Q5}, and MCS for N- and C-terminal fusions to 3×FLAG-tag; *Tc*^{R}	(Kaczmarczyk et al., 2013)
pQH	pQF derivative for C-terminal fusion to 3×FLAG and N-terminal fusion to HA-tag; *Tc*^{R}	(Kaczmarczyk et al., 2013)
pLMB509	*Gm*^{R}, pRU1097 backbone with *tauAp*, *tauR* from *Sinorhizobium meliloti* 1021, N-terminal fusion for His-tag	(Tett et al., 2012)
pUC57-Kan	*kan*^{R}, ColE1 *ori*, CAP binding site, *lacZ, lacI*	GENEWIZ®
pET15b-N-terminal Twin-Strep AOX$^{\Delta 1-24}$	*Amp*^{R}, *lacI*, *lacO,* ColE1 *ori*, rop, N-terminal fusion for twin-strep-tag, *AOX$^{\Delta 1-24}$*	(Fedor et al., 2017)
pET-maeB	*Amp*^{R}, *lacI*, *lacO,* ColE1 *ori*, rop, f1 ori, m*aeB*	(Bologna et al., 2007)
pASK40-fumC	*bla, lacI^{q}*, *lacO*, *t_{lpp}, fl-IG, ompA, fumC*	(Weaver et al., 1995)

Table 2.3. Table of growth media used in this thesis.

Media	Composition	Quantity / L^{-1}	Reference
LB	Tryptone	10 g	(Luria et al., 1960)
	Yeast extract	5 g	
	NaCl	10 g	
	NaOH	to pH 7.2	
SOC	Tryptone	20 g	(Hanahan, 1983)
	Yeast extract	5 g	
	NaCl	10 mmol	
	KCl	2.5 mmol	
	$MgCl_2$	10 mmol	
	Glucose	20 mmol	
	NaOH	to pH 7.0	
Succinate minimal medium	Succinic acid	50 mmol	Modified from (Hahnke et al., 2014)
	NH_4Cl	9.35 mmol	
	$MgSO_4.7H_2O$	2 mmol	
	$CaCl_2.2H_2O$	0.07 mmol	
	KH_2PO_4	0.29 mmol	
	K_2HPO_4	0.69 mmol	
	HEPES	25.2 mmol	
	Trace metal solution	2 mL	
	NaOH	to pH 7.2	
Trace metal solution	Na_2–EDTA	9.8 mmol	(Hahnke et al., 2014)
	$FeSO_4.7H_2O$	4.5 mmol	
	$MnCl_2.4H_2O$	0.05 mmol	
	$CuCl_2.2H_2O$	0.4 mmol	
	Na_2MoO_4	0.5 mmol	
	$ZnCl_2$	1.25 mmol	

2.2. Molecular biology

2.2.1. DNA manipulations

PCR was used to amplify DNA, generate mutations and screen genomic manipulations. DNA for these reactions came from either purified plasmids or from *P. denitrificans* genomic DNA that was extracted from cells by boiling the samples first to 98 ˚C for 10 min. All PCR reactions contained 0.02 units μL^{-1} Q5 High-Fidelity DNA polymerase (NEB), 1 × Q5 Reaction Buffer, 200 µM dNTPs, 0.5 µM of forward and reverse primers and <1,000 ng template DNA. Importantly, Q5 High GC Enhancer buffer was included in all PCR reactions involving *P. denitrificans* DNA due to the high GC content of the *P. denitrificans* genome. This reduced the number of non-specific bands. To further reduce non-specificity of PCR reactions, primers were typically designed with 15–20 bp complementary sequences and PCR reactions were performed at the highest possible primer annealing temperature. For purification of PCR

products, samples were either directly purified using Monarch PCR and DNA Cleanup Kits (NEB) or first separated by DNA gel electrophoresis followed by extraction of gel slices using Monarch DNA Gel Extraction Kits (NEB) (see Section 2.4.8).

Restriction enzyme digests (typically supplied by NEB) were carried out according to the manufacturer's guide including the subsequent enzyme inactivation step. For ligation reactions, the manufacturer's guide was also followed with reactions being carried out either at room temperature for 10 min or overnight at 4 ˚C. All Sanger sequencing was carried out by GENEWIZ®.

2.2.2. Transformation of *E. coli*

Most *E. coli* transformations were performed in NEB 5-α competent cells. DNA (1–100 ng) was mixed with the cell mixture and incubated on ice for 30 min, followed by heat shock at 42 ˚C for 30 s in a water bath. Immediately after, cells were incubated on ice for 10 min, followed by addition of 950 µL of SOC (super optimal broth with catabolite repression) medium and incubation at 37 ˚C for 60 min with shaking at 225 rpm. The cell mixture was centrifuged at 6,000 × g in a benchtop centrifuge for 3 min before the cell pellet was resuspended in 100 µL LB and plated onto LB-agar plates with appropriate antibiotic selection markers. Plates were incubated at 37 ˚C overnight and single colonies selected.

For transformation of lab-grown MFD*pir* cell, competent cells were first prepared. MFD*pir* was grown in LB (250 mL) to mid-exponential phase before harvesting the cells and resuspending in 10 mL ice-cold 100 mM $CaCl_2$ followed by incubation on ice for 20 min. The cells were again centrifuged and the pellet resuspended in 5 mL of 100 mM $CaCl_2$, 5% (v/v) glycerol, before flash freezing in liquid nitrogen. To transform MFD*pir*, the protocol in the above paragraph was repeated but the heat shock treatment at 42 ˚C was extended to 2 min. Diaminopimelic acid (DAP) was present at a concentration of 0.5 mM in all solutions involving MFD*pir* cells.

2.2.3. Bacterial conjugation of *P. denitrificans*

P. denitrificans and *E. coli* MFD*pir* strains were grown overnight at 30 ˚C and 37 ˚C, respectively, with 225 rpm shaking. Cultures were then diluted to the same OD_{600} and mixed at a 3:1 ratio of donor to recipient (*E. coli* to *P. denitrificans*). The mixture was then spotted (30 µL) onto a LB-agar plate containing 0.5 mM DAP (and 10 mM taurine during complex I mutagenesis). The plates were incubated overnight at 30 ˚C before the spot was scraped clean and the cells resuspended and washed in 1 mL sterile water. The cells were then centrifuged and resuspended in 1 mL sterile water before preparing serial dilutions of the cell resuspension

in water. Typically, dilutions were prepared from neat down to 10^{-3} and were then plated on LB-agar plates containing selection antibiotics. Alterations to this protocol are described in the text where appropriate.

2.2.4. Mutagenesis of *P. denitrificans*

The method used to generate unmarked mutations on the *P. denitrificans* chromosomal DNA is expanded upon in Chapters 3 and 4, but is based on previous protocols (Jones et al., 2017; Varghese et al., 2018). Briefly, suicide vector-mediated homologous recombination was used to edit the *P. denitrificans* genome. First, a DNA cassette was designed containing two sequences homologous to regions on either side of the site or gene of interest. Between these two flanking regions, the desired alteration was included/modified in the DNA sequence. One of the flanking regions was followed by a kanamycin (Kan^R) selection marker of 815 bp length. *Eco*RI restriction sites were added to the end of the construct and any *Eco*RI sites within the construct itself were removed by silent mutagenesis during the design of the DNA cassette. The constructs were assembled by GENEWIZ® and then inserted into the *lacZ*-containing pRVS1 suicide plasmid via an *Eco*RI restriction site digestion. The plasmid was transformed into the MFD*pir E. coli* donor strain and conjugated into the desired *P. denitrificans* strain as described above. Successful conjugation and first recombination events were selected on LB-agar plates containing 50 μg mL^{-1} kanamycin. Colonies were picked and re-streaked successive times on fresh plates containing 50 μg mL^{-1} kanamycin to ensure correct selection. Successful colonies were then plated on X-gal (200 μg mL^{-1}), and white colonies were selected as positive for the second recombination event and screened by PCR amplification of the DNA sequence across the gene of interest, followed by gel electrophoresis and Sanger sequencing. Alterations to this protocol are described in the text where appropriate. Successful *P. denitrificans* variants were grown overnight in LB and glycerol stocks prepared and stored at –80 ˚C.

2.2.5. Growth curves

To assess the competence for cell growth of different strains of *P. denitrificans*, cell growth was monitored at an absorbance of 600 nm in either a Molecular Devices SpectraMax 348 96-well plate reader or a BMG Labtech CLARIOstar plus microplate reader. In general, 200 μL of media (LB or succinate minimal medium) were added to wells in a 96-well plate and were inoculated with a pre-culture of cells to a starting optical density of 0.02. The pre-culture (50 mL) was grown overnight in a 250 mL flask at 30 ˚C with 220 rpm shaking. When comparing NDH-2 expression systems, media were also supplemented with different concentrations of inducer (taurine or cumate), and piericidin A (5 μM) was added after two hours where indicated.

Plates were incubated at 30 ˚C with 200 rpm orbital shaking in a BMG Labtech CLARIOstar plus microplate reader or with 5 min shaking every 15 min in a Molecular Devices SpectraMax 348 96-well plate reader.

2.3. Preparation of complex I-containing samples and assay system enzymes

2.3.1. Preparation of SBPs from *P. denitrificans*

All centrifuge steps for SBP preparation were performed at 14,000 × g and at 4 ˚C using SLA-3000 tubes and rotors. *P. denitrificans* was grown aerobically to mid-exponential phase in 500 mL of either LB medium (OD_{600} ~2.5-3.0) or in a succinate minimal medium (OD_{600} ~1.8-2.5) at 30 ˚C, 225 rpm shaking in 2 L flasks (**Table 2.3**). Cells were then harvested by centrifugation for 10 minutes and resuspended in ~400 mL 10 mM Tris-SO_4 pH 7.5 at 4 ˚C, 150 mM NaCl. The resuspended material was centrifuged for a further 10 min and pellets were resuspended in lysis buffer (10 mM Tris-SO_4 pH 7.5 at 4 ˚C, 500 mM sucrose) to an OD_{600} of 7.5. Hen egg-white lysozyme was then added to a final concentration of 250 µg mL^{-1} and incubated at 4 ˚C for 1 hour. Digested cells were centrifuged for 15 min and pellets resuspended in 50 mL 10 mM Tris-SO_4 pH 7.5 at 4 ˚C before topping up to 450 mL with the same buffer. After 15 min, $MgSO_4$ (5 mM final concentration) and a few flakes of bovine pancreatic DNase were added to reduce the viscosity of the solution. The solution was then centrifuged twice for 15 min and the pellet discarded each time. The final supernatant was centrifuged for 1 hour and the pellet collected and resuspended in a small volume of kinetics buffer (10 mM Tris pH 7.5 at 32 ˚C, 250 mM sucrose). The SBPs were stored at −80 ˚C.

2.3.2. Preparation of membranes from *P. denitrificans*

Large scale

Pre-cultures of individually picked *P. denitrificans* colonies were grown for 24 h at 30 ˚C with 225 rpm shaking in 50 mL LB containing rifampicin (50 µg mL^{-1}), gentamicin (20 µg mL^{-1}) and supplemented with 10 mM taurine where appropriate. The pre-cultures (500 µL) were used to inoculate 12 × 500 mL LB (containing no antibiotics) in 2L flasks. Taurine (10 mM) was included in the medium where complex I catalysis was compromised. Flasks were grown for 16–20 h (30 °C, 225 rpm) and harvested at late-log phase when the OD_{600} was 3.5–4.5. Cells were collected by centrifugation in a Sorvall RC 12BP centrifuge and resuspended in 2–2.5 mL of buffer per gram of cells. The resuspension buffer contained 50 mM MES pH 6.5 at 4 °C, 0.002% (w/v) phenylmethanesulfonyl fluoride (PMSF) and one cOmplete™ EDTA-free protease inhibitor cocktail (Roche) per 50 mL. After homogenising the cells, the resuspension

was passed through a Z-plus 2.2 kW cell disruptor (Constant Systems Limited), once at 15,000 psi and twice at 30,000 psi. Cell debris was removed by centrifugation at 31,900 × g in an SLA-1500 rotor (Sorvall) for 1 h and the membrane fraction was collected by ultracentrifugation at 234,800 × g in a Ti45 rotor (Beckman) for 2 h. Membranes were suspended in 50 mM MES pH 6.5 at 4 °C and flash frozen in liquid N_2.

Small scale

P. denitrificans colonies were picked and grown for 24 hours at 30 ˚C, 225 rpm shaking in 5 mL LB containing rifampicin (50 µg mL^{-1}), gentamicin (20 µg mL^{-1}) and supplemented with taurine (10 mM) where appropriate. The pre-culture was used to inoculate 50 mL LB in a 250 mL conical flask containing no antibiotics. Flasks were grown for 16–20 h (30 °C, 225 rpm) and harvested at late-log phase when the OD_{600} was 3.0–4.5. Cells were collected by centrifugation in a Heraeus Primo centrifuge and the cells resuspended in 1 mL resuspension buffer (same buffer as above). Cells were lysed in a Q700 probe sonicator (QSonica) equipped with a 1.6 mm microtip. Sonication was performed at 60% amplitude using a 5 s/45 s on and off cycle for a total sonication time of 1 minute. The membrane fraction was collected by ultracentrifugation at 241,472 × g in a MLA130 for 1 hour and membranes suspended in 50 mM MES pH 6.5 at 4 °C.

2.3.3. Isolation of complex I from *P. denitrificans* membranes

P. denitrificans membranes (200–600 mg) were diluted to a concentration of 9.5 mg mL^{-1} in buffer with a composition of 20 mM MES pH 6.5 at 4 °C, 100 mM NaCl, 5 mM $CaCl_2$, 10% (v/v) glycerol, 0.002% PMSF (w/v) and a cOmplete™ EDTA-free protease inhibitor cocktail tablet. Membranes were solubilised in *n*-dodecyl-β-D-maltoside (DDM) (Anatrace) for 30 min at a 3:1 detergent to protein ratio (w/w) by dropwise addition of the detergent to continuously stirred membranes at 4 °C. Non-solubilised material was removed by centrifugation (172,000 × g, 45 min). Imidazole was added to the supernatant to a final concentration of 20 mM, then the supernatant was passed through a 0.45 µm filter. The supernatant was loaded onto either a 2 or 5 mL HisTrap HP column (Cytiva) and washed with buffer A (20 mM MES pH 6.5 at 4 °C, 400 mM NaCl, 5 mM $CaCl_2$, 10% (v/v) glycerol, 0.1% (w/v) DDM, 80 mM imidazole) before complex I was eluted with buffer B (buffer A plus 200 mM imidazole). Protein yields could be improved, without sacrificing sample purity or activity, by washing with only 40 mM imidazole and eluting with 300 mM imidazole. Buffers A and B were supplemented with 0.02% (w/v) asolectin and 0.02% (w/v) CHAPS (3-[(3-cholamidopropyl)dimethylammonio]-1-propane-sulfonate). Fractions from the single eluted peak were combined, concentrated to 1 mL and loaded onto either a Superdex 200 increase 10/300 GL (for large-scale preparations) or

Superdex 200 5/150 GL (for small-scale preparations) (Cytiva) equilibrated in buffer C (20 mM MES pH 6.5 at 4 °C, 150 mM NaCl, 10 mM $CaCl_2$, 10% (v/v) glycerol, 0.05% (w/v) DDM). For cryo-EM samples, glycerol was excluded from buffer C. Fractions from the first peak corresponding to complex I were collected and concentrated to 10–20 mg mL^{-1} before glycerol was added at 20% (v/v) and the protein flash frozen in liquid N_2.

2.3.4. Preparation of MaeB and FumC

MaeB and FumC enzymes were prepared as previously described (Jones and Hirst, 2013). FumC was obtained from a communal laboratory stock so its purification will not be described here. For MaeB, NEB BL21 (DE3) cells containing the pET32:*maeB* expression vector were grown in 4 × 1 L LB containing ampicillin (100 µg mL^{-1}) at 32 ˚C, 150 rpm to mid-exponential phase (OD_{600} = 0.6) before inducing MaeB expression with 0.1 mM IPTG. Induced cells were then incubated overnight at 20 ˚C, 225 rpm before harvesting in a Sorvall RC 12BP centrifuge at 4,000 × g. Cells were resuspended in ~120 mL buffer (20 mM Tris-SO_4 pH 7.4 at 4 ˚C, 100 mM NaCl, 10% (v/v) glycerol, 25 mM imidazole and 3 × cOmplete™ EDTA-free protease inhibitor cocktail tablets). The suspension was passed through a Z-plus 2.2 kW cell disruptor twice at 30,000 psi. Cell debris was removed by centrifugation at 160,000 × g in a Ti45 rotor for 45 min. The supernatant was passed through a 0.45 µm filter and loaded onto a 25 mL Ni-sepharose 6 Fast Flow column. The column was washed with buffer (20 mM Tris-SO_4 pH 7.4 at 4 ˚C, 100 mM NaCl, 10% (v/v) glycerol, 60 mM imidazole) and eluted with the same buffer + 300 mM imidazole. The eluted protein was concentrated in a 50 kDa molecular weight cut-off filter (Amicon) and dialysed overnight into buffer containing 20 mM Tris-SO_4 pH 7.4 at 4 ˚C, 10% (v/v) glycerol, 20 mM β-mercaptoethanol. The protein was collected and stored at −80 ˚C in 50% (v/v) glycerol.

2.3.5. Preparation of AOX

AOX from *Trypanosoma brucei brucei* was purified as described previously (Fedor et al., 2017; Jones et al., 2016). AOX was overexpressed in a *hemA* deficient derivative of *E. coli* BL21(DE3) (FN102) from the plasmid pET15b-aox and the membranes prepared as described by Fedor et al. (2017). Membranes were solubilised in 1.4% (w/v) octyl-glucoside (OG) on ice for 1 hour at 6 mg mL^{-1} in a final buffer composition of 25 mM Tris-HCl pH 7.5 at 4 ˚C, 200 mM $MgSO_4$ and 20% (v/v) glycerol. The solubilised material was collected by centrifugation at 230,000 × g for 30 min before the supernatant was loaded onto a column containing 10 mL Streptactin Superflow high-capacity resin. The column was washed with AP buffer (20 mM Tris-HCl pH 7.5 at 4 ˚C, 50 mM $MgSO_4$, 160 mM NaCl and 20% (v/v) glycerol, 0.042% (w/v)

DDM) before eluting the protein with AP buffer + 2.5 mM desthiobiotin. AOX was concentrated in 10 kDa molecular weight cut-off filters (Amicon) and dialysed overnight into AP buffer.

2.3.6. Preparation of *P. denitrificans* proteoliposomes

Proteoliposomes containing *P. denitrificans* complex I were prepared using an adapted protocol from Biner et al. (2016). Synthetic lipids were sourced from Avanti Polar Lipids and were stored in a chloroform stock at 25 mg mL^{-1}. Two different lipid compositions were used for reconstitutions mimicking that of either the mammalian inner mitochondrial membrane (8:1:1, 1,2-dioleoyl-*sn*-glycero-3-phosphocholine (DOPC):1,2-dioleoyl-*sn*-glycero-3-phospho-ethanolamine (DOPE):cardiolipin (CDL; 18:1)) or the *P. denitrificans* plasma membrane (52:37:8:3, 1,2-dioleoyl-*sn*-glycero-3-phospho-(1'-rac-glycerol) (DOPG):DOPC:DOPE:CDL) in % w/w. A total lipid mixture (10 mg) was prepared and to this Q_{10} (also from a chloroform stock) was added at typically 10 nmol $(mg\ lipid)^{-1}$. The chloroform was evaporated off under a gentle stream of nitrogen before the lipids were dried further under a vacuum in a desiccator for at least 1 hour. Following this, lipids were hydrated in 1 mL of reconstitution buffer (10 mM MES pH 6.5 at 4 ˚C, 50 mM KCl, 250 mM sucrose) by vigorous mixing to yield a lipid concentration of 10 mg mL^{-1}. This was then extruded 11 times through a 100 nm Nucleopore polycarbonate membrane (Whatman). For the reconstitution of *P. denitrificans* complex I, typically 2 mg of lipids (200 µL of 10 mg mL^{-1} stock) were partially solubilised in 0.5% (w/v) sodium cholate for 10 min on ice. Purified complex I (100 µg) was then added to this mixture and incubated on ice for 15 min. For co-reconstitutions with the F_1F_O-ATP synthase from *E. coli*, 50 µg of the purified ATPase was also added and incubated on ice for a further 10 min. The reaction mixture was made up to 250 µL with reconstitution buffer. The cholate was subsequently removed by passage through a PD10 desalting column (Cytiva). The 1.2 mL of eluted proteoliposomes were collected by centrifugation at 150,000 × g for 1 hour at 4 °C and the pellet resuspended in 50–100 µL of reconstitution buffer. Proteoliposomes were kept on ice or refrigerated at 4 °C before use.

2.4. Analytical methods

2.4.1. Protein quantification

All protein concentrations were determined by bicinchoninic acid (BCA) assay using Pierce™ BCA assay kits following the manufacturer's instructions. The protein concentration is determined by measuring the absorbance increase at 562 nm that occurs when Cu^{2+} is reduced by peptide bonds to Cu^{+}, which is then chelated by BCA (Smith et al 1985). The reaction was incubated at 37 ˚C for 30 min and the absorbance samples were compared to

BSA protein standards in the range 0.05–1 mg mL^{-1}. A range of dilutions for the unknown samples were prepared to fit within the range of the BSA standards.

2.4.2. SDS-PAGE

Purified proteins/membranes/SBPs were diluted 1:1 with 2× loading buffer (0.125 M Tris-HCl pH 6.8, 20% (v/v) glycerol, 4% (w/v) SDS, 0.005% (w/v) bromophenol blue and 0.1 M DTT) and incubated for 10 min at room temperature. Unless otherwise stated, 10 µg protein was typically loaded onto a Novex™ WedgeWell™ 10–20% Tris–glycine gel alongside Precision Plus Protein™ Kaleidoscope™ pre-stained protein standards. Electrophoresis was performed at a constant voltage of 224 V for 40–50 min in SDS running buffer (25 mM Tris (not pH adjusted), 0.192 M glycine and 0.1% (w/v) SDS. Protein bands were visualised by staining with 0.25% (w/v) Coomassie blue R250, 10% (v/v), acetic acid and 40% (v/v) methanol for 10 min followed by destaining overnight in 20% (v/v) methanol and 7% (v/v) acetic acid.

2.4.3. Western blot analyses

Western blot analysis of *P. denitrificans* SBPs was performed to confirm the presence of the His_6 purification tag. First, an SDS-PAGE gel was run as described above with 20 µg of SBPs loaded onto the gel. Instead of staining the gel, proteins were then transferred onto an Immobilon-P PVDF membrane in transfer buffer containing 25 mM Tris, 0.192 M glycine, 20% (v/v) methanol at 4 ˚C and applying 300 mA across the membrane for 1 hour. The membrane was then treated with blocking buffer (1 × Tris-buffered saline (TBS), 5% (w/v) milk) for 1 hour, followed by overnight incubation at 4˚C with a His-tag anti-rabbit antibody at a dilution of 1:10,000. The membrane was washed in 1 × TBS, 0.1% (v/v) Tween-20 for 1 hour followed by incubation with the anti-rabbit IgG horseradish peroxidase (HRP)-conjugate antibody in blocking buffer for 1 hour. The membrane was again washed in 1 × TBS, 0.1% (v/v) Tween 20 for 1 hour followed by a final wash in 1 × TBS. The membrane was imaged on an Amersham imager 680 by detection of the chemiluminescence produced on addition of ECL Prime reagent (Amersham).

2.4.4. Blue native PAGE

To visualise mitochondrial membrane complexes in *P. denitrificans* SBP samples, Blue native polyacrylamide gel electrophoresis (BN-PAGE) was performed (Schägger and Von Jagow, 1991). Coomassie G250 binds to proteins conferring a negative charge without denaturing the protein, allowing protein complexes to be separated according to their size and shape. Coomassie is included in both sample preparation buffer and the cathode running buffer to

provide a continuous source of Coomassie during electrophoresis. All steps were carried out at 4 ˚C. Typically, SBPs were solubilised at 4–5 mg mL^{-1} in detergent. A 2:1 ratio of DDM to protein (w/w) was typically used to visualise individual respiratory complexes, and a ratio of 2:1 lauryl maltose neopentyl glycol (LMNG) to protein (w/w) was used to visualise respiratory supercomplexes. Membranes were solubilised in buffer containing 10 mM Tris-SO_4 pH 7.5 at 4 ˚C, 250 mM sucrose and 150 mM NaCl for 30 min with continuous mixing at 700 rpm in a Thermomixer comfort (Eppendorf). Insoluble material was removed by centrifugation at 30,000 × g for 30 min. Solubilised protein was then diluted in 1 × NativePAGE™ sample buffer also containing Coomassie G250 at a quarter the concentration of the final detergent concentration in the diluted sample. Typically, 10 µg of protein per well was loaded onto a NativePAGE™ Novex™ 3-12% Bis-Tris Protein Gel (Invitrogen). Solubilised membranes from bovine mitochondria, prepared in a similar way to above, were loaded alongside to act as a standard protein marker. The outer chamber contained running buffer (50 mM Bis-Tris pH 6.8, 50 mM Tricine), and the inner chamber contained 1 × running buffer and 1× cathode buffer (0.4% (w/v) Coomassie G-250). Electrophoresis was performed at 80 V for 1 hour before replacing the inner chamber buffer with 1 × running buffer and 0.1 × cathode buffer followed by electrophoresis at 180 V for 2 hours. Protein bands were visualised by staining as described previously for SDS-PAGE.

Complex I in-gel activity stain

Complex I bands that possess flavin site activity were visualised on BN-PAGE using a modified protocol form Zerbetto and co-workers (Zerbetto et al., 1997). Following electrophoresis, gels were washed in Milli-Q water to remove excess Coomassie G250, then incubated for 10 min with 10 mM Tris-SO_4 pH 7.5, 250 mM sucrose, 0.5 mg mL^{-1} nitroblue tetrazolium (NBT, Sigma) and 200 µM NADH. Purple bands were developed before the reaction was stopped by washing with Milli-Q water.

2.4.5. Two-dimensional gel electrophoresis

Two-dimensional gel electrophoresis was used to visualise the subunit composition of membrane complexes without the need to first purify the complex. First, BN-PAGE was performed as described in Section 2.4.4. Then, bands of interest (e.g., ATP synthase) were excised from the gel using a scalpel and incubated in loading buffer (0.125 M Tris-HCl pH 6.8, 20% (w/v) glycerol, 4% (w/v) SDS, 0.005% (w/v) bromophenol blue and 0.1 M DTT) for 30 min at 30 ˚C with mixing at 700 rpm in a Thermomixer comfort. For the second dimension (SDS-PAGE), four gel slices from replicate BN-PAGE samples were stacked horizontally into each

well of a Novex™ WedgeWell™ 10-20% Tris–glycine gel and run as described above for SDS-PAGE.

2.4.6. Complex I crosslinking with bis(sulfosuccinimidyl)suberate (BS^3)

Purified complex I was diluted to 1 mg mL^{-1} and incubated with various concentrations of bis(sulfosuccinimidyl)suberate (BS^3) for two hours on ice. The BS^3 stocks were prepared in buffer containing 20 mM MES pH 6.5 at 4 °C, 150 mM NaCl, 10 mM $CaCl_2$, 10% (v/v) glycerol, 0.05% (w/v) DDM and 1 µL of each stock was added to complex I (10 µL) to give final concentrations of 0.1, 1, 5 and 10 mM BS^3. After incubation, the reactions were quenched by addition of 0.5 µL 1 M Tris pH 7.4 and incubated at room temperature for 15 min. Samples were then analysed by BN-PAGE, as described above (5.6 µg protein loaded in each well), or by kinetic assays.

2.4.7. DNA quantification

DNA was quantified using a NanoDrop™ ND-1000 spectrophotometer (ThermoFisher Scientific) by measuring the absorbance at 260 nm.

2.4.8. DNA gel electrophoresis

To visualise and/or purify DNA from PCR products and digested plasmids, DNA electrophoresis was performed. Agarose gels (1% w/v) were prepared in 1 × TBE buffer (100 mM Tris pH 8, 100 mM boric acid, 2 mM Na_2-EDTA) including a 1 in 25,000 dilution of SYBR™ Safe DNA gel stain (Invitrogen). DNA samples were mixed with gel loading dye (NEB) and loaded onto the agarose gel alongside a MassRuler Express Forward DNA ladder (Thermo Scientific) for estimating DNA length. DNA was separated at 100 V for 40 min and the gel imaged on a ChemiDoc imager (Bio-Rad) using SYBR Safe fluorescence. When required, DNA bands were purified using a Monarch® DNA gel extraction kit (NEB) according to the manufacturer's instructions.

2.4.9. Nano differential scanning fluorimetry

Nano differential scanning fluorimetry (nanoDSF) was performed in a Prometheus NT.48 (NanoTemper Technologies). Isolated complex I was diluted to 0.3 mg mL^{-1} in buffer containing 20 mM MES pH 6.5 at 4 °C, 150 mM NaCl, 10 mM $CaCl_2$, 10% (v/v) glycerol, 0.05% (w/v) DDM and loaded in triplicate into capillaries (10 µL). The fluorescence at 330 nm and 350 nm was recorded as the temperature was increased from 20 ˚C to 80 ˚C at a rate of 4.5 ˚C min^{-1} with an excitation wavelength of 280 nm and the excitation power between 57–65%.

2.5. Kinetic measurements and spectroscopic assays

All kinetic assays were carried out at 32 °C in a Molecular Devices SpectraMax 348 96-well plate reader unless stated otherwise. Typically, assays involving either purified complex I or *P. denitrificans* membranes were carried out in MES assay buffer containing 10 mM MES pH 6.5 at 32 ˚C, 25 mM NaCl and 2 mM $CaCl_2$. Assays containing *P. denitrificans* SBPs were carried out in SBP buffer containing 10 mM Tris-SO_4 pH 7.5 at 32 ˚C and 250 mM sucrose. Proteoliposome assays were carried out in reconstitution buffer containing 10 mM MES pH 6.5 at 32 ˚C, 50 mM KCl and 250 mM sucrose.

2.5.1. Complex I catalytic activity measurements

NADH:ubiquinone oxidoreduction

To measure NADH:ubiquinone oxidoreduction (NADH:O_2) in *P. denitrificans* membranes, SBPs or in proteoliposomes, the change in absorbance as NADH is oxidised to NAD^+ was monitored at 340–380 nm (ε = 4.81 mM^{-1} cm^{-1}). The rate of NADH oxidation was calculated from linear regression analysis of the raw absorbance data, with the maximum slope used to report the rate. Turnover of the more specific complex I substrate deaminoNADH (dNADH) was assessed in the same way. Enzyme catalysis was initiated by the addition of 200 µM NADH to the assay mixture. Typically, 5–10 µg mL^{-1} of membranes, 10–50 µg mL^{-1} of SBPs and 0.5 µg mL^{-1} of outward-facing complex I in proteoliposomes were assayed. For membranes, 12.5–20 µg mL^{-1} of alamethicin, a pore forming antibiotic, was present in all mixtures to ensure NADH could access all complex I active sites that may be otherwise inaccessible due to clumping of membranes and/or the presence of any inward-facing membrane vesicles. For proteoliposomes, the reaction mixture was supplemented with 20 µg mL^{-1} AOX to regenerate Q_{10}. Piericidin A sensitivity in all cases was assessed by the addition of 5 µM piericidin A to the assay. For membrane and SBP preparations of complex I mutants, dNADH was used in place of NADH to initiate catalysis.

NADH:DQ oxidoreduction

Purified complex I activity was assessed using the soluble quinone analogues decylubiquione (DQ) or isoprenylubiquinone (Q_1). Standard assays contained 0.5 µg mL^{-1} complex I, 200 µM NADH, 200 µM DQ/Q_1 0.15% (w/v) asolectin and 0.15% (w/v) CHAPS. Non-complex I background rates were assessed by addition of 5 µM piericidin A.

NADH:$APAD^+$ oxidoreduction

NADH:$APAD^+$ oxidoreduction was measured in *P. denitrificans* membranes, SBPs, purified complex I and in proteoliposomes by monitoring the change of absorbance of $APAD^+$ at 400–

450 nm (ε = 3.16 mM^{-1} cm^{-1}) as it is reduced. NADH:$APAD^+$ oxidoreduction assays were initiated by addition of 100 µM NADH (or dNADH) and 500 µM $APAD^+$. In all samples, Q-reductase activity was inhibited with 0.5–1 µM piericidin A to prevent transfer of electrons from the flavin site to the Q-site. This allowed $APAD^+$ to be reduced to APADH by hydride transfer from the reduced flavin, a transhydrogenase reaction catalysed by complex I. This could be used to assess the integrity of the complex I in purified samples or used as a measure for the complex I content in membranes, proteoliposomes and SBPs (assuming the flavin site activity was unchanged during reconstitution and/or unaffected in complex I variants). The same protein concentrations for each system were assayed as described for NADH:ubiquinone oxidoreduction. Typically NADH:$APAD^+$ was measured in membranes in the presence of 12.5–20 µg mL^{-1} alamethicin to maximise measured rates as described for the measurement of NADH:ubiquinone oxidoreduction. Purified complex I was assayed in the presence of either 0.15% (w/v) asolectin and 0.15% (w/v) CHAPS or 0.2% (w/v) DDM. Proteoliposomes were measured with/without 25 µg mL^{-1} alamethicin and with/without 0.2% (w/v) DDM to determine the orientation and retention of complex I, respectively.

Succinate:NAD^+ oxidoreduction (RET)

Complex I RET was measured in *P. denitrificans* SBPs, grown on succinate minimal medium, using previously established protocols (Kotlyar and Borovok, 2002; Kotlyar et al., 1998). To drive complex I RET, the quinone pool was reduced via succinate oxidation at complex II and a ∆p was generated via uninhibited complex III and IV catalysis. SBPs (20 µg mL^{-1}) were added to a reaction mixture containing 5 mM succinate and 5 mM NAD^+. The SBP assay buffer was also supplemented with 2 mM $MgSO_4$ and 1 mM K_2SO_4. NAD^+ reduction was monitored at 340–380 nm (ε = 4.81 mM^{-1} cm^{-1}). The initial slopes were used to calculate RET rates.

H_2O_2 production

The production of H_2O_2 in purified complex I was measured using the horseradish peroxidase-dependent oxidation of Amplex Red to resorufin (Pryde and Hirst, 2011). The change in absorbance of Amplex Red was monitored at 557–620 nm (ε = 51.6 mM^{-1} cm^{-1}). Amplex Red detects the formation of H_2O_2, either produced directly by complex I or by the dismutation of superoxide production at complex I, assisted by the presence of superoxide dismutase (SOD). The reaction mixture contained 0.5 µg mL^{-1} complex I, 30 µM NADH, 2 units mL^{-1} horseradish peroxidase, 10 µM Amplex Red and 10 units mL^{-1} SOD (bovine erythrocytes) and with/without 5,000 units mL^{-1} catalase (*Corynebacterium glutamicum*).

***N*-Ethylmaleimide labelling of purified complex I**

Labelling of complex I by *N*-ethylmaleimide (NEM) in *P. denitrificans* membranes was performed to assess the ratio of active/deactive states in the bacterial enzyme. Before labelling, membranes (5 mg mL^{-1}) were either left untreated or were incubated at 37 ˚C in the presence of a cOmplete protease inhibitor EDTA-free tablet for 30 min to 'deactivate' the membranes, according to standard protocols for the mammalian enzyme (Agip et al., 2018; Blaza et al., 2018). The samples were then diluted to 2 mg mL^{-1} and incubated for 20 min with either 2 mM NEM or with the equivalent volume of DMSO as a non-labelling control. Membranes were then diluted to 5 µg mL^{-1} and the NADH:O_2 activity was monitored as above.

2.5.2. Complex II catalytic activity measurements

Succinate:ubiquinone oxidoreduction was measured using an enzyme-coupled assay system developed by Jones and Hirst (2013). Fumarate, generated via complex II catalysis, is converted to malate by a fumarate hydratase (FumC), which is subsequently converted to pyruvate by an oxaloacetate decarboxylating malic dehydrogenase enzyme (MaeB), reducing $NADP^+$ into NADPH in the process. The generation of NADPH can be monitored similarly to NADH at 340–380 nm (ε = 4.81 mM^{-1} cm^{-1}). Succinate:ubiquinone oxidoreduction was measured in membranes or SBPs (5–10 µg mL^{-1}) in reaction mixtures containing 60 µg mL^{-1} FumC, 300 µg mL^{-1} MaeB, 2 mM $MgSO_4$, 1 mM K_2SO_4, 1 mM $NADP^+$ and 5 mM succinate. For complex I proton-pumping stoichiometry assays the enzyme concentrations in the reaction mixture were increased (see Section 2.5.5)

2.5.3. ATP hydrolysis measurements

NADH-coupled ATP hydrolysis

ATP hydrolysis in SBPs was measured using a NADH-coupled ATP regenerating enzyme assay. The ADP produced from ATP hydrolysis is regenerated to ATP via pyruvate kinase (PK) as it converts phosphoenolpyruvate (PEP) into pyruvate. The pyruvate is then converted into lactate by a lactate dehydrogenase (LDH), which, in doing so, consumes one molecule of NADH. For every ATP molecule hydrolysed, one NADH molecule is oxidised, which can be monitored spectroscopically as before. Assay mixtures for monitoring ATP hydrolysis reactions contained 200 µM NADH, 200 µM PEP, 200 µM ATP, 50 µg mL LDH from bovine heart and 40 µg mL^{-1} PK from rabbit muscle. Typically, 50 µg mL^{-1} of SBPs were assayed and complex I catalysis was inhibited with 2 µM piericidin A. For measurements in the presence of a Δp, SBPs were first pre-incubated with 2.5 mM succinate for 3 min at 32 ˚C before the hydrolysis reaction was initiated by the addition of NADH, ATP and the detection enzymes of the assay

system. The protonophore gramicidin A (8 μg mL^{-1}) was used for measurements where ∆p was dissipated.

Pyranine fluorescence ATP hydrolysis

A pyranine fluorescence assay system was used to measure ATP hydrolysis in conditions where ATP is not continually regenerated, allowing for the build-up of product ADP. A proton is released during ATP hydrolysis ($ATP^{4-} + H_2O \rightleftharpoons ADP^{3-} + P_i^{2-} + H^+$), which can be detected by the change in fluorescence emission intensity of pyranine as it becomes protonated. Pyranine fluorescence was monitored in a Shimadzu RF-5301 PC spectrofluorometer at 460 nm excitation wavelength and 510 nm emission wavelength with an excitation and emission bandwidth of 3 nm. Assay buffer contained 2.5 mM Tris-SO_4 pH 8.0 at 32 ˚C, 10% (w/v) glycerol, 100 mM KCl, 2.5 mM $MgCl_2$, 1 mM ATP, 2 μM pyranine and 400 μg mL^{-1} SBPs. The pH of each additive was adjusted to 8.0 beforehand and 3 mM ADP and/or 5 mM sulfite were added as required for assessing ADP inhibition and oxyanion activation of ATP hydrolysis. Changes in fluorescence were converted to changes in proton concentration by comparison to a standard curve produced by successive additions of 40 nmol HCl.

2.5.4. ATP synthesis measurements

ATP synthesis in *P. denitrificans* SBPs and proteoliposomes was monitored using a luciferase-luciferin based luminescence ATP detection readout. In this system, ATP generated during ATP synthesis is consumed by luciferase (from firefly) to convert luciferin to luciferyl adenylate and PP_i. The luciferyl adenylate then rapidly converts to oxyluciferin in the presence of oxygen and generates light. The intensity of luminescence is directly proportional to the amount of ATP present. Two different methodologies employing this system were used to measure ATP synthesis and are described below.

Quenched time-course ATP monitoring assay

ATP synthesis in SBPs was monitored using an assay system based on that of Jones et al. (2017). In brief, samples from a reaction mixture synthesising ATP were quenched (catalysis was stopped) at 30 s intervals during a 3 min time course, before the ATP concentration in these samples was measured by the luminescence output after the addition of luciferase/luciferin. For these assays, the SBP assay buffer contained 10 mM Tris-SO_4 pH 7.5 at 32 ˚C, 250 mM sucrose, 2 mM $MgSO_4$, 10 mM KPO_4, 1 mM ADP, 250 μM diadenosine pentaphosphate (Ap5A), 20 units mL^{-1} SOD, 5000 unit mL^{-1} catalase and 12–24 μg mL^{-1} SBPs. The Ap5A was used to inhibit unwanted adenylate kinase activity (Abele and Schulz, 1995). The reaction was initiated with 200 μM NADH or 5 mM succinate (for complex I- and complex II-driven catalysis, respectively) and the substrate oxidation was monitored

spectroscopically in a cuvette as described above. After 1 min, ATP production was monitored by withdrawing and quenching 10 µL aliquots of the reaction mixture into 40 µL of 4% (v/v) trifluoroacetic acid, followed 20 s later by addition of either 250 or 450 µL neutralising buffer (1 M Tris-SO_4 pH 8.0). Each quenched sample was then plated out three times (80 µL each) into a 96-well white flat-bottom luminescence plate and 20 µL of the Roche ATP Bioluminescence Assay Kit CLS-II kit was added to each well. The luminescence at 580 ± 80 nm of each well was measured in a BMG Labtech CLARIOstar plus microplate reader fitted with a luminescence aperture or a Molecular Devices SpectraMax Gemini XPS 96-well microplate reader. The concentration of ATP was calculated in each sample by comparison to a standard curve of samples with known ATP concentrations.

Continuous real-time ATP monitoring assay

ATP synthesis was measured in real time by including the luciferase/luciferin detection system directly into the reaction mixture, which allowed for the continuous monitoring of ATP generation from the luminescence readout in real time (Meyrat and Von Ballmoos, 2019; Von Ballmoos et al., 2016). This assay system was used to monitor ATP synthesis in both SBPs and proteoliposomes (where complex I was co-reconstituted with F_1F_O-ATP synthase from *E. coli*). For SBPs, the assay buffer contained 20 mM Tris-PO_4 pH 7.5 at 25 ˚C, 5 mM $MgCl_2$, 100 µM Ap5A and a 1:50 dilution of luciferase reagent (ATP Bioluminescence Assay Kit CLS-II, Roche) (Von Ballmoos et al., 2016). Typically, 12 µg mL^{-1} SBPs were assayed at room temperature in the presence of 50 µM ADP (Meyrat and Von Ballmoos, 2019). The baseline luminescence (560 nm) was recorded for 30 s before the addition of 1 µM ATP, which was used to calibrate the luminescence. The reaction was initiated by addition of NADH and ATP synthesis was monitored continuously at room temperature in a Promega GloMax 20/20 luminometer using 50 µL reaction volumes (in 1.5 mL tubes). ATP synthesis rates were calculated from the initial slope (10–30 s). For ATP synthesis measurements using proteoliposomes, 1 µg mL^{-1} of outward-facing complex I was used in the reaction and the above buffer was supplemented with 5 µg mL^{-1} AOX.

2.5.5. Complex I proton-pumping stoichiometry measurements

To measure the number of protons pumped by complex I per NADH oxidised (proton-pumping stoichiometry) ATP synthesis rates were compared to the input rates from three different pathways, CI/CIII/CIV, CII/CIII/CIV and CI/AOX, a method based on previous established protocols (Fedor and Hirst, 2018; Jones et al., 2017). The theory behind how this experiment works was described by Jones et al. (2017) and is based on how SMPs and SBPs can be considered as proton circuits, where they generate a Δp by respiration and consume the Δp

by ATP synthesis. Using this comparison, the input energy (number of protons contributing to the ∆p) is considered equal to the output energy (number of protons consumed by ATP synthesis or in leakage back across the membrane). Shown below are the derivations leading to the final equations that can be used to calculate the complex I proton-pumping stoichiometry from experimentally measured rates of ATP synthesis and substrate oxidation, which consider the loss of protons due to membrane leak.

As an example, in the CII/CIII/CIV pathway, six protons are pumped across the membrane per succinate oxidised, a well-established stoichiometry (Crofts et al., 1983; Wikström, 1977). The ATP synthase uses these protons in a defined stoichiometry (*p*) to synthesise ATP based on the stoichiometry of the *c*-ring in each organism (one ATP per 2.67 or 4.0 protons consumed in mammals and *P. denitrificans*, respectively). In addition, the loss of protons due to leakage across the membrane (not consumed during ATP synthesis) is termed the rate of leak (v_{leak}). The rate of succinate oxidation ($v_{\mathrm{CII:CIII:CIV}}$) and rate of ATP synthesis ($v_{\mathrm{ATP(CII:CIII:CIV)}}$) for the CII/CIII/CIV pathway can be combined with these terms to yield **Equation 2.1**.

$$6.v_{\mathrm{CII:CIII:CIV}} = p.v_{\mathrm{ATP(CII:CIII:CIV)}} + v_{\mathrm{leak}} \qquad \textbf{Equation 2.1.}$$

To calculate the number of protons pumped by complex I (n^{CI}), similar equations can be derived for alternative pathways, which provide a different number of input protons (CI/CIII/CIV (n^{CI}+6) vs CII/CIII/CIV (6) vs CI/AOX (n^{CI})), where the number of protons provided by each pathway is in parentheses). Combining **Equation 2.1** with the equivalent equation for the CI/CIII/CIV reaction leads to **Equation 2.2**, which is valid for comparison of the two reactions catalysed by the same system, when rates of ATP synthesis are equal, and so ∆p values are equal, and so are the v_{leak} values.

$$6.v_{\mathrm{CII:CIII:CIV}} = \left(6 + n^{\mathrm{CI}}\right).v_{\mathrm{CI:CIII:CIV}} \qquad \textbf{Equation 2.2.}$$

However, in an imperfect system where ATP synthesis rates cannot be exactly matched and so ∆p is not exactly the same, the proton leak, therefore, also varies between the two cases and **Equation 2.1** can be rewritten as shown in **Equation 2.3** where $k_{\mathrm{leak}} = v_{\mathrm{leak}}/(6.v_{\mathrm{CII:CIII:IV}})$, the fractions of protons lost to leak. The fraction of protons used to synthesise ATP can thus be described by $(1 - k_{\mathrm{leak}})$.

$$(1 - k_{\mathrm{leak}}).6.v_{\mathrm{CII:CIII:CIV}} = p.v_{\mathrm{ATP\ (CII:CIII:CIV)}} \qquad \textbf{Equation 2.3.}$$

An example of the comparison between these rewritten equations for the CI/CIII/CIV and CII/CIII/CIV pathways is shown in **Equation 2.4**. This eliminates the term *p* but introduces a new unknown term ($(1 - k_{\text{leak(CII:CIII:IV)}})/(1 - k_{\text{leak (CI:CIII:CIV)}})$), which cannot be determined experimentally. In a perfect system, where the rates of proton pumping, ATP synthesis and leak are perfectly matched between CI/CIII/CIV and CII/CII/CIV pathways, $(1 - k_{\text{leak (CII:CIII:CIV)}}) = (1 - k_{\text{leak (CI:CIII:CIV)}})$ and the unknown term simplify to 1.

$$\frac{6 + n^{\text{CI}}}{6} = \frac{v_{\text{CII:CIII:CIV}}}{v_{\text{CI:CIII:CIV}}} \cdot \frac{v_{\text{ATP (CI:CIII:CIV)}}}{v_{\text{ATP (CII:CIII:CIV)}}} \cdot \frac{1 - k_{\text{leak (CII:CIII:CIV)}}}{1 - k_{\text{leak (CI:CIII:CIV)}}} \qquad \textbf{Equation 2.4.}$$

Experimentally, the rate of leak in both CI/CIII/CIV and CII/CII/CIV pathways will vary dependent on the ∆p. To eliminate these variations as a substantial source of error, the ratio of ATP synthesis and substrate oxidation rates were measured by Jones et al. (2017) in SMPs at varying degrees of inhibition for each pathway (using inhibitors to modulate the activity). This ratio remained constant and thus, according to **Equation 2.3**, the k_{leak} must also be constant for each pathway. Therefore, the unknown term in **Equation 2.4** is a constant, which can be assigned a value equal to 1 for simplicity. Equations comparing each pathway (CI/CIII/CIV, CII/CIII/CIV and CI/AOX oxidoreduction) in three pairwise comparisons can subsequently be derived leaving only terms that can be experimentally determined (substrate oxidation rates and ATP synthesis rates) (**Equation 2.5–2.7**). Using these equations, the value of protons pumped by complex I can be calculated, which can be triangulated by the three pairwise comparisons between each pathway. By matching ATP synthesis rates as closely as possible between pathways, so that the ∆p are equal and so are the rates of leak, this method was successfully used to show that complex I pumped four protons in SMPs and SBPs (Jones et al., 2017).

$$\frac{6 + n^{\text{CI}}}{6} = \frac{v_{\text{CII:CIII:CIV}}}{v_{\text{CI:CIII:CIV}}} \cdot \frac{v_{\text{ATP(CI:CIII:CIV)}}}{v_{\text{ATP (CII:CIII:CIV)}}} \qquad \textbf{Equation 2.5.}$$

$$\frac{n^{\text{CI}}}{6} = \frac{v_{\text{CII:CIII:CIV}}}{v_{\text{CI:AOX}}} \cdot \frac{v_{\text{ATP(CI:AOX)}}}{v_{\text{ATP (CII:CIII:CIV)}}} \qquad \textbf{Equation 2.6.}$$

$$\frac{6 + n^{\text{CI}}}{6} = \frac{v_{\text{CI:AOX}}}{v_{\text{CI:CIII:CIV}}} \cdot \frac{v_{\text{ATP(CI:CIII:CIV)}}}{v_{\text{ATP (CI:AOX)}}} \qquad \textbf{Equation 2.7.}$$

An adaptation of this protocol by Fedor and Hirst (2018) matched ATP synthesis rates over a range of NADH oxidation activities for CI/CIII/CIV and CI/AOX pathways. The CI/AOX pathway

was substituted for the equivalent CI/Q_1 pathway, previously used by Jones et al. (2017), where CII, CIII and CIV are inhibited and SMPs are supplemented with AOX instead of Q_1. By rearranging **Equations 2.5–2.7**, the number of protons pumped by complex I (n^{CI}) can be calculated using the slope of ATP synthesis versus substrate oxidation, where $slope = \Delta v_{\mathrm{ATP(CI:CIII:CIV)}}/\Delta v_{\mathrm{CI:CII:CIV}}$ or the equivalent for each pathway (**Equations 2.8–2.10**). In this case, as slopes for each pathway were compared, multiple Δp values were compared and so the ATP synthesis rates for each pathway were overlapped with each other to minimise the breakdown of assumptions, such as that of k_{leak} being constant. The data showed these assumptions were valid (the k_{leak} was constant), as a linear dependence of ATP synthesis versus substrate oxidation, which passes through the origin, was observed thus permitting this comparison.

$$n^{\mathrm{CI}} = \frac{6}{\left(\frac{slope_{\mathrm{CI:CIII:CIV}}}{slope_{\mathrm{CI:AOX}}} - 1\right)} \qquad \textbf{Equation 2.8.}$$

$$n^{\mathrm{CI}} = 6 \times \left(\frac{slope_{\mathrm{CI:CIII:CIV}}}{slope_{\mathrm{CII:CIII:CIV}}} - 1\right) \qquad \textbf{Equation 2.9.}$$

$$n^{\mathrm{CI}} = 6 \times \left(\frac{slope_{\mathrm{CI:AOX}}}{slope_{\mathrm{CII:CIII:CIV}}}\right) \qquad \textbf{Equation 2.10.}$$

For proton-pumping stoichiometry measurements performed here in *P. denitrificans* SBPs, the slopes for CI/CIII/CIV, CII/CIII/CIV and CI/AOX pathways were compared. The assay conditions for each pathway were designed to be as similar to each other as possible. ATP synthesis rates were monitored using the quenched time-course ATP monitoring assay and substrate oxidation rates were monitored in real time for each sample in a cuvette, as described above. SBPs used in these assays were grown on succinate minimal medium. Assays were performed at 32 ˚C and all the final assay conditions contained 20 μg mL^{-1} SBPs, 10 mM Tris-SO_4 pH 7.5 at 32 ˚C, 250 mM sucrose, 10 mM KPO_4 (pH 7.5), 2 mM $MgSO_4$, 1 mM K_2SO_4, 1 mM ADP, 250 μM Ap5A, 20 units mL^{-1} SOD, 5000 units mL^{-1} catalase, 5 mM succinate and 20 μg mL^{-1} AOX. For the CI/CIII/CIV pathway, complex II was inhibited with 2 μm atpenin A, AOX was inhibited with 1 μM ascofuranone and 200 μM dNADH was added to initiate catalysis. For the CII/CIII/CIV pathway, complex I was inhibited with 2 μM piericidin A, AOX was inhibited with 1 μM ascofuranone and the buffer also contained 2 mM $NADP^+$, 240 μg mL^{-1} FumC and 1.2 mg mL^{-1} MaeB. For the CI/AOX, pathway, complex II was inhibited with 2 μm atpenin A, complexes III and IV were inhibited with 1 μM antimycin A and 400 μM NaCN, respectively, and catalysis was initiated by 200 μM dNADH. Finally, to modulate substrate oxidation rates

to match ATP synthesis activities, piericidin A and atpenin A were titrated for respective complex I- and complex II-driven pathways.

2.5.6. Characterisation of proteoliposomes

The total phospholipid contents were determined using the Ames phosphate assay as described previously (Jones et al., 2016). Total Q_{10} content was calculated using an HPLC system equipped with a Thermo Scientific Dionex Ultimate 3000RS Electrochemical Detector as described previously (Biner et al., 2020). The orientation and complex I content of the proteoliposomes were determined by comparison of the NADH:$APAD^+$ activity in a known volume of liposomes, with the NADH:$APAD^+$ activity of a known concentration of purified complex I, assuming the flavin site activity was retained during reconstitution. The retention of complex I in the liposomes was calculated by addition of 0.2% (w/v) DDM in the assay buffer, to solubilise all complex I present. The orientation of complex I was calculated by comparison of NADH:$APAD^+$ activity in proteoliposomes with/without 25 µg mL^{-1} alamethicin, where the substrates can access either only outward facing complex I (no alamethicin) or both inward and outward facing complex I (with alamethicin). For measuring the NADH:O_2 activity of complex I in proteoliposomes, 0.5 µg mL^{-1} outward-facing complex I was assayed in reconstitution buffer containing 200 µM NADH and 20 µg mL^{-1} AOX.

2.5.7. ACMA quenching

9-Amino-6-chloro-2-methoxyacridine (ACMA) can be used as a qualitative measure for membrane energisation and coupling in vesicles (Dröse et al., 2005; Dufour et al., 1982). Upon formation of a pH gradient across the membrane, the protonated form of ACMA accumulates in the lumen, leading to quenching of its fluorescence signal (Huang et al., 1983). The extent of quenching and rate of quenching are semi-quantitative to the amount of membrane coupling/energisation. NADH oxidation- or ATP hydrolysis-driven ACMA quenches in SBPs or proteoliposomes were initiated by addition of either NADH (500 µM) or ATP (1 mM) to 1 mL of vesicles (50 µg mL^{-1} SBPs or 1 µg outward-facing CI mL^{-1} proteoliposomes) stirred in buffer containing 0.5 µM ACMA and 100 nM valinomycin. The ionophore valinomycin was added to diminish the $\Delta\Psi$ contribution to the Δp, by moving K^+ ions in the opposite direction to pumped protons, allowing the ΔpH component to build up. The buffer for SBP measurements was composed of 10 mM MOPS pH 7.5 at 32 ˚C, 50 mM KCl and 1 mM $MgCl_2$. The buffer for proteoliposome experiments contained 10 mM MES pH 6.5 at 32˚C, 50 mM KCl and 250 mM sucrose. Membranes were de-energised by addition of 40 mM NH_4Cl or 25 µg mL^{-1} alamethicin after 4 min. The ACMA fluorescence was followed in a Shimadzu RF-5301 PC spectrofluorometer at 419 nm excitation wavelength and 484 nm emission wavelength with an

excitation and emission bandwidth of 5 nm and 10 nm, respectively. The fluorescence was measured every 0.5 s.

2.6. EPR spectroscopy

Electron paramagnetic spectroscopy (EPR) sample preparation, measurements and analyses were performed by Dr John Wright (MRC Mitochondrial Biology Unit, Cambridge). Complex I samples were reduced by the addition of 15 mM NADH under anaerobic conditions in an glove box (Belle Technology). The sample was immediately frozen in dry ice/acetone before transfer to liquid nitrogen for storage. EPR measurements were performed using an X/Q-band Bruker Elexsys E580 Spectrometer (Bruker BioSpin) operating in X-band mode and equipped with a closed-cycle cryostat (Cryogenic Ltd) and X-band split-ring resonator module (ER 4118X-MD5). EPR measurement conditions were 100 kHz modulation frequency, 7 G modulation amplitude, 2 mW microwave power and were performed at various temperatures. All spectra presented are baseline corrected using a buffer-only sample. EPR simulations were performed using the EasySpin package for MATLAB (Stoll and Schweiger, 2006).

2.7. Mass spectrometry

Bands excised from SDS-PAGE gels were digested with trypsin and analysed by matrix-assisted laser-desorption ionisation (MALDI) using an Applied Biosystems spectrometer, or by Orbitrap using a Q-Exactive Plus Orbitrap mass spectrometer, as described previously (Bridges et al., 2017; Varghese et al., 2018). Mass spectrometry experiments were performed by Dr Michael Harbour, Dr Shujing Ding and Dr Ian Fearnley (MRC Mitochondrial Biology Unit, Cambridge). MALDI and Orbitrap spectra were assigned to peptide sequences and their originating proteins using the Mascot 2.4 application (Matrix Science Ltd.) with a peptide precursor mass tolerance of 360 ppm (MALDI) or 5 ppm (Orbitrap) and fragment mass tolerance of 0.8 Da (MALDI) or 0.01 Da (Orbitrap). One or two missed cleavages were allowed for respective MALDI and Orbitrap data, plus methionine oxidation and cysteine propionamide formation as variable modifications were permitted.

2.8. Cryo-EM grid preparation and data collection

2.8.1. Grid preparation

UltrAuFoil® 0.6/1 gold grids (Quantifoil) cryo-EM grids were used in grid making (Russo and Passmore, 2014). These have been successfully used for complex I cryo-EM data collections in the past for mammalian and yeast mitochondrial complex I structures (Blaza et al., 2018; Grba and Hirst, 2020). The grid surface was derivatised to make the surface more hydrophilic

to avoid membrane protein aggregation. First, grids were glow discharged at 20 mA for 90 s to clean the surface, followed by incubation in anaerobic conditions for two days in ethanol with 5 mM PEG-thiol reagent (11-mercaptoundecyl hexaethyleneglycol, SensoPath Technologies) (Blaza et al., 2018; Meyerson et al., 2014). The grids were washed with ethanol and dried before protein application.

2.8.2. Application of protein to grids and freezing

PEGylated grids were placed into an FEI Vitrobot™ Mark IV (Thermo Scientific™) set to 100% relative humidity at 4 ˚C. Complex I fractions from the size-exclusion chromatography were applied directly to the grid without concentrating (2.5 µL per grid, 2–3 mg mL^{-1} protein). The grid was typically blotted with a force of –10 and a blotting time of 10 s before plunge freezing in liquid ethane. Before grid screening and data collection, grids were clipped using an AutoGrid clipping station (FEI, Thermo Scientific™). Grid freezing and clipping were carried out by Dr Zhan Yin (MRC Mitochondrial Biology Unit, Cambridge).

2.8.3. Cryo-EM grid screening and data collection

Grid screening and data collection were assisted and performed by Dr Zhan Yin (MRC Mitochondrial Biology Unit, Cambridge) and Dr Dima Chirgadze (University of Cambridge cryo-EM facility). Grids frozen with complex I from *P. denitrificans* were screened on a 200 keV Talos™ Artica EM microscope (Thermo Scientific™). A grid with suitable ice thickness and particle distribution in the holes was taken forward for data collection. Data collection was performed on a 300 keV FEI Titan Krios at University of Cambridge cryo-EM facility. A Gatan K2 summit camera was used in counting mode and an energy filter at 20 eV. Data were collected on the chosen grid for three days, producing 2278 micrographs. A total dose of 48 electrons $(Å^2)^{-1}$ was used over 25 frames with an exposure time of 10 s, focusing every 10 µm. The C2 and objective apertures were 50 µm and 100 µm, respectively. The defocus range was –1.5, –1.8, –2.1, –2.4, –2.7 and –2.9 µm and the pixel size was 1.05 Å.

2.9. Cryo-EM data processing in RELION

The RELION-3.0 pipeline was used to process the single-particle cryo-EM data collected for complex I from *P. denitrificans* (Zivanov et al., 2018). The typical pipeline was followed for particle analysis. A more specific scheme and analysis is described in Chapter 5, but the basic scheme is introduced here. Steps during this scheme can be repeated and performed in different orders to improve the final reconstruction.

2.9.1. Motion correction

Micrograph movies were imported into the RELION pipeline. Beam-induced, in-plane motion correction of the micrographs and dose weighting was performed using MotionCor2 (Zheng et al., 2017). A default B-factor of 150 was used and the micrographs were split into five-by-five patches. The micrographs were dose weighted with their respective dose-per-frame values. The analysis produced average micrographs that were motion corrected.

2.9.2. CTF estimation per micrograph

CTF (contrast transfer function) correction per motion-corrected micrograph was performed using Gctf version 1.18 (K. Zhang, 2016). No dose weighting of the micrographs was used and equiphase averaging was enabled. From this estimation, micrographs with non-amorphous ice were identified by the distinct Thon rings seen in Fourier transform images of the micrograph. These micrographs were removed from future analysis.

2.9.3. Manual particle picking and 2D template generation

Particle picking was first performed manually, with ~8000 particles picked in a variety of different particle orientations. These were then used to generate a 2D template by 2D classification of the particles. A total of 22 different 2D classes were taken forward as a 2D template for automated particle picking.

2.9.4. Automated particle picking

For the first round of automated particle picking, the 2D templates from 8000 manual picked particles was used as a template. Picking parameters were optimised with a picking threshold of 0.4, a minimum inter-particle distance of 210 Å and a maximum standard deviation of noise of 1.2. This resulted in 73,317 picked particles. These particles were then reclassified using 2D classification to generate improved 2D templates, which were fed back into the autopicking feature to repick micrographs. The picking parameters were again optimised with a picking threshold of 0.1, a minimum inter-particle distance of 200 Å, a maximum standard deviation of noise of 1.2 and a minimum average noise of –0.5. From this, 125,639 particles were picked.

2.9.5. Initial classification – 3D

An initial 3D model was made from the 2D classes generated from the 8000 manually picked particles. This acted as a reference map for 3D classifications. Multiple rounds of 3D classification on the 125,639 auto-picked particles were performed to remove non-protein, aggregated proteins and partially intact complex I particles.

2.9.6. 3D auto-refinement

Classes that resembled complex I with a large particle number were subject to 3D auto-refinement. This process aligns particles with decreasing angular sampling over multiple iterations until it can be improved no further. To improve particle alignment, a mask that surrounds the whole protein was used, which excludes solvent signals. Masks were created in RELION using the class 1 map from the first round of 3D classification, with a map extension of three pixels and a soft edge (to limit masking artefacts) of three pixels. No symmetry (*C*1) was applied to the refinement and the reference map was low-pass filtered to 15 Å. Default automated sampling parameters were used.

2.9.7. CTF estimation per particle

CTF estimation per particle was performed on aligned particles to update the estimates of the defocus and astigmatism for each particle (Zivanov et al., 2018), which takes into account that protein particles sit at different heights within the ice layer on imaging and so have varying defocus values that benefit from tailored CTF correction to their signal.

2.9.8. Bayesian particle polishing

Bayesian polishing uses motion correction data and dose values to improve overall motion trajectory correction, by reducing the weighting of micrograph movie frames that contribute too much radiation damage (typically, the later frames). Bayesian polishing was first trained with 10,000 particles to optimise the parameters for polishing of all particles (Zivanov et al., 2019). After polishing, another round of CTF estimation per particle was performed to improve CTF estimation further.

2.9.9. Final 3D auto-refinement and post processing

After improving CTF estimations and motion correction by per-particle CTF estimation and Bayesian polishing, a final 3D auto-refinement was performed, as described above. Post processing was subsequently performed to obtain a solvent-corrected FSC (Fourier Shell Correlation) resolution estimate. The output map is sharpened with a B-factor value that improves map connectivity and outlines features, such as side chains (Rosenthal and Henderson, 2003). The mask used in the post processing stage was the same as used for 3D refinement with solvent flattening.

2.9.10. Local resolution estimation

Inherent flexibility in complex I leads to heterogeneity in the resolution across the whole complex. To better assess the flexibility and quality of the electron density map, local resolution estimation was performed in RELION (Fernandez-Leiro and Scheres, 2017). A series of resolution estimates are performed over small sections of the 3D reconstruction, which can then be used to sharpen the refined map locally and colour the final 3D reconstruction according to the resolution estimates.

2.9.11. Focused classification – 3D

Persistent heterogeneity within the refined particles, as evidenced by poor reconstruction and the local resolution, was targeted for classification at regions specific to the heterogeneity, i.e. focused classification. Masks for focused classification were generated in RELION on specific regions of the protein, such as the membrane domain. For more details see Chapter 5, and specifically Section 5.4.3 for the membrane domain classification.

3. Activation of ATP hydrolysis in the *P. denitrificans* ATP synthase in order to study complex I RET

3.1. Introduction

3.1.1. Methods to study complex I RET in vitro

Complex I is a thermodynamically reversible enzyme capable of catalysis in both directions: forward electron transfer (FET, NADH:ubiquinone oxidoreduction) and reverse electron transfer (RET, ubiquinol:NAD^+ oxidoreduction). Understanding how the RET reaction proceeds mechanistically is a crucial part of understanding the overall mechanism of complex I catalysis. Possessing a model system that allows coherent investigations of the effects of mutations and small molecules on both the FET and RET reactions would be hugely beneficial in understanding the basic biochemistry of complex I catalysis and how energy is conserved by the enzyme.

To date, RET has predominantly been investigated in vitro using mammalian complex I. This is due to several criteria that must be met to measure RET in in vitro models. To drive RET, both a high QH_2/Q ratio and a Δp is required (**Figure 3.1**). First, well-coupled membrane vesicles must be prepared that can establish and maintain a sufficient Δp across the membrane. Second, the Q-pool must be reduced independently of complex I and, last, the system requires a way to generate a Δp, ideally independent of respiration, that does not re-oxidise the Q-pool.

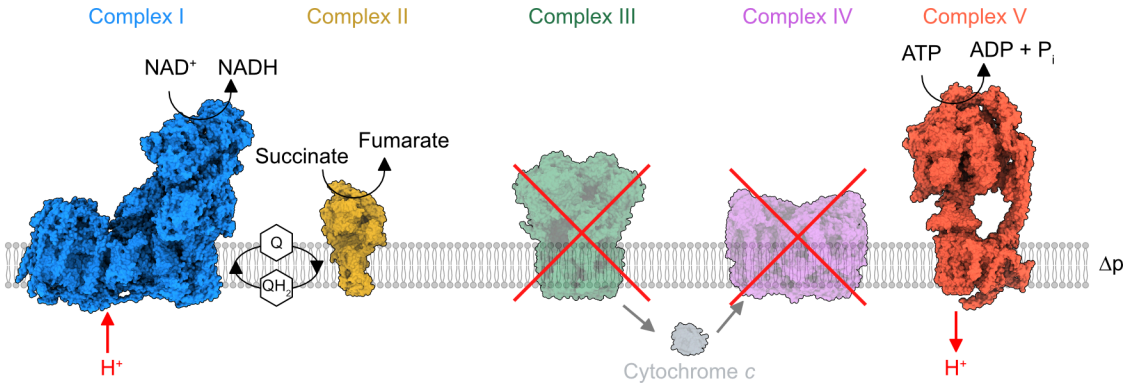

Figure 3.1. Reverse electron transfer (RET) in complex I. The Q-pool is reduced by complex II through succinate oxidation while complex III and IV catalysis is inhibited with antimycin A and KCN, respectively. RET is powered by a Δp generated from ATP hydrolysis at ATP synthase (complex V). The Δp is consumed by complex I to drive QH_2 oxidation and the energetically uphill electron transfer to the flavin site to reduce NAD^+.

Bovine sub-mitochondrial particles (SMPs) satisfy the criteria for RET measurements; they are well coupled so can sustain a ∆p, the Q-pool can be reduced via succinate oxidation at complex II (while complexes III and IV are inhibited to prevent re-oxidation of the Q-pool) and, finally, a ∆p can be generated from ATP synthase working in reverse and hydrolysing ATP. Having met these requirements, RET and the thermodynamic reversibly of complex I can be studied by altering the thermodynamics of the system to favour RET, according to the Nernst equation (**Equation 3.1**) (Pryde and Hirst, 2011). This can be done by changing the ratios of NADH/NAD^+ and succinate/fumarate. When the NADH/NAD^+ ratio is low and the succinate/fumarate ratio is high, the NADH:fumarate oxidoreduction potential (∆*E*) is lower than ∆p so the RET reaction is favoured (succinate/NAD^+ oxidoreduction). The reverse is true for the FET reaction.

$$\Delta E = -0.335 + 0.020 - \frac{RT}{2F}\ln\frac{[\mathrm{NADH}][\mathrm{fumarate}]}{[\mathrm{NAD^+}][\mathrm{succinate}]}$$

Equation 3.1. Nernst equation for complex I FET and RET reactions. The NADH:fumarate oxidoreduction potential (∆*E*) can be calculated and modulated by varying the ratios of substrates for the complex I and complex II reactions. The standard reduction potentials for each redox couple at pH 7.5 are given for NADH/NAD^+ (–0.335 V) and succinate/fumarate (–0.02 V). *R* is the gas constant (8.31 J K^{-1} mol^{-1}), *T* is the temperature (K) and *F* is the Faraday constant (96485 J V^{-1} mol^{-1}). The concentrations of NADH, NAD^+, succinate and fumarate are denoted by square brackets (mM).

When the FET and RET reactions reach equilibrium and there is no net NADH oxidation or NAD^+ reduction, the NADH:fumarate oxidoreduction potential is directly related to the ∆p and number of protons pumped per two electrons (**Equation 3.2**).

$$-2\Delta E = n\Delta\mathrm{p}$$

Equation 3.2. The relationship between ∆*E* and ∆p when complex I is at thermodynamic equilibrium. ∆*E* is the difference in midpoint potentials between the NADH:NAD^+ and succinate:fumarate couples and *n* is the number of protons pumped by complex I (per two electrons)

By modulating the FET and RET reactions, insight can be gained into the reversibility and efficiency of complex I catalysis, an important tool for characterising mutants and understanding the differences and similarities between the FET and RET reactions (Armstrong and Hirst, 2011; Pryde and Hirst, 2011). Hence it is desirable to be able to expand in vitro models to include bacterial models, in particular *P. denitrificans*, in which mutations can be generated.

3.1.2. Studying RET in *P. denitrificans* complex I

P. denitrificans already satisfies most of the criteria for RET measurements. Much like SMPs, sub-bacterial particles (SBPs) can be prepared that can support ATP synthesis, showing that they are well coupled, and the *P. denitrificans* respiratory chain includes complex II, which can be used to reduce the Q-pool (Burnell et al., 1975; John and Whatley, 1977; Jones et al., 2017). However, a limitation to studying RET and complex I reversibility in the *P. denitrificans* model arises with the requirement for the generation of a Δp independent of respiration. This is because the F_1F_O-ATP synthase of *P. denitrificans* does not hydrolyse ATP at a sufficiently fast rate to generate a substantial Δp. Despite this, RET has been demonstrated in *P. denitrificans* complex I with rates of between 0.11 and 0.53 μmol min^{-1} (mg SBPs)$^{-1}$ (Kotlyar and Borovok, 2002; Kotlyar et al., 1998). These studies were able to drive the RET reaction in SMPs and SBPs solely via succinate oxidation, with the Δp generated by proton pumping through complex III and IV. However, this approach had limited reproducibility and does not facilitate the study of the efficiency of complex I reversibility, as the Δp will also change when titrating the redox potential through complex II. In this regard, if ATP hydrolysis could be activated in *P. denitrificans* ATP synthase then it is possible this would allow the measurement of RET and complex I reversibility in *P. denitrificans*, much as has been done previously for SMPs (Fedor and Hirst, 2018; Pryde and Hirst, 2011).

The key motivation for this study was to activate ATP hydrolysis in *P. denitrificans* for the purpose of establishing RET and complex I reversibility studies, thus increasing the functional toolkit available to study complex I mutants. In a parallel strand of investigation, how ATP hydrolysis by the ATP synthase in *P. denitrificans* and other microorganisms is regulated is an intensely studied and debated topic. These organism-specific regulation mechanisms have become a potential target space for the development and design of drugs to treat bacterial infections (Guo et al., 2021; Schulz et al., 2013; Zíková et al., 2009). Therefore, a complete understanding of ATP hydrolysis regulation in *P. denitrificans* is of interest both mechanistically and for its potential exploitation in our work to establish a suitable system for measuring complex I RET in *P. denitrificans.*

3.1.3. Regulation of hydrolysis in ATP synthase

Like complex I, F_1F_O-ATP synthases are, in principle, reversible enzymes: when Δp is low and [ATP]/[ADP] is high, the thermodynamics of the system favour ATP hydrolysis over ATP synthesis, leading to generation of a Δp. This reverse reaction is used by many microorganisms that predominantly generate ATP by fermentation under anaerobic growth conditions. In such cases, these organisms employ ATP synthase as a proton pump to provide

a ∆p required to maintain essential cellular functions (Ferrándiz and De La Campa, 2002; Navon et al., 1977; Ugurbil et al., 1978). However, there are many physiological contexts in which ATP hydrolysis is an unwanted response to a low ∆p. To prevent the rapid depletion of the cellular ATP pool, organisms have evolved distinct mechanisms to limit ATP hydrolysis. In mitochondrial ATP synthases the inhibitory factor 1 (IF_1) inserts into the rotary machinery of F_1, acting like a ratchet to block rotation specifically in the hydrolysis direction (Bason et al., 2011) (**Figure 3.2A**). A similar strategy is thought to be employed by the C-terminal domain of the ε subunit in some bacteria (**Figure 3.2**) (Cingolani and Duncan, 2011; Guo et al., 2019; Keis et al., 2006). In chloroplasts, a different strategy has been adopted. In the dark, when ∆p is no longer maintained by photosynthesis and conditions favour hydrolysis, a reversible disulfide bond is formed within the γ subunit, holding it in a position near the β subunit and preventing rotation in either direction (Hahn et al., 2018; Nalin and McCarty, 1984). Finally, ATP hydrolysis is inhibited by its products, ADP and/or phosphate, in all organisms but to varying degrees (Dou et al., 1998; Jault and Allison, 1994; Lapashina and Feniouk, 2018).

3.1.4. Regulation of hydrolysis in *P. denitrificans* ATP synthase

The mitochondrial and chloroplast ATP synthases are excellent catalysts in both directions, catalysing ATP hydrolysis to drive proton translocation with rates of 400–520 s^{-1} (Junesch and Gräber, 1985; Matsuno-Yagi and Hatefi, 1988). Although similar rates of ATP hydrolysis have been reported for the *E. coli* enzyme (Al-Shawi et al., 1997), many bacterial ATP synthases catalyse hydrolysis with much slower rates, and some of them with essentially no rate at all. The ATP synthase from *P. denitrificans* is effectively unable to catalyse in the hydrolysis direction, and is considered to be unidirectional (Ferguson et al., 1976). Biochemical and structural analyses found that the *P. denitrificans* ATP synthase contains the unique ζ subunit, which bears similarity to the mammalian IF_1 inhibitor protein and was thus predicted to regulate ATP hydrolysis (**Figure 3.2B**) (García-Trejo et al., 2016; Morales-Ríos et al., 2010, 2015; Zarco-Zavala et al., 2014). The ζ subunit was bound at the $\alpha_{DP}\beta_{DP}\gamma$-catalytic interface in a similar way to that of IF_1 with its cognate ATP synthases (Morales-Ríos et al., 2015). While IF_1 is a reversible inhibitor of the mitochondrial enzyme, thought to be ejected when the enzyme switches to synthesis, the ζ subunit appears to be a permanently bound subunit. This may suggest that synthesis is possible while the ζ subunit is bound, in contrast to when IF_1 is bound to mitochondrial ATP synthase. It was shown that deletion of the ζ subunit led to an insufficient two-fold increase in hydrolysis rates, with rates remaining as low as 0.026 μmol min^{-1} mg^{-1}, well below the level expected for a freely hydrolysing enzyme (Varghese et al., 2018). These results suggested that the ζ subunit was not the primary mechanism by which ATP hydrolysis is prevented in *P. denitrificans*. Possible alternative regulatory mechanisms enforcing

unidirectionality in the *P. denitrificans* enzyme could be inhibition by the C-terminal domain of the ε subunit and/or Mg-ADP; however, such mechanisms have yet to be explored.

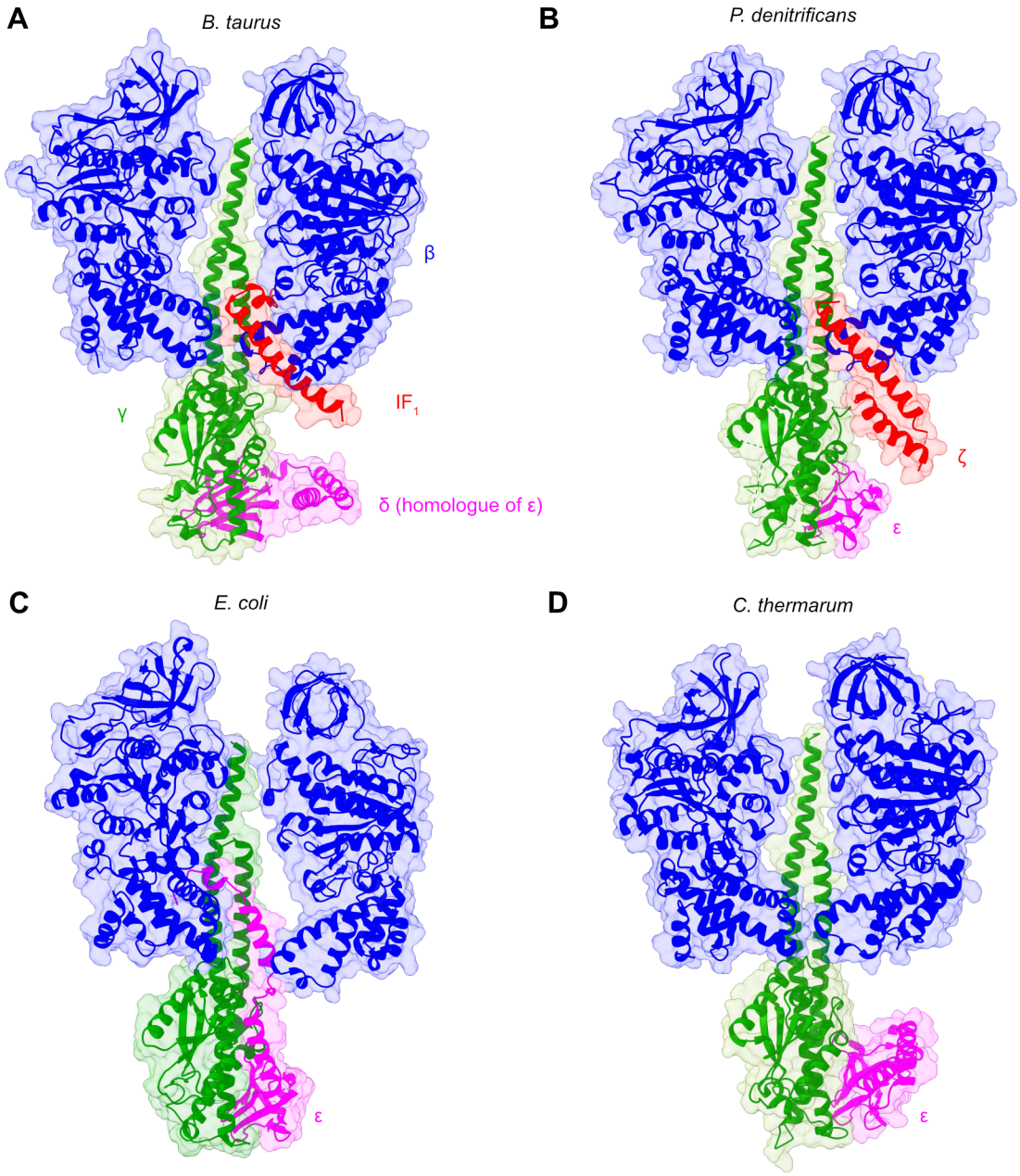

Figure 3.2. Structures of the F_1 domains of four ATP synthase enzymes. All enzymes are in states where ATP hydrolysis is inhibited. For clarity, only two β subunits (blue) are shown with the γ subunit (green), bacterial ε subunit/mitochondrial δ subunit (magenta) and the unique *P. denitrificans* ζ subunit (red) and mitochondrial inhibitor protein IF_1 (red). (A) The F_1 domain from *Bos taurus* with a monomeric form (residues 1–60) of the inhibitor protein IF_1 bound (PDB: 2V7Q) (Gledhill et al., 2007). Residues 8–50 of IF_1 are resolved. (B) The F_1 domain from *P. denitrificans* with the partially resolved ζ subunit and the resolved region of the ε subunit shown; the two α-helices of the ε-CTD are not resolved (PDB: 5DN6) (Morales-Ríos et al., 2015). (C) The F_1 domain from *Escherichia coli* with the ε subunit in the inhibitory 'up' state (PDB: 3OAA) (Cingolani and Duncan, 2011). (D) The F_1 domain from *Caldalkalibacillus thermarum*, which is unable to hydrolyse ATP even with the ε subunit in the 'down' state (PDB: 5HKK) (Ferguson et al., 2016).

3.1.5. ε Subunit inhibition

The ε subunit is comprised of two domains, an N-terminal flattened β-sandwich and a C-terminal domain (ε-CTD), which consists of two antiparallel α-helices (Cingolani and Duncan, 2011; Guo et al., 2019). The N-terminal domain has been shown to be important for connecting the F_1 and F_O domains (Kuki et al., 1988; Sternweis, 1978) and is required for the correct assembly and function of the enzyme. In some organisms the ε-CTD is considered to play a role in regulating ATP hydrolysis by interconverting between two different conformations (Tsunoda et al., 2001; Yagi et al., 2007) (**Figure 3.2C+D**). When the two α-helices are parallel to each other and are localised near the β-sheets the ε-CTD is in the non-inhibitory conformation known as the 'down' or 'hairpin' conformation (**Figure 3.2A+D**). This state can be stabilised by ATP binding by the ε-CTD in some organisms, such as *Bacillus* PS3 (Yagi et al., 2007). However, it is believed that in some organisms and under certain conditions, the ε-CTD can extend or exists in a rod-shaped conformation parallel to the γ subunit, where it is inserted at the αβγ catalytic interface (**Figure 3.2C**). This 'up' state is described as the 'inhibitory' conformation, which blocks rotation in the hydrolysis direction (Cingolani and Duncan, 2011; Shirakihara et al., 2015). Currently, the species-specific roles of the bacterial ε subunit, and how it regulates ATP hydrolysis are widely debated and poorly understood (Feniouk et al., 2006; Krah et al., 2018; Nakanishi-Matsui et al., 2016). In the case of the *E. coli* enzyme, removal of the ε-CTD increased ATP hydrolysis rates from 0.80 to 1.20 μmol min^{-1} mg^{-1} but, conversely, decreased proton pumping, suggesting that the ε-CTD is further required to maintain coupling between ATP hydrolysis and proton translocation (Cipriano and Dunn, 2006). In the isolated F_1 domain from *Caldalkalibacillus thermarum* (TA2.A1) hydrolysis rates increased more markedly, from 0.12 to 0.85 μmol min^{-1} mg^{-1}, upon removal of the ε-CTD (Keis et al., 2006). However, the crystal structure (**Figure 3.2D**) of the F_1 domain showed that the ε-CTD was in an ATP-bound 'down' conformation (Ferguson et al., 2016), a state where it is unlikely to prevent hydrolysis. In addition, mutations to ablate the ATP binding site did not lead to an increase in ATP hydrolysis, suggesting that the 'down' conformation was also not itself inhibitory (Ferguson et al., 2016). These examples highlight the variation in the role that the ε subunit plays in ATP hydrolysis regulation between species. In *P. denitrificans*, the ε-CTD was considered to have no role in the regulation of ATP hydrolysis because crosslinking and proteolysis experiments suggested the ε-CTD was in a non-inhibitory 'down' conformation (García-Trejo et al., 2016). However, the crystal structure of the ATP synthase from *P. denitrificans* could only resolve the N-terminal domain of the ε subunit and the ε-CTD was not modelled, leading to some ambiguity (Morales-Ríos et al., 2015). While it was initially thought that an inhibitory role of the ε-CTD had been transferred to the ζ subunit, the deletion of the ζ subunit did not wholly activate the enzyme without the addition of further activating

supplements (Mendoza-Hoffmann et al., 2018; Varghese et al., 2018). This suggests a role of the ε-CTD in the inhibition mechanism of *P. denitrificans* may still be a possibility.

3.1.6. Mg-ADP inhibition

Universal to all ATP synthases is the inhibition of ATP hydrolysis by Mg-ADP (Hirono-Hara et al., 2005; Jault and Allison, 1994; Jault et al., 1995; Lapashina and Feniouk, 2018; Matsui et al., 1997). Despite this, the mechanism remains poorly understood partly because Mg-ADP inhibition varies in potency between different organisms. It is thought that Mg-ADP binds or is retained in the active site after ATP hydrolysis but without the presence of phosphate. This induces a conformational change in the catalytic portion of F_1, locking in the Mg-ADP and preventing further catalysis (Hirono-Hara et al., 2005; Jault and Allison, 1994). Further to this, non-catalytic sites in the α subunits also may play a role in Mg-ADP inhibition. Mutational studies on the F_1 domain from the thermophilic *Bacillus* PS3 showed that binding of nucleotides to non-catalytic sites in the α-subunits also affected the entrapment/release of Mg-ADP from the catalytic sites, underlining a complex interplay between sites (Jault et al., 1995; Matsui et al., 1997). To confuse things further, it is known that the establishment of a Δp leads to a release of this Mg-ADP inhibition, activating ATP hydrolysis in mitochondria (Galkin and Vinogradov, 1999), chloroplasts (Carmeli and Lifshitz, 1972) and multiple bacterial species (Feniouk et al., 2007; Pacheco-Moisés et al., 2000; Zharova and Vinogradov, 2003). However, it is unclear how Mg-ADP inhibition interacts with the putative inhibition from the ε-CTD. Earlier studies have suggested that the ε-CTD is preventative to the release of Mg-ADP induced by Δp (Feniouk et al., 2007). However, more recent studies suggest the Mg-ADP and the ε-CTD have opposing roles, in which they are distinct from one another and even compete (Haruyama et al., 2010; Konno et al., 2011; Milgrom and Duncan, 2020; Mizumoto et al., 2013; Shah et al., 2013). This competitive nature is supported by observations that addition of the inhibitor azide, which stabilises the Mg-ADP-inhibited state, favours the non-inhibitory hairpin conformation of the ε-CTD (Bowler et al., 2006; Shah et al., 2013). Furthermore, Mg-ADP inhibition in the F_1 of *B. subtilis* ATP synthase is relieved by the presence of the ε subunit, as its deletion increases the strength of Mg-ADP inhibition (Mizumoto et al., 2013).

Overall, it is unclear first, whether *P. denitrificans* is inhibited by the ε-CTD; second, what governs the strength of Mg-ADP inhibition in *P. denitrificans*; and, finally, what interplay there may be between the putative regulatory components (the ε-CTD, ζ subunit and Mg-ADP). Through investigation of these questions, it is hoped that conditions can be found in which ATP hydrolysis can be activated in the *P. denitrificans* ATP synthase for application in complex I RET studies.

3.2. Aims of this chapter

- Truncate the C-terminus of the ε subunit of *P. denitrificans* ATP synthase and characterise and establish its role in the regulation of ATP hydrolysis.
- Understand the various regulatory mechanisms of *P. denitrificans* ATP synthase and how they relate to each other.
- Activate ATP hydrolysis in the *P. denitrificans* ATP synthase to generate a ∆p independent of respiration for RET measurements of complex I.
- Measure ATP-dependent RET through *P. denitrificans* complex I.

3.3. Genetic manipulation of *P. denitrificans*

To assess the role of the ε subunit in the regulation of ATPase activity in the ATP synthase of *P. denitrificans*, it was necessary to remove the subunit C-terminus by genomic deletion. However, the genetic manipulation of *P. denitrificans* is non-trivial and thus, I first discuss the genetic approach taken here to edit the genome of *P. denitrificans*. The same approach will also be applied in later chapters.

3.3.1. Bacterial conjugation

Like many bacteria, *P. denitrificans* will not take up DNA directly from its surroundings through heat shock or electrophoretic transformations. Instead, DNA must be inserted into *P. denitrificans* through bacterial conjugation (Baker et al., 1998). Bacterial conjugation or 'mating' is the direct transfer of DNA between cells, which occurs through cell-to-cell contact. Simply, a donor strain containing DNA on a conjugative plasmid contacts another cell or recipient cell via a *pilus*, eventually forming a mating bridge, where DNA transfer can occur through a controlled pore. Typically for *P. denitrificans* conjugation, an *E. coli* donor strain is used containing broad-host-range RP4 conjugation machinery. Historically, the donor strain used was SM10 λ*pir*, which had been lysogenised with a Mu phage, that contained the RP4 conjugative machinery. However, it was identified in 2010 that the bacteriophage Mu was also being transferred silently to the recipient cell at high frequency during conjugation, resulting in further mutagenesis of the genome and inconsistencies in generating site-specific mutations (Ferrières et al., 2010). Further to this, genomic *E. coli* DNA could also be transferred during mating. To address these issues a new strain was developed, MFD*pir* (Mu-free donor), which had the Mu phage removed while still containing the essential RP4 conjugative machinery. Further mutations were also generated in the RP4 *oriT* locus preventing transfer of genomic DNA. In addition, the DapA gene required for the synthesis of diaminopimelic acid (DAP), a component needed for bacterial cell wall synthesis, was disrupted by *pir*, yielding an

auxotrophic strain that requires DAP for cell growth. This allowed DAP to be used as a selective agent to remove the donor strain after conjugation.

3.3.2. Suicide vector-mediated homologous recombination

The genetic manipulation of the chromosomal DNA of *P. denitrificans*, be it insertions, deletions or point mutations, can be achieved using suicide vector-mediated homologous recombination (Van Spanning et al., 1991). This involves the exchange of DNA between a suicide plasmid and the chromosomal DNA of *P. denitrificans* through recombination of homologous regions present in both DNAs. The general strategy for this is outlined below and shown in **Figure 3.3**.

A. A gene construct is prepared containing the desired mutation and a kanamycin selection marker.
B. The gene construct is inserted into a suicide vector.
C. The vector is transformed into an *E. coli* donor strain.
D. The vector is inserted into *P. denitrificans* via bacterial conjugation.
E. The suicide vector cannot be maintained in its episomal form so it first integrates into the *P. denitrificans* chromosomal DNA by undergoing a single crossover event at homologous flanking regions. At this stage, plasmid integrant strains can be selected for by their kanamycin resistance.
F. Homologous recombination occurs between the vector and *P. denitrificans* chromosomal DNA at a second flanking region (second crossover event), resulting in the generation of an unmarked genomic mutation and the loss of the vector that is no longer integrated in the *P. denitrificans* genome.
G. Successful mutants are identified by selection markers, PCR and DNA sequencing.

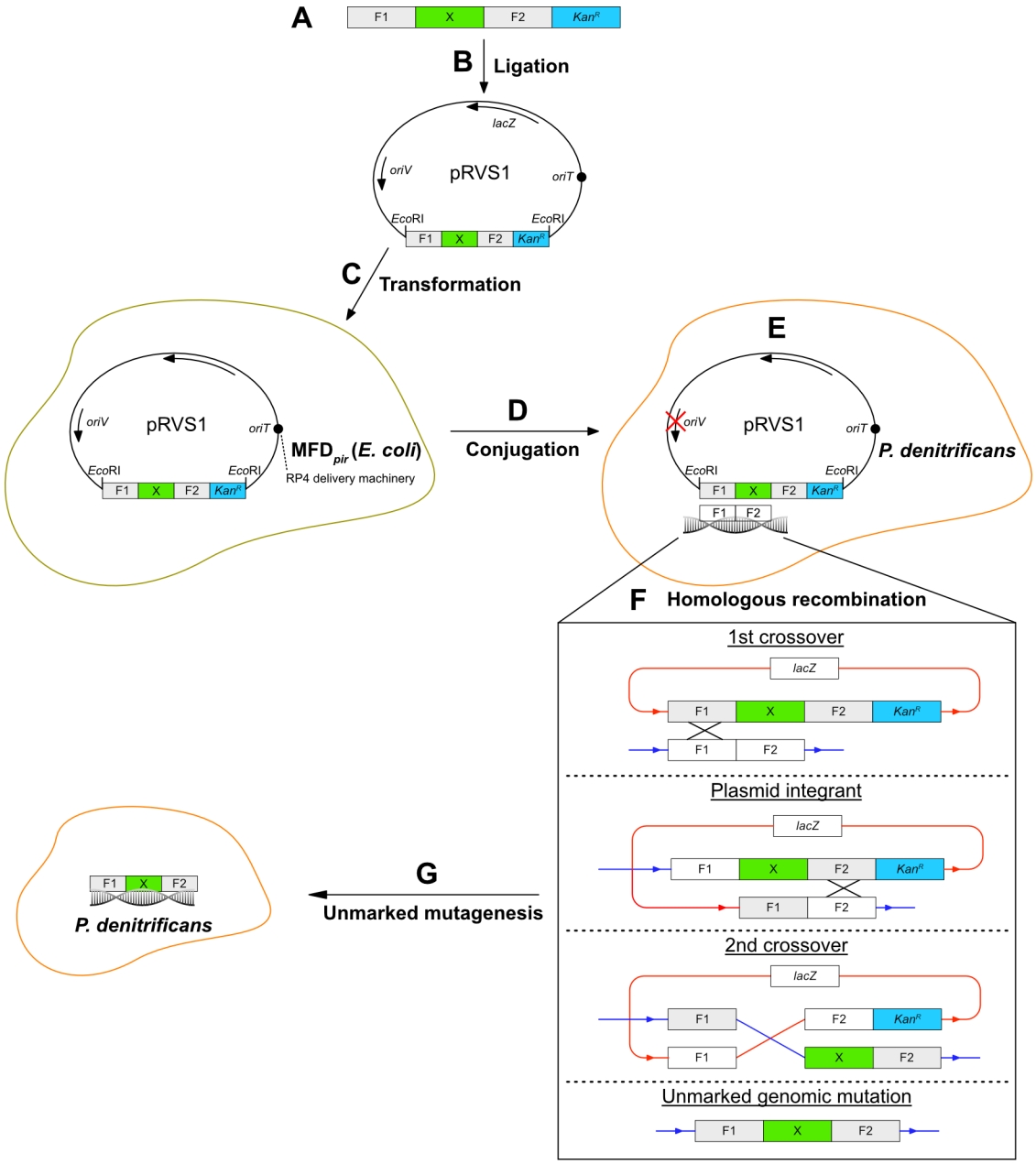

Figure 3.3. Overview of steps to generate an unmarked insertion of gene X into the *P. denitrificans* genome through homologous recombination. This strategy can also be used for site-directed mutagenesis and genomic deletions. (A) Design of the DNA construct with two regions homologous to the sequence on the bacterial chromosome surrounding the gene of interest. (B) Construct ligated into the suicide vector pRVS1 via *Eco*RI restriction sites. (C) Transformation of the construct into the MFD*pir* conjugative donor strain containing RP4 delivery machinery. (D) Bacterial conjugation of the suicide vector into *P. denitrificans*. (E) The suicide vector cannot replicate in *P. denitrificans* unless it integrates into the *P. denitrificans* genome by homologous recombination. (F) Integration of the construct into the bacterial genome by homologous recombination at a single flanking region (first crossover event). Plasmid integrant strains can be selected for by their kanamycin resistance. A second crossover event may then occur at the other flanking region leading to the creation of the unmarked genomic mutation and subsequent loss of the suicide plasmid. (G) A *P. denitrificans* strain is created containing an unmarked genomic mutation.

3.3.3. Gene constructs for homologous recombination

To perform bacterial homologous recombination a construct needs to be prepared containing two stretches of DNA that are homologous to the bacterial genome. These are usually between 500 and 2000 bp in length each, and are designed to flank both sides of the site of mutagenesis. As well as these 'flanking regions', an antibiotic resistance gene can be included after a flanking region, as a selection marker for identifying the integration of the plasmid into the *P. denitrificans* genome and subsequent recombination. Alternatively, the antibiotic resistance gene may be included in the construct between the two flanking regions, at the site of mutagenesis, which would result in a marked mutation by insertion of the antibiotic resistance gene into the genome, while removing or inserting the desired sequence. Here, the former placement of the antibiotic resistance gene is favoured as it allows the generation of an unmarked chromosomal mutation in the *P. denitrificans* genome. This has the additional benefit of maintaining antibiotic sensitivity, allowing for further mutagenesis to be performed on the same strain via the same approach, such as for compound mutagenesis studies.

3.3.4. Suicide vectors

Many suicide plasmids have been used for genomic mutagenesis of *P. denitrificans* (Moir and Ferguson, 1994; Quandt and Hynes, 1993; Simon et al., 1983; Van Spanning et al., 1991). The vector pRVS1 designed by Van Spanning and co-workers has been successfully used within our laboratory to create deletions in the *P. denitrificans* genome (Jones et al., 2017; Van Spanning et al., 1991; Varghese et al., 2018). The pRVS1 plasmid is large, at 11.6 kb, but contains properties making it a suitable vector for the purposes of this study. First, it contains an origin of transfer (*oriT*) required for the transfer of the conjugative plasmid to the recipient cell. Second, it possesses an origin of replication (*oriV*), which allows replication of the plasmid in the *E. coli* donor strain but which is incompatible in *P. denitrificans*, meaning it cannot be maintained in the episomal form and must integrate into the bacterial genome to replicate (Van Spanning et al., 1991). Third, the plasmid contains a set of unique cloning sites for insertion of gene constructs. Finally, the plasmid contains a *lacZ* gene that allows for selection of integration of the plasmid through blue-white screening by growing cells in the presence of the substrate X-gal. When the plasmid is integrated, the *lacZ* gene will be transcribed and β-galactosidase produced, which will break down the substrate X-gal to form a blue-coloured product. This can be used to screen for plasmid integration. When the plasmid is no longer integrated, either due to the completion of recombination or reverting back to wild type, no β-galactosidase will be produced and colonies will remain white as X-gal will not be hydrolysed. Further to this, the X-gal breakdown product appears to be toxic to *P. denitrificans* (Van

Spanning et al., 1991). This is convenient as it provides an additional selection pressure for the gene construct to recombine and eject the *lacZ*-containing suicide vector, providing an effective way to screen colonies for genomic mutagenesis.

3.3.5. Homologous recombination

After the gene construct is inserted into the pRVS1 vector and placed into *P. denitrificans* via bacterial conjugation, homologous recombination can then occur between the bacterial genome and the suicide vector, creating an unmarked mutation of the genome. First, one of the homologous flanking regions will recombine with the genomic DNA, resulting in the plasmid becoming integrated into the chromosome. This step is necessary for the maintenance of the suicide plasmid and successful plasmid-integrant colonies can be selected by their resistance to the antibiotic engineered on the gene construct (as well as ampicillin resistance present on the pRVS1 conjugative vector). To allow the second recombination event to progress, the plasmid-integrant strains are plated onto antibiotic-free plates, removing the requirement for the suicide plasmid to remain integrated. At this stage, one of three things can occur. (1) The plasmid remains integrated despite no antibiotic selection pressures. (2) The first flanking region that has already recombined reverts or 'flips' back to the original sequence. (3) The second homologous flanking region recombines, introducing the mutation at the site between the two flanking regions. In these last two cases, the plasmid will no longer be integrated in the bacterial genome. These two cases can be separated from the plasmid-integrant strains by the loss of the *lacZ* gene present on the pRVS1 vector, resulting in 'white' colonies in blue-white screening. To screen for successful mutagenesis, 'white' colonies can be sequenced or, where the length of the genomic DNA has changed significantly, colony PCR can be performed.

3.4. Design of ε-CTD truncation cassettes

3.4.1. Identifying sites of truncation

The ε subunit of ATP synthase is important for the assembly of a functional ATP synthase (Kuki et al., 1988; Sternweis, 1978). Hence, to study the potential role of the ε-CTD in inhibiting ATP hydrolysis in the ATP synthase of *P. denitrificans*, only the C-terminal domain of the ε subunit should be deleted, retaining the subunit N-terminus, which should be sufficient for complex assembly. The N-terminal region of the ε subunit is modelled in the only available structure of the *Pd*-F_1F_O-ATP synthase, but unfortunately the ε-CTD is not resolved (**Figure 3.2B**). One reason for this may simply be that the detergent used for solubilisation disrupts the

ε-CTD or makes it more flexible. Alternatively, the ε-CTD may be naturally mobile and insert itself only when F_1 begins to rotate during ATP hydrolysis or in the presence of a Δp.

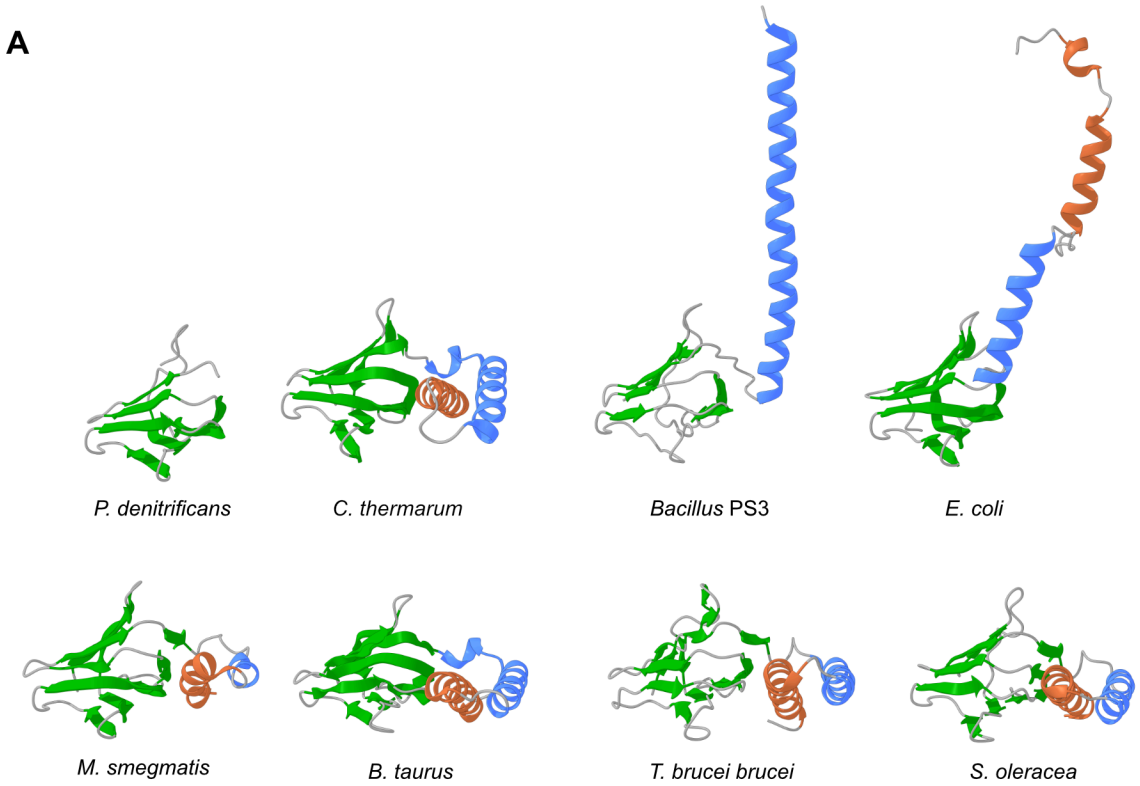

Figure 3.4. Comparison of ε-CTD subunit sequences and conformations across multiple species. (A) Comparison of ε subunit structures. The β-sheets are highlighted in green, the first α-helix in blue and the second α-helix in light brown. (B) Sequence alignment and secondary structures of the ε-CTD from structurally characterised ATP synthases. The sequences were aligned using Clustal Omega (Madeira et al., 2019) by Dr Olivier Biner (MRC Mitochondrial Biology Unit, Cambridge). The α-helices of the ε-CTD of *P. denitrificans* were predicted using JPred4 (Drozdetskiy et al., 2015). All other secondary structures were resolved in structural analyses: *P. denitrificans* (PDB: 5DN6) (Morales-Ríos et al., 2015), *C. thermarum* (PDB: 5HKK) (Ferguson et al., 2016), *Bacillus* PS3 (PDB: 6N2Y) (Guo et al., 2019), *E. coli* (PDB: 3OAA) (Cingolani and Duncan, 2011), *Mycobacterium smegmatis* (PDB: 6FOC) (A. T. Zhang et al., 2019), *B. taurus* (PDB: 5ARA) (Zhou et al., 2015), *Trypanosoma brucei brucei* (PDB: 6F5D) (Montgomery et al., 2018) and *Spinacia oleracea* (PDB: 6FKF) (Hahn et al., 2018). Sites of truncation for the *P. denitrificans* ε-CTD are shown by black triangles.

Secondary structure predictions of the ε subunit were performed using JPred4 to help select the truncation sites. The predictions suggest that the *P. denitrificans* ε-CTD consists of two α-helices that are connected by a short linker, similar to that of the *E. coli* enzyme and other homologues (**Figure 3.4**) (Cingolani and Duncan, 2011). Multiple sequence alignments of the ε-CTD from different species with known secondary structures were performed showing a similar overall expected structure (**Figure 3.4**). Interestingly, the *P. denitrificans* ε-CTD also appears to be one of the longest. Based on both the secondary structure predictions and multiple sequence alignments, two sites of truncation were chosen. One truncated the ε-CTD after residue 88 removing both α-helices ($\varepsilon^{\Delta 88}$) and the other truncated after residue 110 removing only the C-terminal α-helix ($\varepsilon^{\Delta 110}$). This allows the assessment of whether only the terminal α-helix is involved in any potential ATP hydrolysis inhibition or the whole ε-CTD.

3.4.2. Design of ε-CTD truncation cassettes

The ε-CTD truncations were generated in *P. denitrificans* by the suicide vector-mediated homologous recombination approach described in Section 3.3.2. To design constructs that can be used to delete the ε-CTD regions via homologous recombination, the genome map surrounding the ε subunit-coding region was examined using USCS Microbial Genome Browser (**Figure 3.5**) (Chan et al., 2012). The ε subunit (Pden_3819) is found at nucleotide position 959291-959737 on chromosome 2. Truncation cassettes were designed containing two sequences homologous to regions on either side of the ε-CTD. The first homologous flanking region began at nucleotide position 957857 and extended to positions 959617 or 959551, giving a flanking region of length 1761 and 1695 bp for respective $\varepsilon^{\Delta 110}$ and $\varepsilon^{\Delta 88}$ constructs. Directly following this, the next flanking region began at position 959735, which misses out the ε-CTD but includes the encoding STOP codon (959735-959737) at the end of the ε subunit. The flanking region extended to position 960958 for a total length of 1224 bp. This second flanking region is followed by a kanamycin (Kan^R) selection marker of 815 bp length. For completeness, regions 959618-959734 (117 bp) and 959552-959734 (183 bp) on chromosome 2 were deleted in $\varepsilon^{\Delta 110}$ and $\varepsilon^{\Delta 88}$ constructs, respectively.

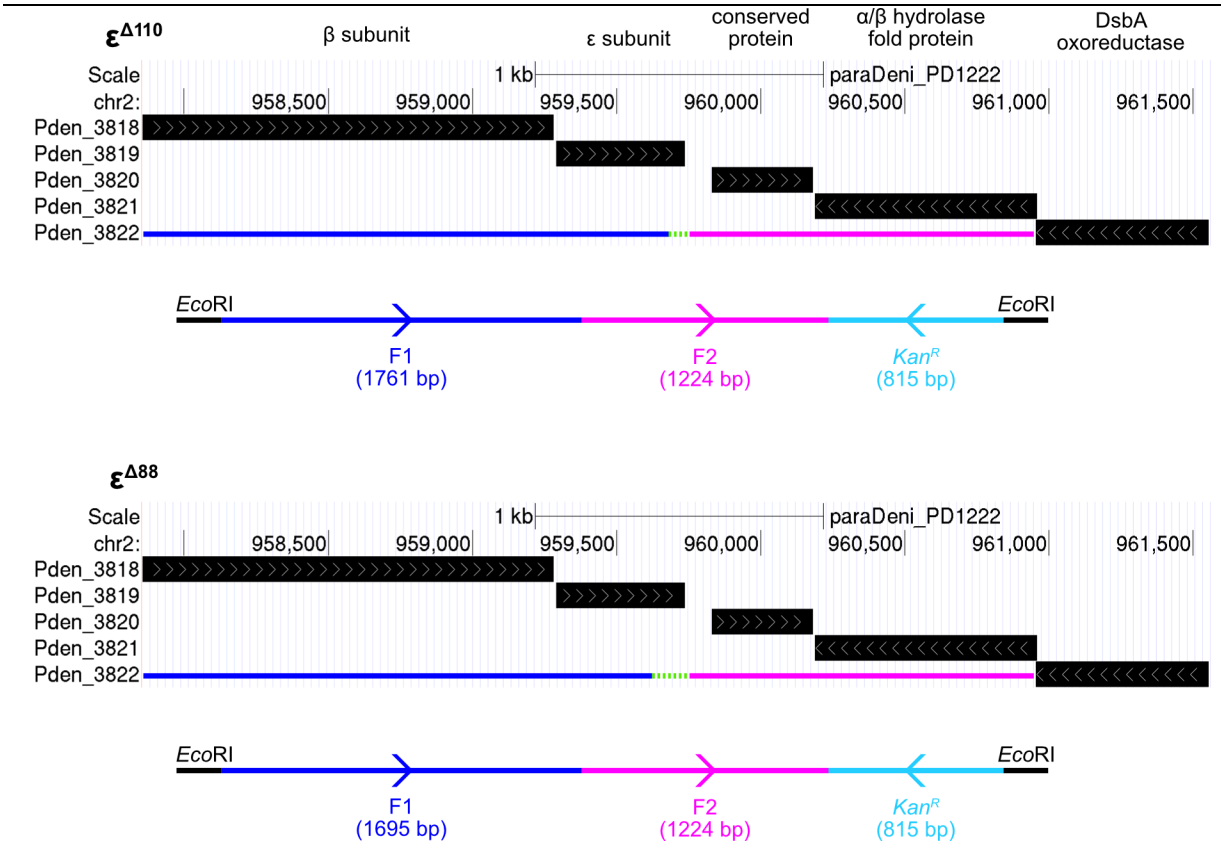

Figure 3.5. Genome map of *P. denitrificans* showing the position of the ε gene (Pden_3819) created in USCS Microbial Genome Browser at chromosome 2 positions 957857 to 961580. Design of constructs $\varepsilon^{\Delta 110}$ (top) and $\varepsilon^{\Delta 88}$ (bottom) are shown. The black rectangles represent open reading frames with white and coloured arrows showing the direction of transcription. Proteins encoded by each gene are shown above the black rectangles. The construct (as shown below each genome map) is assembled as shown by the coloured lines: flanking region F1 (blue), flanking region F2 (magenta) and *Kan*^{R} gene (cyan). The green dotted line represents the ε-CTD region to be removed from the genome and is not included in the construct. *Eco*RI sites are included on both ends of the constructs. The sequence length of each flanking region are shown.

In addition to the construct designed above, two *Eco*RI restriction sites were included on the 5' and 3' ends of the whole construct. These were used to insert the construct into the pRVS1 vector. Unfortunately, the planned construct itself contained *Eco*RI restriction sites that would also be digested and so these were removed using single base pair substitutions that were silent mutations in the construct. Specifically, the GAA codon in the *Eco*RI site was switched to GAG, which retains the encoded glutamic acid residue. The GAG codon is also a commonly used codon in the *P. denitrificans* genome (Baker et al., 1998).

The designed sequence of the construct was synthesised and assembled by GENEWIZ® and the sequence maintained in a standard pUC57-*Kan*^{R} plasmid. Only the $\varepsilon^{\Delta 110}$ construct was synthesised, as the $\varepsilon^{\Delta 88}$ construct could be easily generated from it by PCR (**Figure 3.6A**). To do this, 5' phosphorylated primers were designed to amplify the construct, including the storage

plasmid, while missing out the encoding region for the first C-terminal helix, which was present in $\varepsilon^{\Delta 110}$ but not in $\varepsilon^{\Delta 88}$. The PCR reaction was performed at different primer annealing temperatures to obtain a single product band. The highest primer annealing temperature frequently resulted in the best results. The PCR product was purified, ligated, digested with *Dpn*I to remove template backbone and transformed into NEB 5-α cells. Colonies were then screened for successful transformation of the $\varepsilon^{\Delta 88}$-containing construct by isolating plasmids and performing a double restriction digest with *Bbs*I and *Nde*I restriction enzymes. *Nde*I cuts at a single site in the backbone of the pUC57 vector and *Bbs*I cuts at a single site in the encoding region for the first C-terminal helix, which will be absent in the $\varepsilon^{\Delta 88}$ construct. Hence, only a single product band will be seen if the colony contained the $\varepsilon^{\Delta 88}$ construct and two bands if the original template ($\varepsilon^{\Delta 110}$) was transformed. Only one colony screened contained the $\varepsilon^{\Delta 88}$ construct and the rest contained the original template (**Figure 3.6B**). This was confirmed by sequencing of the construct. The low efficiency was perhaps due to unsuccessful digestion of the $\varepsilon^{\Delta 110}$ template by *Dpn*I due to old enzyme.

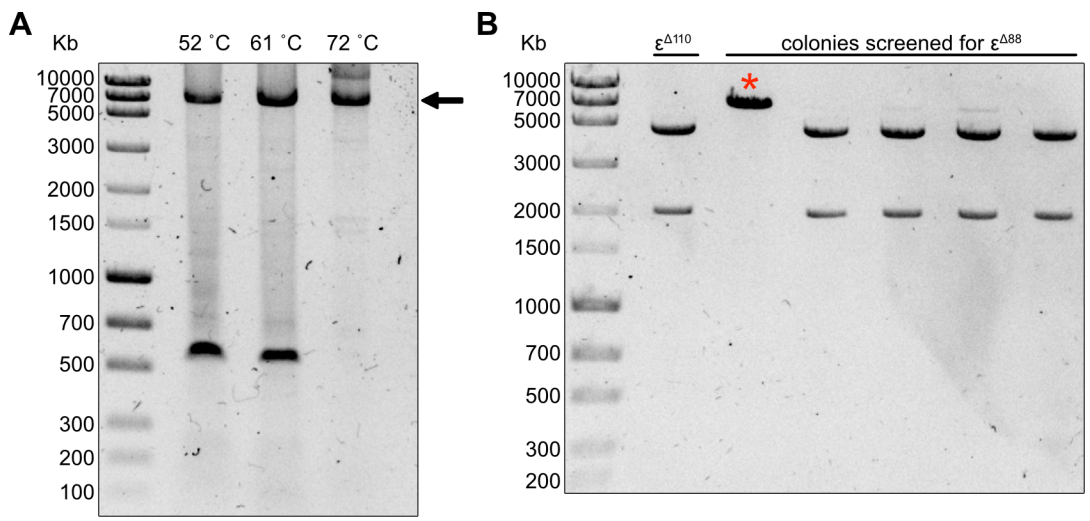

Figure 3.6. Generating the $\varepsilon^{\Delta 88}$ strain from the $\varepsilon^{\Delta 110}$ template. (A) PCR of the $\varepsilon^{\Delta 110}$ template to generate the $\varepsilon^{\Delta 88}$ construct at different primer annealing temperatures. Expected product band size is marked by an arrow. The highest primer annealing temperature (72 ˚C) resulted in the cleanest product, which was taken forward for transformation. (B) Screening isolated plasmids from colonies for the generation of the $\varepsilon^{\Delta 88}$ construct. Products from double digestion with *Nde*I and *Bbs*I restriction enzymes are shown. The lane highlighted by the red asterisk was the only successful $\varepsilon^{\Delta 88}$ construct colony obtained.

3.5. Creation of ε-CTD truncation variants

To study the effects of both the ε-CTD and ζ subunits independently and in combination with each other, both ε-CTD truncations were generated in two different *P. denitrificans* strains; either possessing (WT) or devoid (Δζ) of the ζ subunit. The *P. denitrificans* parental strain used

here was based on the fully sequenced standard *P. denitrificans* strain (*Pd1222*), which is resistant to rifampicin. A modified version of this strain was used which had the hydrogenase encoding operon removed. This strain, *Pd1222*Δhydrogenase (ΔHy), was created previously to prevent interference from hydrogenase activity, which could otherwise rapidly reduce ubiquinone by oxidising atmospheric hydrogen (Jones et al., 2017). This could compromise future experiments, such as proton-pumping stoichiometry measurements where the reduction of the respiratory chain needs to be well defined and tightly controlled. For simplicity, the ΔHy strain is referred to as wild type in this chapter.

The $\varepsilon^{\Delta 110}$ and $\varepsilon^{\Delta 88}$ constructs were digested with *Eco*RI and the products separated on an agarose gel (**Figure 3.7A**). The upper band corresponding to the construct was extracted, purified and ligated into the pRVS1 backbone, which was itself digested with *Eco*RI. The product was then transformed into competent MFD*pir* conjugative donor cells (**Figure 3.7B**). All colonies screened contained the construct.

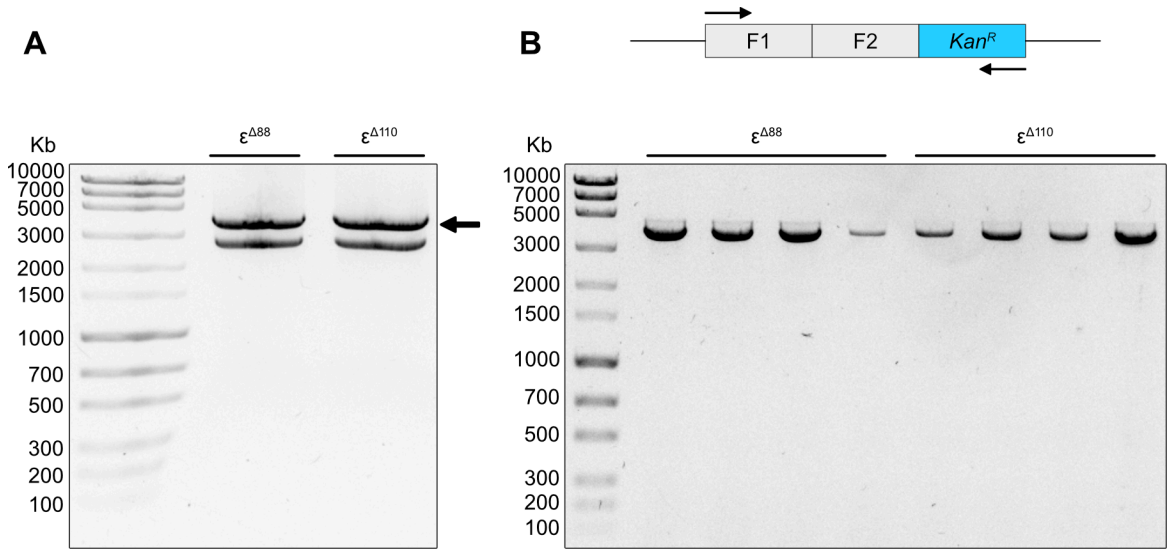

Figure 3.7. Insertion of $\varepsilon^{\Delta 110}$ and $\varepsilon^{\Delta 88}$ constructs into pRVS1 and the transformation into MFD*pir* conjugative donor strain. (A) DNA digestion products separated on an agarose gel after *Eco*RI digestion. The arrow indicates the desired construct band to be extracted, with the vector backbone running lower on the gel. (B) Colonies of MFD*pir* conjugative strain screened for construct-containing plasmid. The primers used to identify the construct bind to the flanking region of the construct and *Kan*^{R} gene, as shown by the arrows in the diagram.

The construct was next inserted into *P. denitrificans* to initiate homologous recombination and truncate the ε-CTD. The MFD*pir* donor strain and *P. denitrificans* strains were grown to mid-exponential phase and plated together on antibiotic-free plates of LB-agar to allow bacterial

conjugation. These plates were supplemented with DAP to maintain the MFD*pir* strain. Two days incubation at 30 ˚C resulted in a lawn of cells, from which successfully conjugated *P. denitrificans* cells were selected. This was done by scraping clean the cell lawn, preparing serial dilutions of the cell resuspension in LB and subsequently plating onto LB-agar containing both rifampicin and kanamycin but no DAP to select for only *P. denitrificans* colonies that had taken up the construct. With the construct inserted into *P. denitrificans* homologous recombination could then occur, generating the mutant strains. A depiction of the events that occur during homologous recombination are shown in **Figure 3.8**.

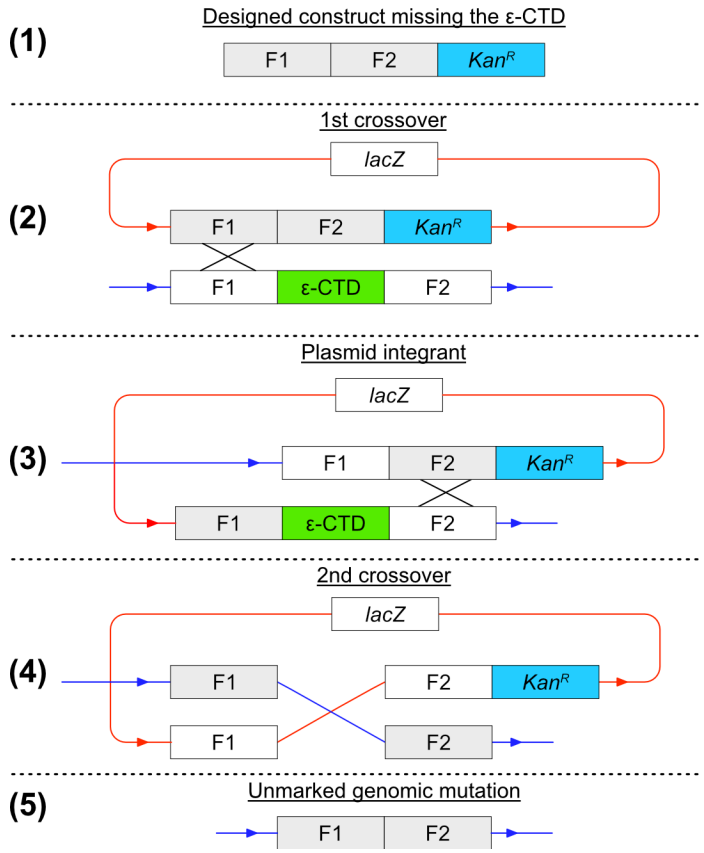

Figure 3.8. Depiction of homologous recombination steps for deletion of the ε-CTD. (1) The construct was designed containing two flanking regions homologous to the *P. denitrificans* genome but missing the ε-CTD and also contains the *Kan*^{R} selection marker. (2) The construct in the pRVS1 suicide vector is inserted into *P. denitrificans* via bacterial conjugation. (3) To be maintained, the plasmid must integrate itself into the bacterial genome by undergoing a first recombination event at one of the homologous flanking regions. The plasmid confers kanamycin resistance to *P. denitrificans* at this point. (4) The second recombination event may occur, resulting in the deletion of the ε-CTD and loss of the plasmid and kanamycin resistance. Loss of the *lacZ* gene also occurs, which can be screened for using X-gal and blue-white screening. (5) The unmarked deletion of the *P. denitrificans* genome.

Colonies were screened for the plasmid integration (first recombination) using primers binding to the end of the constructs (**Figure 3.9**). All colonies screened showed a single band of the

expected size. The wild-type control showed multiple bands, probably due to non-specific binding of the primers in the absence of the *Kan*^{R} gene sequence to which one of the primers binds.

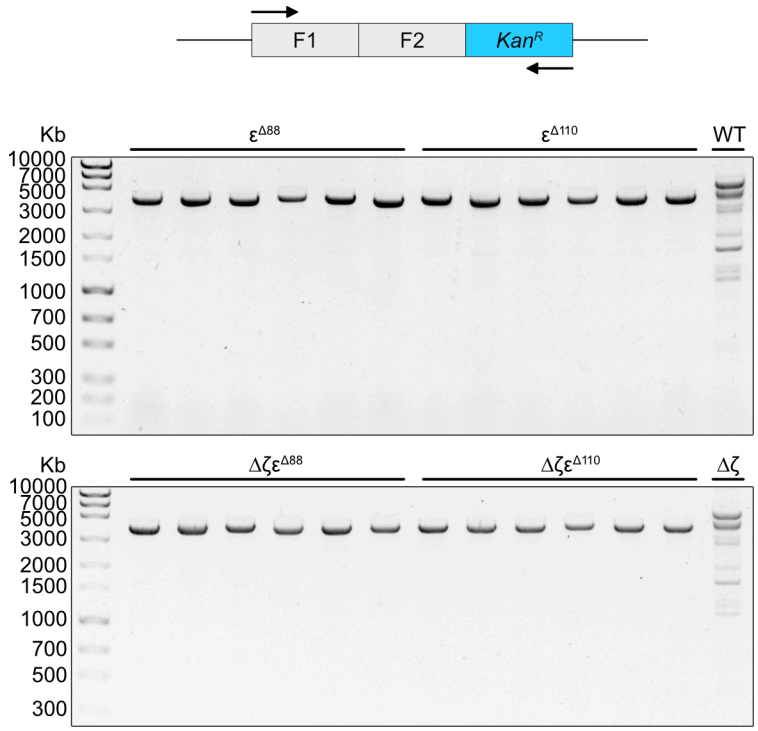

Figure 3.9. Colonies screened for successful plasmid integration/first recombination event in both WT (top gel) and Δζ (bottom gel) strains. Colonies from WT and Δζ strains, which have not been conjugated with the construct, are shown as controls in the last column for each gel. Primers used to identify successful plasmid integration bind to the flanking region of the construct and *Kan*^{R} gene, as shown by the arrows in the diagram above.

To screen for the second recombination event and successful mutagenesis of the *P. denitrificans* genome, colonies that had undergone the first recombination were grown overnight at 30 ˚C on LB containing rifampicin but not kanamycin. X-gal was also added to the medium to provide an additional selection pressure, as the X-gal breakdown product is toxic to the cell, limiting growth and making the loss of the plasmid encoding the *lacZ* gene favourable. After overnight growth, cells were streaked out onto LB-agar containing rifampicin and X-gal. Most colonies were very small and blue indicating that they had not recombined and still contained the suicide vector. The white colonies were assayed for successful recombination by colony PCR, amplifying the region surrounding and including the ε subunit. Multiple colonies (between 10 to 40) were screened, with the majority having reverted to wild type rather than undergoing the second recombination. Mutants that were generated successfully are shown clearly by the difference in size of the ε subunit (**Figure 3.10**). For all

variants, the whole ATPase operon was sequenced showing that the correct amino acids were encoded for in all subunits.

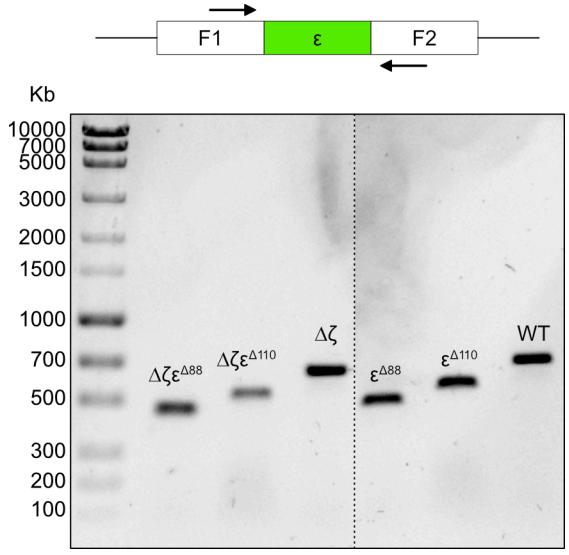

Figure 3.10. PCR products for successfully mutated *P. denitrificans* colonies. PCR primers bind 100 bp upstream and downstream of the ε subunit, as shown by the arrows. Successful colonies are shown compared to both the WT and Δζ starting strains.

3.6. Characterisation of ε-CTD variants by BN-PAGE and mass spectrometry

Four new ATP synthase variants ($\varepsilon^{\Delta 110}$, $\varepsilon^{\Delta 88}$, $\Delta\zeta\varepsilon^{\Delta 110}$ and $\Delta\zeta\varepsilon^{\Delta 88}$) were assessed on the protein level by Blue native PAGE (BN-PAGE) and mass spectrometry analyses. First, SBPs were prepared for each strain grown on LB medium, including the WT and Δζ strains, as described in the Materials and Methods (Section 2.3.1). The SBPs were then solubilised in *n*-dodecyl β-D-maltoside (DDM) detergent (2:1 detergent to protein (w/w)) and analysed by BN-PAGE as described in the Materials and Methods (Section 2.4.4). The truncation of the ε-CTD did not appear to affect the assembly of the intact enzyme, as a clear band representing the F_1F_O complex was visible in all strains, consistent with the expected molecular mass (558 kDa in wild type) (**Figure 3.11A**). The corresponding bands were excised and analysed by a second dimension of SDS-PAGE to visualise the individual subunits. A similar subunit composition was seen in each case. The only differences were a shift in the wild-type ε band (15.83 kDa) in the truncated ε-CTD strains and the absence of a band in the ζ region (11.67 kDa) for the ζ knockout strains (**Figure 3.11B**).

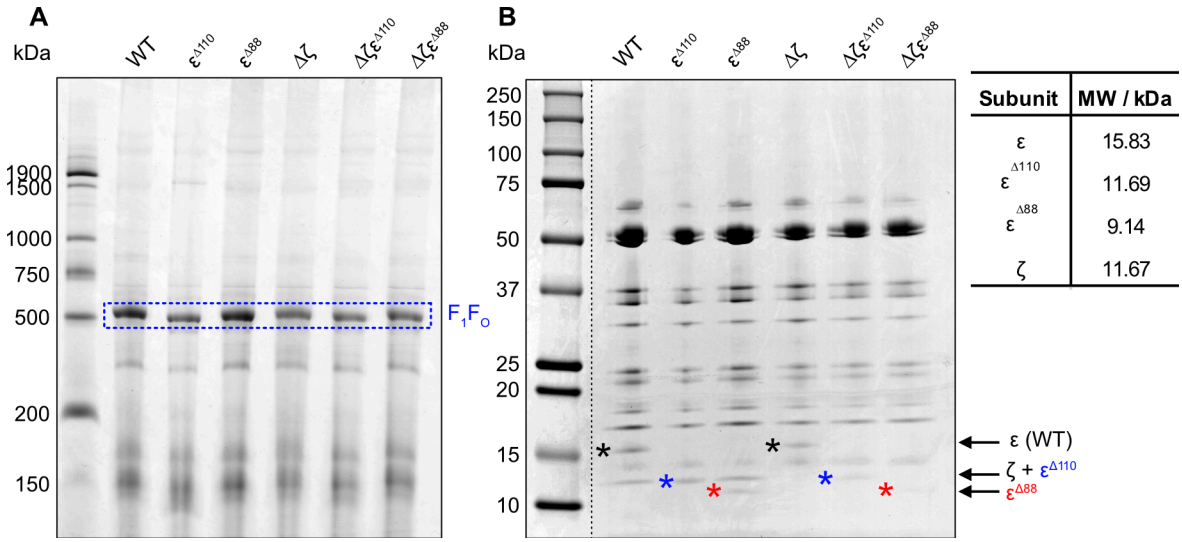

Subunit	MW / kDa
ε	15.83
$\varepsilon^{\Delta 110}$	11.69
$\varepsilon^{\Delta 88}$	9.14
ζ	11.67

Figure 3.11. Confirmation of enzyme assembly and ε subunit truncations. (A) BN-PAGE analyses of SBPs from each strain. Proteins were solubilised using DDM and the bands corresponding to intact ATP synthase (F_1F_O) are indicated. (B) SDS-PAGE of ATP synthase bands excised from the BN-PAGE gel. Bands assigned, by mass spectrometry analyses (see below), to the ε subunit are highlighted by black (wild type), blue ($\varepsilon^{\Delta 110}$) and red ($\varepsilon^{\Delta 88}$) asterisks. The ζ subunit co-migrates with the $\varepsilon^{\Delta 110}$ protein. Shown also is a table of masses for the subunits of interest and truncated subunits, calculated based on genomic sequence composition.

Finally, the bands belonging to the ε and ζ subunits were excised, digested with trypsin and analysed by LC-orbitrap mass spectrometry. As expected, no ζ subunit was identified in the Δζ-derived strains. In the case of the ε subunit, two N-terminal peptides (labelled 1 and 2 in **Figure 3.12**) were detected in all strains, albeit peptide 2 was below the ion score cut-off. A third peptide (peptide 3, residues 88-103), characteristic of the first of the two C-terminal helices, was present in the $\varepsilon^{\Delta 110}$ variants but not in the $\varepsilon^{\Delta 88}$ variants. Two other peptides (4 and 5), characteristic of the second of the two C-terminal helices, were absent in both $\varepsilon^{\Delta 110}$ and $\varepsilon^{\Delta 88}$ variants. These data confirm the truncation of the ε-CTD on a protein level.

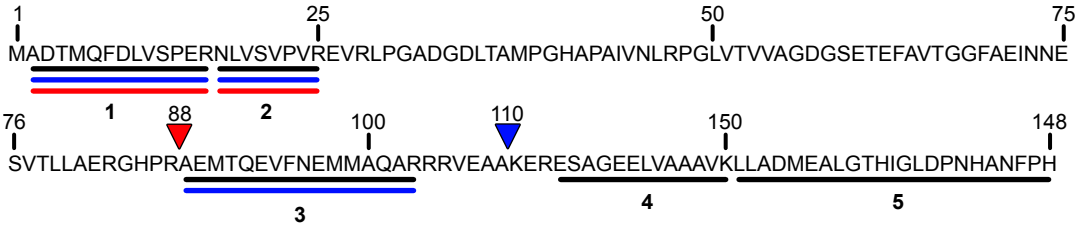

Peptide	Peptide	Ion Score / 45					
		WT	$\varepsilon^{\Delta 110}$	$\varepsilon^{\Delta 88}$	$\Delta\zeta$	$\Delta\zeta\varepsilon^{\Delta 110}$	$\Delta\zeta\varepsilon^{\Delta 88}$
1	ADTMQFDLVSPER	73	92	106	106	86	92
2	NLVSVPVR	37	39	37	37	39	39
3	AEMTQEVFNEMMAQAR	57	80	–	66	78	–
4	ESAGEELVAAAVK	53	–	–	78	–	–
5	LLADMEALGTHIGLDPNHANFPH	57	–	–	50	–	–

Figure 3.12. Key tryptic peptides identified by mass spectrometry in bands containing the ε subunits excised from the SDS-PAGE gel. The amino acid sequence for the ε subunit is shown, with the key peptides identified (1-5) in the wild-type (black), $\varepsilon^{\Delta 110}$ (blue) and $\varepsilon^{\Delta 88}$ (red) ε subunits, in both the ζ knockout and ζ-containing strains. Mascot ions scores for each peptide for the Orbitrap analyses are shown in comparison to the $p < 0.05$ ions score cut-off (45 for all peptides).

3.7. Growth of ε-CTD truncation variants

To investigate a possible effect that the truncation of the ε-CTD may have on the growth of *P. denitrificans*, each strain was grown under aerobic conditions in both LB and a defined succinate minimal medium. All strains grew similarly under both conditions suggesting they contained a functional ATP synthase with no obvious detrimental effect on the cells (**Figure 3.13**).

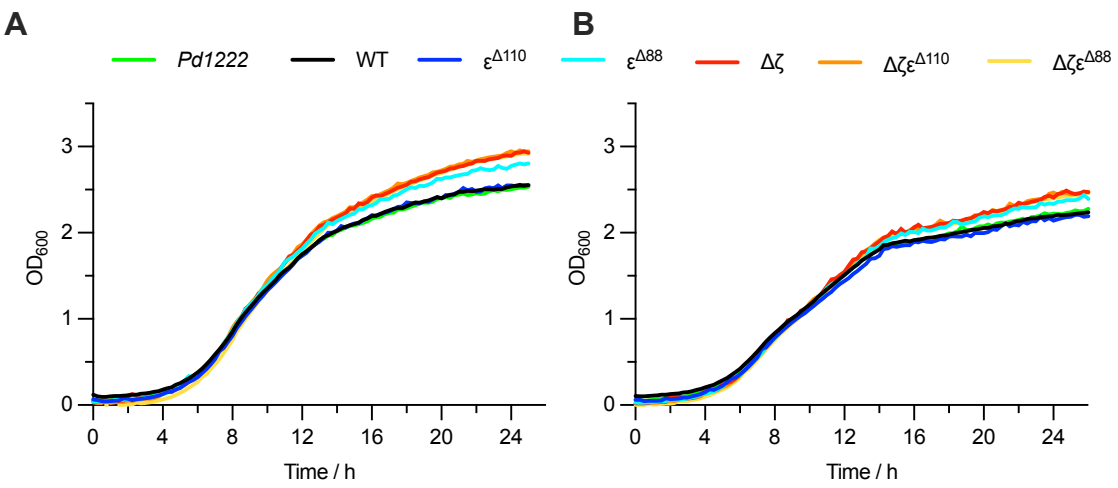

Figure 3.13. Comparison of growth curves for *P. denitrificans* cells from the parental *Pd1222* strain, the ΔHy strain referred to here as the wild type, and the ε subunit truncations in both the wild-type and Δζ strains. Cells were grown in 1 mL of either (A) LB or (B) succinate minimal medium at 30 ˚C with 200 rpm orbital shaking in a CLARIOstar *Plus* microplatereader. Optical density was recorded every 15 min. Experiments were initiated using a freshly grown stationary-phase starter culture added to a starting optical density of 0.02 and carried out in triplicate.

3.8. Catalytic activity – ATP hydrolysis

3.8.1. Overview of ATP hydrolysis assay methods

To measure the rate of ATP hydrolysis in SBPs for each variant, two different assay systems were used, each with their own advantages and disadvantages. Most ATPase assays were performed using an NADH-coupled ATP regenerating system unless stated otherwise. This system employs an enzyme cascade to regenerate ATP from the product ADP, with the overall result being the oxidation of NADH, which can be followed spectroscopically (**Figure 3.14A**). However, for studying the effects of ADP on ATP hydrolysis, it is necessary to use a different method, which does not remove ADP from the system. For this purpose, ATP hydrolysis was measured using pH-dependent fluorescence of pyranine (**Figure 3.14B**) (Pacheco-Moisés et al., 2000). During ATP hydrolysis, a proton is released ($ATP^{4-} + H_2O \rightleftharpoons ADP^{3-} + P_i^{2-} + H^+$), which acidifies the external buffer and can be detected by the change in fluorescence intensity of the pyranine probe (see Section 2.5.3, Materials and Methods). This technique is less sensitive than the NADH-coupled assay and can only be measured individually. Furthermore, to determine rates of ATP hydrolysis, a calibration must be performed by addition of known amounts of acid.

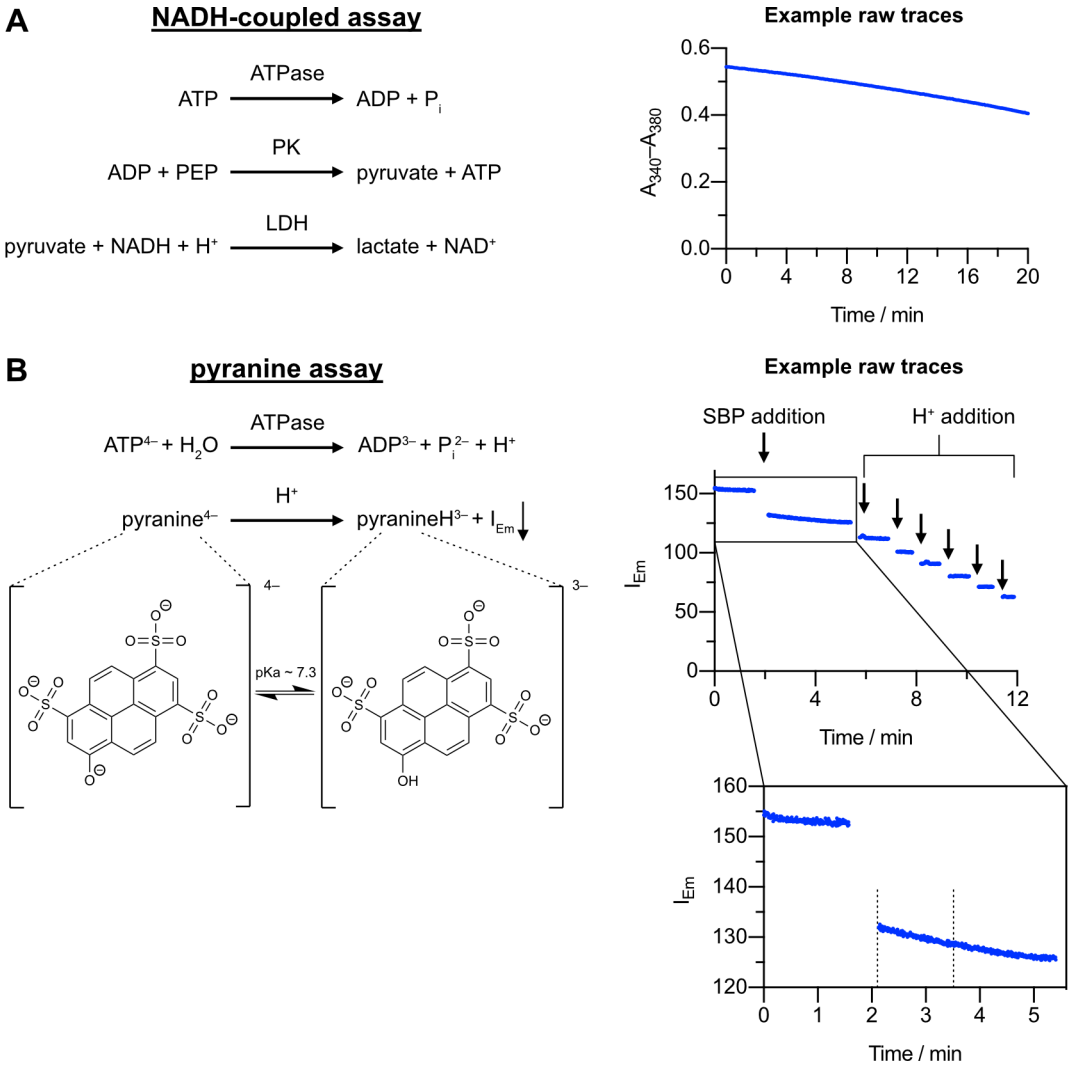

Figure 3.14. Overview of two different ATPase detection systems used. (A) NADH-coupled ATP regenerating assay. Phosphoenolpyruvate (PEP), pyruvate kinase (PK) and lactate dehydrogenase (LDH) are added to the assay system. An example of the raw data is shown. (B) Pyranine ATPase assay – pyranine is protonated during ATP hydrolysis resulting in the decrease in intensity of fluorescence (I_{Em}) (excitation at 460 nm, emission at 510 nm). An example of the raw data for the pyranine assay is shown indicating addition of SBPs to initiate the reaction and the addition of acid for calibration. ATP hydrolysis is measured as the initial rate of change of I_{Em}.

3.8.2. ATP hydrolysis – effect of ε-CTD deletion

The effect of truncating the ε subunit on ATP hydrolysis was determined in *P. denitrificans* SBPs. The amount of ATP synthase enzymes per mg of SBPs varied between different SBP preparations, so the ATP hydrolysis rates were normalised relative to wild type to account for these differences. This was done by comparing the band intensities in BN-PAGE analyses for each SBP preparation, such as shown in **Figure 3.11**. Three separate solubilisations of each strain were performed and compared to the average intensity of all the bands on the gel (**Table**

3.1). An example of these types of analyses is shown in **Figure 3.15** where band intensities have been compared using Fiji software (Schindelin et al., 2012). These data show that the band intensity scales linearly with the amount of total protein loaded, suggesting that the assessment of enzyme content relative to wild type can be performed between bands on the same gel. This normalisation was performed for all ATP hydrolysis analyses unless stated otherwise.

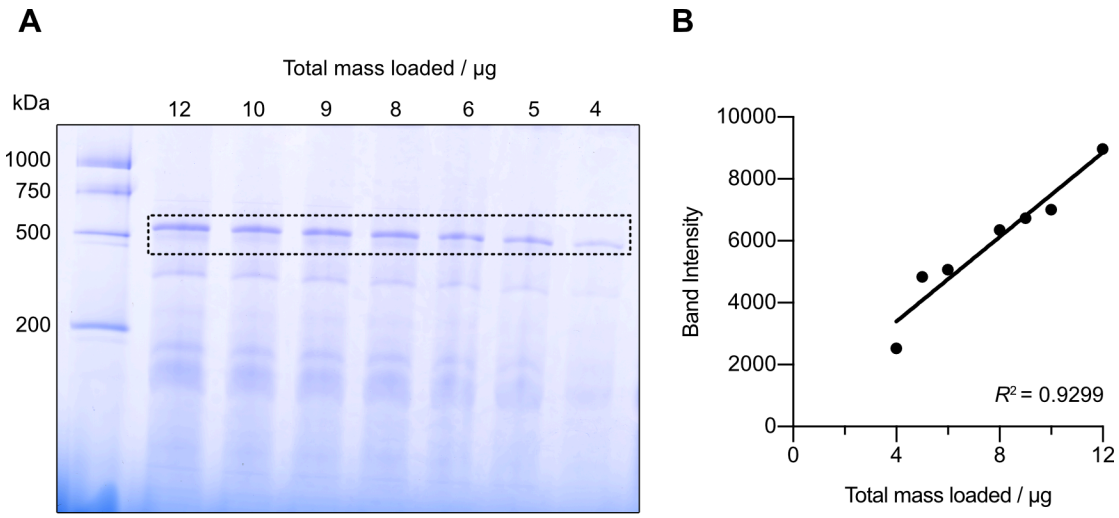

Figure 3.15. Example of the relative quantification of the ATP synthase enzyme using band intensities obtained from BN-PAGE analyses. (A) BN-PAGE of different amounts of wild-type SBPs loaded per well. (B) The intensity of the BN-PAGE band plotted versus the total protein mass loaded per lane. The ATP synthase band on BN-PAGE scales linearly with total protein loaded onto each lane of the gel.

Table 3.1. Table of relative band intensities from BN-PAGE analyses for each strain. Two independently prepared sets of SBPs are shown. Intensity is show relative to the average band intensity of each gel. Average of three gels ± S.E.M. is shown.

Strain	Relative BN-PAGE band intensity	
	SBP prep 1	SBP prep 2
WT	1.295 ± 0.043	1.074 ± 0.023
$\varepsilon^{\Delta 110}$	0.946 ± 0.084	1.251 ± 0.058
$\varepsilon^{\Delta 88}$	1.368 ± 0.023	0.895 ± 0.009
$\Delta\zeta$	0.667 ± 0.066	0.970 ± 0.065
$\Delta\zeta\varepsilon^{\Delta 110}$	0.744 ± 0.062	0.974 ± 0.087
$\Delta\zeta\varepsilon^{\Delta 88}$	0.882 ± 0.066	0.836 ± 0.070

The removal of the ε-CTD did not appear to significantly increase the ATP hydrolysis rates in either the presence or absence of the ζ subunit, with rates not exceeding more than twice that

of wild type (**Table 3.2**). The rates therefore remain extremely low, in the region of background levels. This is significantly below the level of more freely hydrolysing enzymes, such as from *E. coli* and *B. taurus* (0.38 and 1.24 μmol min^{-1} mg^{-1}, respectively) measured under similar conditions (Varghese et al., 2018). Thus, similar to removing the ζ subunit (Varghese et al., 2018), removing the ε-CTD (either independently or in combination with the ζ subunit) is not sufficient to activate ATP hydrolysis in *P. denitrificans* ATP synthase. The removal of the ε-CTD in *Bacillus* PS3 resulted in a much higher, five-fold increase in activity, suggesting either that the ε-CTD behaves differently in the two enzymes, or that additional regulatory mechanisms mask the effect of removing it in the *P. denitrificans* enzyme (Kato-Yamada et al., 1999).

Table 3.2. Table of ATP hydrolysis rates in SBPs from various strains. Data are the average of three technical replicates ± S.E.M.

Strain	ATP hydrolysis / μmol min^{-1} mg^{-1}
WT	0.028 ± 0.009
$\varepsilon^{\Delta 110}$	0.032 ± 0.005
$\varepsilon^{\Delta 88}$	0.040 ± 0.009
Δζ	0.039 ± 0.018
$\Delta\zeta\varepsilon^{\Delta 110}$	0.052 ± 0.009
$\Delta\zeta\varepsilon^{\Delta 88}$	0.044 ± 0.017

3.8.3. ATP hydrolysis – effect of additives LDAO and selenite

Clearly, neither the ζ subunit nor the ε-CTD provide the primary mechanism by which ATP hydrolysis in *P. denitrificans* is prevented. A possible alternative mechanism is inhibition by Mg-ADP, which has already been described as very strong in *P. denitrificans* (Pacheco-Moisés et al., 2000; Zharova and Vinogradov, 2003). Mg-ADP inhibition can be relieved by the addition of the zwitterionic detergent LDAO (lauryldimethylamine N-oxide), oxyanions, such as sulfite and selenite, and a Δp (Amano et al., 1999; Dou et al., 1998; Du and Boyer, 1990; Jault et al., 1995; Pacheco-Moisés et al., 2002). However, these methods of activation can also influence, or be influenced by, the ε-CTD, which makes it difficult to define the mechanism of activation (Dunn et al., 1990; Lötscher et al., 1984; Milgrom and Duncan, 2020). To disentangle their effects on the ε-CTD and Mg-ADP inhibition, both oxyanions and LDAO were titrated against SBPs prepared from all strains and the effect on ATP hydrolysis monitored (**Figure 3.16A+B**).

For LDAO, the wild-type, $\varepsilon^{\Delta 88}$ and $\varepsilon^{\Delta 110}$ strains had similar maximum rates, of between 0.28 and 0.34 μmol min^{-1} mg^{-1} (**Figure 3.16A**). These are nearer to the rates previously observed in *E.*

coli membrane vesicles (Varghese et al., 2018) but measured in the absence of LDAO. As expected from previous reports, the ∆ζ strains (∆ζ, $\Delta\zeta\varepsilon^{\Delta 88}$ and $\Delta\zeta\varepsilon^{\Delta 110}$) all displayed around two-fold higher rates (0.65 to 0.80 µmol min^{-1} mg^{-1}, **Figure 3.16C**) than their ζ-containing counterparts following activation by LDAO (Mendoza-Hoffmann et al., 2018; Varghese et al., 2018). Only the increases observed upon deleting the ζ subunit were statistically significant, suggesting that truncating the ε-CTD does not affect the extent of activation by LDAO. The substantial rates observed with LDAO suggest it relieves the primary mechanism of inhibition of ATP hydrolysis in *P. denitrificans* ATP synthase. Furthermore, all six strains exhibit similar $[A]_{50}$ values (the concentrations at which the rates are half maximal) for LDAO activation (**Figure 3.16D**), suggesting that LDAO is unlikely to act at a point where the ε-CTD and/or ζ-subunit interact with the αβγ interface, as has been suggested previously (Lötscher et al., 1984; Mendoza-Hoffmann et al., 2018). It is likely that LDAO, being a zwitterionic detergent, facilitates the release of entrapped ADP by disrupting subunit interfaces, or 'loosening' the enzyme structure, allowing Mg-ADP to be released.

Selenite (SeO_3^{2-}) was chosen as the oxyanion to titrate into SBPs (instead of phosphate and sulfite) as it is less uncoupling to the membrane due to its larger size. Like LDAO, higher maximum rates of ATP hydrolysis were observed in the ∆ζ strains than in the ζ-containing strains, with no obvious effect on the maximum rates imposed by the ε-CTD (**Figure 3.16B+C**). However, there are two notable differences between selenite and LDAO activation. First, the maximum rates for each strain were lower for selenite than LDAO activation and, second, a lower concentration of selenite is required to achieve maximum rates in the four strains with truncated ε-CTDs. The $[A]_{50}$ values for selenite activation decrease from 12.2 mM in the wild type to 4.0 and 3.6 mM in the $\varepsilon^{\Delta 110}$ and $\varepsilon^{\Delta 88}$ strains, respectively, and the same pattern is replicated in the three ∆ζ strains (**Figure 3.16D**). It appears that truncating the ε-CTD facilitates activation by selenite, and the different patterns of behaviour with LDAO and selenite suggest that they occupy different binding sites. Oxyanions such as sulfite and selenite resemble phosphate, so their mode of activation probably involves them binding to the (nucleotide) phosphate binding sites, either in the catalytic sites in the β subunits or the non-catalytic sites in the α subunits, helping to promote ADP release (Du and Boyer, 1990; Recktenwald and Hess, 1977). These data suggest that the ε-CTD may stabilise an ADP inhibited state, because less selenite is required to attenuate inhibition in the $\varepsilon^{\Delta 110}$ and $\varepsilon^{\Delta 88}$ variants than in the wild-type variant. This is irrespective of the presence of the ζ subunit, the deletion of which exerts a consistent two-fold activating effect independent of the selenite concentration.

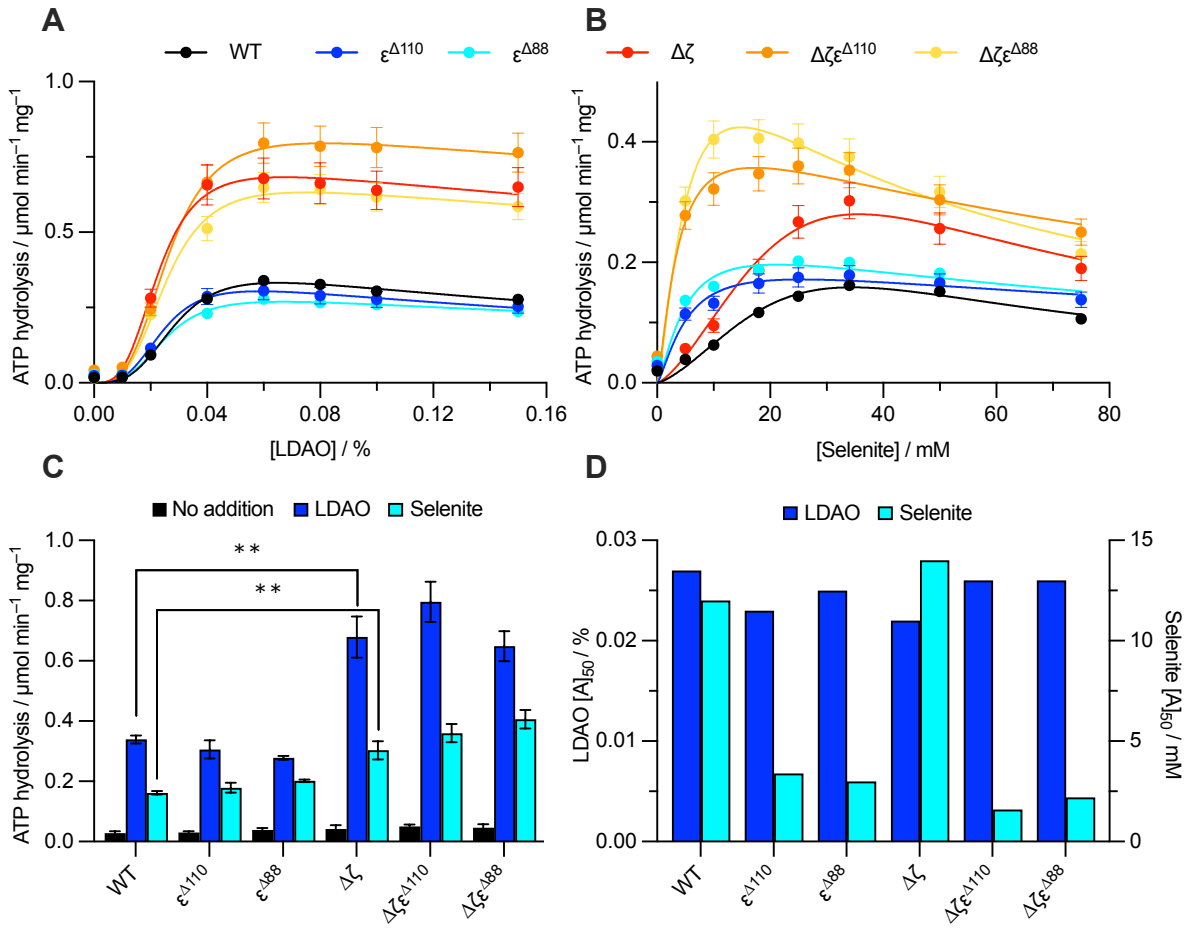

Figure 3.16. ATP hydrolysis in all six strains activated by increasing concentrations of (A) LDAO and (B) selenite. Rates of ATP hydrolysis have been normalised to the amount of ATP synthase present in the wild-type sample by comparing the band intensities in BN-PAGE analyses. The traces are mean average data from three technical replicates with error bars showing the S.E.M. Curves are fit to the data to guide the eye using the model: $Y=V_{max}*x^h/(K_m{}^h + x^h(1+x/K_i))$ with the slope h constrained to a shared value between all measurements and K_m and K_i to values greater than zero. (C) The maximum rates of ATP hydrolysis achieved during the titration of LDAO (blue) and selenite (cyan) in each strain. Statistical significance was calculated by one-way ANOVA followed by Tukey's test comparing each strain to wild type under each condition. For clarity, only two examples are shown. The $\varepsilon^{\Delta 88}$ and $\varepsilon^{\Delta 110}$ strains were not significantly increased relative to wild type under each condition. All ζ deficient strains were significantly increased relative to wild type in the presence of LDAO or selenite, $^{**}p < 0.01$. (D) The $[A]_{50}$ values for LDAO and selenite activation as read directly off the curves in panels A and B.

3.8.4. ATP hydrolysis – effect of ADP

To further investigate whether oxyanions activate ATP hydrolysis by stimulating the release of inhibitory Mg-ADP, hydrolysis was activated by oxyanions and followed by addition of extra ADP to compete against oxyanion binding, to reverse the activation. Hydrolysis was measured by using the pH-sensitive probe pyranine to monitor the release of protons during ATP hydrolysis (Pacheco-Moisés et al., 2000). The pH sensing assay was performed in a solution with a low buffering capacity (2.5 mM Tris-SO_4 pH 8.0) to allow the pyranine probe to detect

the pH change. Problematically, the addition of oxyanions provided additional buffering to the assay mixture, decreasing the sensitivity of the assay. Sulfite (SO_3^{2-}) was found to be more compatible than selenite because it buffered less strongly. In addition to this, only low amounts of sulfite (5 mM) were added to the assay, which may not result in a fully activated ATP hydrolysis rate. Previous studies have shown sulfite activates ATP hydrolysis in wild-type and ∆ζ strains (Varghese et al., 2018), as well as relieving ADP inhibition in *E. coli* (Milgrom and Duncan, 2020). Therefore, it is reasonable to assume that sulfite activates similarly to selenite. The addition of 3 mM ADP to sulfite-activated SBPs reduced ATP hydrolysis more than five-fold, back to the pre-activated levels, in all strains measured (**Figure 3.17**). While this data would initially suggest that ADP inhibition is the primary mechanism of inhibition and is partly released by oxyanion addition, it is difficult to disentangle the compounding effect that ADP has on the system; ADP will also act as a competitive inhibitor of ATP hydrolysis as it is a product of the reaction. Hence, this experiment does not specifically assess the presence of a tightly bound Mg-ADP inhibited state and should not be overinterpreted. A more conclusive experiment would be to first incubate the SBPs in a high concentration of Mg-ADP and subsequently dilute the SBPs before assaying them, effectively washing away residual Mg-ADP, as has been done previously for the *B. subtilis* F_1-ATPase (Mizumoto et al., 2013). This experiment was suggested in correspondence following completion of this work and so was not performed here.

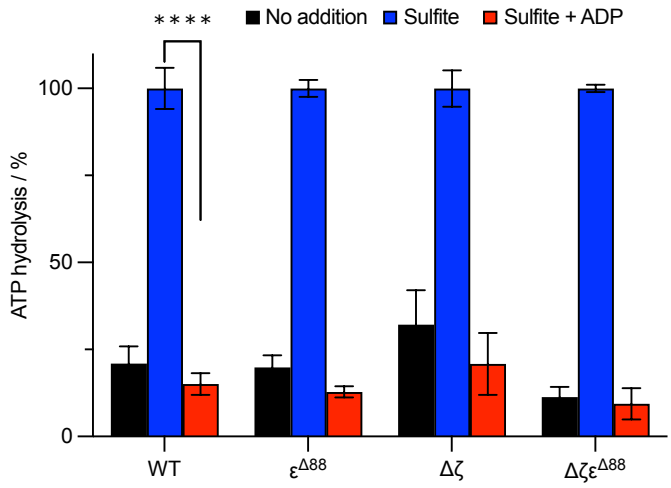

Figure 3.17. Rates of ATP hydrolysis normalised to the activated value for each strain were measured using the pH-dependent pyranine assay in the presence of 5 mM sulfite (blue), or 5 mM sulfite and 3 mM ADP (red). Non-activated ATP hydrolysis rates (measured by NADH-coupled assay) are shown for comparison (black). Data are the average from three technical replicates with error bars showing the S.E.M. Statistical significance was calculated by one-way ANOVA followed by Tukey's test comparing each assayed condition within each strain. In each case, the sulfite-activated rate is significantly different from the no addition and sulfite + ADP rates; one example is shown, ****$p < 0.0001$.

3.8.5. ATP hydrolysis – effect of ∆p

It has been shown that ATP hydrolysis in SBPs from *P. denitrificans* can be activated by formation of a ∆p (Pacheco-Moisés et al., 2000; Zharova and Vinogradov, 2004, 2003). To test this, a ∆p was established by succinate oxidation (coupled to proton pumping via complexes III and IV) and the effect on ATP hydrolysis was assessed for all six variants (**Figure 3.18**). It should be noted that activation via this method is subject to variations in the succinate oxidation rates and membrane coupling. However, it is clear the formation of a ∆p increases the rates of ATP hydrolysis in all strains (**Figure 3.18**). The activation was slow, taking minutes to reach maximal turnover rates. In addition, it can be seen from the raw traces that ATP hydrolysis also gradually increases even in the absence of succinate, although much more slowly. This slow activation does not occur when the uncoupler gramicidin is added to the membranes either with/without succinate present, suggesting that, in the absence of succinate, slow ATP hydrolysis gradually builds a low ∆p, which initiates a positive feedback loop by activating hydrolysis to increase ∆p further. Importantly, ATP hydrolysis was increased significantly compared to wild type for both deletion of the ζ subunit and truncation of the ε subunit. This is again different from the effects observed for selenite and LDAO activation. Thus, the picture of how ATP hydrolysis in *P. denitrificans* is inhibited remains complicated, yet it appears to be a multicomponent mechanism. All three modes of activation (LDAO, oxyanions and ∆p) are considered to act by relieving inhibition by Mg-ADP, however, they exhibit different characteristics that probably reflect their different activation mechanisms, which are either unaffected or influenced by the ε-CTD.

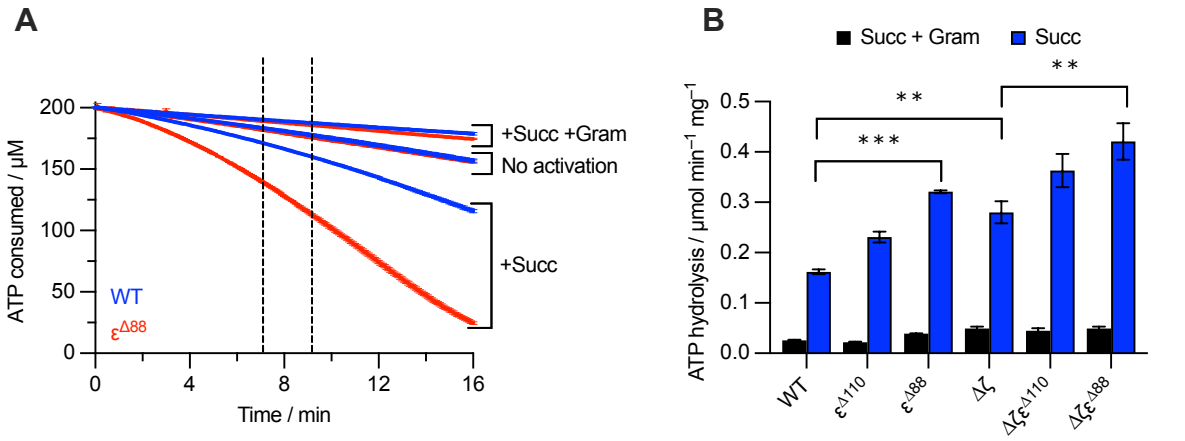

Figure 3.18. Activation of ATP hydrolysis by Δp in wild-type and variant SBPs. (A) Examples of kinetic traces monitoring ATP hydrolysis in the wild-type (blue) and $\varepsilon^{\Delta 88}$ (red) strains in the presence/absence of succinate-induced membrane energisation, and the presence/absence of 8 µg mL^{-1} gramicidin A to dissipate Δp. (B) ATP hydrolysis by wild type and variants of *P. denitrificans* ATP synthase upon membrane energisation by addition of 2.5 mM succinate. Rates were measured between 7 and 9 min, as indicated in panel A, where the maximum activation was achieved before depletion of NADH in the assay detection system became limiting. The traces are mean average data from three technical replicates with error bars showing the S.E.M. Statistical significance was calculated by one-way ANOVA followed by Tukey's test comparing all strains and conditions to each other. For clarity, only three examples are shown, $^{**}p < 0.01$, $^{***}p < 0.001$.

3.8.6. ATP hydrolysis – effect of ε-CTD truncation on proton pumping

Data from the *E. coli* ATP synthase have suggested that truncation of the ε-CTD, while increasing ATP hydrolysis, resulted in decreased proton pumping compared to wild-type (Cipriano and Dunn, 2006; D'Alessandro et al., 2017). However, a separate study suggested that proton pumping in *E. coli* ATP synthase is not significantly affected by ε-CTD removal, despite a >2-fold increase in ATP hydrolysis activity (Shah and Duncan, 2015). This makes it unclear whether the ε-CTD plays a role in the coupling of ATP hydrolysis to proton pumping. The effect of removing the ε-CTD of the *P. denitrificans* ATP synthase on the coupling of ATP hydrolysis to proton pumping was investigated using 9-amino-6-chloro-2-methoxyacridine (ACMA) quenching of SBPs (see Section 2.5.7, Materials and Methods,). ATP hydrolysis in all six variants was activated by addition of 10 mM selenite to generate sufficient ATP hydrolysis for detection (**Figure 3.19**).

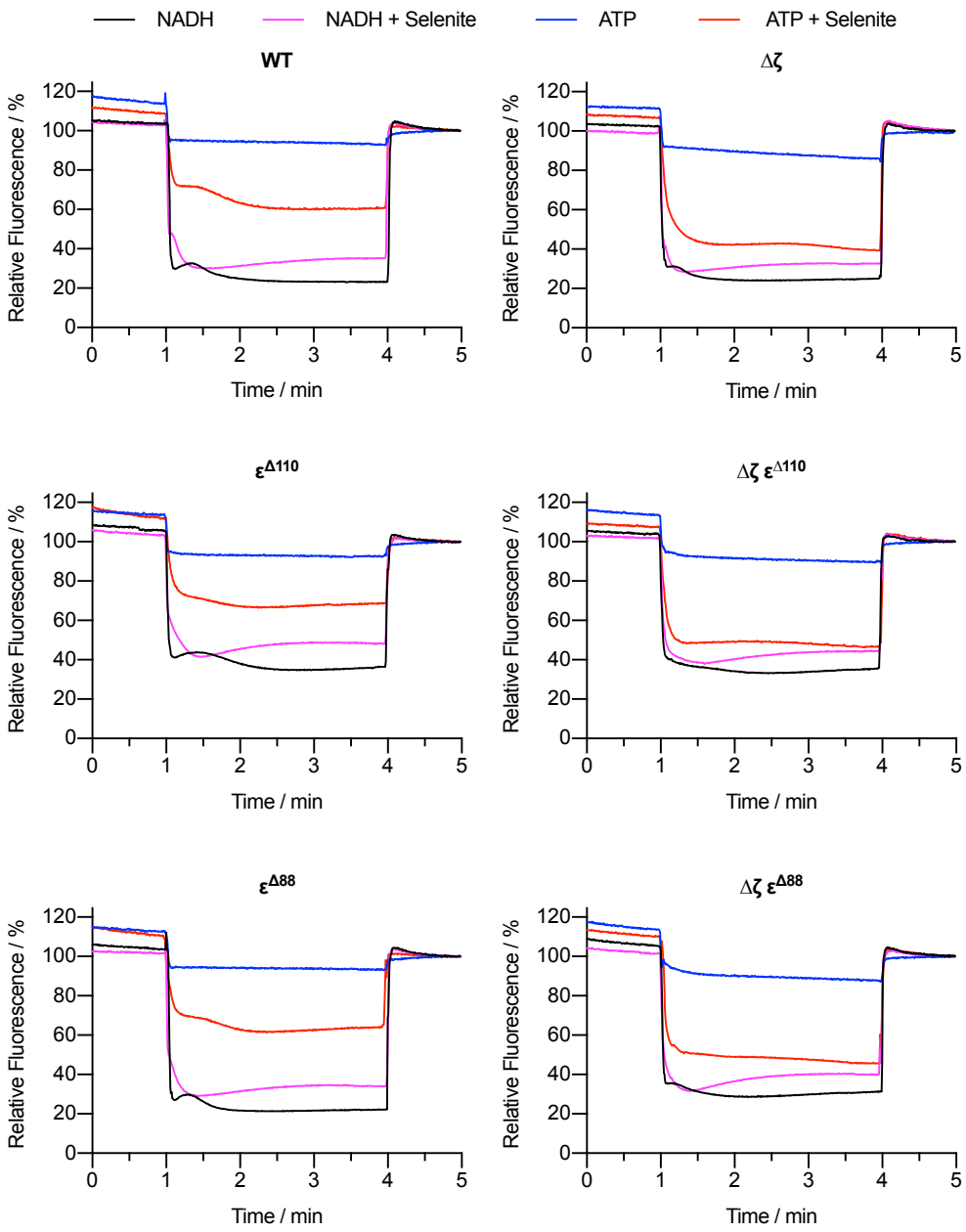

Figure 3.19. Comparison of membrane energisation in SBPs from each strain during NADH oxidation or ATP hydrolysis, monitored by the quenching of the fluorescence of ACMA at 32 ˚C. Reactions were initiated by addition of either NADH (500 μM) or ATP (1 mM) to 1 mL of 50 μg mL^{-1} SBPs stirred in buffer containing 10 mM MOPS (pH 7.5), 50 mM KCl, 1 mM $MgCl_2$, 0.5 μM ACMA and 100 nM valinomycin, with or without 10 mM selenite. Membranes were de-energised by addition of 40 mM NH_4Cl after 4 min.

As a control, the quench in the ACMA fluorescence signal was also monitored for NADH oxidation via complex I turnover in the presence/absence of selenite. In the NADH controls, the extent of quenching remained similar with and without selenite, showing selenite did not substantially uncouple the membrane. For proton pumping coupled to ATP hydrolysis, ACMA quenching was measured again in the presence/absence of selenite. Without selenite, the

extent of quenching was low for all six strains, as expected for the low rates of ATP hydrolysis. Clearer effects were seen in the presence of selenite, producing larger quenches, where the extent of quenching was similar in wild-type, $\varepsilon^{\Delta 110}$ and $\varepsilon^{\Delta 88}$ strains, showing that the removal of the ε-CTD did not result in an obvious loss of proton pumping coupled to ATP hydrolysis, as was seen for *E. coli* (Cipriano and Dunn, 2006; D'Alessandro et al., 2017). This effect is replicated for the $\Delta\zeta$, $\Delta\zeta\varepsilon^{\Delta 110}$ and $\Delta\zeta\varepsilon^{\Delta 88}$ strains but with a larger extent of quenching, as expected for the higher ATP hydrolysis rates achieved in the absence of the ζ subunit. The same experiment is not possible with LDAO as, being a detergent, it compromises the integrity of the membrane.

3.9. Catalytic activity – ATP synthesis

Following the conclusion that Mg-ADP is a significant component of inhibition in the ATP synthase from *P. denitrificans* and that the ε-CTD may help to stabilise it, the effect of deleting the ε-CTD on ATP synthesis was investigated. To measure ATP synthesis two different assays were employed. In both cases NADH was added to SBPs to create Δp by respiratory chain catalysis, and ATP production was monitored using a luminescence readout generated on the addition of luciferase/luciferin (**Figure 3.20**). The first method uses continuous, real-time ATP monitoring by including luciferase and luciferin in the reaction mixture. However, there is a possibility that the luciferase may itself interfere with respiration (it depletes oxygen in the reaction mixture), and the luciferase activity is also highly sensitive to changes in temperature and pH, which can be a problem when testing different reaction conditions. The second method does not include luciferase/luciferin in the reaction mixture. Instead, small aliquots of the reaction mixture are quenched into acid at set time intervals over a given time course. Luciferase/luciferin is then added to these quenched samples and a single luminescence readout for each sample can be compared to ATP standards. This assay is more demanding than the real-time assay but eliminates any potential luciferase interference that there may be in the reaction.

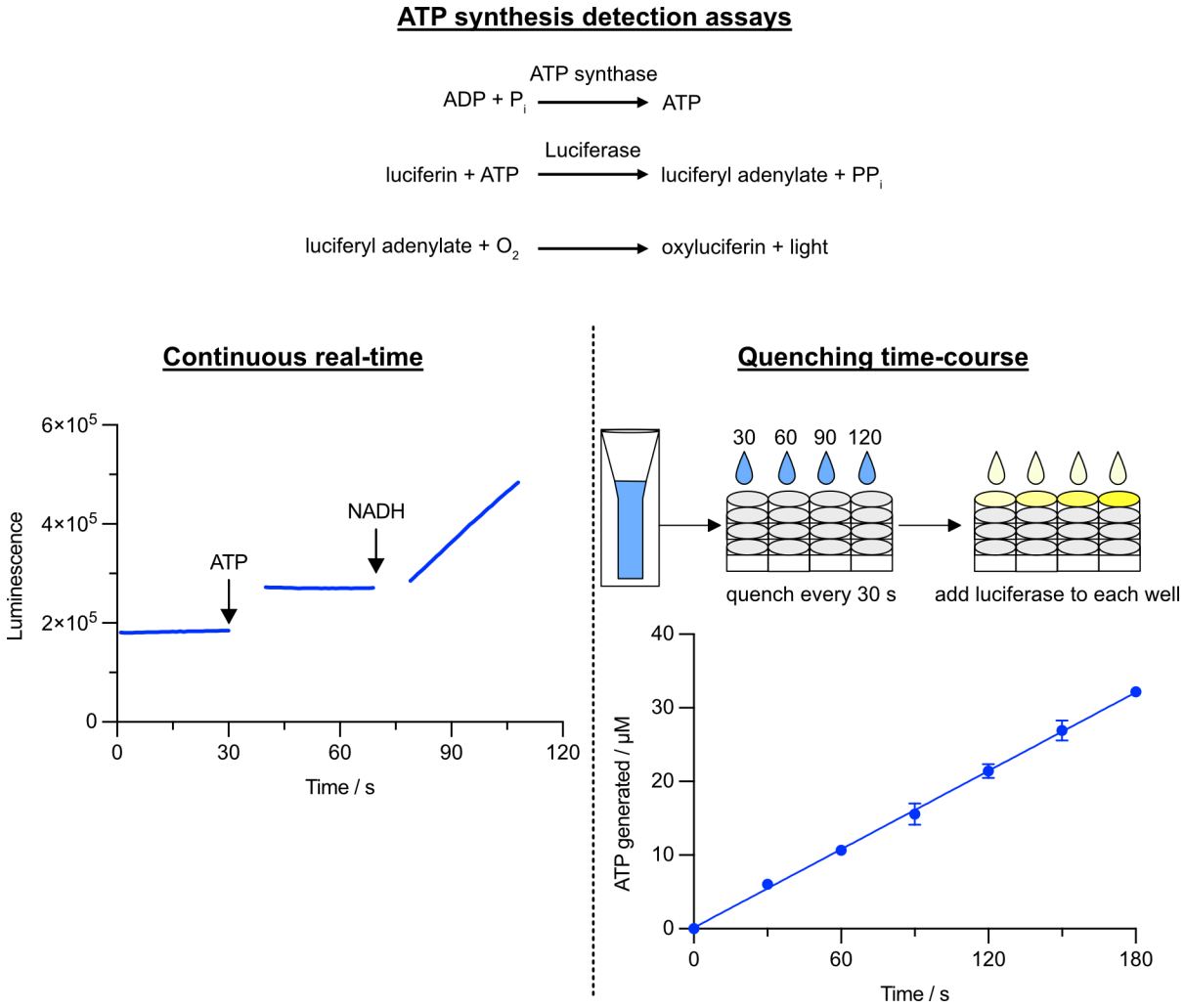

Figure 3.20. Overview of two methods used to measure ATP synthesis in SBPs. ATP is detected by addition of a cocktail containing luciferase from firefly and luciferin substrate. The overall reaction results in ATP being used to generate light, the intensity of which is dependent on the ATP concentration present in the sample. An example raw trace for the continuous real-time assay is shown (left). Background luminescence is first monitored, followed by the addition of a known amount of ATP to calibrate the luminescence response. A Δp is generated via NADH oxidation through complex I, which drives ATP synthesis. The evolution of ATP over time is monitored by the slope of the luminescence signal. A schematic and an example of the data for the quenching time-course assay is shown (right). A reaction mixture containing SBPs, NADH, ADP and P_i is prepared. Every 30 s a sample of the reaction mixture is quenched into acid in a 96-well plate over a course of 3 minutes. The luciferase/luciferin cocktail is then added to each sample and the endpoint luminescence is measured for each. A set of ATP standards treated in the same way are used to convert the luminescence signal into a concentration of ATP in each sample.

3.9.1. ATP synthesis – effect of removing the ε-CTD

The initial rates of ATP synthesis were measured in wild-type and $\varepsilon^{\Delta 88}$ strains at different ADP concentrations using the real-time continuous assay (**Figure 3.21A**). The K_M values for ADP remained similar between wild-type and $\varepsilon^{\Delta 88}$ strains (23.0 ± 2.3 and 21.7 ± 1.8 µM, respectively)

suggestive of a similar affinity for ADP despite the absence of the ε-CTD. The V_{max} values of 0.775 ± 0.025 (wild type) and 1.293 ± 0.034 ($\varepsilon^{\Delta 88}$) μmol min^{-1} mg^{-1} suggest that the ε-CTD strains are faster at synthesising ATP. However, this data has not been normalised to ATP synthase concentration in the membrane and other factors, such as extent of SBP coupling.

To normalise the different enzyme concentrations in the SBPs and membrane coupling between strains, ATP synthesis was measured under two different conditions, and the number of ATP molecules generated per NADH oxidised was calculated. Normalising ATP synthesis to NADH oxidation accounts for variations in the purities of the SBP preparations (affecting the proportion of ATP synthase and other respiratory enzymes in the system). This was considered a reasonable method to normalise the data, as the rate of ATP synthesis depends linearly on the rate of NADH oxidation (**Figure 3.21B**) (Fedor and Hirst, 2018). Differences in the membrane coupling were harder to account for.

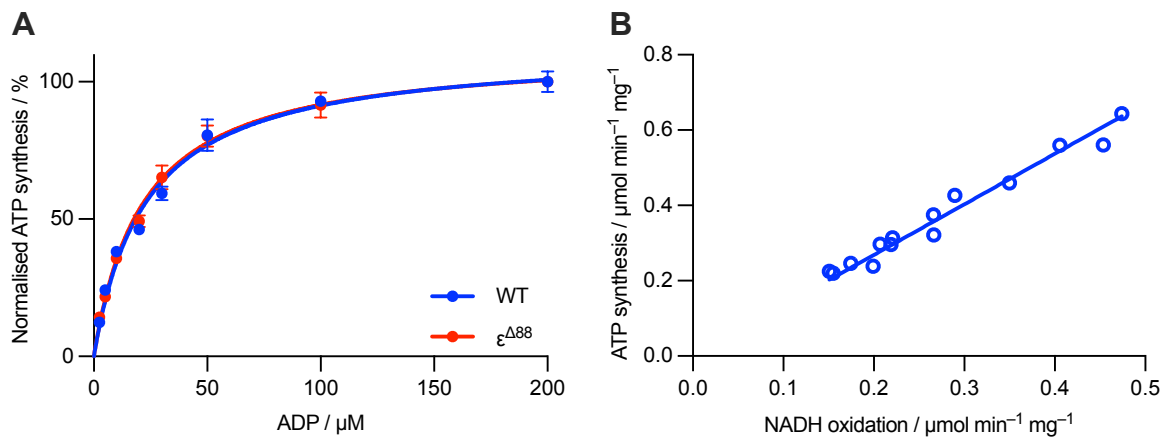

Figure 3.21. (A) Dependence of the rate of ATP synthesis on ADP concentration for SBPs from the wild-type and $\varepsilon^{\Delta 88}$ strains. The V_{max} values are 0.78 ± 0.03 (wild type) and 1.29 ± 0.03 ($\varepsilon^{\Delta 88}$) μmol min^{-1} mg^{-1} and the K_M values are 23.0 ± 2.3 (wild type) and 21.7 ± 1.8 ($\varepsilon^{\Delta 88}$) μM. The rates are mean averages ± S.E.M. (*n* = 3). (B) Dependence of the rate of ATP synthesis on NADH oxidation for wild-type SBPs. The NADH oxidation rate was modulated with different concentrations of piericidin A and ATP synthesis measured using the quenching time-course assay. Each data point represents a single measurement.

The number of ATP molecules generated per NADH oxidised was measured in four independent SBP preparations for each strain (**Figure 3.22**). Two sets of SBPs were measured at 32 ˚C using the time-course assay and two were measured at room temperature using the real-time assay. If the SBPs were perfectly coupled for ATP synthesis then one would expect 2.5 ATP molecules produced per NADH (from 10 H^+ pumped per NADH and 3 ATP produced per 12 H^+) (Jones et al., 2017; Morales-Ríos et al., 2015). The SBPs measured at 32 ˚C showed higher coupling to ATP synthesis (~1.3 molecules of ATP per NADH for wild type)

compared to those measured at room temperature in the real-time assay (~0.5 molecules of ATP per NADH for wild type). However, both datasets showed there was no statistically significant difference in ATP synthesis between the wild-type and mutant strains. Thus, the ε-CTD does not appear to compromise ATP synthesis when it is removed, suggesting that the enzyme remains well coupled.

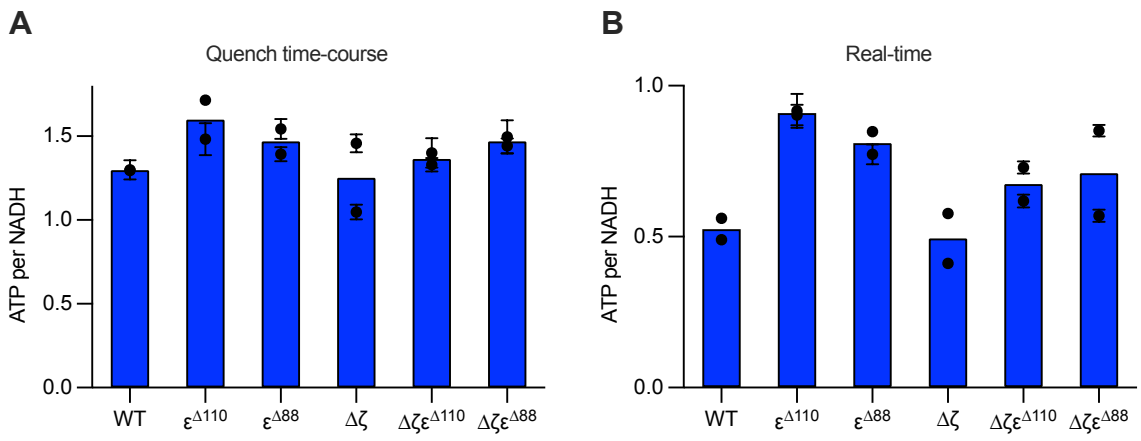

Figure 3.22. The number of ATP molecules generated per NADH molecule oxidised for all six strains, measured by two different ATP synthesis assays. (A) Quench-based ATP quantification assay. Rates were measured at 32 ˚C in the presence of 1 mM ADP. (B) Real-time ATP quantification assay. Rates were measured at room temperature in the presence of 50 μM ADP. Data points represent two biological replicates with rates reported as the average of three technical replicates ± S.E.M. All rate comparisons between strains were non-significant according to one-way ANOVA using Tukey's test.

3.10. Summary of the regulation of ATP hydrolysis in *P. denitrificans*

In summary, inhibition by Mg-ADP is the dominant mechanism by which *P. denitrificans* ATP synthase is prevented from catalysing ATP hydrolysis. Deletion of the ζ subunit, which resembles IF_1, only activated low-level catalysis by around two-fold (García-Trejo et al., 2016; Morales-Ríos et al., 2010, 2015; Zarco-Zavala et al., 2014). Removing the ε-CTD was also not sufficient to activate hydrolysis in *P. denitrificans* (the rate remains very slow with both the ζ subunit and ε-CTD removed), and this argues against direct inhibition by the ε-CTD, as observed in *Bacillus* PS3 (Kato-Yamada et al., 1999). Additionally, while the ε-CTD in *Bacillus* PS3 possesses an ATP binding domain that controls its conformation in response to the ATP concentration (Yagi et al., 2007), the *P. denitrificans* ε-CTD contains no such binding site. Although recent evidence for the *E. coli* and *Bacillus* PS3 enzyme points to a destabilising/competing role of the ε-CTD on Mg-ADP, it appears the opposite could be true in *P. denitrificans* (Haruyama et al., 2010; Konno et al., 2011; Milgrom and Duncan, 2020; Mizumoto et al., 2013; Shah et al., 2013). In *P. denitrificans*, the increase in the enzyme's sensitivity to oxyanion activation and its activity in the presence of Δp when the ε-CTD is

removed may suggest it stabilises Mg-ADP inhibition. An alternative explanation is that the increased sensitivity to oxyanions on removal of the ε-CTD is a result of the ε-CTD destabilising the oxyanion-bound state rather than stabilising Mg-ADP inhibition. Alternatively, it has been suggested that there is a mixture of inhibited states present in the ATP synthase population, which are affected by ∆p and oxyanions differently (Pacheco-Moisés et al., 2000). It is thus possible that removing the ε-CTD could instead result in a change in the distribution of these states, altering the fraction of the enzyme population that is susceptible to activation by ∆p. However, this would imply that a substantial portion of the enzyme population remains inactive even in the presence of a ∆p. Further evidence is required to distinguish these possible models and disentangle the different roles of the ε-CTD in different organisms.

Finally, it is striking that, thermodynamically, ∆p opposes the hydrolysis, proton-pumping reaction, yet ∆p activates ATP hydrolysis. It appears that ∆p kinetically assists but thermodynamically opposes the same reaction. Prior work reinforces the view that the *P. denitrificans* enzyme is inhibited by Mg-ADP and that ∆p prevents the formation of the Mg-ADP inhibited state (Zharova and Vinogradov, 2004, 2003). It was suggested that, on the collapse of ∆p, phosphate dissociates first from the β subunit, leaving the enzyme trapped in an inactive Mg-ADP inhibited state. It is possible that in the cell, where the ∆p varies, the ζ subunit and the ε-CTD may take on greater importance in preventing ATP hydrolysis.

3.11. Activating ATP hydrolysis for RET

The motivation for this chapter was to activate ATP hydrolysis of the *P. denitrificans* ATP synthase so that it can be used to establish a ∆p independent of respiration that is sufficient to drive RET in complex I. While the removal of the ζ subunit and ε-CTD did not activate ATP hydrolysis sufficiently for these purposes, addition of LDAO, oxyanions and the presence of a ∆p were able to relieve Mg-ADP inhibition and activate ATP hydrolysis. The compatibility of each method of activation was considered with respect to the RET assay requirements. LDAO, while providing the greatest activation in ATP hydrolysis, is a zwitterionic detergent that uncouples the membranes so precludes a ∆p from being established. Selenite activation, on the other hand, did not uncouple the membrane, as seen by the establishment of an ACMA quench, and that proton pumping by NADH oxidation appeared unaffected (**Figure 3.19**). The addition of selenite to SBPs under RET conditions, in which complexes III and IV were inhibited and the Q-pool was reduced by succinate oxidation, showed no NAD^+ reduction. It appears either selenite does not activate ATP hydrolysis sufficiently for RET purposes or the selenite itself could interfere with the RET measurement. Even when using the $\Delta\zeta\varepsilon^{\Delta 88}$ variant, which

facilitated higher ATP hydrolysis rates at lower selenite concentrations, no rates of RET could be observed.

The last approach investigated for RET reactions was the activation of ATP hydrolysis by a ∆p. This method has the advantage of not requiring additional additives that could interfere with the complex I activity, as is the case for selenite or LDAO. Simply, in *P. denitrificans*, ATP hydrolysis could first be activated by a ∆p generated via succinate oxidation and proton pumping via complexes III and IV. Once activated, complexes III and IV could then be inhibited to prevent re-oxidation of the Q-pool. This should lend itself well to the establishment of conditions necessary for measuring RET. Unfortunately, however, the ∆p-activated ATP hydrolysis rates are lost almost instantaneously when complexes III and IV are inhibited, as the ATP synthase reverts to a non-catalysing state (**Figure 3.23**). The ∆p necessary for driving RET is thus no longer sustained. This result provides further evidence that, in the absence of a ∆p, the ATP synthase collapses back into a stable inhibited state, probably with a Mg-ADP nucleotide tightly bound. As tests were carried out in the $\Delta\zeta\varepsilon^{\Delta 88}$ variant, the ADP inhibited state is likely re-established independently of the ζ subunit or ε-CTD subunit, providing further evidence for ADP inhibition being the primary mechanism by which ATP hydrolysis is regulated in *P. denitrificans.*

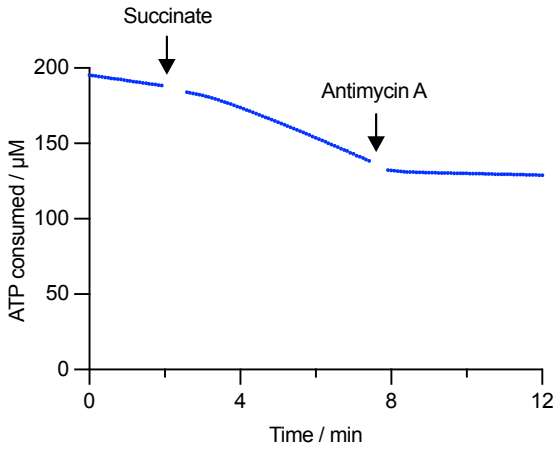

Figure 3.23. ATP hydrolysis in $\Delta\zeta\varepsilon^{\Delta 88}$ strain of SBPs. Generation of a ∆p on succinate addition speeds up ATP hydrolysis. Addition of antimycin A to inhibit complex III and IV catalysis instantly collapses ∆p and ATP hydrolysis stops as the enzyme returns to a non-catalysing state.

3.12. Conclusions and future work

Unfortunately, methods aimed at activating ATP hydrolysis in the *P. denitrificans* ATP synthase were not successful and therefore did not enable measurements of RET in complex I. Efforts

to establish a method to study RET in *P. denitrificans* complex I are still of key interest and must now be pursued through different avenues. One potential approach is to fuse SBPs with lipid vesicles containing an alternative proton pump, such as a more freely hydrolysing F_1F_O-ATP synthases or a *p*-type ATPase, which could hydrolyse ATP at sufficiently high rates to establish a Δp. The fusion protocol must retain sufficient coupling in SBPs for this to be practical.

An alternative method one could envisage is to combine purified enzymes to create a minimal RET system. This would involve the purification of three different enzymes; complex I, a proton pump, such as the *E. coli* ATP synthase, and a Q-pool reducing enzyme, such as complex II. These would then have to be reconstituted together into liposomes. Recently, both bovine complex I and the ATP synthase from *E. coli* have been reconstituted into Q_{10}-containing liposomes using a simple one-pot method (Biner et al., 2020). The proteoliposomes were able to support complex I-driven ATP synthesis, showing that they remained well coupled. If this approach could be applied to purified complex I from *P. denitrificans*, then the basis for a simple RET measurement system may be possible. The reconstitution or addition of a Q-reductase to the system would also be required for this to be realised. A robust purification procedure for complex I from *P. denitrificans* first needs to be developed to achieve this. Developing a protocol to isolate intact complex I from *P. denitrificans* will also be crucial for characterising complex I variants and will pave the way for future structural studies of the wild-type enzyme and variants. The next chapter describes the development of a purification protocol for complex I to be used for proteoliposome, structural and mutagenesis studies.

4. Developing a genetically tractable strain of *P. denitrificans* and the characterisation of isolated complex I

4.1. Introduction

Complex I is essential to *P. denitrificans*. This means the cell cannot survive if complex I catalysis is severely compromised. While a Δp can be maintained by succinate-driven complex III and IV catalysis, there are no alternative enzymes in *P. denitrificans* that can turnover NADH to maintain the low $NADH/NAD^+$ ratio in the cell cytoplasm (Finel, 1996; Yagi, 1991; Zickermann et al., 1998). A low $NADH/NAD^+$ ratio is required for unimpeded glycolysis, as well as for many other dehydrogenase enzymes that rely on the $NADH/NAD^+$ balance (Stein and Imai, 2012). It is therefore likely that maintaining the $NADH/NAD^+$ ratio underpins the essential role of complex I for *P. denitrificans* survivability. The study of pathogenic mutations and potential deleterious mutations of key catalytic residues in complex I are limited by this dependency on complex I.

To permit the study of pathogenic and deleterious mutations, a bypass mechanism must be introduced to regenerate the NAD^+ pool and allow the cell to survive when complex I cannot function. The simplest bypass mechanism is an additional NADH dehydrogenase enzyme. A suitable candidate is the alternative NADH dehydrogenase (NDH-2), a membrane-bound single-subunit enzyme of around 40-60 kDa, which catalyses the transfer of electrons from NADH to Q without the pumping of protons across the membrane (**Figure 4.1**). NDH-2 has previously been used as a complex I bypass in other model organisms encountering similar problems. For instance, complex I is also essential in the strictly aerobic yeast *Y. lipolytica*, with deficiencies in complex I subunits ultimately proving lethal to the cell (Kerscher et al., 2001). Although *Y. lipolytica* already possesses an NDH-2, it was found to be located on the external face of the IMM and so did not compensate for loss of NADH oxidation by complex I in the matrix (Kerscher et al., 2001). By redirecting this NDH-2 to the matrix face, complex I mutations were no longer lethal and cell growth was rescued. In *E. coli*, cells already express and correctly localise an NDH-2, so no further modifications were required for complex I mutagenesis.

P. denitrificans does not possess a native NDH-2. However, past studies have shown that the replacement of *nqo8* and *nqo9* genes with the *ndh2* gene from *E. coli* rescued lethality (Finel,

1996) and enabled mutations of the Nqo8 subunit to be studied. To generate these mutations, variants of the *nqo8* gene were inserted into the *nqo8*-lacking strain, with the variant gene either replacing the previously inserted *ndh2* gene or inserting adjacent to it (Kurki et al., 2000). While this study employed NDH-2 to facilitate the creation of deleterious mutants, the approach described is not ideal because knockout strains are required for each subunit and *ndh2* is incorporated at each location, preventing the creation of multi-subunit mutations and further downstream mutagenesis. The constitutive expression of NDH-2 in the complex I operon also complicates downstream study of complex I mutants because both enzymes will catalyse NADH oxidation, but only complex I will translocate protons. To circumvent this complication, the substrate deaminoNADH (dNADH) can be used in place of NADH, as it can be catalysed by complex I but not NDH-2. Further to this, NDH-2 is insensitive to some commonly used complex I Q-site inhibitors such as piericidin A. While these compensations allow for a degree of control when monitoring specific complex I catalysis, they add unnecessary complications when investigating mutants that are non-lethal.

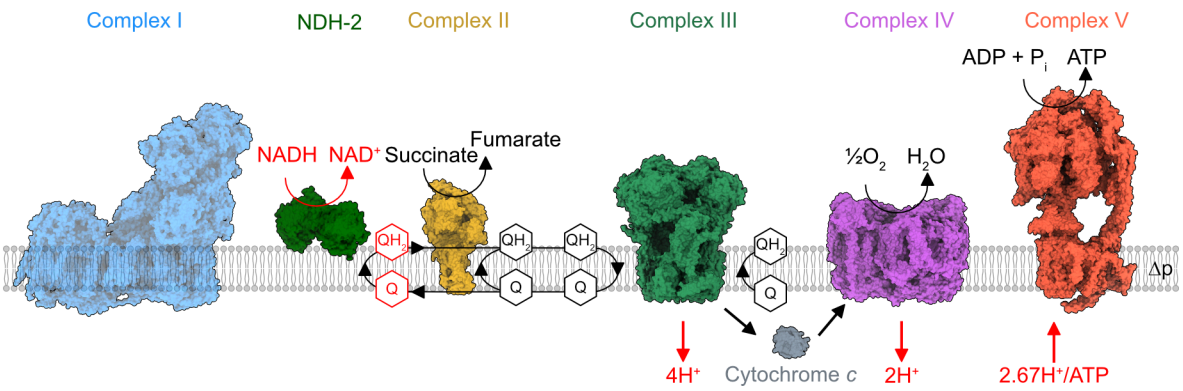

Figure 4.1. Canonical electron transport chain, including the alternative NADH dehydrogenase (NDH-2) (PDB: 4NWZ). When complex I catalysis is compromised, such as by deleterious mutagenesis, the presence of NDH-2 allows complex I to be bypassed, ensuring the NAD^+ pool is regenerated and ubiquinone is reduced to drive respiration.

Previous attempts in the Hirst laboratory to replicate or improve on the above methodology for the insertion of NDH-2 into *P. denitrificans* have been unsuccessful, including attempts to insert *ndh2* into a constitutively expressed operon independent of complex I (Varghese, 2016). In this chapter, to generate a strain of *P. denitrificans* that is amenable to complex I mutagenesis, NDH-2 was inserted into *P. denitrificans* using an inducible expression plasmid. This allows NDH-2 expression to be switched on or off, limiting the complications caused by constitutive NDH-2 expression. Overall, this approach should allow the generation and study of any complex I mutation in *P. denitrificans*.

In addition to generating a genetically tractable strain of *P. denitrificans*, a robust purification protocol for the isolated enzyme is also developed and described in this chapter, facilitating the use of *P. denitrificans* as a fully faceted model for studying complex I mutants. To date, only one method for the isolation of complex I from *P. denitrificans* has been described (Yip et al., 2011), but it has not been further replicated in the literature and early attempts to repeat it in the Hirst laboratory were not successful. The published method purified native complex I from *P. denitrificans* membranes using three ion-exchange steps followed by size-exclusion chromatography, but took multiple days to perform. In *Y. lipolytica*, complex I isolation has benefitted substantially from the genomic insertion of a purification tag composed of six histidine residues connected to the C-terminus of the NDUFS3 (Nqo5) subunit by six alanine linker residues (Kashani-Poor et al., 2001). Using Ni-affinity chromatography followed by size-exclusion chromatography, complex I could be rapidly isolated from detergent-solubilised membranes. The addition of a similar purification tag to *P. denitrificans* complex I would vastly improve the isolation of complex I and benefit the development of this model system. In this chapter, the same purification tag was introduced onto the Nqo5 subunit in *P. denitrificans* complex I and the resulting enzyme was isolated and fully characterised.

4.2. Aims of this chapter

- Develop a strategy to bypass complex I dependency in *P. denitrificans* to facilitate the creation of deleterious complex I mutations.
- Genetically engineer a purification tag onto *P. denitrificans* complex I.
- Develop a robust purification procedure to isolate pure, stable and active complex I from *P. denitrificans*.
- Characterise the isolated complex I from *P. denitrificans.*
- Optimise the reconstitution of *P. denitrificans* complex I into liposomes.

4.3. A genetically tractable model system to study complex I variants

4.3.1. Inducible expression plasmids for NDH-2 expression in *P. denitrificans*

There are few regulated gene expression systems that have been developed for *P. denitrificans*. Most systems that have been described work through a transcriptional repressor that tightly binds to the operator sites of the gene promoter sequence, preventing transcription of the gene. An inducer molecule can then be introduced, which allosterically binds and inhibits the transcriptional repressor, allowing the transcription of the downstream gene. The ideal expression system for introducing NDH-2 into *P. denitrificans* would be tightly controlled, without any leak of expression in the absence of inducer. To date, few regulatable expression

systems have been tested and optimised for *P. denitrificans*. The first considered here was pIND4, an IPTG-inducible expression plasmid with kanamycin resistance (Ind et al., 2009). Unfortunately, while expression appeared to be tightly controlled by IPTG induction in *Rhodobacter sphaeroides*, a study has shown that in *P. denitrificans*, the gene expression was leaky in the absence of IPTG (Ind et al., 2009). Two alternative regulated gene expression systems are the pLMB509 and pQF derived plasmids, which confer gentamicin and tetracycline antibiotic resistance, respectively (Kaczmarczyk et al., 2013; Tett et al., 2012). Both these systems were shown, by prior studies, to be tightly regulated in *P. denitrificans* and use taurine or cumate (4-isopropylbenzoic acid) as their respective induction molecules. Further details on these plasmids can be found in **Table 2.2** (Materials and Methods) (Kaczmarczyk et al., 2013; Tett et al., 2012).

While not required here, the pQF plasmid encodes 3×FLAG tags on both termini. A pQF derivate, pQH, replaced the C-terminal FLAG-tag with a HA-tag. Both were tested here in case the different tags had different effects on NDH-2 activity. Similarly, the pLMB509 vector used encoded a N-terminal His_6-tag.

4.3.2. Insertion of *ndh2* into expression vectors

The NDH-2 from *E. coli* was chosen for insertion into *P. denitrificans*. However, unlike *E. coli, P. denitrificans* has a GC-rich genome (~65% GC (Baker et al., 1998)). To ensure that the *ndh2* gene would be translated properly and not limited by a different distribution of tRNA codons, the *E. coli ndh2* sequence was codon optimised for the GC-rich codons common in *P. denitrificans* (Baker et al., 1998). Codon optimisation was performed automatically by GENEWIZ® and the gene then synthesised by GENEWIZ® and stored in a pUC57-Kan storage vector. To insert *ndh2* into each expression vector (pQF, pQH and pLMB509), the gene was amplified off the plasmid using primers containing overhangs, which encoded enzyme restriction sites plus a random 10 bp sequence to provide a handle for restriction enzyme binding. For the pQF and pQH vectors, *Xba*I and *Sac*I restriction sites were added upstream and downstream to the gene, respectively. For the pLMB509 vector, *Nsi*I and *Sac*I restriction sites were added upstream and downstream to the gene, respectively. The PCR products were purified, digested and ligated for 10 minutes with pre-digested pQF, pQH and pLB509 vectors. The products were then transformed into NEB 5-α storage strain and screened (**Figure 4.2**). Of note, the encoded N-terminal His_6-tag on the pLMB509 vector was removed during the insertion of *ndh2*.

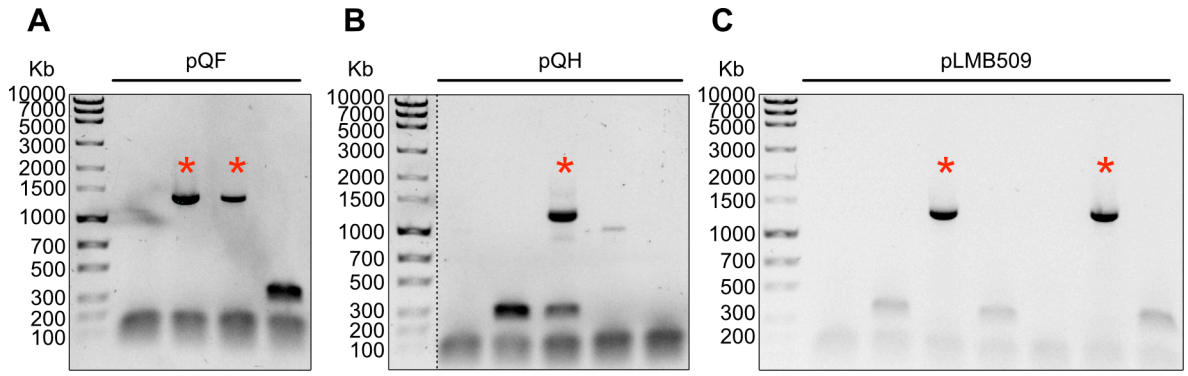

Figure 4.2. Screening for NEB 5-α colonies containing *ndh2* inserted into each expression vector. Colonies were identified by amplification of the *ndh2* gene and by detecting a PCR product band of size 1305 bp by gel electrophoresis. Gels for each vector are shown: (A) pQF, (B) pQH and (C) pLMB509. Colonies with successful *ndh2* insertion are highlighted by red asterisks.

4.3.3. Insertion of *ndh2* into *P. denitrificans*

The expression plasmids containing *ndh2* were transformed into the MFD*pir* donor strain (**Figure 4.3A**), followed by mating with the *P. denitrificans* strain, ΔHy, as described in Chapter 3 and Materials and Methods (**Figure 4.3B**). Many *P. denitrificans* colonies successfully contained the pLMB509 vector – they displayed gentamicin resistance and the *ndh2* gene could be detected by PCR (**Figure 4.3B**). However, extensive screening for the conjugation of pQF and pQH into *P. denitrificans* was less successful, with no colonies containing the pQH vector (and *ndh2*) observed, and only four colonies identified for the pQF vector (**Figure 4.3B**). It is unclear why the conjugation was less successful for pQF and pQH since they have been used previously in *P. denitrificans*. Potentially, the antibiotic tetracycline was used at too high a concentration for selection directly following conjugation. Only the colonies containing *ndh2* on the pLMB509 and pQF vectors were compared for the next stage.

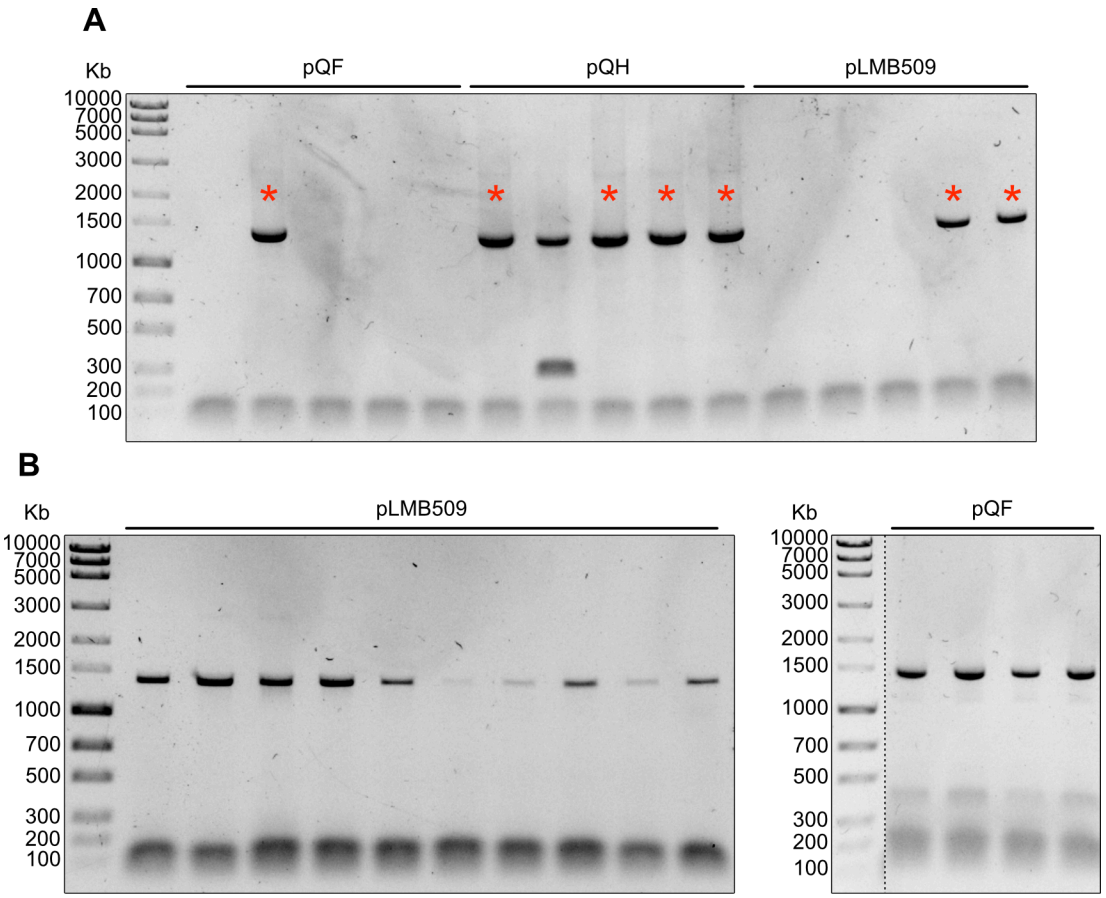

Figure 4.3. Identification of *ndh2*-containing colonies for the MFD*pir* donor strain and the *P. denitrificans* recipient strain. In both cases, colony PCR is performed with primers that bind directly to the start and end of the *ndh2* gene, producing a 1305 bp PCR product. (A) Colonies of MFD*pir* screened for the presence of *ndh2* in cells transformed with each vector. Colonies with successful *ndh2* insertion are highlighted by red asterisks. (B) Colonies of *P. denitrificans* screened for the presence of *ndh2* for each conjugated vector. No colonies conjugated with the pQH vector are shown, as no successful conjugations were identified.

4.3.4. Rescuing *P. denitrificans* growth with NDH-2

To assess whether NDH-2 expression would permit cell growth when complex I catalysis was inhibited, growth of each strain was compared under different conditions. Cells were grown in 50 mL LB medium, in the presence of antibiotics, until an OD_{600} of ~0.3 was reached before transferring 200 µL of cells to a 96-well plate to be induced (or untreated) with different concentrations of inducer: 0.1, 1 and 10 mM taurine for pLMB509 and 10, 20 and 50 µM cumate for pQF. The concentrations of inducer chosen were based on previous studies (Kaczmarczyk et al., 2013; Tett et al., 2012). First, the effect of the inducer and expression of NDH-2 was compared to cells growing without any induction. Expression of NDH-2 from both pLMB509 and pQF did not change the growth rate of the cells (**Figure 4.4A**). However, cells containing the pQF vector exhibited slower growth than cells containing pLMB509, reaching

lower maximum OD_{600}. This could be caused by toxicity from the expression vector or the leaky expression of unfolded NDH-2. In addition, the tetracycline antibiotic, required for maintenance of the pQF vector, is a more potent antibiotic for *P. denitrificans* than gentamicin, which may also be limiting cell growth at the concentration used here (20 μg mL^{-1}).

Second, to investigate whether expression of NDH-2 rescued cell growth when complex I was inhibited, mimicking a deleterious mutation, cells grown in the presence of different inducer concentrations were exposed to the complex I inhibitor piericidin A (5 μM) after two hours (**Figure 4.4B**). Cell growth was halted in both strains when NDH-2 was not expressed. In the case of pLMB509, the induction of NDH-2 expression rescued growth. Importantly, by varying the concentration of taurine, the extent of cell growth could be modulated, with higher concentrations (10 mM) resulting in a better recovery of growth, and lower concentrations (0.1 mM) proving ineffective. The regulation of NDH-2 expression therefore appears to be tightly controlled in the pLMB509 plasmid. Expression of NDH-2 in the pQF vector showed continued growth after inhibition of complex I but the growth was marginal and different inducer concentrations did not appear to modulate NDH-2 expression as stringently as when induced from pLMB509. This could be due to the concentrations of cumate used being too low to induce sufficient NDH-2 expression, or that the initiation of induction was too slow to rescue cell growth two hours before inhibition of complex I.

Finally, the growth of uninhibited cells was compared to the growth of cells inhibited with piericidin A but expressing NDH-2 at the maximum inducer concentrations tested (10 mM taurine and 50 μM cumate) (**Figure 4.4C**). For cells expressing NDH-2 off the pLMB509 vector, cell growth was similar to uninhibited cells. However, expression off the pQF vector, while permitting some cell growth, was clearly lower than in uninhibited cells. The strain containing the pLMB509 vector was thus considered a better fit for further studies. Overall, the results show that the expression of NDH-2 allowed the complex I dependency in *P. denitrificans* to be bypassed, paving the way for future complex I mutagenesis.

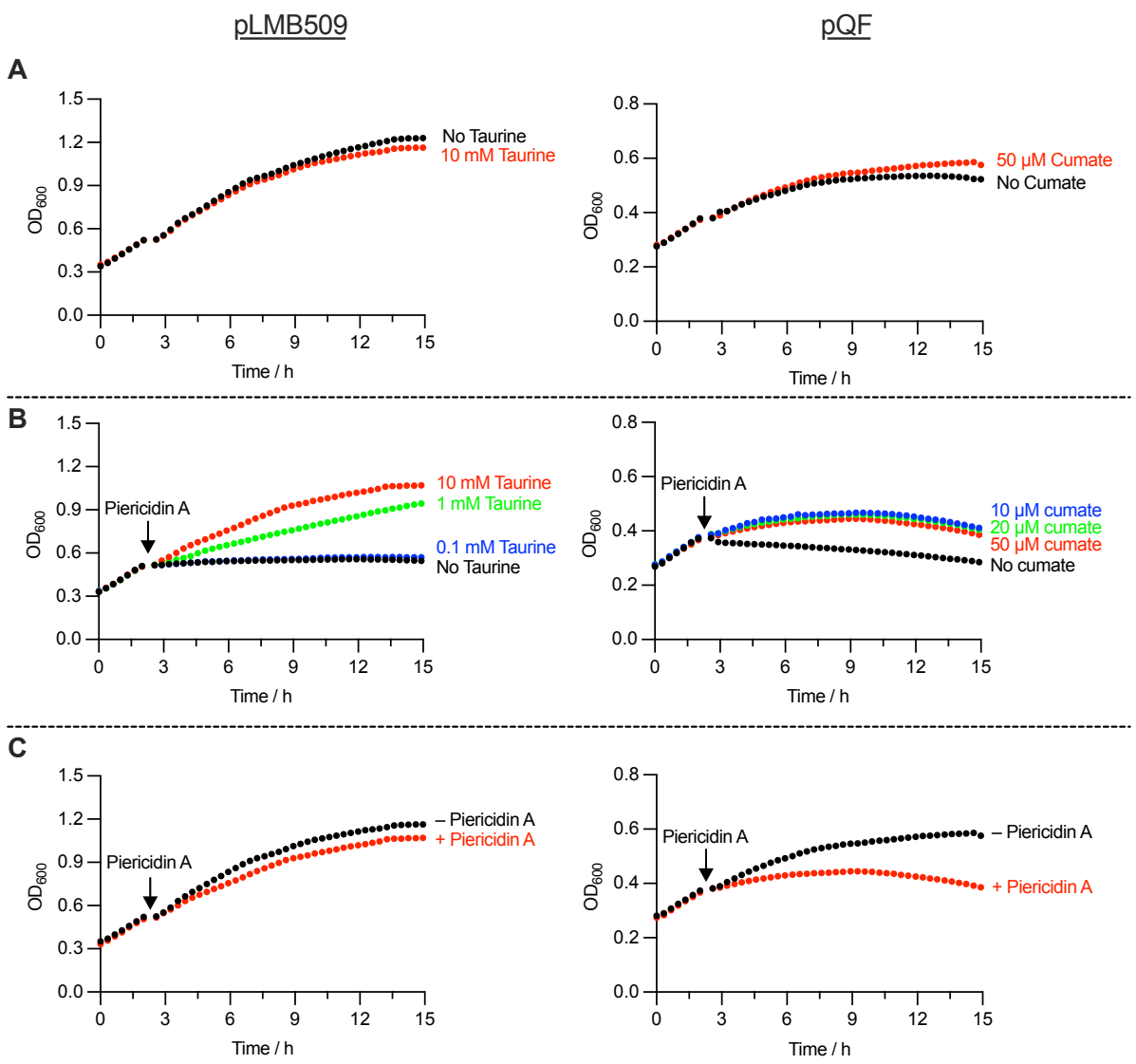

Figure 4.4. Growth on LB medium for *P. denitrificans* strains containing *ndh2* inserted in inducible expression plasmids pLMB509 (left) and pQF (right). Growth curves were measured in a Molecular Devices SpectraMax 348 96-well plate reader at 30 ˚C with 5 min shaking before each measurement at 20 min intervals. The LB medium contained rifampicin (50 µg mL^{-1}) and either gentamicin (20 µg mL^{-1}) or tetracycline (20 µg mL^{-1}) for pLMB509 and pQF vectors respectively. (A) Comparison of growth in presence/absence of a high concentration of inducer (taurine for pLMB509 and cumate for pQF). (B) Comparison of growth at different inducer concentrations following addition of 5 µM piericidin A after two hours to inhibit complex I activity. Point of addition shown by arrow. (C) Comparison of growth during NDH-2 expression at the highest inducer concentration after addition of either piericidin A or ethanol control. For clarity, the mean average data from three technical replicates are shown.

4.4. Design and creation of a complex I purification tag

4.4.1. Design of His_6-tag constructs

The next improvement for the *P. denitrificans* model system was to add a purification tag onto complex I, which would facilitate efficient isolation of the enzyme for both structural and functional characterisation. The design and location of the affinity tag used to purify *Y. lipolytica* complex I was reproduced here for the *P. denitrificans* enzyme (Kashani-Poor et al., 2001). To introduce the His_6-tag onto the C-terminus of the Nqo5 subunit a DNA construct was designed that was suitable for suicide vector-mediated homologous recombination (described in Chapter 3). First, a sequence encoding 6×His followed by a 6×Ala linker was designed (5'-GTG ATG GTG ATG ATG ATG CGC GGC TGC CGC GGC GGC-3'). The *nqo5* gene (Pden_2248) is found on chromosome 2 at nucleotide positions 2250063 to 2250689. The DNA cassette was designed containing two sequences homologous to flanking regions either side of the Nqo5 subunit C-terminus (**Figure 4.5A+B**). The first flanking region (F1) contained *nqo4* and included the STOP codon of *nqo5*, giving a total length of 1295 bp. Directly following this, the 36 bp sequence encoding the His_6Ala_6-tag was inserted (between nucleotide positions 2250065 and 2250066). The rest of the *nqo5* sequence followed until nucleotide position 2251760. This was the second homologous flanking region (F2) and was 1695 bp in length. Attached to F2, a kanamycin resistance gene was included (815 bp). As before, two *Eco*RI restriction sites were included at the beginning and end of the whole construct and internal *Eco*RI restriction sites were edited out by changing the glutamic acid codon from GAA to GAG.

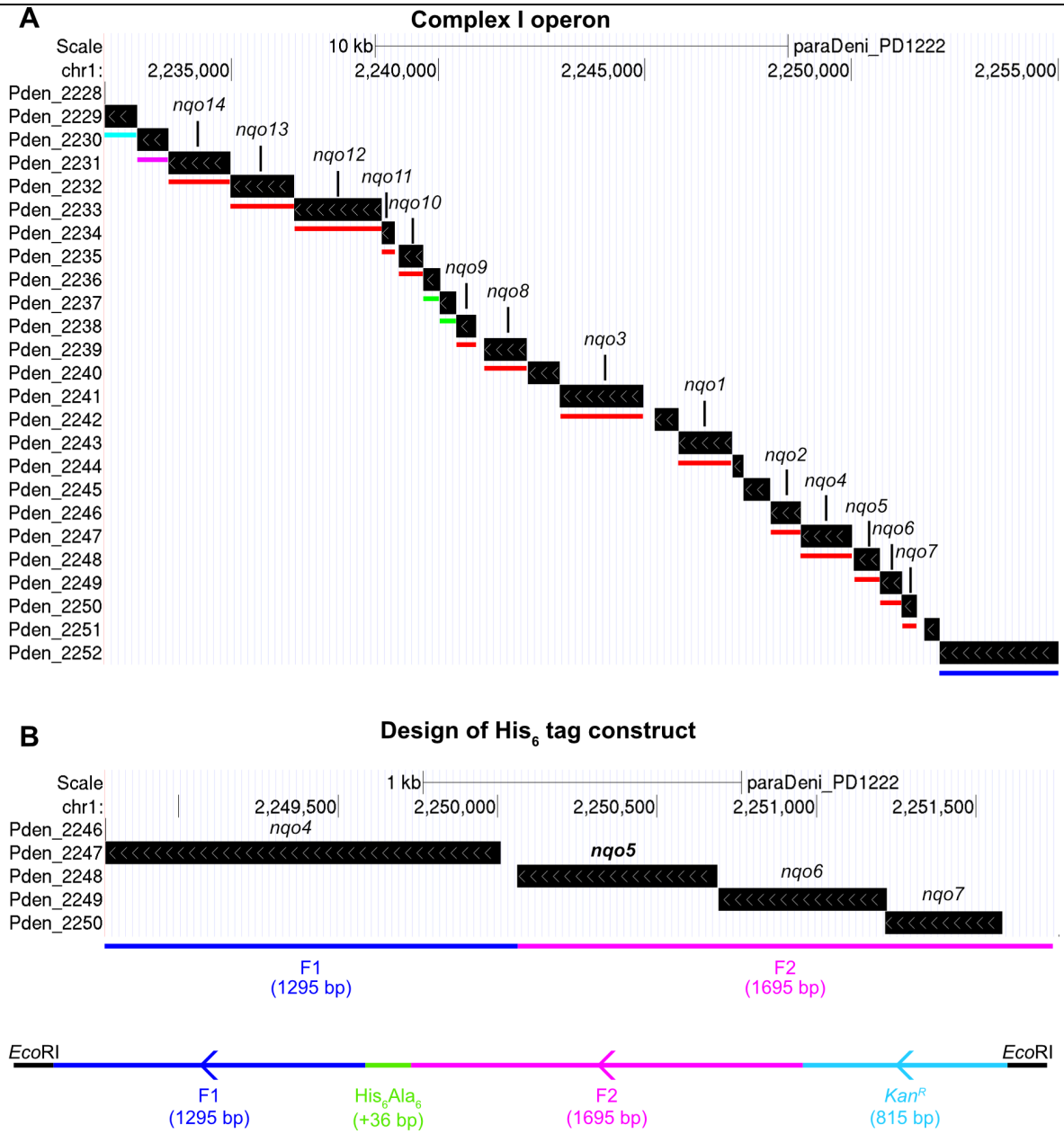

Figure 4.5. (A) Genome map of *P. denitrificans* showing the whole complex I operon created in USCS Microbial Genome Browser at chromosome 1 positions 2231939 to 2255008. White arrows show the direction of transcription. Genes encoding complex I subunits are labelled and coloured red. Other genes in the operon encode the following proteins: exinuclease ABC subunit A (blue), carboxymuconolactone decarboxylases (green), biotin-acetyl-CoA-carboxylase ligase (magenta) and pantothenate kinase (cyan). Genes not labelled encode conserved proteins with unknown function. (B) Design of the construct for adding a purification tag to the C-terminus of Nqo5. The genome map surrounding the *nqo5* gene is expanded to show where the homologous flanking regions were designed; flanking region F1 (blue) and flanking region F2 (magenta). The designed construct is shown at the bottom. The DNA encoding His_6Ala_6-tag was inserted between the flanking regions (green) and a Kan^R gene (cyan) was included after F2. *Eco*RI sites were added to both ends of the construct (black). The lengths of each sequence are indicated.

4.4.2. Insertion of His_6-tag onto the Nqo5 subunit

The designed construct (**Figure 4.6A**) was synthesised by GENEWIZ® and ligated into the pRVS1 vector pre-digested with *Eco*RI. The product was first transformed into NEB 5-α for replication and the purified plasmid then transformed into MFD*pir*, with successful colonies identified by resistance to kanamycin, and subsequent PCR amplification of the construct (**Figure 4.6B+C**).

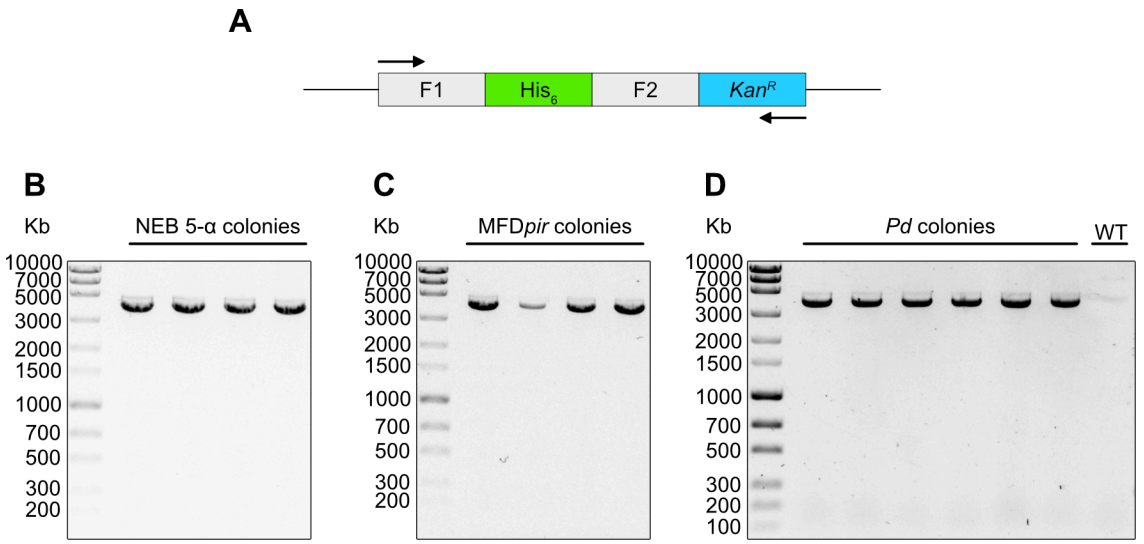

Figure 4.6. Screening for colonies that have successfully taken up the His_6-tag construct at each stage. (A) Depiction of where primers bind on the construct to screen for its presence by PCR and gel electrophoresis. (B) Colony PCR screening for the His_6 construct inserted into pRVS1 and maintained in NEB 5-α cells. (C) Colony PCR screening for the presence of the His_6 construct in MFD*pir* conjugative donor strain. (D) Colony PCR screening of *P. denitrificans* cells that have integrated the His_6 construct by undergoing a single recombination event at either F1 or F2. No construct was present in the wild-type control, where cells were not exposed to bacterial conjugation.

A similar conjugation and homologous recombination protocol to that described in Section 3.5 (Chapter 3) was followed but, importantly, at all stages 10 mM taurine was included in all media to induce expression of NDH-2 in *P. denitrificans.* The His_6-tag is not expected to kill complex I activity, but NDH-2 was expressed as a precaution for any disruption to the complex I operon during homologous recombination, which could prevent successful mutagenesis. A depiction of the events leading to the unmarked insertion of the His_6 construct into the *P. denitrificans* genome by homologous recombination is shown in **Figure 4.7**. *P denitrificans* colonies were screened for the plasmid integration or first recombination using primers binding to the end of the constructs (**Figure 4.6A+D**). All colonies screened showed a single band of the expected size for the construct and no band was present for cells not conjugated with MFD*pir*.

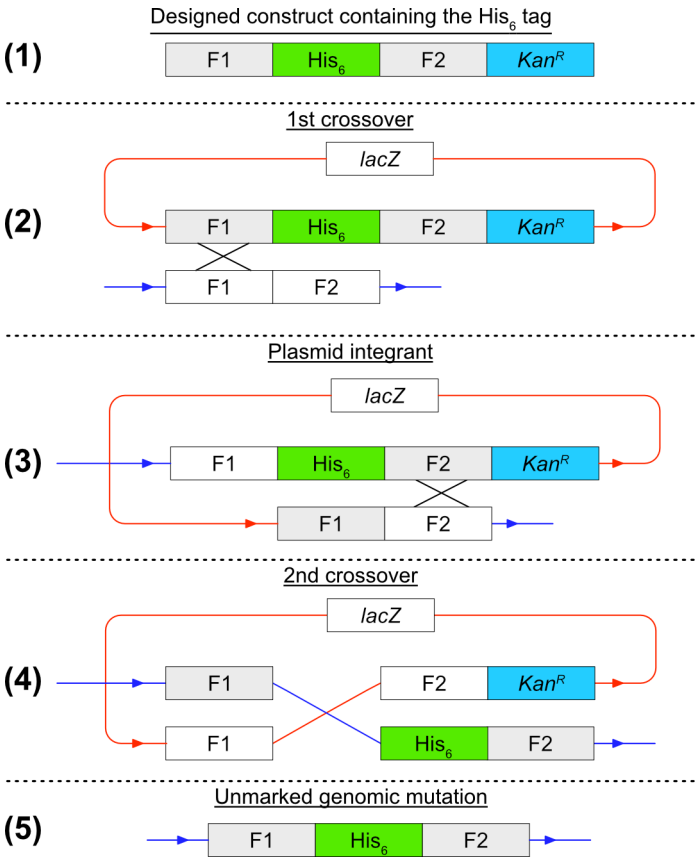

Figure 4.7. Depiction of events that occur during homologous recombination to insert the His_6-tag into the *P. denitrificans* genome. (1) DNA construct designed with the His_6-tag DNA sequence flanked by two regions of sequence homologous to the point of genomic insertion (F1 and F2). A kanamycin resistance gene is included following F2. (2) To be maintained, the plasmid integrates itself into the bacterial genome by undergoing a first recombination event at one of the homologous flanking regions (first crossover). (3) Plasmid integrant strain, which confers kanamycin resistance to *P. denitrificans*. (4) The second recombination event may occur (second crossover), resulting in the insertion of the His_6 tag and the loss of the plasmid and kanamycin resistance. Loss of the *lacZ* gene also occurs, which can be screened for using X-gal and blue-white screening. (5) The unmarked insertion of the *P. denitrificans* genome.

The second recombination event was monitored by blue-white screening, as described in Section 3.5 (Chapter 3). White colonies were identified and assayed for successful recombination by two separate PCR reactions and DNA gel electrophoresis. The first reaction amplified the region surrounding and including the His_6-tag, and the second reaction used a primer that binds to the sequence encoding the His_6-tag, which would only be present if the tag had been successfully inserted into the genome. Multiple colonies (50) were screened with most reverted to wild type instead of undergoing the second recombination event. Three colonies had successfully recombined and inserted the His_6-tag onto the C-terminus of the Nqo5 subunit (**Figure 4.8**). This strain is denoted as *Pd*-Nqo5^{His6} for the rest of this chapter. The whole complex I operon (spanning ~18 kb was sequenced to ensure there were no other mutations in the sequence. This ensured the complex I sequence (excluding the His_6-tag)

could be considered 'wild type' and future mutagenesis studies had a fully sequenced parental strain to compare with. The data confirmed the integrity of the *Pd*-Nqo5^{His6} strain.

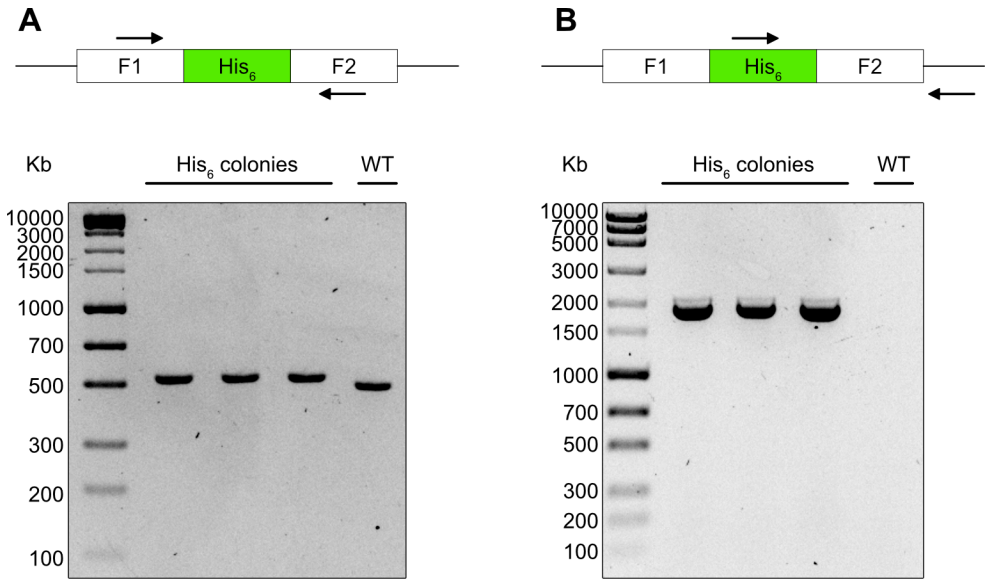

Figure 4.8. PCR reactions of *P. denitrificans* colonies that had successfully recombined and incorporated the His_6-tag into the cell genome. (A) PCR reaction where primers bind 250 bp upstream and downstream of the point of His_6 insertion, as shown by the schematic. The small increase in size of the PCR product in the His_6 colonies compared to the wild-type colonies is evident. (B) PCR reaction where the first primer binds to the His_6-tag encoding sequence and the second primer to the genomic DNA downstream of the construct, which is not included in the construct. A PCR product can be seen in the DNA gel for successfully recombined His_6 colonies but not for wild-type colonies.

4.5. Characterisation of the *Pd*-Nqo5^{His6} strain

4.5.1. Confirming translation of the His_6-tag

To confirm the presence of the His_6-tag on the Nqo5 subunit of complex I, SBPs for the *Pd*-Nqo5^{His6} and wild-type strain were prepared and SDS-PAGE was performed, followed by western blot analysis for the His_6-tag. Proteins separated by SDS-PAGE were transferred to a membrane and blotted against an anti-His_6 primary antibody followed by incubation with an HRP-conjugate anti-rabbit IgG secondary antibody. Chemiluminescence of the membrane was detected after addition of ECL Prime reagent. A single band just below 25 kDa can be seen in the *Pd*-Nqo5^{His6} strain, corresponding to the molecular weight of Nqo5 (23.9 kDa). This band was absent in the wild-type SBPs and confirmed the His_6-tag was correctly expressed and present (**Figure 4.9A**).

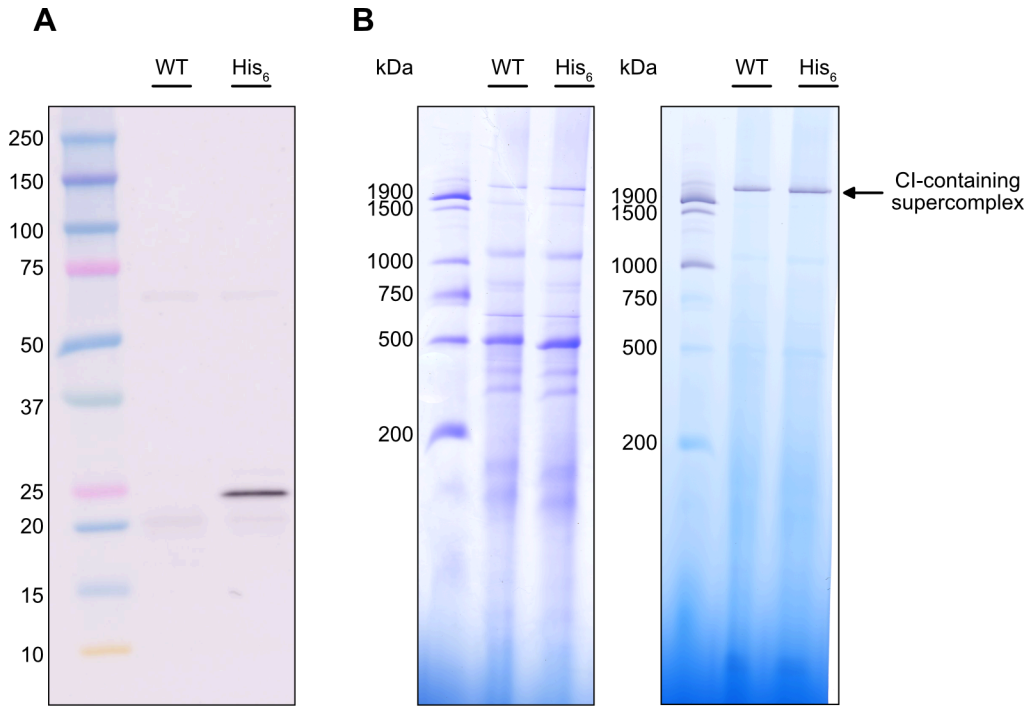

Figure 4.9. Identification of the expression and correct assembly of complex I in the *Pd*-Nqo5^{His6} strain (A) Wild-type and *Pd*-Nqo5^{His6} SBPs analysed by SDS-PAGE and blotted for the presence of the His_6-tag. The tag is clearly present only in the *Pd*-Nqo5^{His6} strain. (B) BN-PAGE of SBPs solubilised in LMNG showing a similar band pattern between wild-type and *Pd*-Nqo5^{His6} SBPs. Complex I-containing supercomplexes are seen in both strains in the topmost band in the gel. The gels are stained using Coomassie (left) or for complex I in-gel activity using nitroblue tetrazolium (NBT), which reacts with the complex I flavin site (right). The complex I (CI)-containing supercomplex shows in-gel NADH oxidation activity and is highlighted by the arrow. Bovine membranes solubilised in digitonin are shown for size comparison on the left-hand lane.

To determine whether the His_6-tag disrupted assembly of complex I, BN-PAGE analyses of detergent-solubilised SBPs was performed. Unfortunately, isolated complex I from *P. denitrificans* is known to dissociate during the mild electrophoretic conditions of BN-PAGE and so it can only be visualised as part of a supercomplex (Stroh et al., 2004). To confirm that complex I was still associated with the supercomplex, and thus probably fully assembled, SBPs were solubilised in lauryl maltose neopentyl glycol (LMNG) detergent at a 2:1 ratio of detergent to protein (w/w). The conditions solubilise *P. denitrificans* supercomplexes but do not extract the isolated complex I from the supercomplex. Supercomplex formation could be seen in BN-PAGE analyses for both wild-type and *Pd*-Nqo5^{His6} strains suggesting that the His_6-tag did not disrupt complex I assembly and/or supercomplex assembly and so the enzyme remained structurally intact (**Figure 4.9B**).

4.5.2. Catalytic activity of *Pd*-Nqo5^{His6} complex I

The *Pd*-Nqo5^{His6} strain did not require NDH-2 expression to grow, suggesting that its complex I was still functional. To probe the activity of the complex I, SBPs were prepared for both the wild-type and *Pd*-Nqo5^{His6} strains, and the flavin site (NADH:APAD$^+$) and Q-reductase (NADH:O_2) activities were compared. As seen in Chapter 3, independent SBP preparations often differ in terms of their purity, membrane coupling and protein content. For comparison here, it is assumed that the flavin site activity is unaffected by introduction of the His_6-tag and that NADH:APAD$^+$ activity could be used as a relative measure for the amount of complex I present. The *Pd*-Nqo5^{His6} strain showed lower NADH:O_2 activity than the wild-type strain but this was accompanied by a lower NADH:APAD$^+$ activity (**Table 4.1**). Normalisation of the Q-reductase activities, using the relative complex I content between strains (the NADH:APAD$^+$ ratio), showed that the *Pd*-Nqo5^{His6} strain appeared to be more active than wild type. However, additional SBP preparations would be required to show where this result lies with respect to the biological error between sample preparations. Importantly, these data suggested a fully functional and intact complex I. Both strains were 95-98% sensitive to piericidin A showing NDH-2 expression was strictly repressed in both strains, further emphasising the benefit of the NDH-2 expression system developed earlier in this chapter (Section 4.3).

Table 4.1. Table of activities for wild-type and *Pd*-Nqo5^{His6} SBPs. The NADH:O_2 activities for each strain are shown, including the *Pd*-Nqo5^{His6} strain after normalisation to the relative complex I content between WT and *Pd*-Nqo5^{His6} strains. Normalisation was performed by dividing the NADH:O_2 activities by the relative NADH:APAD$^+$ rates. Rates reported as averages ± S.E.M.

Catalytic reaction / µmol min^{-1} mg^{-1}	**WT**	***Pd*-Nqo5^{His6}**	***Pd*-Nqo5^{His6} (normalised)**
NADH:O_2 (coupled)	0.869 ± 0.003	0.669 ± 0.013	1.061 ± 0.030
NADH:O_2 (uncoupled)	1.746 ± 0.022	1.272 ± 0.016	2.017 ± 0.048
NADH:O_2 + Piericidin A	0.040 ± 0.001	0.032 ± 0.001	0.051 ± 0.002
NADH:APAD$^+$	0.306 ± 0.006	0.193 ± 0.001	–

4.6. Purification of complex I from *P. denitrificans*

A strategy was developed to isolate complex I from *P. denitrificans* membranes via the His_6-tag. Membranes were chosen rather than SBPs as they are easier to prepare in large quantities. To prepare membranes from *P. denitrificans* cells a protocol developed by Yip and co-workers was followed with minor alterations, including replacing the Bis-Tris buffering component with MES (at the same pH) (see Section 2.3.2, Materials and Methods) (Yip et al., 2011). A three-step strategy to isolate and purify complex I was then devised, which included

solubilisation of the membrane proteins followed by Ni-affinity and size-exclusion chromatography.

4.6.1. Solubilisation of *P. denitrificans* membranes

Suitable conditions were established for the solubilisation of complex I, to maximise the yield of isolated enzyme without compromising its stability/activity and limiting protein aggregation. The only published protocol solubilised *P. denitrificans* membranes for four hours (Yip et al., 2011), an excessive length of time compared to other organisms (30 min for mouse (Agip et al., 2018), 20 min for bovine (Sharpley et al., 2006), 5 min for *Y. lipolytica* (Kashani-Poor et al., 2001) and 1 hour for *E. coli* (Sazanov et al., 2003)). Excessive exposure to high concentrations of detergent could be detrimental to protein stability and prolongs the total preparation time. To determine a more appropriate solubilisation time, membranes were treated with DDM (3:1 DDM to protein (w/w)) for increasing periods and the total soluble protein content and NADH:APAD$^+$ activity, to assess the protein integrity, were compared (**Figure 4.10**). The results show that a long four-hour solubilisation decreases activity over time without substantial benefit to the yield and that sufficient solubilisation could be achieved much faster, greatly speeding up the purification process.

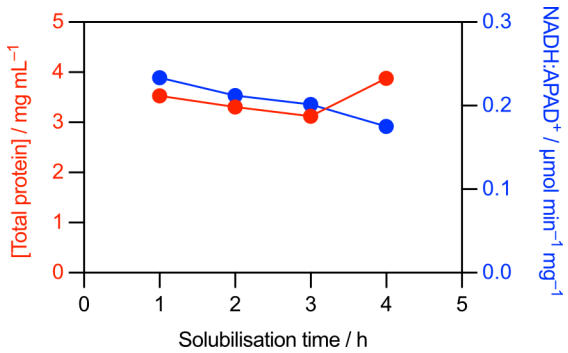

Figure 4.10. Solubilisation of *P. denitrificans* membranes for different lengths of time. Solubilisation buffer included 20 mM Bis-Tris-propane pH 6.5, 10% glycerol, 10 mM $CaCl_2$, 100 mM NaCl, 1.2% DDM (3:1 DDM to protein). (A) The concentration of total protein in the soluble fraction, as measured by BCA, and the NADH:APAD$^+$ specific activity for complex I after different solubilisation times are shown in red and blue, respectively.

The final solubilisation conditions taken forward were 30 min at 4 ˚C in buffer containing 20 mM MES pH 6.5 at 4 ˚C, 100 mM NaCl, 5 mM $CaCl_2$, 10% (v/v) glycerol, 0.002% (v/v) PMSF, 2.85% (w/v) DDM (3:1 DDM to protein). The isolated (solubilised) *P. denitrificans* complex I is stabilised by $CaCl_2$ and glycerol, hence these were included in the solubilisation and chromatography steps where appropriate (Yip et al., 2011). Furthermore, a buffer pH of 6.0–

6.5 was shown to be optimum for stability for both *P. denitrificans* and *E. coli* enzymes, so buffers were all titrated to pH 6.5 (Sazanov et al., 2003). Notably, the optimal pH for the purification for mammalian complex I (pH of 7.5) differs from the bacterial enzyme.

4.6.2. Ni-affinity chromatography

Solubilised *P. denitrificans* membranes were separated from the insoluble fraction by centrifugation and purified by Ni-affinity chromatography (HisTrap), enabling the separation of the His_6-tagged complex I from other solubilised proteins (**Figure 4.11**). The supernatant was loaded onto the column and the protein washed in buffer containing 80 mM imidazole. Complex I and any other strongly bound proteins were then eluted with 200 mM imidazole. The wash and elution buffers were supplemented with 0.02% (w/v) asolectin and 0.02% (w/v) CHAPS to supply lipids to help stabilise the complex, as this has been shown to improve the activity of both bovine and *Y. lipolytica* purified samples (see Section 2.3.3) (Parey et al., 2018; Sharpley et al., 2006). The buffers also contained $CaCl_2$ and glycerol to provide stability to complex I.

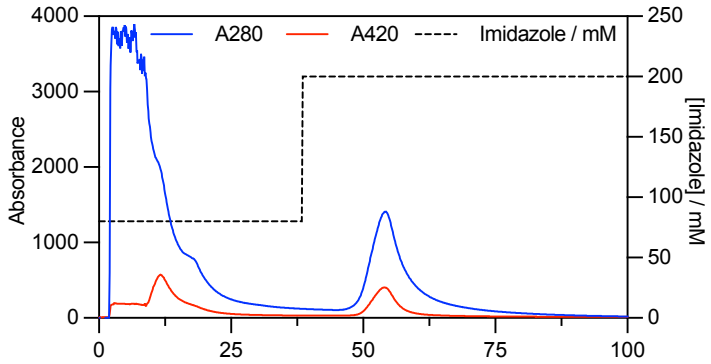

Figure 4.11. Example elution profile for Ni-affinity chromatography of *P. denitrificans* complex I. Solubilised membrane supernatant was loaded onto a HP HisTrap column and washed with 80 mM imidazole. Complex I was eluted with 200 mM imidazole. Imidazole concentrations shown by dotted line. The absorbance at 280 nm and 420 nm were monitored, indicating protein elution.

4.6.3. Size-exclusion chromatography

The protein gathered after Ni-affinity chromatography was clearly contaminated, as there was a strong green colour indicative of cytochrome *c* oxidase. Size-exclusion chromatography was then performed to separate the intact complex I (596 kDa) from the smaller oxidase (131 kDa) (**Figure 4.12**). The fractions eluted from the HisTrap were concentrated and loaded onto a pre-equilibrated Superdex 200 increase gel filtration column. The first peak, which showed flavin site activity and was thus identified as complex I, was well separated from the large amount of contaminating complex IV. It eluted at the volume expected for intact complex I from *P.*

denitrificans, as predicted from the eluted volumes of standard proteins given in the manufacturer's guide (Cytiva).

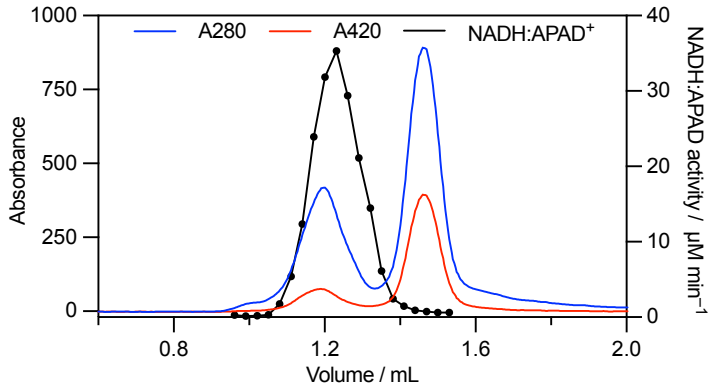

Figure 4.12. Example elution profile for size-exclusion chromatography of *P. denitrificans* complex I. Pooled fractions from the Ni-affinity chromatography step were concentrated to roughly 100 µL and loaded onto a pre-equilibrated Superdex 200 increase 5/150 GL. Proteins were separated at a flow rate of 0.05 mL min^{-1} in column buffer containing 20 mM MES (pH 6.5 at 4 ˚C), 150 mM NaCl, 10 mM $CaCl_2$, 10% glycerol and 0.1% DDM. The absorbance at 280 nm and 420 nm were monitored indicating protein elution of complex I (first peak) and complex IV (second peak). The NADH:$APAD^+$ activity at 32 ˚C was measured in each protein-containing 30 µL fraction. Each assay contained 0.5 µL of the fraction, 100 µM NADH, 500 µM $APAD^+$ and was measured in a buffer containing 10 mM MES (pH 6.5 @ 32 ˚C), 25 mM NaCl, 2 mM $CaCl_2$. The activity measurements are single-point reads.

4.7. Characterisation of isolated complex I from *P. denitrificans*

4.7.1. BN-PAGE of isolated complex I

The purity of the isolated complex I from *P. denitrificans* (*Pd*-CI) was first assessed by BN-PAGE analyses, which has been routinely used to characterise and assess the assembly of mitochondrial complex I from *Bos taurus* and *Y. lipolytica* (Bridges et al., 2017; Varghese et al., 2015). However, as previously mentioned, BN-PAGE treatment is too harsh for the isolated *P. denitrificans* complex I, which breaks apart during electrophoresis (Stroh et al., 2004). BN-PAGE experiments confirmed that the isolated enzyme, while stable in solution and eluting from the gel filtration step as expected for the 596 kDa fully intact complex, dissociates during electrophoresis, and multiple bands predicted to be complex I subcomplexes were observed (**Figure 4.13**). Treatment of the isolated complex with increasing concentrations of the crosslinker BS^3, which crosslinks primary amines within 11 Å of each other (see Section 2.4.6, Materials and Methods), resulted in the appearance of a band with complex I activity and the correct mass for the fully intact enzyme (**Figure 4.13**), concomitant with decreased intensities for the lower molecular weight bands. However, crosslinking the isolated enzyme in solution eliminated the complex I activity. It is curious that bands showed NADH activity staining in the

BN-PAGE but NADH:APAD$^+$ activity was reduced in crosslinked samples. Perhaps a low level of flavin site activity remains after crosslinking, which is sufficient to be visualised on the gel. As complex I activity was eliminated, crosslinking, at least with BS^3, was not a suitable method for improving the stability of the enzyme, even though increasing the stability could potentially be important for aiding downstream applications and structural analyses. Overall, these results suggested that, in solution, the isolated complex I is intact, but it remains unstable during the mild electrophoretic conditions of BN-PAGE. Thus, care must be taken during sample handling. In addition, BN-PAGE analyses are not suitable for determining the purity or the correct assembly of isolated complex I from *P. denitrificans*. Size-exclusion chromatography should be used instead for assessing the structural integrity of future complex I variants.

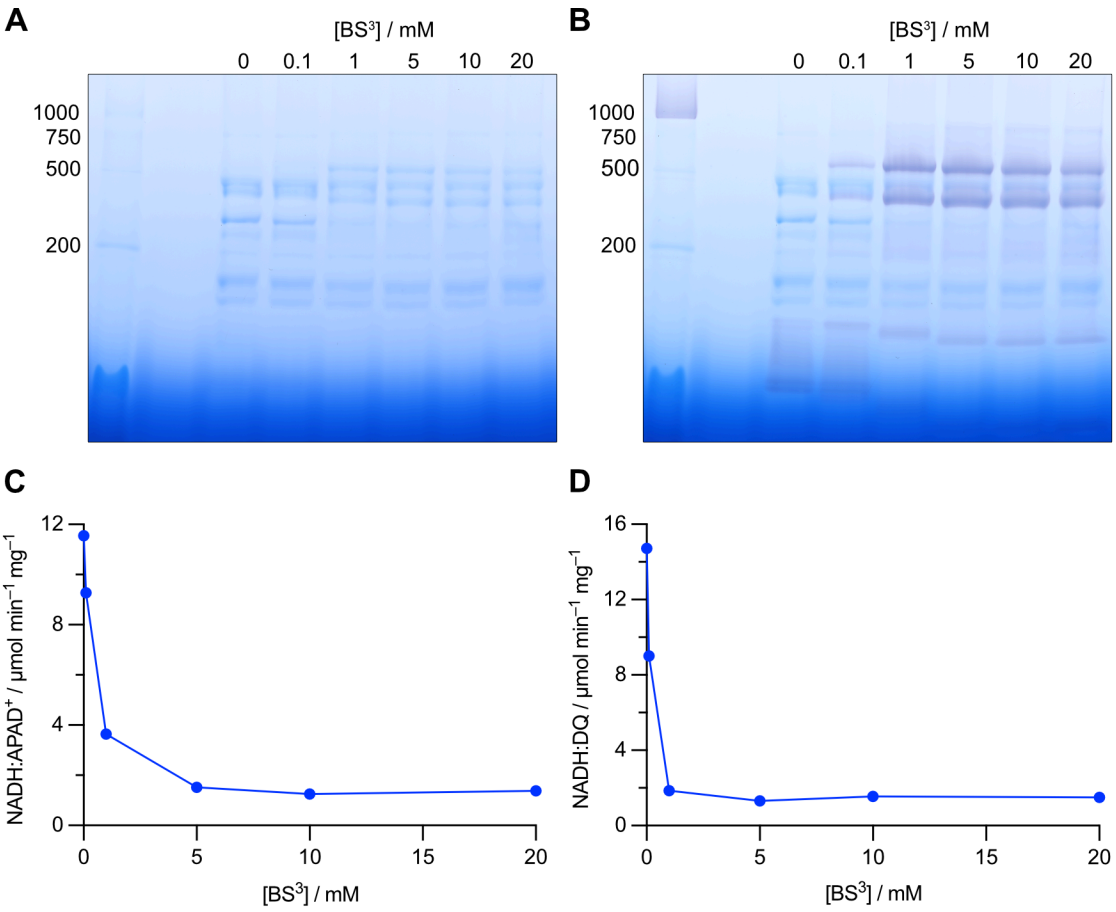

Figure 4.13. BN-PAGE analyses of *P. denitrificans* complex I (*Pd*-CI) treated with increasing concentrations of the crosslinker BS^3 with the gel imaged (A) without any staining and (B) with staining for complex I in-gel activity using NBT. (C) The NADH:APAD$^+$ activity of *Pd*-CI samples after incubation with increasing concentrations of BS^3. (D) The NADH:DQ activity of *Pd*-CI samples after incubation with increasing concentrations of BS^3.

4.7.2. Subunit composition and purity of isolated complex I

The purity and subunit composition of *Pd*-CI were investigated by SDS-PAGE analyses and mass spectrometry. Individual bands from the SDS-PAGE were excised and digested with trypsin. The resulting peptides were analysed by MALDI-TOF/TOF mass spectrometry and then assigned to complex I subunits (**Figure 4.14**, **Table 4.2**). A total of 12 of the 14 core subunits were identified, as well as the three supernumerary subunits previously observed in *Pd*-CI (PdN7BM, PdNUYM, PdNUMM) (Yip et al., 2011). Identifying subunits Nqo12, Nqo13 and Nqo8 was important for showing the complex was intact, because these distal subunits on the toe and heel of the membrane domain have been shown to dissociate easily (Efremov et al., 2010; Holt et al., 2003). No peptides were detected for subunits Nqo7 and Nqo11 which connect the hydrophobic and membrane domain of complex I. These subunits are probably missed from the analysis due to their small hydrophobic nature, which is typical for complex I mass spectrometry analysis (Bridges et al., 2017; Yip et al., 2011). Nevertheless, the isolated complex I appeared to be highly pure (all major bands were assigned to complex I) and correctly assembled. The mass spectrometry analyses also identified several additional proteins with varying degrees of confidence (**Table 4.2**). Most of these are probably minor contaminants and are unlikely to be associated with complex I, such as elongation factor Tu, transcription termination factor Rho and subunits from other respiratory complexes. A small number of other proteins were identified, notably a protein-L-isoaspartate O-methyltransferase (23.5 kDa), which cannot be excluded from or assigned to complex I using these data alone. Structural studies on the purified enzyme, as described in Chapter 5, revealed that protein-L-isoaspartate O-methyltransferase was in fact a subunit of the enzyme.

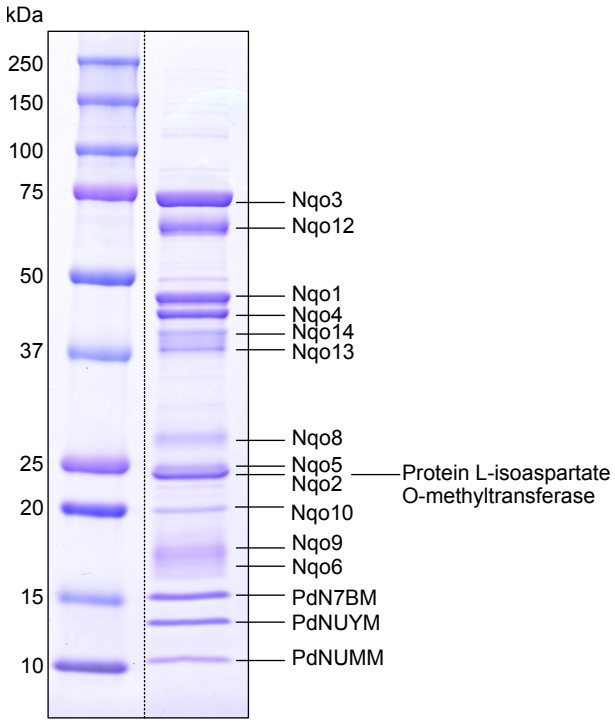

Figure 4.14. SDS-PAGE of purified *Pd*-CI. Individual complex I subunits were identified and assigned by excising each band, treating the sample with trypsin and analysing the resultant peptides by mass spectrometry. Peptides were assigned to a subunit/protein by peptide mass fingerprinting.

Table 4.2. Complex I subunits and proteins identified in *Pd*-CI. Complex I constituents were resolved by SDS-PAGE and protein bands were excised, digested with trypsin and peptides identified by MALDI-TOF/TOF mass spectrometry and assigned to a subunit/protein by peptide mass fingerprinting. The number of unique peptides identified with scores above the Mascot 95% confidence limit are shown along with the protein score and total Mascot MS/MS ion score for the protein.

		Peptide mass fingerprinting			Tandem MS	
Subunit/protein	**PRIDE/Pden number**	**Mascot score**	**Peptides (*n*)**	**Coverage (%)**	**Peptides (n)**	**Mascot MS/MS score**
Nqo1	A1B491/Pden_2243	228/50	9	19	3	182/21
Nqo2	A1B494/Pden_2246	368/50	5	27	4	278/22
Nqo3	A1B489/Pden_2241	657/50	13	16	7	453/21
Nqo4	A1B495/Pden_2247	244/50	5	14	3	225/21
Nqo5	A1B496/Pden_2248	124/50	2	17	1	110/22
Nqo6	A1B497/Pden_2249	337/50	6	29	5	210/21
Nqo7	A1B498/Pden_2250	n. d.	n. d.	n. d.	n. d.	n. d.
Nqo8	A1B487/Pden_2239	56/50	4	4	1	21/21
Nqo9	A1B486/Pden_2238	483/50	9	37	7	286/21
Nqo10	A1B483/Pden_2235	292/50	4	32	3	203/21

Nqo11	A1B482/Pden_2234	n. d.	n. d.	n. d.	n. d.	n. d.
Nqo12	A1B481/Pden_2233	646/50	8	18	8	473/21
Nqo13	A1B480/Pden_2232	112/50	4	7	2	82/21
Nqo14	A1B479/Pden_2231	240/50	4	14	4	167/21
PdN7BM	A1B1H8/Pden_1267	513/50	4	63	4	420/21
PdNUYM	A1B1M0/Pden_1309	436/50	8	70	5	318/21
PdNUMM	A1B357/Pden_1854	149/50	4	56	2	74/21
Transcription termination factor Rho	A1AXX5/Pden_0002	257/50	2	10	2	233/21
Protein-L-isoaspartate O-methyltransferase	A1B5L6/Pden_2726	152/50	2	20	2	129/21
Elongation factor Tu	A1B002/Pden_0734	105/50	1	4	1	105/21
Glutamine–fructose-6-phosphate aminotransferase	A1AZN7/Pden_0619	50/50	3	2	1	44/21
cytochrome b	A1B4F3/Pden_2306	35/50	1	4	1	35/21
Ubiquinol-cytochrome c reductase iron-sulfur subunit	A1B4F2/Pden_2305	43/50	2	4	1	30/21
Type I secretion target repeat protein	A1B5Q1/Pden_2761	28/50	1	2	1	28/21
Sulfate adenylyltransferase subunit	A1BAB5/Pden_4395	22/50	1	5	1	22/20
Uncharacterised protein	A1AY62/Pden_0089	22/50	1	2	1	21/21

4.7.3. EPR characterisation of purified complex I

To investigate the electron transfer pathway in *Pd*-CI and compare it to its mitochondrial counterpart, electron paramagnetic resonance (EPR) spectroscopy was performed. EPR sample preparation, measurements and analyses were performed by Dr John Wright (MRC Mitochondrial Biology Unit, Cambridge). Previous EPR studies of complex I from *P. denitrificans* have been limited to membrane particles, which makes deconvolution of the complex I-specific signals difficult (Albracht et al., 1980; Kotlyar et al., 1998; Meinhardt et al., 1987). Here, the EPR spectra of the purified enzyme could be measured. *Pd*-CI was treated with NADH to reduce the FeS clusters and EPR spectra were measured at different temperatures (**Figure 4.15A**). The spectra clearly show the presence of four reduced FeS clusters (N1b, N2, N3 and N4), confirming the integrity of the hydrophilic domain in the purified enzyme. A single axial FeS cluster can be seen at 40 K corresponding to the slow-relaxing [2Fe-2S] N1b. As the temperature is decreased, additional [4Fe-4S] FeS signals appear in

accordance with the established relaxation properties for mammalian complex I (N1b < N2 < N3 < N4) (Ohnishi, 1998; Reda et al., 2008). At 7 K, the FeS signals from N2 and N4 are largely saturated. Previously, overexpression of the *P. denitrificans* Nqo3 (NDUFS1) subunit in *E. coli* has given rise to a signal attributed to the fast-relaxing N5 cluster (Yano et al., 2003); however, no signal for this cluster was observed during these experiments as high power and low temperature are typically required to resolve its signal.

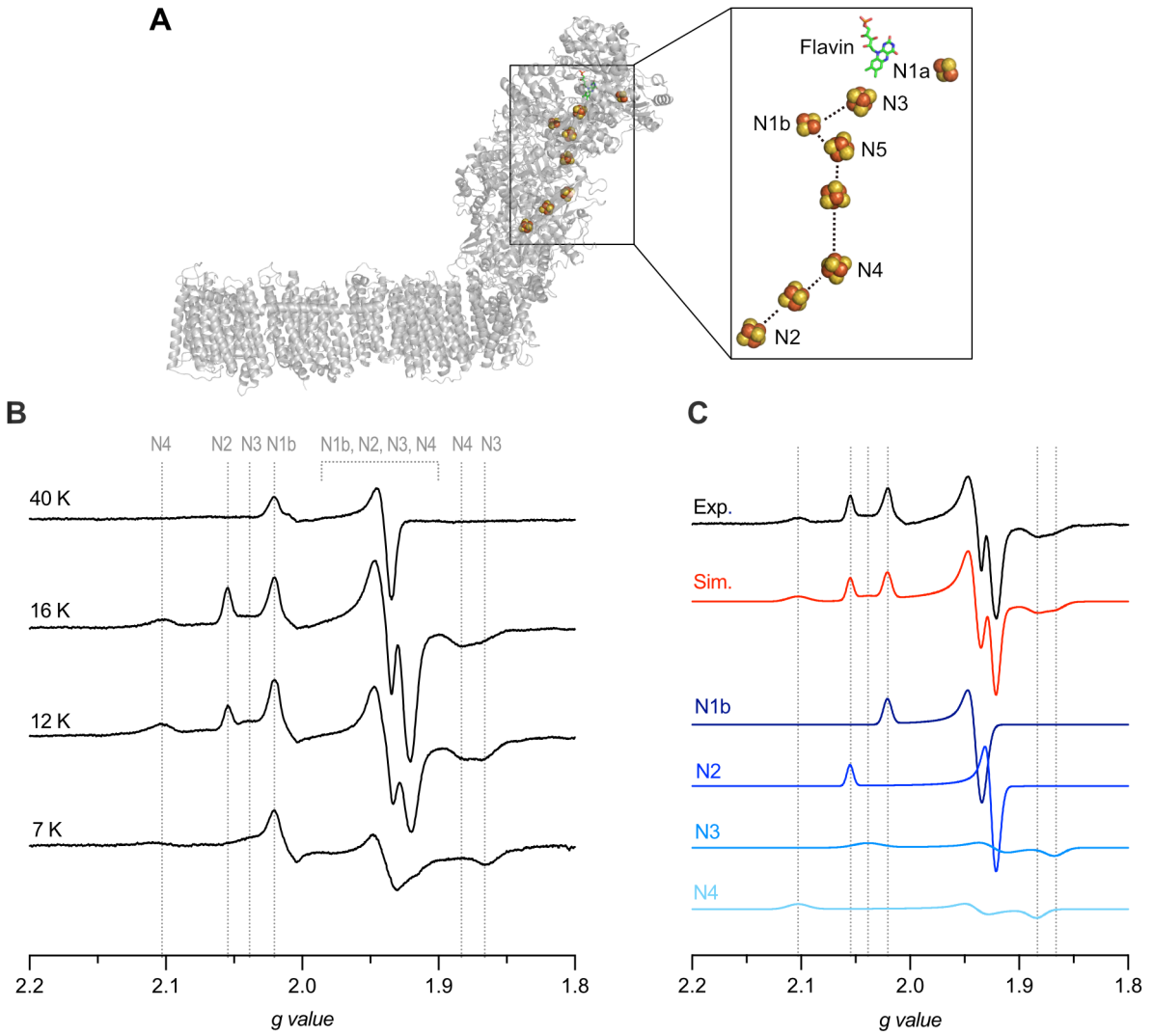

Figure 4.15. EPR spectra of NADH-reduced *Pd*-CI. (A) Depiction of the FeS clusters in complex I from *T. thermophilus*. Clusters detected by EPR are labelled. (B) Complex I (5.8 mg mL^{-1}) was reduced anaerobically with 15 mM NADH. EPR spectra were recorded at 100 kHz modulation frequency with a modulation amplitude of 7 G and a microwave power of 2.02 mW at the temperatures indicated. Vertical lines correspond to the *g* factors for the individual FeS clusters. (C) Simulation of the EPR spectrum of purified *Pd*-CI at 16 K. The total simulation of the combined FeS cluster signals is shown in red, with the individual simulations labelled according to each cluster. FeS clusters N1b, N2, N3 and N4 were simulated at a 1:1 ratio. Simulation parameters are given in **Table 4.3**.

Table 4.3. EPR simulation parameters for the *Pd*-CI FeS clusters.

Cluster	g_x	g_y	g_z
N1b	1.936	1.939	2.021
N2	1.923	1.924	2.055
N3	1.867	1.924	2.039
N4	1.884	1.939	2.103

The measured *Pd*-CI EPR spectrum recorded at 16 K was simulated, showing an equal stoichiometry for the four reduced clusters (**Figure 4.15B**). This 'signature' spectrum for *Pd*-CI is remarkably similar to that observed for mitochondrial complex I from *Y. lipolytica*, which could also be simulated with an equal stoichiometry for the same four reduced clusters (Djafarzadeh et al., 2000). In contrast, mammalian complex I exhibits sub-stoichiometric reduction of N1b when reduced with NADH, owing to its low reduction potential (Reda et al., 2008). In *E. coli* the N3 cluster is reduced sub-stoichiometrically by NADH, whereas it is fully reduced in both mitochondrial and *Pd*-CI (De Vries et al., 2015; Verkhovskaya et al., 2008).

In addition, the [2Fe-2S] cluster in Nqo2 (NDUFV2), referred to as N1a, is not reduced in NADH-treated samples of *Pd*-CI or in the mammalian and yeast complexes. In contrast, *E. coli* complex I spectra show N1a is a high potential cluster, which is reduced during turnover. In *P. denitrificans* the EPR signal for N1a has so far only been observed when Nqo2 was overexpressed and reduced with sodium dithionite. The N1a cluster displays characteristic *g* values of 2.00, 1.94 and 1.9253, but these are clearly not present in the *Pd*-CI EPR signals here (Zu et al., 2002). The absence of the reduced N1a signal in *Pd*-CI is consistent with the N1a reduction potential being below that of NADH (Birrell et al., 2013; Zu et al., 2002) and with data on mammalian complex I that show N1a can only be reduced by dithionite in the flavoprotein subcomplex and not in the intact enzyme (Barker et al., 2007; Birrell et al., 2013; Reda et al., 2008). Hence, the pattern of FeS cluster reduction and the properties of the N1a cluster establish a close similarity between *Pd*-CI and mitochondrial complex I and further highlight the suitability of *P. denitrificans* as a model for the mitochondrial enzyme, especially in comparison to the *E. coli* enzyme.

4.7.4. Activity of purified complex I from *P. denitrificans*

To assess the integrity and catalytic competence of the purified enzyme, the catalytic activity was measured. First, the assay buffer was optimised for the purified enzyme. As expected, based on the conditions required for purification and prior optimisation work for both the *P.*

denitrificans and *E. coli* enzymes (Sazanov et al., 2003; Yip et al., 2011), the enzyme activity was seen to be highest in buffer at pH 6.5 and in the presence of divalent cations Ca^{2+} and Mg^{2+} (**Figure 4.16**). The Ca^{2+} ions increase activity to a greater extent than Mg^{2+} ions. The addition of sucrose to the assay buffers to create a more hypertonic solution had no effect. Based on these data the final assay buffer consisted of 10 mM MES pH 6.5, 2 mM $CaCl_2$, 25 mM NaCl, the same as used by Yip et al. (2011).

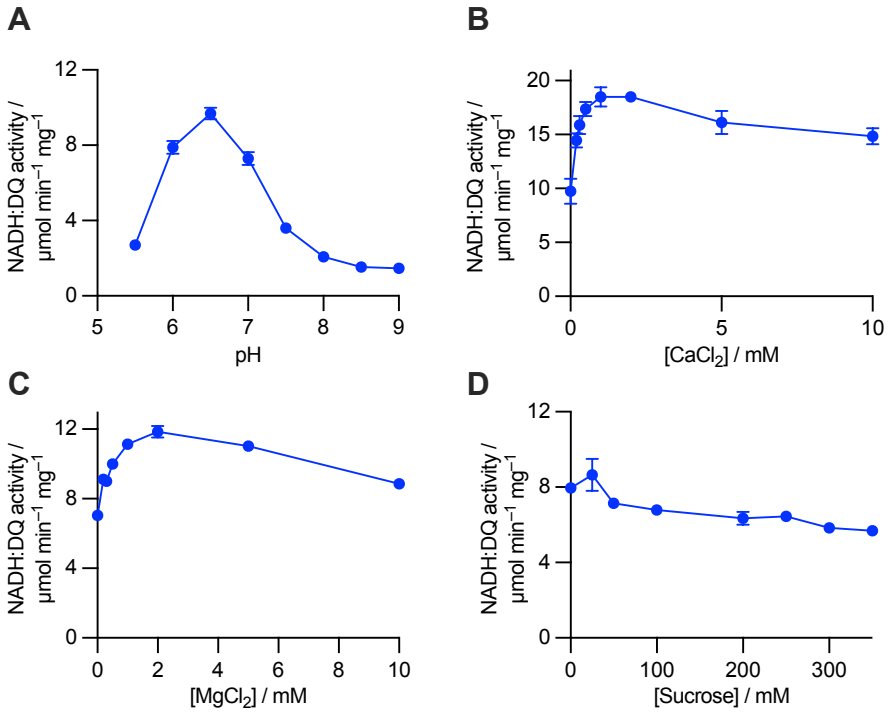

Figure 4.16. Optimisation of buffer conditions for measuring *Pd*-CI activity. Assays contained a mixed buffer of 5 mM MES and 5 mM Bis-Tris propane titrated to various pH values. The buffer also contained 25 mM NaCl in all cases. For the titration of cations and sucrose, the buffer was at pH 6.5. (A) pH dependence of complex I. (B) $CaCl_2$ titration in pH 6.5 buffer. (C) $MgCl_2$ titration in pH 6.5 buffer. (D) Sucrose titration in pH 6.5 buffer in the absence of divalent cations. Data points show average NADH:DQ activity for three technical replicates ± S.E.M.

Under these optimised assay conditions, *Pd*-CI was able to catalyse the reduction of 200 µM decylubiquinone (DQ) by NADH at rates of 21.9 ± 4.2 µmol min^{-1} mg^{-1} (~204 s^{-1}, S.D. from 11 independent purifications). For comparison, the purified bovine, ovine and *Y. lipolytica* enzymes have been reported to catalyse the reduction of 200 µM DQ at 22.2–24.7 µmol min^{-1} mg^{-1} (~390 s^{-1}) (Blaza et al., 2018), 5–6 µmol min^{-1} mg^{-1} (~90 s^{-1}) (Kampjut and Sazanov, 2020) and 13.9 µmol min^{-1} mg^{-1} (~208 s^{-1}) (Parey et al., 2018), respectively, and the bacterial enzyme from *E. coli* to catalyse reduction of 100 µM DQ at 20–25 µmol min^{-1} mg^{-1} (~206 s^{-1}) (Sazanov et al., 2003; Verkhovsky et al., 2012). Hence, the preparation of *Pd*-CI appears to be highly active, with rates similar to purified of complex I from other species.

To estimate the highest possible activity that may be achieved for purified enzyme, activities were compared between the membrane and soluble forms of the enzyme. The membranes and isolated enzyme were able to catalyse flavin-catalysed NADH:APAD$^+$ oxidoreduction at 0.497 ± 0.015 μmol min^{-1} mg^{-1} and 9.98 ± 0.05 μmol min^{-1} mg^{-1}, respectively (S.E.M. of three technical replicates). By making the assumption that the flavin site activity is fully retained during purification, and that the NADH:APAD$^+$ activity in the membrane comes solely from complex I, the complex I content of the membranes was estimated at 5.0 ± 0.2% (by protein mass). Based on this estimation, the Q-reductase activity of native *Pd*-CI in the membranes was calculated. The membranes were able to catalyse Q reduction at 2.02 ± 0.09 μmol min^{-1} mg^{-1}, which translates to an estimated complex I Q-reductase activity of 40 ± 2 μmol min^{-1} mg^{-1}. Hence, the rate of DQ reduction in the purified enzyme (21.9 ± 4.2 μmol min^{-1} mg^{-1}) suggests that 54 ± 11% of the Q-reductase activity is retained during enzyme preparation. It is worth noting that greater activities may be observed at higher concentrations of DQ, or by using the native Q_{10} as the electron acceptor. Overall, these data provide clear evidence that the preparation of *Pd*-CI is highly active for NADH:ubiquinone oxidoreduction.

4.7.5. Titration of soluble quinone analogues and inhibitors

To assess the suitability of soluble quinone analogues as a substrate for *Pd*-CI, the activities with DQ and Q_1 were compared for the same preparation (**Figure 4.17A**). *Pd*-CI was able to catalyse DQ at higher rates than Q_1, but neither electron acceptor was a good substrate for *Pd*-CI as both exhibited high K_M values (169 ± 15 μM and 124 ± 8 μM for DQ and Q_1, respectively). It is also worth noting that DQ and Q_1 have limited solubility in aqueous solution and so activities recorded at high substrate concentrations are not accurate. Due to their tendency to aggregate and form micelles at high concentrations, a standard concentration of 200 μM DQ is used for comparisons.

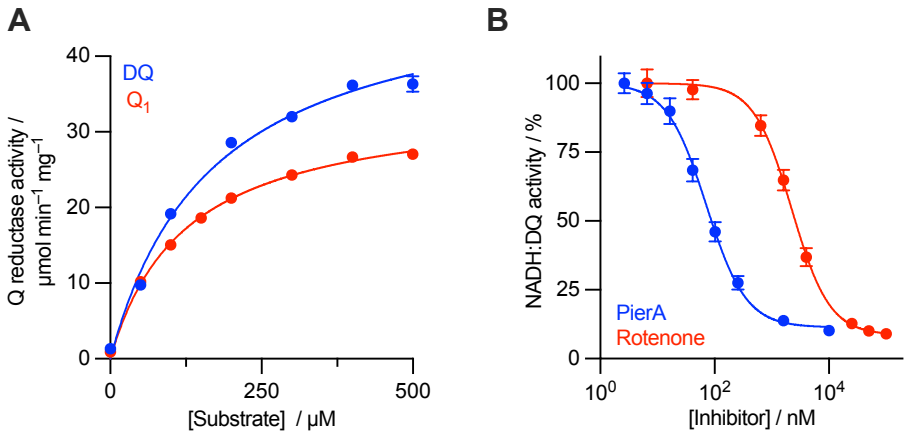

Figure 4.17. Characterisation of purified complex I from *P. denitrificans*. (A) K_M curve for DQ and Q_1 substrates for a typical sample of soluble complex I. The K_M values for DQ and Q_1 are 169 ± 15 and 124 ± 8 µM, respectively (± S.E. of the fit). (B) Piericidin A and rotenone IC_{50} titration curves for soluble complex I, using 200 µM DQ as the substrate. The IC_{50} values of piericidin A and rotenone are 72 ± 7 nM and 2226 ± 185 nM, respectively (± S.E. of the fit).

The sensitivity of *Pd*-CI to canonical complex I inhibitors was investigated (**Figure 4.17B**). The NADH:DQ activity was measured with 200 µM DQ and it was seen that both the inhibitors piericidin A and rotenone inhibited complex I activity ≥ 90%. The enzyme was significantly more sensitive to piericidin A (IC50: 72 ± 7 nM) than rotenone (IC50: 2226 ± 185 nM). This is consistent with studies in membranes, which show that *Pd*-CI is poorly inhibited by rotenone, unlike in the mitochondrial enzyme (Kotlyar and Borovok, 2002). Surprisingly, it was reported by Yip et al. (2011) that their preparation of *Pd*-CI exhibited similarly high sensitivities to both rotenone (IC_{50}: 170 nM) and piericidin A (IC_{50}: 100 nM) despite similar buffer and assay conditions. It is possible that during the faster enzyme preparation developed here (hours vs days) the enzyme maintains greater structural integrity at known rotenone binding sites in the Q-channel and near the transverse helix (Kampjut and Sazanov, 2020), upholding the native properties observed in membranes.

4.7.6. Generation of ROS by *Pd*-CI

The rate of H_2O_2 generation by *Pd*-CI was also measured using the HRP-dependent oxidation of Amplex Red to resorufin. The H_2O_2 formed, either directly or by the dismutation of superoxide (assisted by SOD), was detected by the Amplex Red assay system. In *Pd*-CI, H_2O_2 was generated at a rapid rate of 139 ± 1 nmol min^{-1} mg^{-1} (78 min^{-1}, S.E.M. of three technical replicates) in the presence of 30 µM NADH, which was used to supply electrons to the complex I flavin site to be picked up by oxygen and to generate superoxide or H_2O_2. The rate was approximately four times faster than that generated by purified complex I from bovine heart mitochondria (21.1 ± 2.9 nmol min^{-1} mg^{-1}, 21 min^{-1}) (Kussmaul and Hirst, 2006). However, the

different pH values at which the two assays were performed (pH 6.5 vs pH 7.5) may also influence the rate of H_2O_2 production (Kussmaul and Hirst, 2006).

4.8. Optimisation and characterisation of *Pd*-CI in liposomes

4.8.1. Optimisation of *Pd*-CI reconstitution into liposomes

To study catalysis of wild-type and mutated complex I when turning over the native Q_{10} electron acceptor and in a controlled minimal membrane environment, a protocol needed to be established for the reconstitution of complex I into proteoliposomes (PLs). Proteoliposomes are lipid vesicles containing reconstituted purified proteins that provide a well-defined, minimal system to study complex I catalysis. (**Figure 4.18**). Importantly, it is possible to prepared PLs that can support a Δp across the membrane, which provides a useful tool for investigating the proton-pumping properties of wild type and mutants. The optimisation for the reconstitution of *Pd*-CI into PLs was primarily performed with Dr Olivier Biner (MRC Mitochondrial Biology Unit, Cambridge). The assembly of proteoliposomes consisting of mitochondrial complex I, Q_{10} and *Trypanosoma brucei brucei* alternative oxidase (AOX) has already been well established (Biner et al., 2020; Fedor et al., 2017; Jones et al., 2016). In this system, AOX re-oxidises ubiquinol to ubiquinone and reduces oxygen to water, facilitating unimpeded turnover of complex I by maintaining the Q-pool in an oxidised state (**Figure 4.18A**) (Fedor et al., 2017; Jones et al., 2016). In addition, a protocol was recently established for the co-reconstitution of the mammalian enzyme with the purified F_1F_O-ATP synthase from *E. coli*, allowing study of complex I-driven ATP synthesis in a well-defined system (**Figure 4.18B**) (Biner et al., 2020).

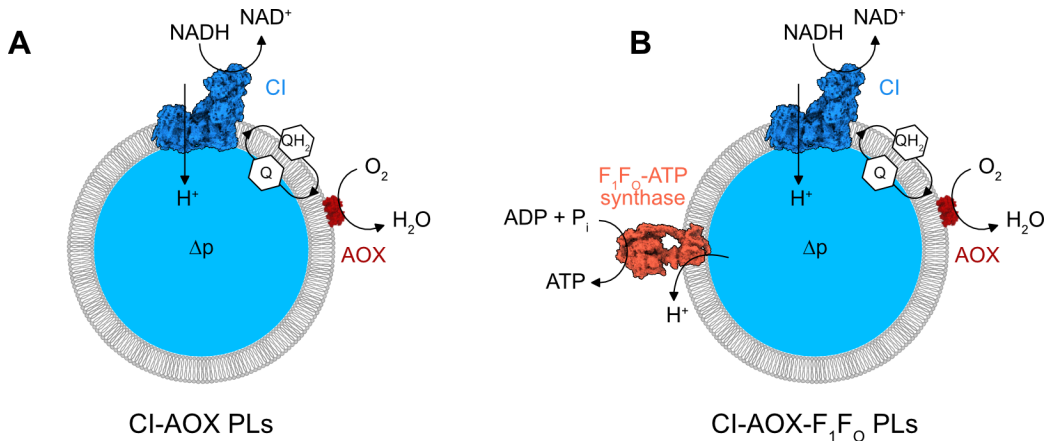

CI-AOX PLs CI-AOX-F_1F_O PLs

Figure 4.18. Schematic of proteoliposome systems developed to study complex I catalysis. (A) CI-AOX PLs, where complex I is reconstituted into liposomes containing its native electron acceptor, Q_{10}. AOX can be added to the assay buffer and will associate with the lipid membrane. AOX is added in a molar excess to maintain a fully oxidised Q-pool, allowing complex I turnover to be non-rate limiting. (B) Co-reconstitution of complex I with the F_1F_O-ATP synthase from *E. coli*. This is an extension of the proteoliposome system shown in A, in which turnover and proton pumping by complex I can drive ATP synthesis.

To optimise the reconstitution of *Pd*-CI into liposomes a protocol developed for the reconstitution of mammalian complex I was adapted to suit the bacterial enzyme (Biner et al., 2020). For more details see Section 2.3.6 (Materials and Methods). For the reconstitution of the bacterial enzyme, the pH of the reconstitution buffer was lowered to pH 6.5 and MES was used as the buffering component. The standard lipid mixture used for mammalian complex I reconstitutions was designed to mimic the inner mitochondrial membrane lipid composition and was composed of 8:1:1, 1,2-dioleoyl-*sn*-glycero-3-phosphocholine (DOPC):1,2-dioleoyl-*sn*-glycero-3-phospho-ethanolamine (DOPE):cardiolipin (CDL; 18:1) in % (w/w). The reported lipid composition of membranes from exponentially growing *P. denitrificans* cells is 52:37:8:3 1,2-dioleoyl-*sn*-glycero-3-phospho-(1'-rac-glycerol) (DOPG):DOPC:DOPE:CDL in % (w/w) (Wilkinson et al., 1972). Complex I activities from proteoliposomes prepared from both lipid mixtures were compared, with no significant differences (**Figure 4.19A**). Although there was no effect on the activity, all future reconstitutions in this chapter were performed using the lipid mixture mimicking the *P. denitrificans* membrane composition. To improve activities further, 250 mM sucrose was included in the reconstitution and assay buffers to improve enzyme stability. In both lipid mixtures described above, the addition of sucrose significantly improved turnover rates in liposomes (**Figure 4.19A**). In addition, the AOX concentration in the assay was titrated to determine optimum amounts for catalysis (**Figure 4.19B**). AOX is a monotopic membrane protein that associates spontaneously to the liposomal membrane, and thus it was added after reconstitution (to the mature proteoliposomes) in all experiments. Between 40 and 80 µg mL^{-1} AOX was found to be optimum for 0.5 µg mL^{-1} outward-facing complex I in the assay, which is the equivalent of 1200-2400 molecules of AOX per complex I, a huge molar excess.

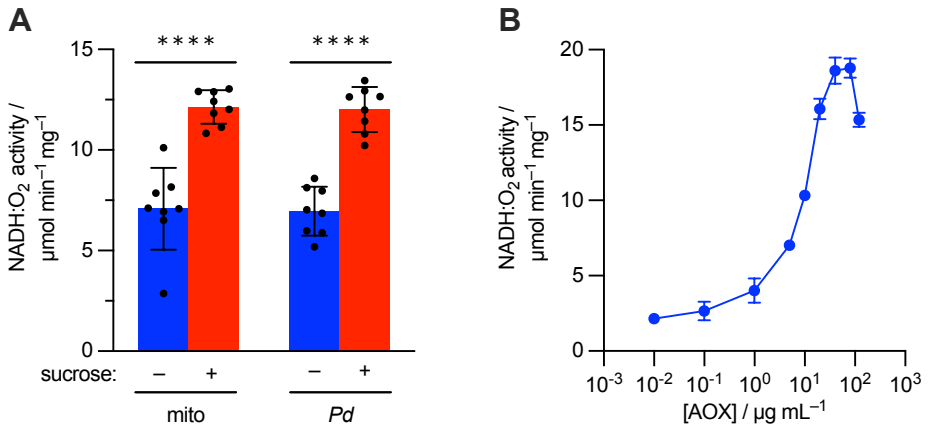

Figure 4.19. Optimisation for the reconstitution of *Pd*-CI into liposomes performed by Dr Olivier Biner (MRC Mitochondrial Biology Unit, Cambridge). (A) Liposomes contained 10 nmol Q_{10} (mg lipids)$^{-1}$ and phospholipid mixtures either mimicking the membrane composition of the inner mitochondrial membrane or the cytoplasmic membrane of *P. denitrificans* were compared. The reconstitutions were carried out in buffer containing 10 mM MES, pH 6.5 at 4 °C, 50 mM KCl and in the presence or absence of 250 mM sucrose. Two independent reconstitutions were performed for each condition and the NADH:O_2 activity was measured in technical replicates for each (n = 4). The average for eight technical replicates is shown with S.D. Statistical significance between all conditions was calculated by one-way ANOVA followed by Tukey's test comparing all conditions to each other. On the graph only the statistical significance between the absence/presence of sucrose has been highlighted within the same phospholipid mixture, ****p < 0.0001. The phospholipid composition did not significantly affect the activity. (B) Titration of AOX into the assay containing 0.5 µg mL^{-1} outward-facing *Pd*-CI PLs, prepared in optimised reconstitution conditions. Data are shown as mean averages ± S.E.M. from three technical replicates.

4.8.2. Characterisation of *Pd*-CI proteoliposomes

Several independent preparations of *Pd*-CI PLs were made, using the optimised reconstitution protocol, to determine their properties. Between 9 and 11 independent reconstitutions were prepared from four separate preparations of the enzyme. By measuring the NADH:APAD$^+$ oxidoreductase activity of complex I in the presence/absence of the pore-forming antibiotic alamethicin, which allowed NADH to cross the membrane and access both inward and outward facing complex I (a measured of the total complex I present in PLs), 46.7 ± 16.8% (n = 9) of complex I was found as outward facing in the PLs. With no clear preference for outward or inward facing, complex I insertion of *Pd*-CI appears random. The average protein retention of complex I during the reconstitution was low, at 36.9 ± 12.7% (n = 10). It is worth noting that the addition of sucrose to the reconstitution buffer was probably detrimental to the recovery of liposomes, as the increased density of the sucrose precluded their efficient pelleting during centrifugation. Future optimisation of the reconstitution protocol would benefit from improvements to the recovery of complex I to reduce protein wastage. After reconstitution into liposomes, the PLs were analysed by SDS-PAGE and compared to the soluble enzyme to check that the enzyme remained fully intact (**Figure 4.20**). Despite smearing on the gel due to

the high lipid content in the sample, the subunit composition of the enzyme appears to match that of the soluble enzyme, suggesting the enzyme is fully intact after reconstitution.

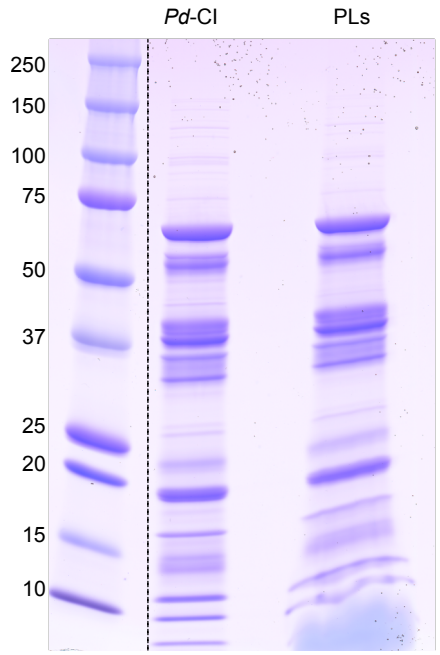

Figure 4.20. SDS-PAGE of soluble *Pd*-CI and *Pd*-CI reconstituted into PLs. Samples were prepared in SDS-PAGE loading buffer before pelleting out insoluble material by centrifugation at 131,000 × g in a TLA100 rotor. A 10 µg portion of protein was loaded onto each lane. A protein ladder was run on the same gel but is cropped to appear next to the samples for clarity.

The average NADH:O_2 activity of outward-facing complex I was measured at 24.5 ± 8.4 µmol min^{-1} mg^{-1} (n = 11). Although the NADH:O_2 varied substantially, between 13.8 and 41.5 µmol min^{-1} mg^{-1}, more than 50% of the preparations were between 22.6 and 26.6 µmol min^{-1} mg^{-1}. Overall, there was no significant loss (or gain) in activity on reconstitution of *Pd*-CI into liposomes with the native Q_{10} electron acceptor. When the membrane of the PLs were uncoupled with the protonophore gramicidin A, the NADH:O_2 activities increased only marginally with a uncoupled vs coupled ratio (respiratory control ratio) of 1.2 ± 0.2 (n=8, S.D.), similar to that observed in bovine PLs (Jones et al., 2016). Unless otherwise noted, all activities in PLs have been measured in the absence of gramicidin A.

4.8.3. Titration of Q_{10} and inhibitors in *Pd*-CI proteoliposomes

The K_M for native Q_{10} was measured in *Pd*-CI PLs by preparing PLs at different Q_{10} concentrations, with the amount of Q_{10} per phospholipid accurately quantified (**Figure 4.21A**) (Fedor et al., 2017; Jones et al., 2016). The V_{max} for the enzyme was 27.9 ± 1.2 µmol min^{-1} (mg CI)$^{-1}$, a typical rate achieved when reconstituting *Pd*-CI. The K_M for Q_{10} was 1.1 ± 0.2 mM

(where mM refers to the concentration in the membrane), similar to the reported range for the mammalian enzyme (0.48–3.94 mM), and suggesting the enzymes have similarly low affinities for Q_{10} (Biner et al., 2020; Fedor et al., 2017; Jones et al., 2016). The inhibitors piericidin A and rotenone were titrated into proteoliposomes to investigate the effect the membranes had on inhibition in comparison to the soluble enzyme (**Figure 4.21B**). As is the case for the soluble enzyme, *Pd*-CI was more sensitive to piericidin A (IC_{50}: 24.3 ± 3 nM, where nM refers to the overall concentration) than rotenone (IC_{50}: 452 ± 48 nM). For both inhibitors, the IC_{50} values are lower in PLs than in the soluble enzyme, probably due to the smaller hydrophobic phase volume in the PL measurements, which concentrates the inhibitor in the vicinity of the enzyme. In this regard, comparison of IC_{50} values between soluble and membrane systems is not particularly useful.

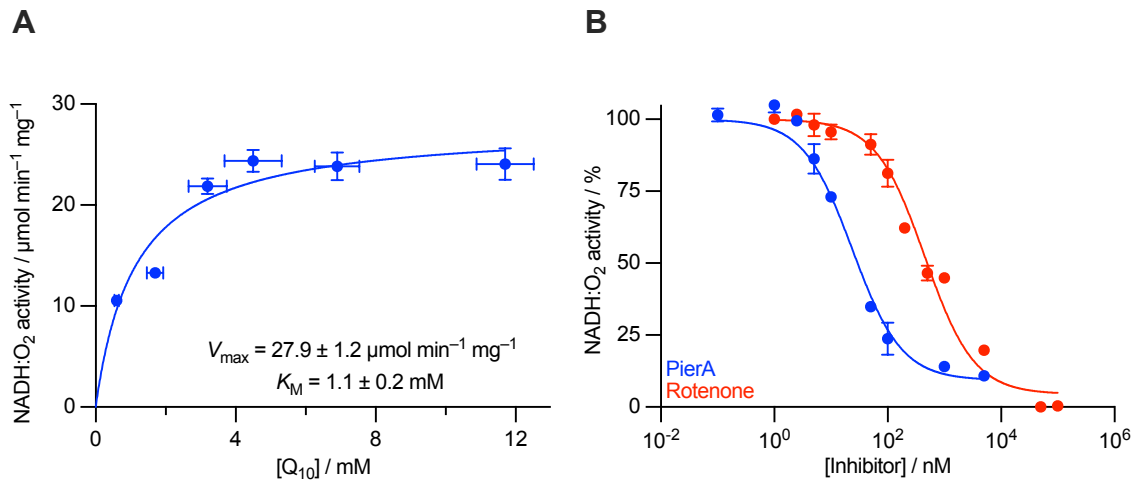

Figure 4.21. Q_{10} kinetics and inhibitor sensitivity in *Pd*-CI proteoliposomes. Experiments were performed by Dr Olivier Biner (MRC Mitochondrial Biology Unit, Cambridge). (A) K_M curve for Q_{10} in proteoliposomes. The K_M and V_{max} values were determined to be 1.1 ± 0.2 mM and 27.9 ± 1.2 µmol min^{-1} (mg CI)$^{-1}$, respectively (± S.E.M. of the fit). (B) Inhibition by piericidin A and rotenone. The measured IC_{50} values for piericidin A and rotenone were 24 ± 3 nM and 452 ± 48 nM, respectively (± S.E. of the fit).

4.8.4. Proton-pumping measurements in *Pd*-CI PLs

Proteoliposomes can support a Δp across the membrane, allowing for proton-pumping measurements of reconstituted proteins. The proton-pumping capacity of the reconstituted complex I from *P. denitrificans* was assessed by measuring ACMA fluorescence quenching (**Figure 4.22A**). Addition of NADH energised the membrane in complex I-containing liposomes but not in empty liposomes, leading to a quench in fluorescence. Addition of alamethicin (25 µg mL^{-1}) dissipated the ΔpH. In an additional experiment, complex I was co-reconstituted into liposomes with the purified F_1F_O-ATP synthase from *E. coli*, a protocol already established for the bovine enzyme (Biner et al., 2020), which was successfully reproduced using the optimised

conditions for the *Pd*-CI enzyme. A lower AOX concentration of 5 μg mL^{-1} was used in the assay to support NADH turnover while minimising potential membrane uncoupling from high concentrations of AOX, as well as unwanted interference with the luciferase detection system. The proteoliposomes were able to support a sufficient Δp through turnover of NADH at complex I to drive ATP synthesis (**Figure 4.22B**). Synthesis was abolished when the membrane was uncoupled with gramicidin (20 μg mL^{-1}) or complex I catalysis was inhibited with piericidin (2 μM). In addition, PLs containing only F_1F_O-ATP synthase (no *Pd*-CI) could not synthesise ATP. Overall, this shows that the *Pd*-CI was functionally intact and competent for proton pumping. These data are important as they demonstrate that the purification and reconstitution protocols developed in this chapter have not decoupled the Q-reductase activity from the proton translocation machinery. In summary, proteoliposomes can now be used to study purified complex I variants from *Pd*-CI.

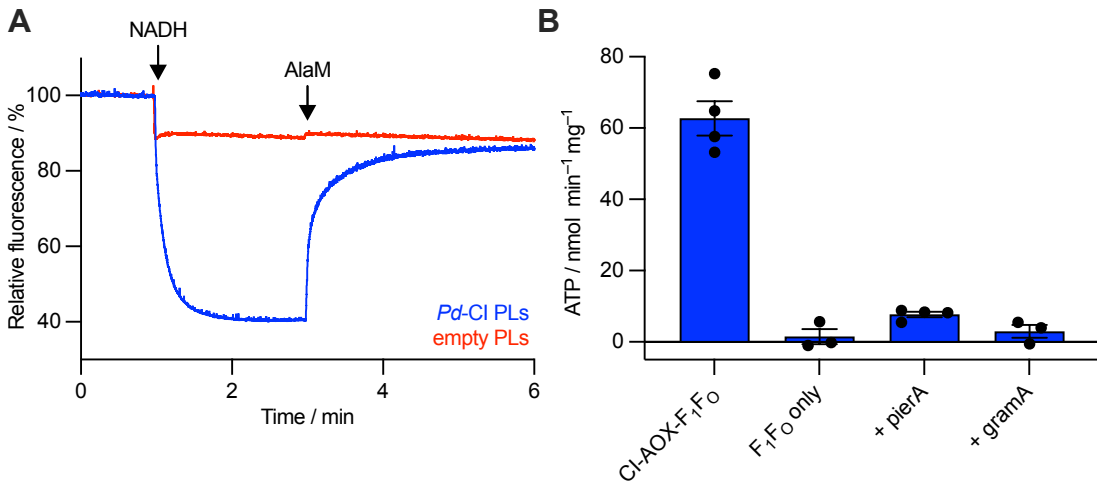

Figure 4.22. (A) Proton pumping measured by an ACMA fluorescence quench assay. Proton pumping was initiated by addition of 1 mM NADH and proteoliposomes uncoupled by addition of 25 μg mL^{-1} alamethicin (AlaM). Liposomes without *Pd*-CI were added as a control. AOX was directly added to the assay mixture at 20 μg mL^{-1}. (B) *Pd*-CI was co-reconstituted into liposomes with *E. coli* ATP synthase (CI-AOX-F_1F_O) and NADH-coupled ATP production was monitored using the luciferase-based real-time luminescence assay shown in Chapter 3 (Section 3.9). AOX was directly added to the assay mixture at 5 μg mL^{-1}. Data in panel B were produced by Dr Olivier Biner (MRC Mitochondrial Biology Unit, Cambridge).

4.9. Summary and conclusions

In this chapter, protocols and resources were developed for facilitating the use of *P. denitrificans* as a model for mitochondrial complex I. First, a strain of *P. denitrificans* was created that was amenable to deleterious complex I mutagenesis. Second, a protocol was developed for the robust purification of intact complex I that was both highly pure and highly active. Last, reconstitution of *Pd*-CI into PLs was optimised and characterised. Through these developments, complex I from *P. denitrificans* can be studied in various forms; in the native membrane environment (membranes or SBPs); in its detergent-solubilised form (purified *Pd*-CI); and in a minimal membrane environment that can support a Δp (PLs). These developments have greatly expanded the toolkit available for studying *P. denitrificans* complex I variants and the thorough characterisation of the wild-type enzyme performed here will be essential for evaluating them. The remaining chapters of this thesis discuss how the methods and protocols established here have been used to solve the structure of *P. denitrificans* complex I (Chapter 5) and to investigate key residues in the proton-pumping mechanism (Chapter 6).

5. Structural studies of *P. denitrificans* complex I by single-particle cryo-EM

5.1. Introduction

5.1.1. Single-particle cryo-EM of complex I

X-ray crystallography continues to be an invaluable technique for solving the structures of biological proteins and complexes. However, the need to form good diffracting crystals for the protein of interest can be limiting for some proteins. Recent advancements in single-particle cryogenic electron microscopy (cryo-EM) have provided new avenues for determining the structure of large biological molecules without the need for crystallisation. In particular, cryo-EM has recently been gainfully employed to solve the structure of large membrane-bound proteins and complexes, such as the ribosome and respiratory chain complexes/supercomplexes (Agip et al., 2019; Guo et al., 2017; Kühlbrandt, 2019; Nogales et al., 2015; Spikes et al., 2020).

In 2013, the first fully intact complex I structure was determined by X-ray crystallography from the bacterium *T. thermophilus* at a resolution of 3.3 Å (Baradaran et al., 2013). Since then, cryo-EM has been the technique of choice for complex I structural studies, being successfully employed to resolve the native mammalian, yeast, plant and bacterial complex I structures (Fiedorczuk et al., 2016; Grba et al., 2020; Klusch et al., 2021; Kolata et al., 2021; Parey et al., 2021; Zhu et al., 2016). The first structure of mammalian complex I was resolved in 2014 (Vinothkumar et al., 2014), and in 2016 the first near-complete models from ovine and bovine complex I were published at 3.9 Å and 4.2 Å, respectively (Fiedorczuk et al., 2016; Zhu et al., 2016). These models have since been improved to respective resolutions of 2.3-2.5 Å (Kampjut and Sazanov, 2020) and 2.3-3 Å (Chung et al., 2022). While the structure from the yeast genetic model *Y. lipolytica* could be solved to 3.6–3.9 Å by X-ray crystallography (Zickermann et al., 2015), more recent structures of *Y. lipolytica* complex I used cryo-EM to reach resolutions of 2.7 Å and ~2.1 Å (Grba and Hirst, 2020; Parey et al., 2021). Plant complexes, such as from *Arabidopsis thaliana* and *Polytomella* sp., have also been resolved at 3.4–3.5 Å and 3.1 Å, respectively (Klusch et al., 2021).

In addition to the native 'as-prepared' preparations of the enzyme, structures of complex I with inhibitors bound, in the presence of substrates and with single point mutations have been resolved more recently (Bridges et al., 2020; Chung et al., 2022; Galemou Yoga et al., 2020; Gu et al., 2022; Gutiérrez-Fernández et al., 2020; Hameedi et al., 2021; Parey et al., 2018; Yin

et al., 2021). These structural analyses have mainly been performed on the mammalian and yeast mitochondrial enzymes. Interestingly, despite the bacterial complex I from *T. thermophilus* being the first complete model of complex I, there is a distinct lack of complex I structures of the bacterial enzyme resolved by cryo-EM, other than a couple of recent studies from *T. thermophilus* and *E. coli* (Gutiérrez-Fernández et al., 2020; Kolata and Efremov, 2021). Obtaining bacterial complex I structures, from a suitable model organism, such as *P. denitrificans*, would be beneficial for mechanistic studies, which can be complemented with entire-complex mutagenesis.

5.1.2. Basics of single-particle cryo-EM

Single-particle cryo-EM follows a different workflow to that of X-ray crystallography for sample preparation and data collection. An overview of the key steps in the cryo-EM workflow are shown in **Figure 5.1**. First, the protein of interest is purified and then applied onto a grid (requiring just a few µL of sample). The grid can be made of various scaffolding materials, such as carbon or gold, and contains many holes (commonly, around 1 µm in diameter). The protein applied to the grid is blotted with filter paper to create a thin film of liquid, which is then rapidly frozen in liquid ethane. The protein sample is frozen in an amorphous or vitreous state of non-crystalline ice, which has the advantage of preventing damaging ice crystal formation (liquid ethane freezes the samples more efficiently than liquid nitrogen, consequently the sample is frozen faster than the rate at which hydrogen bond formation can occur (Dubochet et al., 1988; Adrian et al., 1984)). Samples prepared in this way are thus considered to be in the hydrated state and have visible internal protein structures, which would not be suitably resolved in negative-stain imaging. In addition, maintaining the sample at cryogenic temperatures during imaging allows the sample to withstand greater radiation damage from incident electrons, enabling structural information to be collected before sample damage occurs (Henderson et al., 1990).

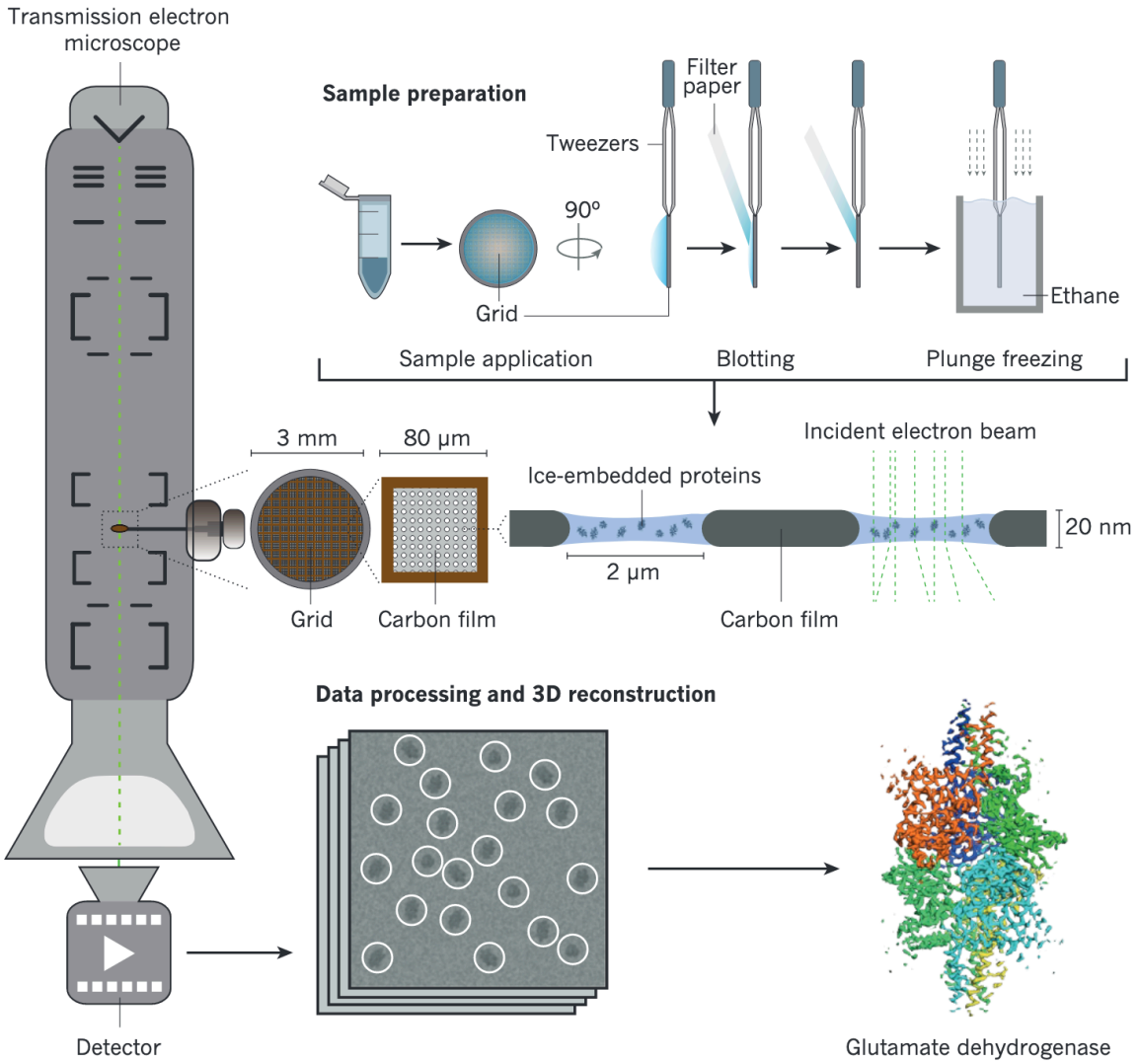

Figure 5.1. Overview of the cryo-EM workflow for single-particle analysis. Figure taken from Fernandez-Leiro and Scheres (2016). Shown on the left is the electron microscope producing a beam of electrons, which pass through a protein sample applied to a 'grid' and are detected by an electron sensor. The grid is prepared by application of purified protein to the grid before blotting it and plunge freezing it into liquid ethane to form vitrified ice. The 2D images obtained from the microscope can then be reconstructed into a 3D protein structure.

The frozen grids containing the protein are then loaded into an electron microscope, maintained in cryogenic conditions and incident electrons are passed through the sample hole-by-hole. The reflected electrons are detected at an electron sensor (direct electron detector), which yields 2D movies, where the frames are averaged into 2D images, with improved contrast (micrographs), of the sample suspended in vitreous ice in the holes. Many images are captured and the individual protein 'particles' within these images can be 'picked'. Importantly, these particles should be present in a range of orientations in the vitrified ice for successful in silico reconstruction. Using a processing pipeline, such as that in the software RELION, a 3D reconstruction of the molecule can be created from these 2D images (Scheres, 2016).

5.1.3. Single-particle cryo-EM of *P. denitrificans* complex I

P. denitrificans has historically been the chosen model organism for studying respiratory chain complexes, both because of its greater similarity to the mitochondrial respiratory chain and because the ETC complexes exist in their most simple form; they contain a minimal number of subunits (Iwata et al., 1995; Trumpower, 1991). The first ever structure of the cytochrome *c* oxidase complex (complex IV) was resolved from *P. denitrificans* (Iwata et al., 1995) and the mechanisms of energy transfer and energy transduction in the bc_1 complex (complex III) have also been explored using *P. denitrificans* as a paradigm (Trumpower, 1991). For *Pd*-CI, no high-resolution structural information currently exists, limiting its use as a model system. Obtaining the *Pd*-CI structure and building an atomic model would allow mechanistic studies of complex I to combine mutagenesis with insightful structural and functional characterisations. There are two possible routes to solve the *Pd*-CI structure by single-particle cryo-EM. One could either attempt to solve the structure of the intact isolated enzyme or the much larger complex I-containing respiratory supercomplex. BN-PAGE analysis has suggested that complex I in *P. denitrificans* is more stable as a supercomplex, with subunit/domain dissociation observed on the gel when extracted from this higher order structure (Stroh et al., 2004). This would indicate that the intact complex I structure from *P. denitrificans* can only be obtained via supercomplexes. However, Chapter 4 showed fully intact complex I from *P. denitrificans* could be isolated, which is suitable for structural studies. Further to this, Yip et al. (2011) imaged the isolated *Pd*-CI enzyme by negative-stain EM on a Philips/FEI Tecnai 12 microscope operating at 120 kV. A low-resolution reconstruction of the 2D classes of complex I could be generated, showing its distinct 'L' shape and indicating the presence of the core subunits. Because the peripheral arm was better resolved for *Pd*-CI than in equivalent analyses on the *E. coli* enzyme (Sazanov et al., 2003), it was suggested that *P. denitrificans* complex I is actually more stable than that of the *E. coli* enzyme (which does not exist in supercomplexes) (Anraku and Gennis, 1987). This study, and the results of Chapter 4, suggest that it is possible to perform cryo-EM on isolated *Pd*-CI, a much simpler system to work with compared to supercomplexes, which would require the development of a new purification protocol and modelling of complex III and IV components.

In this chapter our attempts to solve the *P. denitrificans* complex I structure by cryo-EM are described. This work was heavily supported by Dr Zhan Yin (MRC Mitochondrial Biology Unit, Cambridge), who made and screened cryo-EM grids, Dr Dima Chirgadze (University of Cambridge cryo-EM facility), who set up the cryo-EM data collection, and Dr Daniel Grba (MRC Mitochondrial Biology Unit, Cambridge), who helped with the RELION data processing.

5.2. Aims of this chapter

- Resolve the structure of isolated complex I from *P. denitrificans* by single-particle cryo-EM.
- Assign all subunits present in the complex.
- Analyse the overall architecture of the *P. denitrificans* complex I in relation to mammalian complex I.
- Investigate key structural features of *P. denitrificans* complex I.

5.3. Single-particle cryo-EM data collection and processing

To perform single-particle cryo-EM on complex I from *P. denitrificans*, the protein was purified as described in Chapter 4. The only alteration to the protocol was that glycerol was omitted from the size-exclusion chromatography buffer because this would reduce the contrast of the protein in the vitreous ice on the cryo-EM grids. Removal of glycerol from the size-exclusion chromatography buffer did not result in a loss in activity of the purified enzyme, with a piericidin A-sensitive rate of 20.88 μmol min^{-1} mg^{-1} being retained. Three different concentrations of complex I were applied to the grids to assess the optimal particle distribution (2.1, 2.6 and 3.0 mg mL^{-1}). Grids were then blotted and plunge frozen as described in Section 2.8.2 (Materials and Methods). Grids were screened on a 200 keV Talos™ Artica EM microscope and a grid prepared with 3.0 mg mL^{-1} of protein was considered to have the best ice thickness and particle distribution and so was taken forward for data collection (**Figure 5.2**). Squares with similar ice thickness were picked for data collection and, in general, more particles were seen with thicker ice and fewer particles in squares with thinner ice. Data were collected for three days on a 300 keV FEI Titan Krios at University of Cambridge cryo-EM facility using a Gatan K2 summit camera (Section 2.8.3, Materials and Methods). One movie (micrograph) was captured per hole and a total of 2278 micrograph images were collected.

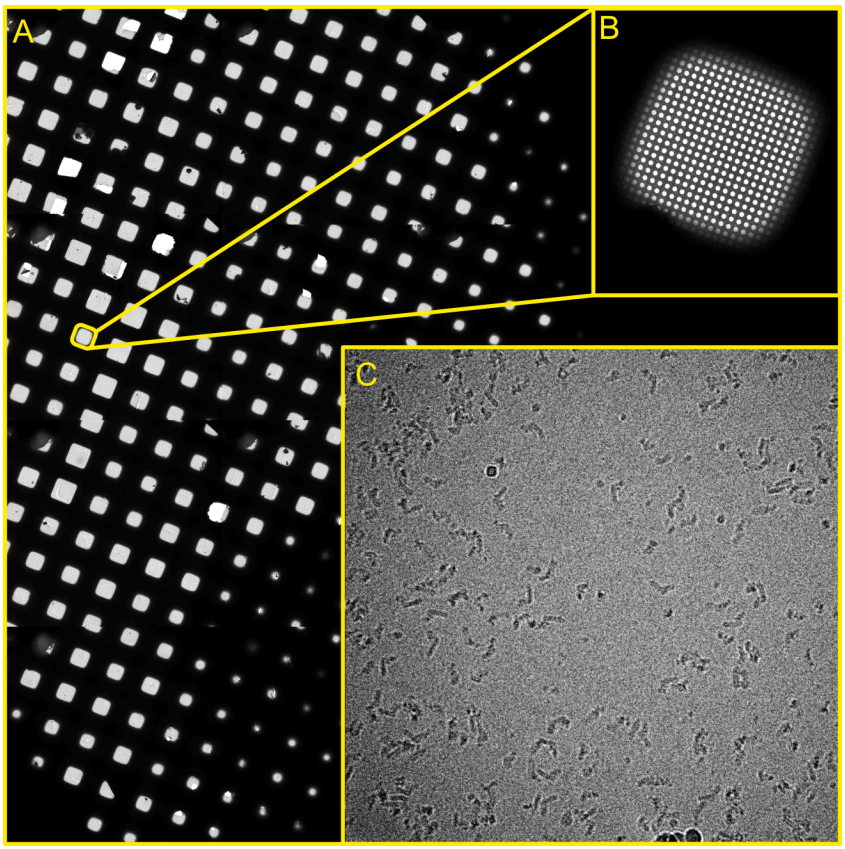

Figure 5.2. Image of the cryo-EM grid used for data collection. (A) Atlas of the grid (grid overview) showing a range of ice thickness (the smaller the size of the square, the thicker the ice). (B) Close-up view of a typical grid square showing individual foil holes in which images were collected. (C) Typical image from a single hole showing the particle distribution. The distinct 'L' shape of complex I can be seen in the micrographs.

5.4. Cryo-EM data processing in RELION

5.4.1. Optimising automated particle picking

To process the micrograph images obtained from the data collection, the RELION-3.0 processing pipeline was followed (Zivanov et al., 2018). The general pipeline and processing details are described in Materials and Methods (Section 2.9) and will not be described again here. Initially 8000 particles were manually picked from micrographs that had been motion corrected and the contrast transfer function (CTF) was estimated. These particles were manually picked with the aim of representing a variety of orientations of complex I in the micrograph. The particles were then combined and classified into 50 separate clusters of particles or 'classes', in which particles were aligned with the same orientation or viewpoint. From this 2D classification, 22 'good' classes were selected that represented complex I in different orientations and the non-complex I particles were removed (**Figure 5.3A**). These 2D classes were then used as a template for automated particle picking from all micrographs,

yielding 74,377 picked particles (**Figure 5.3B**). These were again sorted by 2D classification into 50 classes, as shown in **Figure 5.3C**. From this, 34 2D classes, which were of better quality than the manually picked 2D classes, were chosen for a final round of automated particle picking from the 2D templates. This yielded 128,270 picked particles.

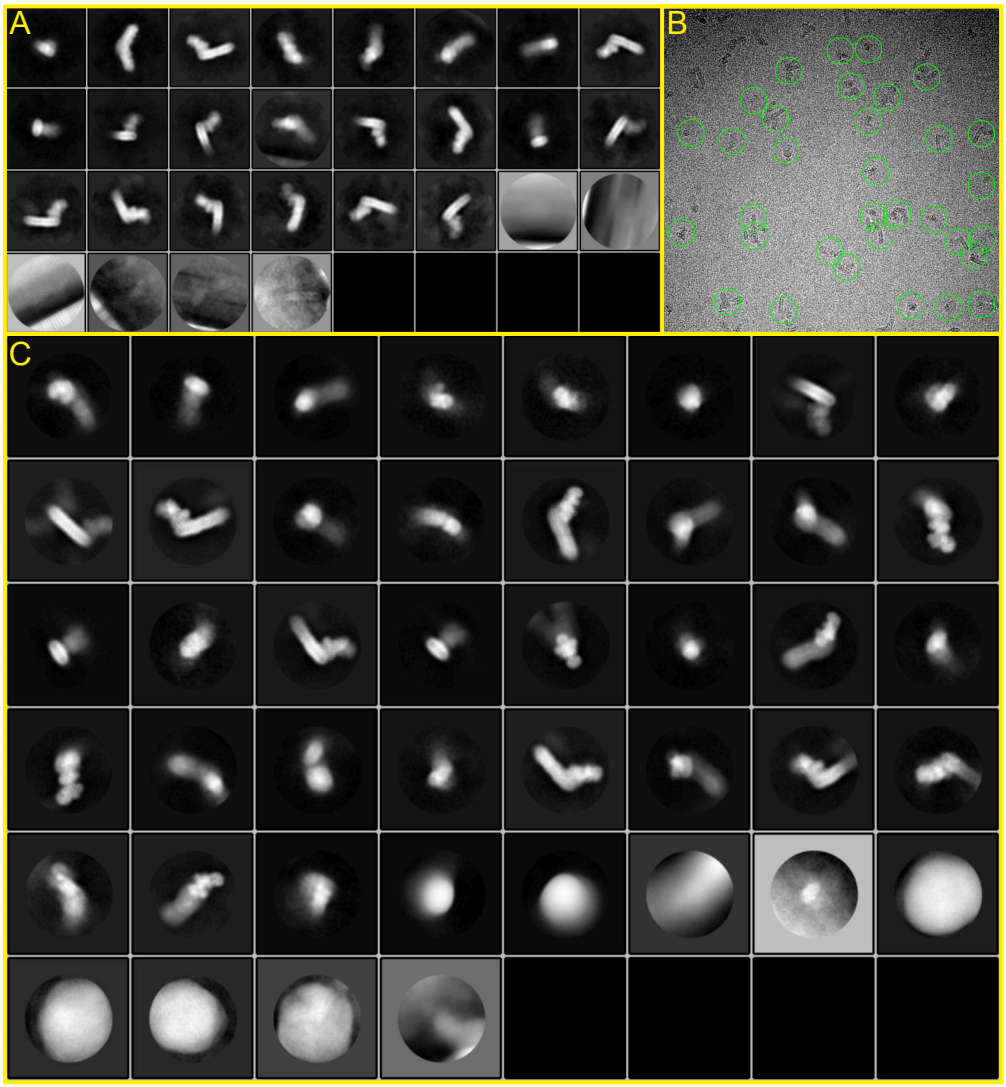

Figure 5.3. 2D classification and automated particle picking from a 2D template. (A) 2D classes from 8000 manually picked particles. (B) Example of the automated picking of particles using a 2D template. Green circles represent each particle picked in a single micrograph. (C) 2D classes generated from 74,377 particles picked using a 2D template from 8000 manually picked particles. Complex I-like 2D classes were used as a template for a second round of automated particle picking yielding 128,270 particles.

All particles were then divided into five 3D classes to separate intact complex I, partially assembled/broken complex I and non-complex I particles, as shown in **Figure 5.4**. Class 1 contained 24% of picked particles (31,037 particles) and was taken forward for further processing as the intact class of complex I. This class first underwent 3D auto-refinement

followed by a second round of 3D classification, separating the particles further into three subsets. The second class (class 2) appeared to be fully intact complex I and contained most particles (19.2k particles). This major class was 3D auto-refined. At this stage, in a bid to maximise the number of particles of intact complex I selected from the micrographs, some of which may have been missed during automated particle picking from 2D classes, automated particle picking was repeated using a 3D template generated from this class of intact complex I particles.

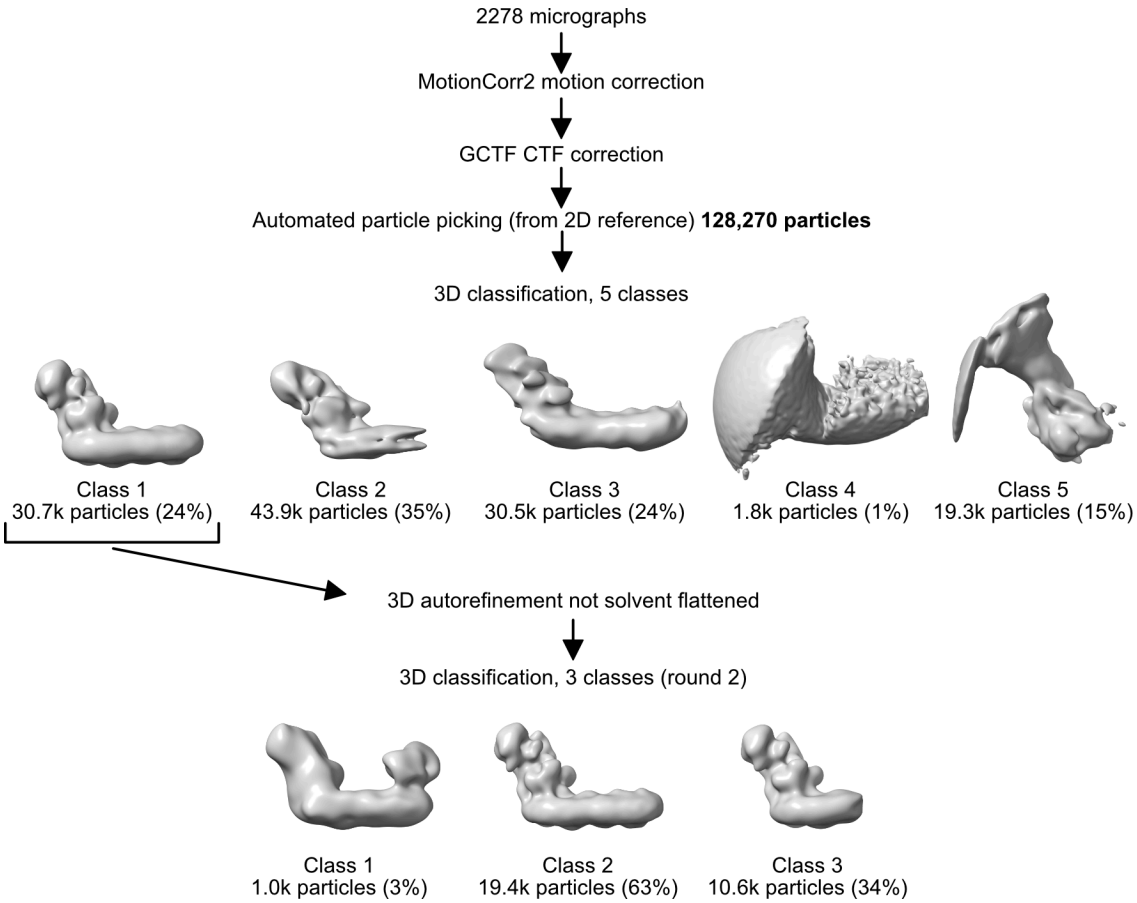

Figure 5.4. Classification scheme used in RELION-3.0 to generate a 3D template for improved automated particle picking of complex I. From a 2D reference, 128,270 particles were picked, which were then separated into groups by two separate rounds of 3D classification. This separated fully intact complex I from partially intact complex I and non-complex I particles. Particles in class 2 from the final round of 3D classification was used as a template for further automated particle picking using this class as a 3D reference.

5.4.2. Reconstruction of overall map of complex I from *P. denitrificans*

Using the 3D template for complex I produced in **Figure 5.4**, 125,639 particles were re-picked from the original micrographs. This was fewer particles than the automated picking using a 2D template, but should represent higher quality particles, which are more likely to be of the intact enzyme. As before, these particles were first separated into five groups by 3D classification, followed by a second round of 3D classification into three groups, as shown in **Figure 5.5**. After the second round of classification, class 1 contained a small subset of particles that possessed two complex I molecules coordinated to each other in the toe region of the complex. Class 3 appeared to be a group of complex I particles that was missing part of the hydrophobic domain (the toe region, composed of subunits Nqo13 and Nqo12). The major class of particles was found in class 2 (51.3k) and represented the intact enzyme. This was over double the final number of particles from the equivalent class after automated particle picking from a 2D reference (51.3k vs 19.4k). This class was 3D refined followed by two rounds of both CTF refinement and Bayesian polishing (Materials and Methods, Sections 2.9.7 and 2.9.8). The map was then refined with a mask to exclude the non-complex I signal (solvent flattening) and post processed (**Figure 5.5**).

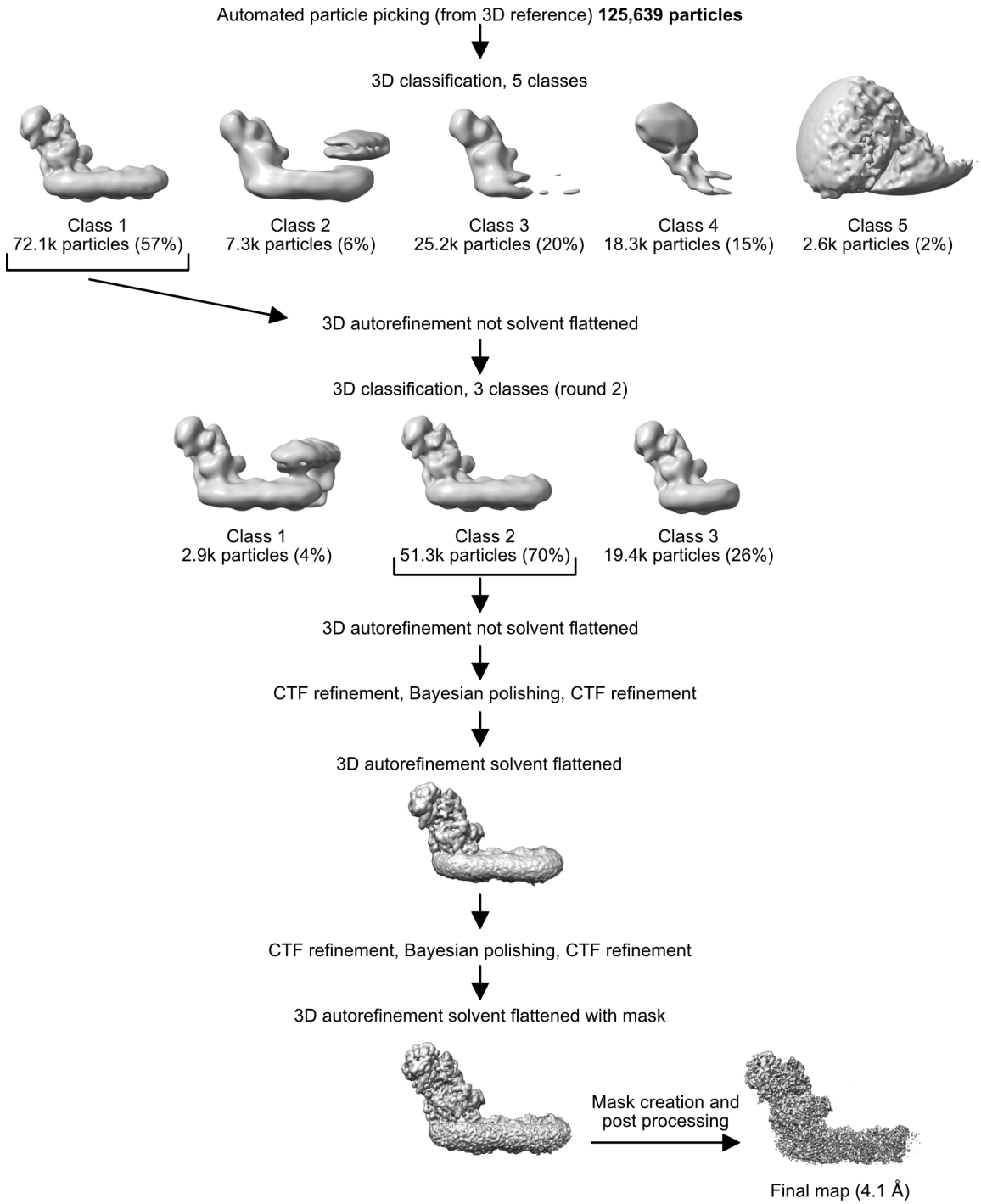

Figure 5.5. Final classification scheme used in RELION-3.0 for *P. denitrificans* complex I. 125,639 particles were picked using the 3D reference generated in **Figure 5.4**. Two rounds of 3D classifications were performed as before. Particles in class 2 from the second round of 3D classification underwent multiple rounds of 3D auto-refinement, per-particle CTF refinement and Bayesian polishing. A final map of complex I was obtained at an overall resolution of 4.1 Å.

The overall resolution of the final map was 4.1 Å as determined by where the FSC curve intersects the line at 0.143 (**Figure 5.6A**). However, flexible heterogeneity in the protein resulted in variation in the resolution across the whole complex. To assess the local resolution in the protein, local resolution estimation was performed across the whole complex I (**Figure 5.6B**). While the overall 'L' shape architecture of complex I is established, there is a significant decrease in the local resolution in the membrane domain. In particular, the toe region, containing subunits Nqo12 and Nqo13, are at poor resolution and the electron density in the transmembrane helices (TMHs) is substantially broken and non-continuous in this region. Therefore, it is impossible to accurately model this region of the protein in its current state. To try and improve the quality and resolution in this region, focus refinement and further classification was performed on the membrane domain.

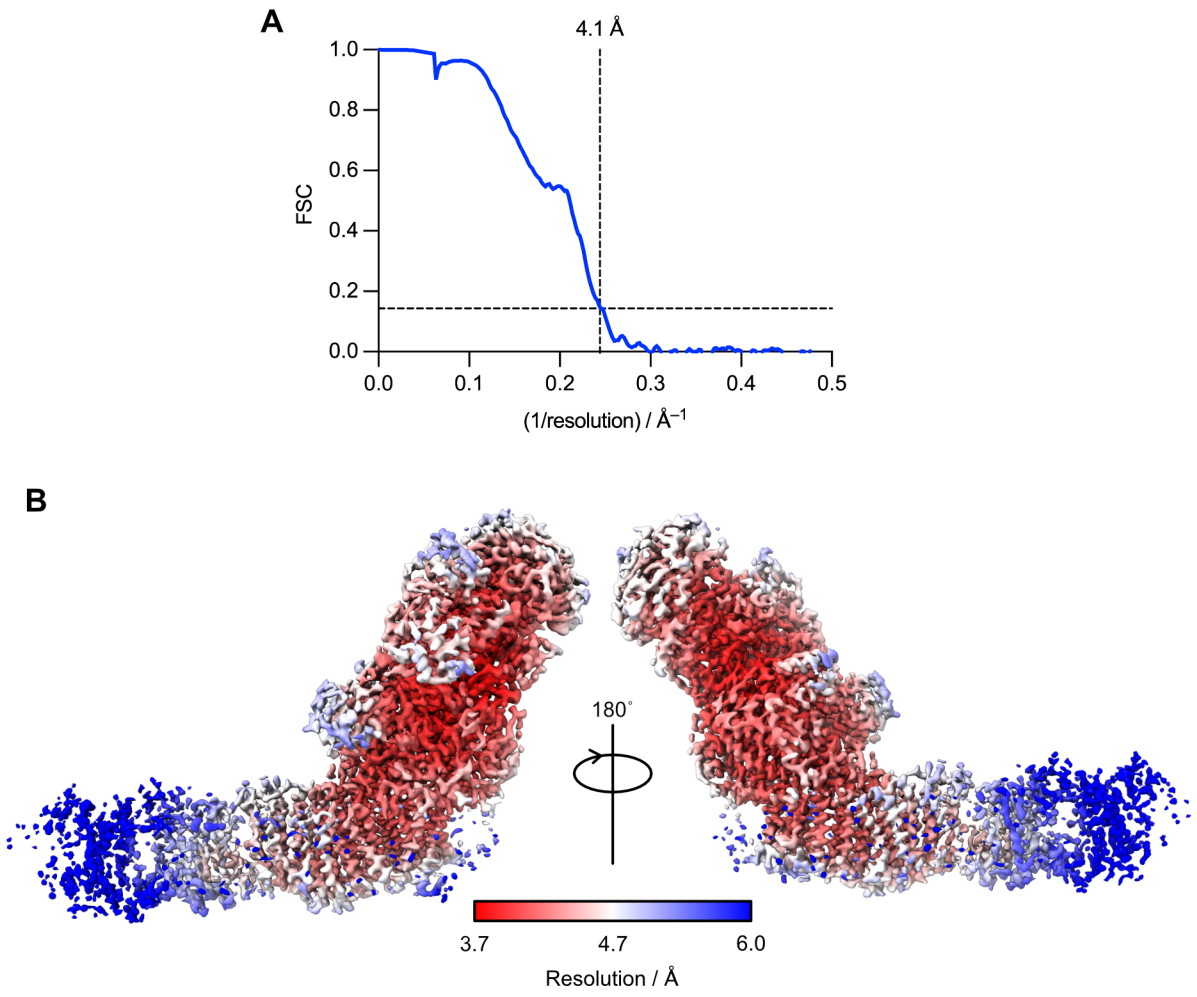

Figure 5.6. Resolution estimation of the entire map of *P. denitrificans* complex I, as well as the local resolution estimation. (A) Overall resolution estimate defined by where the FSC curve crosses the line at FSC = 0.143. (B) Local resolution estimation of the final map of *P. denitrificans* complex I. Resolution is coloured according to the scale bar.

5.4.3. Improving membrane domain quality

A mask covering the entire membrane domain but not the peripheral arm was created and used to refine and align all particles present in the final map to the membrane domain, without the well-resolved hydrophilic domain signal influencing alignment. This map was then post processed using the same membrane domain mask and the local resolution was estimated (**Figure 5.7**). Focused refinement on the membrane domain revealed the toe region subunits (Nqo12 and 13) were still associated with complex I despite being poorly resolved in the overall map. However, the resolution remained poor in this region and the features, particularly in the TMHs, were less well defined. In addition, after focused refinement, the peripheral arm of complex I was no longer well aligned and so lacked definition. This led to the conclusion that the membrane domain is very flexible in *Pd*-CI, making it hard to align this region in comparison to the hydrophilic domain. The membrane domain of *Pd*-CI may occupy different conformations/positions between particles, leading to a poor resolution and washed-out features in the membrane due to averaging of these different states in the cryo-EM analysis, rather than subunit dissociation.

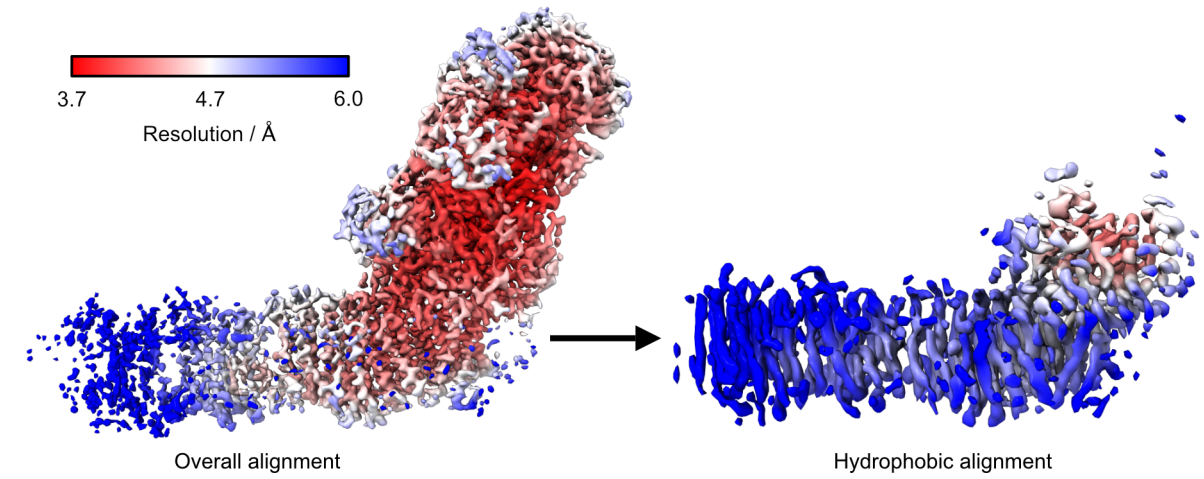

Figure 5.7. Local resolution estimation before and after focus refinement on the membrane domain of complex I. Complex I was aligned and refined to the membrane domain using a mask that contained only the membrane domain. This was then post processed and the local resolution estimated as shown by the scale bar. Little or no improvement in the resolution was observed in the membrane domain, and the TMHs, while showing marginally improved continuous electron density, were more featureless.

To detect and separate potential different angles in the membrane domain, the particles from the final overall map were first aligned to the hydrophilic domain using a hydrophilic mask (**Figure 5.8A**). This should exaggerate and separate out a range of different positions in the membrane domain. 3D classification was then performed on these hydrophilic aligned particles by using a mask that we have called a 'fishtail' mask, which accommodates for a wide range of potential movement in the membrane domain, such as from side-to-side and up-and-down (**Figure 5.8A**). Classification using this mask was performed without further particle alignment and particles were separated into five classes (**Figure 5.8B**). Class 1 showed there was still a subset of particles (5.1k, 10%) that appear to be missing the Nqo12 and Nqo13 subunits, and these could be discarded. Two minor classes (classes 3 and 4) which contained 8% of the particles between them, and two major classes, class 2 (26.2k particles, 51%) and class 5 (15.9k particles, 31%), were identified. Both these major classes were taken forward for 3D auto-refinement and compared to each other. There is clear movement in the membrane domain between the two classes, as shown in **Figure 5.8C**. A bending motion from side-to-side and up-and-down in the plane of the membrane can be seen. Averaging these two main classes together probably resulted in a poorer resolution or quality of map in the toe region, as the helices in these regions do not overlap well, leading to the washed-out features in the TMHs.

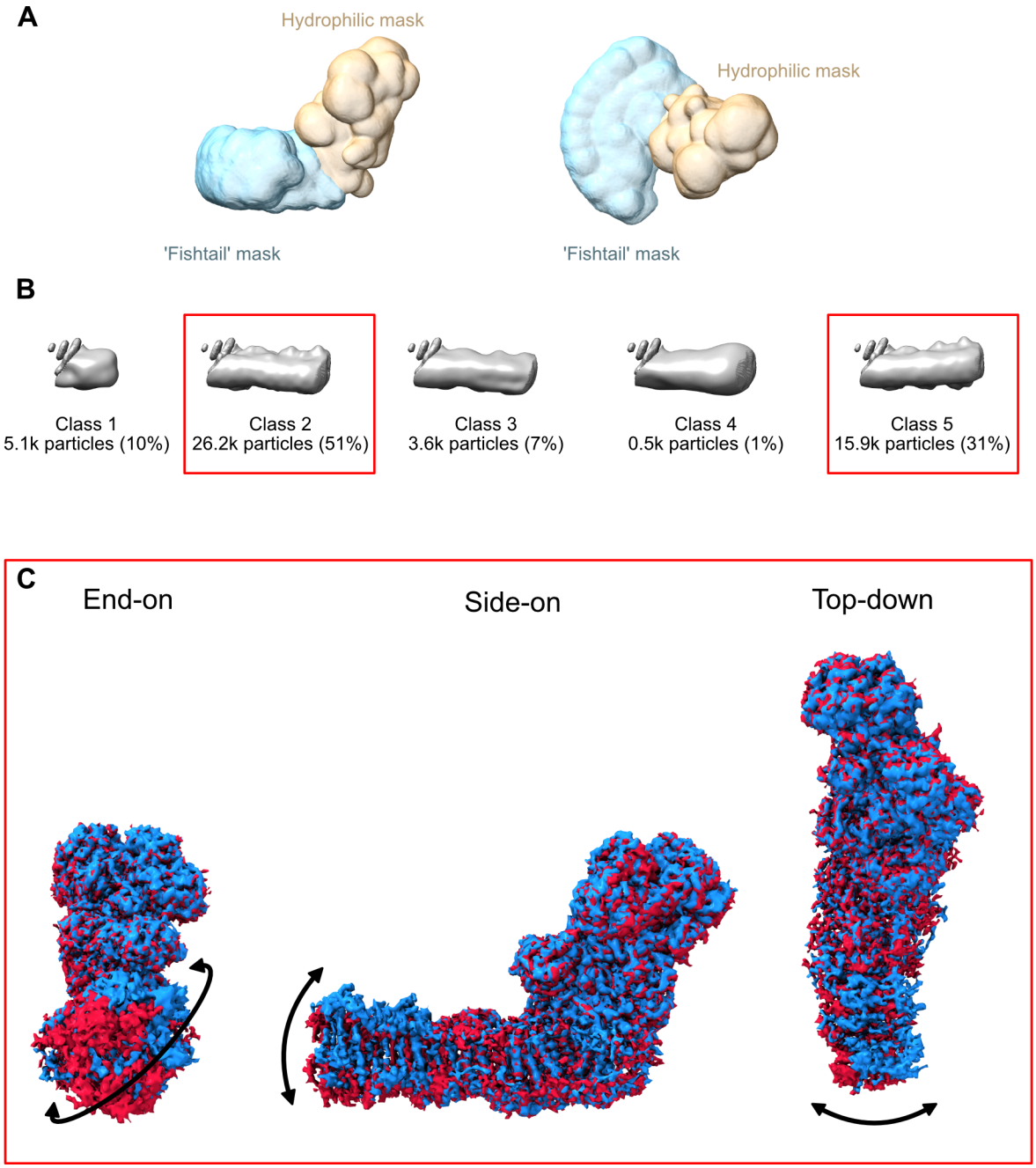

Figure 5.8. Classification of membrane domain movement in *Pd*-CI. (A) Depiction of the two masks used to separate out membrane domain motion. Particles were first aligned to the hydrophilic domain using the mask shown in wheat colour. Particles were then classified into five classes with no further alignment, using the 'fishtail' mask shown in cyan. (B) Five 3D classes after classification using the 'fishtail' mask. The two major classes are highlighted by the red box and were taken forward for further analysis. (C) Comparison of classes 2 (red) and 5 (blue) after 3D classification with fishtail mask and subsequent auto-refinements. Three views are shown of complex I and the motion in the membrane domain between the two classes is highlighted by the arrows.

Focus refinement on the particles from classes 2 and 5 (as well as the particles before classification) were performed using masks, which covered either the hydrophilic or the hydrophobic domains. The local resolution across the protein for each class was compared to

the initial set of particles before ‘fishtail’ 3D classification (**Figure 5.9**). Due to the large range in resolution across the whole complex, it was inappropriate to assign a single B-factor to the whole map during post processing, as a high B-factor, which improves the connectivity in low-resolution regions, will reduce the outline of features in high-resolution regions. Hence, for comparison, the filtered maps are shown where the B-factor applied across the map is varied based on the local resolution output. This allowed for the features across the highly heterogeneous maps to be highlighted.

In the particles aligned to the hydrophilic domain, before ‘fishtail’ classification, the resolution of the toe region of the membrane domain is extremely poor, further highlighting the flexibility in this region between particles (**Figure 5.9**). After classification and hydrophilic alignment, there was a slight improvement in the density of the toe region in both classes, however the map continued to be extremely poor and non-continuous. Focused refinement on the membrane domain showed an improvement in the definition of the membrane domain features in both sets of classified particles. In class 2, the resolution and features of the membrane domain noticeably increased in quality and the hydrophilic domain was also better resolved. However, flexible heterogeneity between the two domains was still evident in these particles. Particles in class 5, while also showing better definition in the membrane domain, showed no significant increase in resolution. The lack of sufficient particles in both classes, particularly in class 5, prevented significant improvements in the resolution despite a more homogenous population of particles. This also precluded further focused classifications to further improve the maps. For future structural studies of *Pd*-CI, perhaps a bigger dataset with more particles present in the final classifications would lend itself well to resolving the membrane domain and separating the inherent flexibility in the toe region into distinct classes, while retaining enough particles to resolve each class to a high resolution. Other approaches to limit the flexibility in the membrane domain should also be considered, such as stabilisation of *Pd*-CI by reconstitution into lipids or crosslinking of the membrane domain.

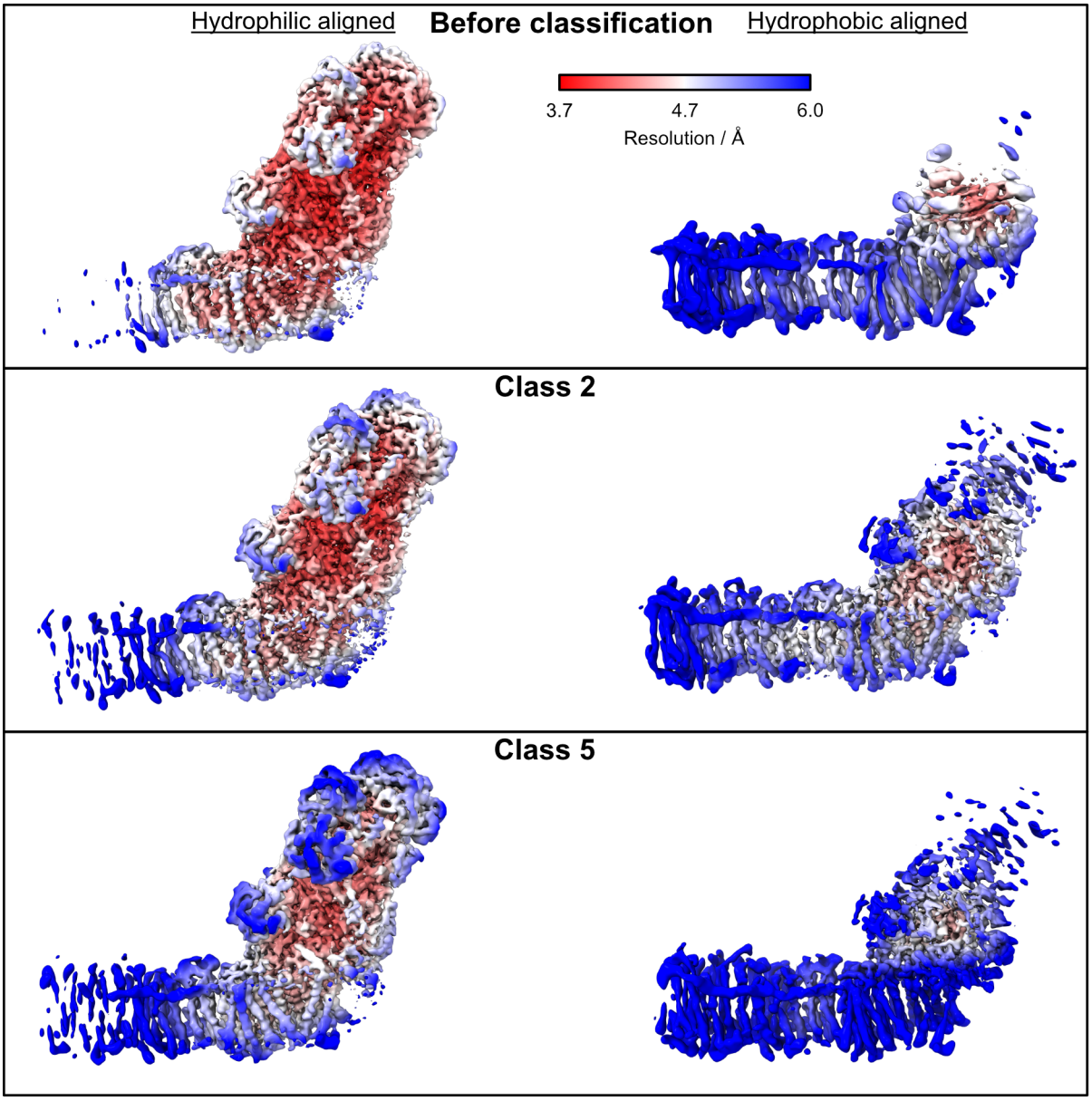

Figure 5.9. Local resolution estimation of *Pd*-CI after classification of different conformations/positions of the membrane domain using a 'fishtail' mask. Particles were aligned and 3D auto-refined to either the hydrophilic or hydrophobic domains using masks that cover each domain. In the top panel, all particles from the final map were aligned to each respective domain. The two major classes after 3D classification using a 'fishtail' mask are shown (classes 2 and 5). These were also aligned to each respective domain and the local resolution was estimated across the maps. Resolution range is shown by the colour key. The locally filtered maps are shown for clarity.

5.5. Features of the partially resolved complex I from *P. denitrificans*

The overall final map shown in **Figure 5.6** is sufficiently good to be able to model a significant portion of complex I. However, attempts to improve the quality of the density map in the toe region of the membrane domain were not entirely successful, making it impossible to build an atomic model into this region of the map. Due to this limitation, it was deemed inappropriate to model the structure of the *Pd*-CI until a sufficiently stabilised and fully resolved electron density map was obtained. Despite this, the well-resolved regions of the *Pd*-CI map were analysed by fitting the atomic model of the core complex I subunits from mouse into the map. By doing this, various features of the *P. denitrificans* enzyme could be identified and analysed on a large scale, providing insight into the purified *P. denitrificans* enzyme in the absence of a complete atomic model.

5.5.1. Missing subunits in the mass spectrometry data are present in the structure

The Nqo7 and Nqo11 subunits of *Pd*-CI were not identified in the purified enzyme by SDS-PAGE and mass spectrometry analyses (see Section 4.7.2). In the electron density map from the *Pd*-CI, these subunits were clearly present, as seen when the active mouse atomic model (PDB: 6ZR2) was fit into the electron density map (**Figure 5.10**). This not only confirms these subunits are present in the purified enzyme, but also highlights that the electron density is well resolved in the membrane domain around the Q-binding site and the resolution in the *Pd*-CI map only suffers significantly in the antiporter-like subunits (Nqo12, 13 and 14).

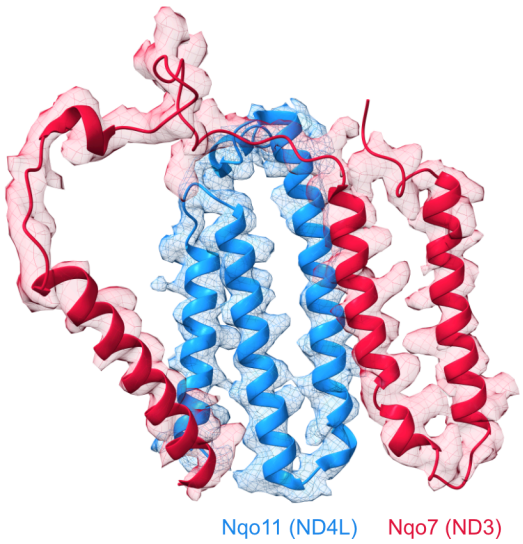

Figure 5.10. Electron density of Nqo7 and Nqo11 subunits from the final overall map of *Pd*-CI. The *Pd*-CI electron density map is shown in a red and blue transparent surface with mesh overlay. Models of the Nqo7 and Nqo11 subunits from mouse complex I (PDB: 6ZR2) are fit into the density to show that they are present. The Nqo7 subunit is in red and the Nqo11 subunit is in blue.

5.5.2. Identification of a new supernumerary subunit

The atomic coordinates of the core subunits from the active mouse enzyme (including the three known homologous supernumerary subunits (PdN7BM (NDUFA12), PdNUYM (NDUFS4) and PdNUMM (NDUFS6)) were fit into the *Pd*-CI map. First, the overall structure is very similar to the mammalian complex I, but the angle between the peripheral arm and the membrane domain is much larger in the bacterial enzyme, which is similarly seen in *T. thermophilus* complex I (Baradaran et al., 2013). Focusing on the peripheral arm, the mouse atomic model appears to fit into the *Pd*-CI map very well, filling most of the electron density. However, there is a key region of additional electron density not modelled by the core subunits and known supernumeraries of *Pd*-CI, suggesting there is a previously unidentified supernumerary subunit bound to complex I (**Figure 5.11A)**. To identify this subunit, it was cross-referenced with the mass spectrometry data of the purified enzyme as analysed in Section 4.7.2. From this, a potential candidate for this additional subunit was identified: protein-L-isoaspartate-O-methyltransferase (PIMT), which repairs L-isoaspartyl and D-aspartyl side chains in proteins that have been damaged in aged proteins (Griffith et al., 2001). This protein was a strong 'hit' in the mass spectrometry data, with a molecular mass of 23.5 kDa and, at the time, could not be excluded or assigned to complex I on mass spectrometry data alone. The PIMT crystal structure from *E. coli* (PDB: 3LBF) was fit into this region of the *Pd*-CI map, showing the atomic model fit extremely well into the electron density (**Figure 5.11B**) (Fang et al., 2010). Thus, a novel subunit of *Pd*-CI has been identified, which has no known homologues in the supernumerary subunits of the mitochondrial enzyme (Carroll et al., 2003).

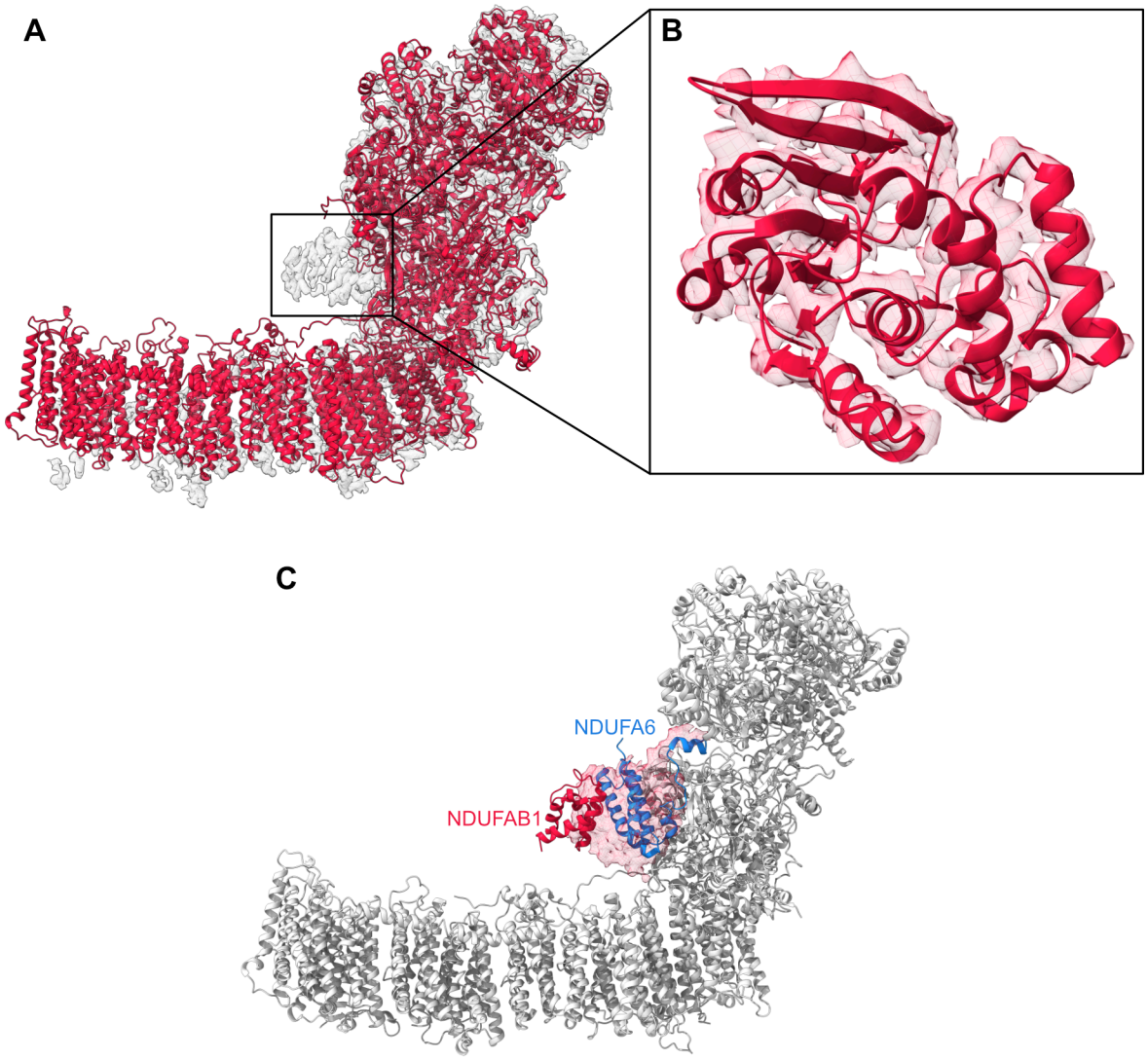

Figure 5.11. Identification of a new supernumerary subunit in *Pd*-CI. (A) Atomic model from mouse complex I (PDB: 6ZR2) fit into the overall electron density map from *Pd*-CI. The 14 core subunits of complex I are shown, as well as the three known supernumerary subunits identified in *Pd*-CI that are known homologues of mammalian supernumerary subunits (PdN7BM (NDUFA12), PdNUYM (NDUFS4) and PdNUMM (NDUFS6)). The *Pd*-CI electron density map is shown in a transparent surface with mesh overlay. The hydrophilic domain and 'heel' of complex I fits well into the resolved electron density. The atomic model does not account for a region of electron density highlighted in the box. (B) PIMT crystal structure from *E. coli* (PDB: 3LBF) fit into the electron density from *Pd*-CI. (C) Core atomic model from mouse complex I in grey with the electron density surrounding the PIMT subunit in the *Pd*-CI map highlighted in red. The supernumerary subunits NDUFA6 and NDUFAB1 from mouse complex I are shown in blue and red cartoons, respectively. Both these subunits appear to occupy the space that PIMT occupies in *Pd*-CI, despite being structurally different from PIMT.

Interestingly, despite no known homologues of PIMT being so far discovered bound to complex I in other organisms, the space occupied by this novel supernumerary subunit is frequently occupied by other supernumerary subunits in the mitochondrial and plant complex I (**Figure 5.11C**) (Agip et al., 2018; Grba and Hirst, 2020; Klusch et al., 2021). At this location, subunits NDUFA6 and NDUFAB1 (human nomenclature) are bound to complex I in mitochondrial and plant enzymes. NDUFAB1 is one of the two acyl carrier proteins (ACPs) bound to mitochondrial complex I, and NDUFA6 belongs to the family of LYR proteins. Canonically, the ACP is a cofactor in fatty acid synthesis, and LYR proteins are accessory factors, which can control mitochondrial homeostasis, FeS cluster biogenesis and have been found to be important for assembly of different ETC complexes (Steger et al., 2014). In mitochondrial complex I, the NDUFA6 subunit anchors the NDUFAB1 subunit to complex I and is essential for complex I activity, possibly providing a pathway for protonation of ubiquinone (Galemou Yoga et al., 2020; Steger et al., 2014). Bacterial complex I from *T. thermophilus* and *E. coli* does not appear to have any additional subunits bound at this location, despite being catalytically active, so NDUFA6 is not necessary for complex I activity in all organisms, particularly in these more basic, minimal models (Baradaran et al., 2013; Kolata and Efremov, 2021). The exact function of the PIMT subunit in *Pd*-CI is not yet established and would require further exploration to determine whether it has an essential role, similar to that of the NDUFA6 and NDUFAB1 subunits bound in the mitochondrial enzyme.

5.5.3. *P. denitrificans* complex I is in the ‘active’ state

Mammalian complex I has been observed to exist in two distinct states, termed the ‘active’ and ‘deactive’ states (Agip et al., 2018; Blaza et al., 2018; Kotlyar and Vinogradov, 1990). Distinct structural features of the active and deactive states in mouse complex I have been identified and are shown in **Table 5.1**. Only one major class of enzyme was identified for *Pd*-CI in the classification schemes (excluding the classification for the toe region heterogeneity). Here, the active (PDB: 6ZR2) and deactive models (PDB: 7AK5) from mouse complex I were fit into the electron density map of *Pd*-CI and compared, to determine which state the *Pd*-CI map matched best. Identifying features are highlighted in **Table 5.1** and in **Figure 5.12**.

Table 5.1. Features of active and deactive states in mouse complex I and suggested by the *Pd*-CI map.

Region	*Pd*-CI electron density map	Active mouse (PDB: 6ZR2)	Deactive mouse (PDB: 7AK5)
Nqo10 (ND6)–TMH3	α-helix	α-helix	π-bulge
Nqo8 (ND1)–TMH5-6 loop	Ordered	Ordered	Disordered (residues 204–213 absent from model)
Nqo4 (NDUFS2)–β1–β2 loop	Ordered	Ordered	Disordered (residues 55–59 absent from model)
Nqo8 (ND1)–TMH4	Bent (side chain density pointing in)	Bent (Tyr127 pointing in)	Straight (Tyr127 pointing out)
Nqo7 (ND3)–TMH1-2 loop	Ordered density for Cys47 present	Ordered Cys39 present/hidden	Disordered (residues 26–50 absent from model) Cys39 absent/solvent exposed

First, the TMH3 of the Nqo10 (ND6) subunit exists as an α-helix in the active state but as a π-bulge, a small stretch of π-helix geometry, in the deactive state. A π-helix is an alternative hydrogen bonding arrangement to the more common α-helical bonding arrangement. In a π-helix a hydrogen bond exists between the N–H group of one amino acid and a C=O group of another amino acid five residues apart. In a standard α-helix the hydrogen bond forms between the N–H and C=O that are four residues apart. As a result of the π-bulge formation in the deactive state, the Phe67 and Tyr69 residues (in mouse) are swung round compared to the active structure (**Figure 5.12A**) (Agip et al., 2019). In *P. denitrificans*, both these residues are Phe residues and the electron density in the map appears to show bulky density for both these residues positioned in similar orientations to the active mouse structure.

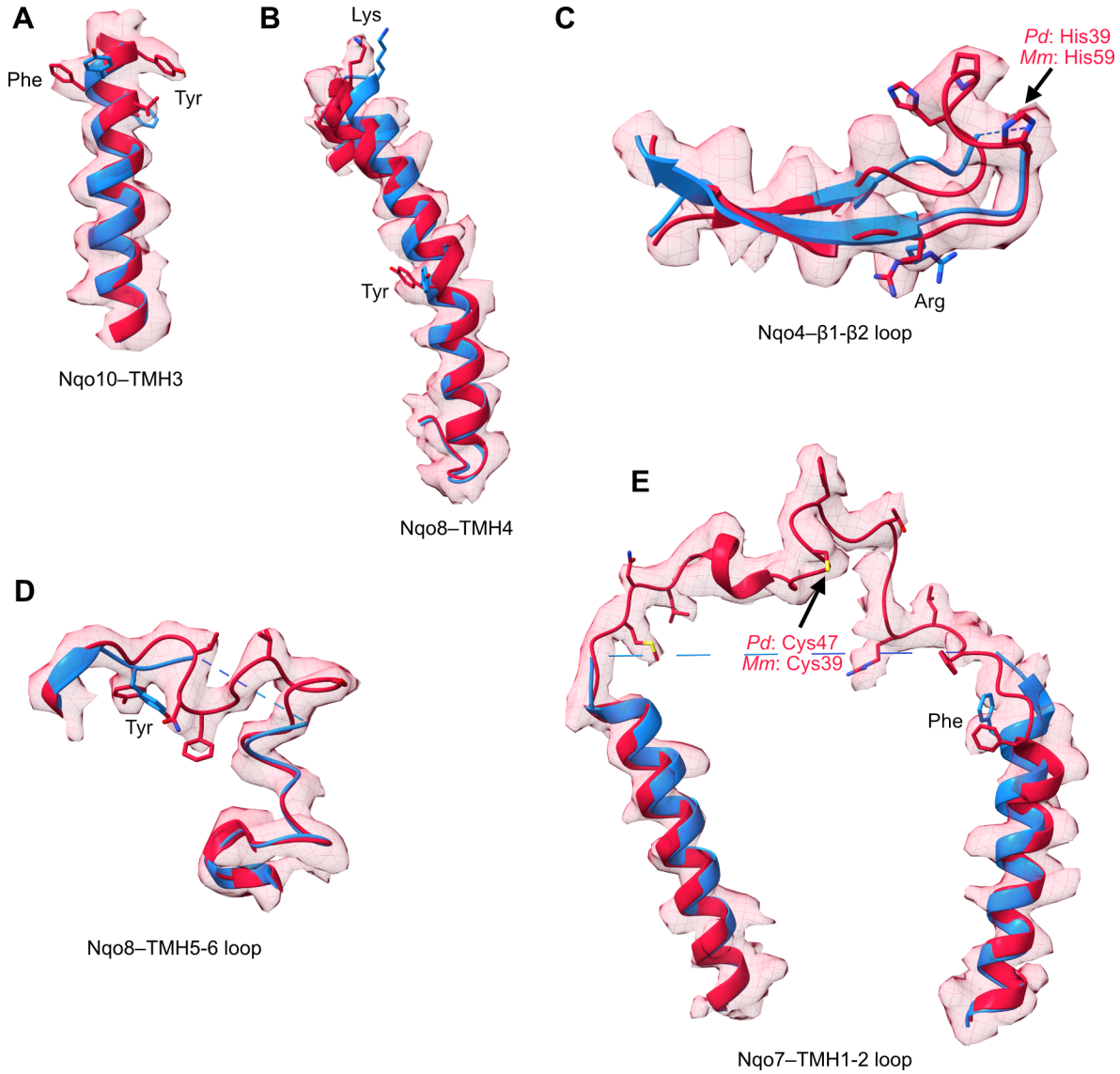

Figure 5.12. Comparison of active and deactive mouse complex I structure fit into the electron density map from *Pd*-CI. The active mouse is shown in red and the deactive mouse is shown in blue. The *Pd*-CI electron density map is shown in a red transparent surface with mesh overlay. Select key residues are shown to highlight side chain differences in the active and deactive models and how they fit into the *Pd*-CI map. Regions of the protein are shown: (A) TMH3 in Nqo10 subunit, (B) TMH4 in Nqo8 subunit, (C) β1-β2 loop in Nqo4 subunit, (D) TMH5-6 loop in Nqo8 subunit, (E) TMH1-2 loop in Nqo7 subunit.

A second feature of the active state is that the TMH4 of Nqo8 is slightly bent relative to the deactive state (**Figure 5.12B**). This results in some key changes in the orientation of some residues, although it is hard to confirm this without modelling the *Pd*-CI density. About halfway down the helix, Tyr142 (mouse numbering) points in different directions in the active and deactive models. The *Pd*-CI map appears to favour the active orientation of this residue. At the top of the helix, a Lys (K126, mouse) is shifted. Again, the active mouse model fits this Lys residue in the *Pd*-CI map.

A general feature of the active mouse model is that many loops in the Q site are well ordered compared to the deactive state. In the *Pd*-CI map, these loops appeared to be well ordered in the structure and adopt similar conformations, further suggesting an active conformation of the enzyme. The ordered loops shown in **Figure 5.12C–E** are the β1-β2 loop in Nqo4, the loop of TMH5-6 in Nqo8, and the loop of TMH1-2 in Nqo7. It is noteworthy that residue His59 (mouse) in the β1-β2 loop of Nqo4 is proposed to coordinate to ubiquinone, along with Tyr108 (mouse), positioning the quinone head group next to the terminal N2 cluster (Fedor et al., 2017; Gu et al., 2022). In the TMH1-2 loop of Nqo7, the cysteine residue that can be labelled with NEM in the deactive state, due to loop disordering, can be seen (Galkin et al., 2008). Here the residue is placed on a well-ordered loop buried in the protein structure. While the features of the *Pd*-CI map suggest *Pd*-CI is wholly in the active state, we also assessed this by labelling *Pd*-CI in membranes with NEM (**Table 5.2**). *P. denitrificans* membranes as prepared were incubated with NEM (or DMSO as a control) followed by measuring the NADH oxidation rate, where NEM-linked complex does not undergo turnover. After incubation with NEM, the as-prepared sample showed similar activities to the DMSO control, suggesting no complex I in the membrane was derivatised by NEM and therefore could not be assigned to a 'deactive' state. Membranes were then 'pre-deactivated' before NEM treatment by heating the membranes to 37 ˚C for 30 min, conditions in which bovine and mouse complex I fully deactivates (Agip et al., 2018; Blaza et al., 2018). This pre-treatment did not appear to result in the formation of a NEM-sensitive deactive state of *Pd*-CI complex I, as full activity was retained between NEM-treated and DMSO-treated samples. These assays underpin the conclusions from the structural analysis that *Pd*-CI is in the active state and that no active/deactive transition has been identified in the *P denitrificans* enzyme.

Table 5.2. N-ethylmaleimide (NEM) sensitivity of *P. denitrificans* membranes. Membranes (5 mg mL^{-1}) were either incubated on ice for 30 min or 'deactivated' by incubation at 37 ˚C for 30 min in the presence of a cOmplete™ EDTA-free protease inhibitor cocktail. Membranes were then diluted to 2 mg mL^{-1} and incubated with 2 mM NEM or DMSO (control) for 20 min on ice. The NADH:O_2 oxidoreduction activities of the membranes were then measured. Activities are reported as average ± S.E.M. (*n* = 3 technical replicates).

Pre-treatment	NADH:O_2 activity / μmol min^{-1} mg^{-1}	
	+ NEM	+ DMSO
As-prepared	0.854 ± 0.019	0.812 ± 0.055
Pre-deactivation	0.800 ± 0.022	0.817 ± 0.043

The A/D transition has so far been described to occur in the mitochondrial enzyme from mammalian species, and in fungi such as *Y. lipolytica* and *Neurospora crassa* (Grivennikova et al., 2003; Kotlyar and Vinogradov, 1990; Maklashina et al., 2003). However, in bacteria such

as *P. denitrificans*, no A/D transition has been observed, agreeing with the structural data here (Grivennikova et al., 2003). In *E. coli*, a different transition called the resting/active transition has been observed, which has similarities to the A/D transition but can occur much faster (seconds vs minutes) and so is unlikely to be associated with large domain movements (Belevich and Verkhovskaya, 2016). *E. coli* lacks the labelling cysteine on the Nqo7 loop, which prevents assessment of these states by NEM labelling and, structurally, a recently resolved *E. coli* complex I model only identified a single state, corresponding to the 'resting' state of the enzyme (Kolata and Efremov, 2021). This resting state was structurally distinct from the mitochondrial deactive state and was considered an uncoupled conformation of the enzyme where proton pumping was disconnected from electron transfer (Kolata and Efremov, 2021).

It is worth noting that there is currently an ongoing debate in the field as to whether the mitochondrial active and deactive states are on-cycle catalytic intermediates rather than off-pathway, bona fide resting states. Further structural and biochemical data would be required to answer these questions, including structures of complex I actively turning over in the presence of native ubiquinone. Complex I from *P. denitrificans* fits very well into the defined active state of the mouse mitochondrial enzyme and does not possess its own distinct conformation like the *E. coli* enzyme. As *Pd*-CI is present entirely in the active state, and appears to lack an A/D transition (it cannot form the deactive state), this model system could be extremely valuable in distinguishing between the catalytic intermediate and resting state proposals. In this way, *Pd*-CI could be used to study the catalytic turnover mechanism in the absence of complicating features of the A/D transition, which may have significant overlap with properties of enzyme turnover. Mutational studies on the *Pd*-CI mechanism can be interpreted without potential complications stemming from changes to the A/D transition that these mutations may have affected in the mitochondrial enzyme.

5.6. Assessing flexibility in the *Pd*-CI membrane and improving stability for cryo-EM

There are several reasons why the membrane domain of *P. denitrificans* complex I may have greater inherent instability and flexibility compared to the mitochondrial enzyme, which resulted in poor-quality electron density in the toe of the membrane domain during cryo-EM analyses. First, complex I exists as a respiratory supercomplex in *P. denitrificans* cells (Stroh et al., 2004). Coordination of complexes III and IV at the membrane region probably helps to stabilise the membrane domain and restrict its flexibility. Here, extracting complex I from its supercomplex may result in a greater degree of instability in this region. This is not surprising as intact complex I was previously shown to dissociate on BN-PAGE, whereas the

supercomplex remains intact (Stroh et al., 2004). It is possible that, to resolve the structure of *Pd*-CI, the entire supercomplex will need to be extracted using mild detergents, such as digitonin, and imaged by cryo-EM to reduce this conformational heterogeneity in the membrane domain.

Mitochondrial complex I can also exist as supercomplexes yet it is still sufficiently stable when extracted from the supercomplex. Mitochondrial complex I is probably stabilised by its large number of supernumerary subunits (39 in the mammalian enzyme), which appear to form a cage around the membrane domain, and which are lacking in the bacterial complex I. *P. denitrificans* only contains three (now four) supernumerary subunits, all of which are found in the hydrophilic domain and which do not stabilise the membrane domain. It is clear from the distinct lack of bacterial complex I structures resolved by cryo-EM that these supernumerary subunits are probably beneficial for isolating a fully intact and stable complex I. A recent attempt to solve the cryo-EM structure of the *E. coli* enzyme also had a similar problem to that seen here (Kolata and Efremov, 2021). The resolution of the overall structure was around 3.3-3.7 Å, but the membrane domain was at a significantly poorer resolution than the hydrophilic domain, with the antiporter-like subunits (Nqo12, 13 and 14) resolved below 8 Å. This is very similar to the issues found in the *P. denitrificans* map here and lends credence to the suggestion that supernumerary subunits in the membrane domain are required to improve membrane domain stability and reduce conformational flexibility in this region of the enzyme. *E. coli* complex I does not exist in higher order supercomplexes, so it should otherwise remain intact in the cell membrane.

To eventually solve the complete *E. coli* complex I structure, the protein was reconstituted into lipid nanodiscs, which are amphipathic helices that wrap around complex I, enclosing it in a lipid bilayer. This helped restrict the conformational heterogeneity and prevent subunit dissociation in *E. coli* complex I (Efremov et al., 2010; Kolata and Efremov, 2021). Reconstitution into lipid nanodiscs, however, did not fully stabilise the membrane domain relative to the peripheral arm and it is notable that to resolve the *E. coli* structure around ten times more particles (1,256,734) were picked than for the *P. denitrificans* enzyme, yet there were still issues arising from conformational heterogeneity. Another recent structure of the detergent-solubilised *E. coli* complex I showed near-identical results to the work here—a poorly resolved membrane domain, which could not be modelled (Schimpf et al., 2022). Even though a milder detergent than DDM, lauryl maltose neopentyl glycol (LMNG), was used to solubilise the enzyme, the same issues were found as seen for the *P. denitrificans* enzyme. This appears to emphasise that issues with the solubilised enzyme are due to inherent flexibly in the membrane domain of the bacterial enzyme, rather than with the solubilisation. Both these

recent *E. coli* structures were published after the project here was initiated and so attempts to stabilise *Pd*-CI were not pursued earlier. In addition, given the greater stability of *Pd*-CI compared to *E. coli*, from biochemical analyses, it was considered sensible to attempt to resolve the detergent-purified structure first (Sazanov et al., 2003).

5.7. Conclusions

The lack of a complete atomic model for *P. denitrificans* complex I remains a key limitation for using this bacterium as a model system for complex I mechanistic studies. However, recent success in determining the *E. coli* complex I structure, by reconstitution into lipid nanodiscs to restrict the conformational flexibility and improve stability of the enzyme, suggest this could be replicated in the *P. denitrificans* enzyme to resolve a complete *Pd*-CI map. This work is currently under investigation and the initial data have shown that the quality of the map in the membrane domain has been significantly improved, allowing a complete model of the enzyme to be built. Until a complete model of *Pd*-CI is available, mutations of *Pd*-CI can be designed based on current published models, as the architecture of the enzyme was shown to be very similar. The creation of point mutations to study the proton-pumping mechanism of complex I is discussed next in Chapter 6.

6. Investigating energy transduction and proton translocation in the Nqo13/ND4 subunit of complex I by site-directed mutagenesis

6.1. Introduction

The Nqo13/ND4 subunit of complex I was chosen as a focus for mutagenesis. It forms the central core of the three antiporter subunits, connecting Nqo14/ND2 to the terminal Nqo12/ND5 subunit, and it interacts with the lateral helix of Nqo12 that runs alongside it. The Nqo13 subunit also features an asymmetric chain of conserved charge residues along the central axis, similar to the other antiporter subunits (as discussed in Section 6.1.1), and therefore is considered to have a crucial role in synchronising and coupling proton translocation. Accordingly, the Nqo13 subunit presents an attractive site for investigating proton translocation and energy coupling in the membrane domain, as well as for probing the role of the lateral helix. This chapter focuses on three important features of the Nqo13 subunit (described in Sections 6.1.1. to 6.1.3.), and their proposed roles based on current evidence. The three features are then investigated by site-directed mutagenesis in the *P. denitrificans* model system, using the experimental strategies and system developed in the preceding chapters. Due to the high structural conservation of the three antiporter subunits in published structures from different species, together with the high sequence conservation and the presence of all the key residues in the *P. denitrificans* genome, it is confidently expected that the structure of the *P. denitrificans* membrane domain will also be closely similar to the membrane domains in existing complex I models. Thus, in the absence of a high-resolution structure for *P. denitrificans* complex I itself, currently available structures (and evidence based on them) provide crucial information to inform our investigations.

6.1.1. A chain of conserved charge residues

The three antiporter-like subunits of complex I (Nqo12/ND5, Nqo13/ND4 and Nqo14/ND2) share a common core bundle of ten TMHs (TMHs 4–13). In mouse complex I, three TMHs have been lost from the N-terminus of Nqo14 and so TMHs 1–10 in mouse Nqo14 correspond to TMHs 4–13 in Nqo12/13. For simplicity, in the mouse model used here as a proxy for a *P. denitrificans* model, equivalent TMHs are all numbered according to the Nqo12/13 numbers (TMHs 4–13). In all three subunits, TMH7 and TMH12 form discontinuous helices, each broken by a loop in the centre (**Figure 6.1**). They can be visualised in the *P. denitrificans* enzyme by

using the AlphaFold predicted structures of the antiporter subunits, which further highlight the expected similarities between models (**Figure 6.1**) (Ronneberger et al., 2021).
Important residues in the antiporter subunits have been identified by extensive site-directed mutagenesis studies of the *E. coli* enzyme. A substantial amount of this work was performed by Yagi and co-workers, with each core membrane domain subunit individually assessed by single point mutations and knockouts, coupled to activity measurements (Kao et al., 2005; Nakamaru-Ogiso et al., 2010; Sato et al., 2013, 2014; Torres-Bacete et al., 2007, 2012). However, detailed interpretations were limited as most of these studies predated the structure of complex I, and because limited biophysical and functional measurements were reported. Key residues identified by these previous studies, and later revealed in structural data, are arranged as a chain of conserved charge residues along the central axis of the membrane. Protonation and deprotonation events along this chain may play a crucial role in transmitting the energy from Q reduction through the membrane domain, driving proton pumping. These residues and their proposed roles in energy transduction are discussed below with specific focus on the Nqo13 subunit (**Figure 6.1**). The residues are numbered according to the *P. denitrificans* enzyme for simplicity.

First, Glu residues are located near the middle of TMH5 in each antiporter subunit (E141 in Nqo13), forming 'closed' Glu-Lys ion pairs with a central Lys on TMH7 (K232 in Nqo13) (**Figure 6.1**). On the basis of molecular simulations, opening and closing of these Glu-Lys ion pairs has been proposed to control channel hydration and thus facilitate proton pumping and/or energy transduction (Kaila, 2021; Mühlbauer et al., 2020). The proposal is that opening of the ion pair results in the Glu on TMH5 coordinating to a Glu/Lys on TMH12 instead, in the adjacent subunit (inter-subunit ion pair formation), causing the energy barrier for subunit hydration to decrease and so providing a possible mechanistic route for controlling proton channel activity (Mühlbauer et al., 2020). The inter-subunit ion-pair interactions in the open conformation are as follows; Nqo14-TMH5-Glu134 to Nqo11-TMH3-Glu73 (not shown), Nqo13-TMH5-Glu141 to Nqo14-TMH12-Lys391, and Nqo12-TMH5-Glu146 to Nqo13-TMH12-Glu405 (**Figure 6.1**). Removal of the charges from the Glu-Lys ion pairs in Nqo13 (E141 and K232 mutations) abolished complex I activity in the *E. coli* enzyme (Euro et al., 2008; Sato et al., 2014; Torres-Bacete et al., 2007), which is consistent with them playing a key role in structure or catalysis. In the equivalent subunit to Nqo13 in the structurally related Mrp complexes of Na^+/H^+ antiporters, (MrpD), Na^+ translocation activities were also abolished when these residues were mutated to Ala or Gln (Morino et al., 2010; Steiner and Sazanov, 2020). However, no cryo-EM structures have so far captured any movement of these residues to provide evidence that they change conformation during catalysis, including for samples that were described as being frozen during turnover (Kampjut and Sazanov, 2020; Parey et al., 2021). Interestingly,

mutations of the Glu and Lys on TMH 5 and 7, respectively, in Nqo14 were much milder, retaining activities of 53–72% of wild type. It was suggested that loss of the Glu is compensated by a conserved Glu in the adjacent Nqo11 (ND4L) subunit, as mutations of both residues to Ala reduced activity to 20% of wild type (Amarneh and Vik, 2003; Sato et al., 2013). Overall, the role of the Glu-Lys pairs is still not well understood and many questions remain, such as do they move during catalysis, do they transport protons via protonation/deprotonation events or do they propagate energy through the membrane domain only through electrostatic interactions?

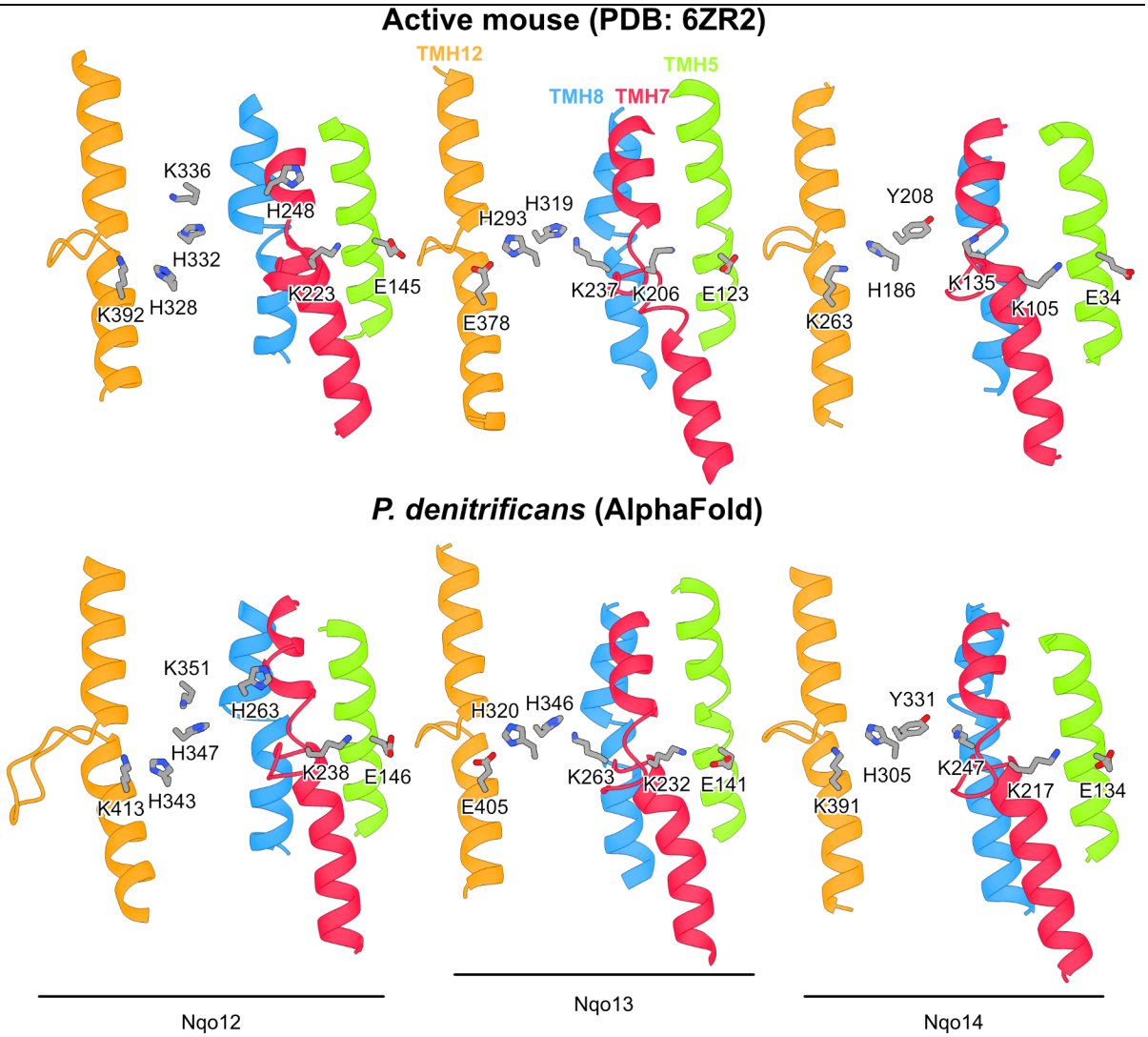

Figure 6.1. Conserved charge residues along the central axis of the membrane domain. The active mouse complex I structure (PDB: 6ZR2) (top) and the *P. denitrificans* complex I structure, predicted by AlphaFold (Ronneberger et al., 2021) (bottom), are shown. The predicted Nqo12, Nqo13 and Nqo14 *P. denitrificans* structures were individually aligned to the equivalent subunit in the active mouse enzyme structure. Only TMHs 5 (green), 7 (red), 8 (blue) and 12 (orange) are shown for clarity in each antiporter subunit. For simplicity, the Nqo14 TMHs of mouse complex I are labelled/coloured based on the equivalent TMHs in Nqo12/13. Key conserved charge residues are highlighted on the enzyme as described in the text for both mouse and *P. denitrificans*. Helices interrupted by substantial loops can be seen in TMH7 and TMH12.

A conserved central Lys on TMH8 in Nqo13 (K263) is considered a candidate to mediate lateral proton/charge transfer (**Figure 6.1**) (Mühlbauer et al., 2020; Röpke et al., 2020). In molecular simulations, protonation of this residue was seen to rapidly close the above Glu-Lys ion pair (and deprotonation to retain the ion pair in the open conformation in the hydrated state) (Mühlbauer et al., 2020). However, the substitution of K263 to an Ala in *E. coli* retained a significant proportion of Q-reductase activity (35–55% of wild type) (Euro et al., 2008; Torres-Bacete et al., 2007) and no equivalent Lys on TMH8 is present in Nqo12 (there is a His instead), making it unclear if this residue is essential to the enzyme mechanism and whether its removal would prevent downstream proton translocation.

As part of the chain of charge residues, conserved Lys residues sit along the central axis near the broken loop of TMH12 in Nqo12 (K413) and Nqo14 (K391), but are replaced by a Glu in Nqo13 (E405) (**Figure 6.1**). This substitution creates an asymmetry between the antiporter subunits, which may be important for the enzyme mechanism and maintaining electrostatic balance during synchronised proton pumping (Kampjut and Sazanov, 2020). No study, to the best of our knowledge, has so far performed mutagenesis on this Glu (E405) residue and so it is an attractive residue to investigate further using the *P. denitrificans* model.

Completing the chain of charged residues along the central axis are His and other conserved charged residues that connect TMH8 to the terminal Lys/Glu on TMH12. In Nqo12 (ND5), this chain of charged residues sits slightly above the plane of the central axis compared with the Nqo13 and Nqo14 subunits (**Figure 6.1**). Mutation of the conserved His residues to Ala in Nqo13 in *E. coli* showed near-wild-type activities in one study (Torres-Bacete et al., 2007) but reduced activities in another, which were accompanied by lower proton-pumping activity, as measured by ACMA and Oxonol VI quenching reactions (Mühlbauer et al., 2020). It was proposed that alternative neighbouring residues and water networks could compensate for the loss of the His residues and enable energy, proton or ‘electrostatic wave’ propagation, but also that the variant enzyme would exhibit reduced proton-pumping stoichiometry. However, lack of suitable methods for quantitatively determining the proton-pumping stoichiometry in the *E. coli* enzyme precluded further investigation.

Overall, disparity in the outcomes of mutational studies, together with a paucity of structural and biophysical data, particularly the lack of ability to determine proton-pumping stoichiometries accurately, provides clear motivation to reassess these residues using the *P. denitrificans* system developed here.

6.1.2. The transverse helix and its connection to Nqo13/ND4

The lateral or transverse helix of Nqo12 is one of the defining features of complex I, but its role remains unclear. Based on various structural and biochemical data, different proposals have been presented. A mechanistic role for the lateral helix has been proposed in which it coordinates the proton pumping of each antiporter subunit. Based on the first structures of the membrane domain, it was suggested that it could act as a piston to drive proton translocation in the individual proton pumps (Efremov et al., 2010). However, there is little evidence to suggest the transverse helix changes its length during turnover. Alternatively, it has also been considered as a 'coupling rod', which moves back and forth (without changing length) instigating and synchronising proton pumping in the three antiporter subunits. In both cases, it should be noted that the lateral helix is not one long, continuous rigid 'rod', but contains a more flexible loop insert at its start and its centre (**Figure 6.2**). In support of these 'coupling' concepts, single point substitutions in the lateral helix at D648 (D563 in *E. coli*) led to a reduction in ACMA quenching by one-quarter relative to NADH oxidation in the *E. coli* enzyme, suggesting the substitution had disengaged the proton-pumping machinery in the Nqo13 subunit (Steimle et al., 2012). D648 on the lateral helix coordinates to the Nqo13 H239 and Y315 residues, forming the connection between the two. However, other studies have not corroborated the suggestion that the helix moves like a piston or rod during turnover. Notably, crosslinking of cysteine pairs introduced along the span of the helix (one in the lateral helix and the other nearby in the Nqo12/13/14 subunit) showed no significant decrease in Q-reductase activity and proton pumping when the lateral helix movement was constrained (Zhu and Vik, 2015). However, these data do not eliminate the possibility that smaller, mechanistically relevant movements, allowed within the constraints of crosslinking, may occur during catalysis.

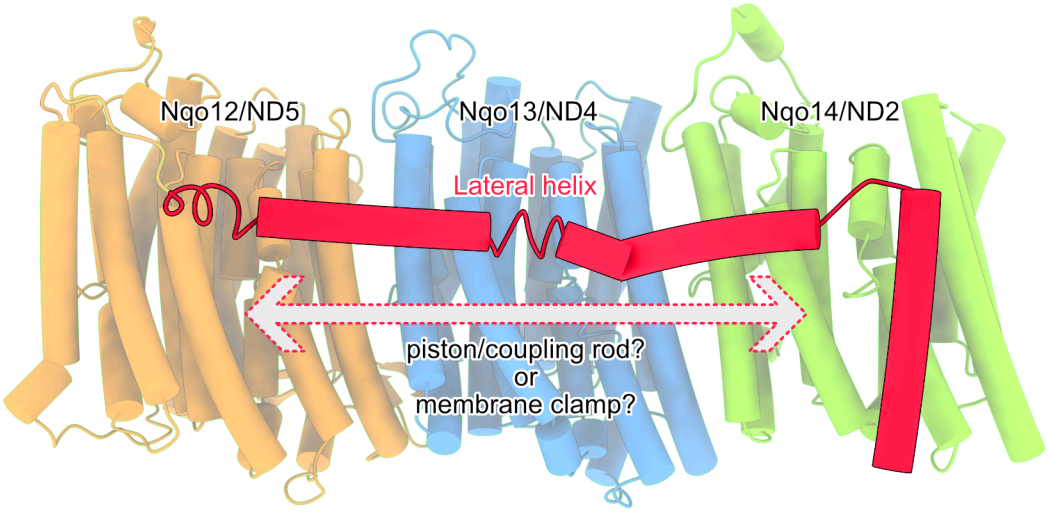

Figure 6.2. Depiction of the lateral helix of Nqo12/ND5 shown in red in the active mouse model (PDB: 6ZR2). Does it act as a piston or coupling rod for synchronising proton translocation across the antiporters or is it just for structural support, clamping the antiporter subunits together?

More simply, the lateral helix may just be an important structural feature for enzyme stability, clamping the membrane domain subunits together and connecting them to the rest of the enzyme. As seen in Chapter 5, the membrane domain is inherently flexible, and so it is entirely possible that the lateral helix has evolved to prevent subunit dissociation. Supporting this, knockout of the Nqo12 subunit, or truncations of the lateral helix in the *E. coli* enzyme, resulted in complex I being unable to fully assemble and no Q-reductase activity was observed (Belevich et al., 2011; Torres-Bacete et al., 2011). In addition, based solely on lower flavin site activities and slower cell growth, enzyme assembly/production was also interpreted as being disrupted in mutants where the lateral helix was extended by 6–7 amino acids at different locations, or where small sections of the helix were replaced with predicted unstructured flexible loops (Belevich et al., 2011). In one variant, a flexible insertion between Nqo12 and Nqo13 designed to disconnect only the Nqo12 subunit, to test the 'coupling rod' hypothesis, showed a much more significant reduction of proton pumping activity (to 20–25% of wild type), as measured by ACMA quenching, than the expected one-quarter reduction (Belevich et al., 2011). Without further structural information for this variant, it is entirely possible that the opposite is true, and that instead only the Nqo12 subunit remained connected to the proposed coupling rod. However, the reduction in proton pumping was accompanied by an equally significant reduction in Q-reductase activity, which makes any further interpretation of this data impossible without more quantifiable measures of proton pumping that take into account the turnover rates of ubiquinone. These studies predated high-resolution structural information, which could better inform the structural implications of the mutations, yet it was clear that enzyme stability was often compromised when the lateral helix was manipulated. This points

to a role of the lateral helix in stabilising the enzyme, but makes it hard to disentangle whether it also plays a mechanistic role.

In other studies, truncations of the lateral helix and the Nqo12 subunit have produced a partially assembled enzyme, which retained some activity. In one study in *E. coli*, truncation of the lateral helix and Nqo12 knockout variants retained Q-reductase activities, and a reduced $H^+/2e^-$ stoichiometry of two or fewer was proposed based on a reduced ACMA quench relative to wild type (Steimle et al., 2011). The subunit composition of the enzyme was not well defined, and it is also probable that other subunits, such as Nqo13, were also missing. More convincingly, in *Y. lipolytica* complex I, a serendipitous supernumerary subunit knockout generated a partially assembled complex I missing the Nqo12 and 13 subunits, which was otherwise intact and had retained ~38% of the wild-type activity (Dröse et al., 2011). It also showed a reduced proton-pumping stoichiometry, translocating half the normal number of protons, as measured by ACMA fluorescence experiments with complex I reconstituted into proteoliposomes (Dröse et al., 2011). These studies may suggest the lateral helix is critical in connecting Nqo13 to the rest of the enzyme, but, crucially, they also advocate the hypothesis that each antiporter subunit pumps only one proton across the membrane, and show that enzyme turnover can proceed despite being coupled to the translocation of fewer protons. A recent hypothesis based on cryo-EM structures proposed that all protons may be ejected to the P side of the membrane via the Nqo12 subunit alone, in disagreement with these studies (Kampjut and Sazanov, 2020; Parey et al., 2021). Clearly, questions remain about the role of the transverse helix in proton translocation, and whether the enzyme lacking one or more antiporter subunits is still able to translocate protons. Considering the inconsistencies of the above studies, it is imperative to definitively investigate the function of the lateral helix and the role it may play in driving and coupling proton translocation—is it a 'coupling rod' or a structural clamp, and are fewer protons pumped by complex I when antiporter subunits are deleted or disconnected from the lateral helix?

6.1.3. Gating mechanisms for controlling half-channel hydration in Nqo13

Water channels, where protons from the N-side of the membrane may enter the protein, have been proposed in each antiporter subunit. Recently, various residues have been suggested to control the opening and closing of these channels during catalysis and so may be crucial in the enzyme mechanism (**Figure 6.3**). Hydration simulations in the *T. thermophilus* structure revealed a half channel between TMHs 7b, 8 and 10, which can fill with water (Di Luca et al., 2017, 2018), and its hydration was coupled to changes in the backbone bonding between a Leu-His pair and the tilting of TMH7. Interestingly, a complex I structure from *Y. lipolytica*

showed the same Leu residue to be shifted in Nqo14 compared to Nqo12 and Nqo13, and more water molecules, which could be modelled for the first time in this high-resolution structural information, were observed in the Nqo14 subunit channel (**Figure 6.3A**) (Grba and Hirst, 2020). This led to the proposal that the Leu is acting as a gate for the channel, where, depending on its position, either pointing into the channel or away from the channel, it blocks or permits its hydration. An adjacent, conserved Trp also changed position and it was suggested that this Trp may be important in positioning the gating Leu residue (Grba and Hirst, 2020). This Leu-His-Trp triad may therefore play an important role in governing proton translocation in Nqo13 by controlling water access. Protonation of the central Lys on TMH8 (K263) has been suggested to open this gating mechanism (Di Luca et al., 2018).

Another gating mechanism has been described based on a second high-resolution structure of *Y. lipolytica* complex I, which also showed the Nqo14 subunit to be the most hydrated in the half channel connected to the N-side (**Figure 6.3B**) (Parey et al., 2021). A different conformation of TMH11 in Nqo13 compared to Nqo14 positioned a Phe (F343 in *Y. lipolytica*) near the channel, which blocked hydration, much like the above-proposed gating leucine residue. In silico remodelling of the Phe to a different position allowed rapid hydration of the channel in simulations (**Figure 6.3B**) (Parey et al., 2021). To explore the Leu and Phe gating mechanism further, mutations designed to disrupt or remove these residues should be investigated, with the potential to reveal how this mechanism for controlling channel hydration is important for lateral energy transduction from the Q-site and/or proton pumping in the antiporter subunits.

Finally, as part of the half channel, a highly conserved His (H246) in Nqo13, which sits above the Leu-gating residue, has been proposed to be a key residue in importing protons or forming an ordered water network from the N-side to the central axis of the subunits (**Figure 6.3B**) (Di Luca et al., 2017; Kampjut and Sazanov, 2020). However, no prior mutagenesis studies of this residue have been performed to confirm its importance. Thus, its mutagenesis presents an attractive target for investigating what happens to enzyme turnover when this water channel is disrupted, and how removal/modification of this residue may prevent proton translocation in Nqo13 if it acts as a key ‘stepping stone’ in the proton import route.

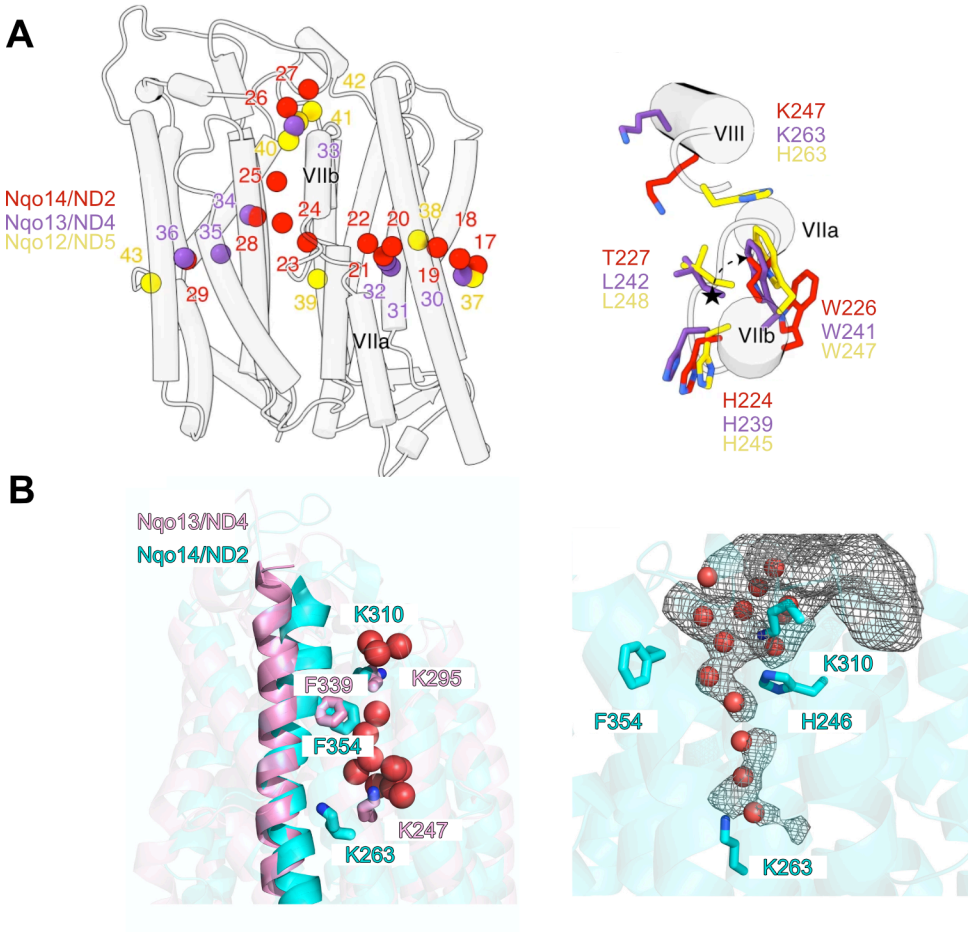

Figure 6.3. Proposed gating mechanisms for the import of protons into the half channel connecting the N-side with the central axis. (A) Leu-His-Trp triad gating mechanism as proposed by Grba and Hirst (2020). The Nqo12 (yellow), Nqo13 (purple) and Nqo14 (red) subunits are overlaid and the water molecules and residues of the Leu-His-Trp triad are highlighted. Greater hydration in the Nqo14 subunit can be seen (red spheres, left panel) when the Leu (and Trp) residue has moved away from the channel (right panel). Figure adapted from Grba and Hirst (2020). (B) Possible Phe-gating residue on TMH11 as proposed by Parey et al. (2021). The left panel shows overlaid Nqo13 (cyan) and Nqo12 (pink) subunits with distortion in the TMH11, positioning F354 away from the proposed half channel. Modelled water molecules from the Nqo14 subunit are shown as red spheres. The right panel shows the Nqo13 subunits after in silico remodelling of the F354 residue away from the half channel. The mesh shows simulated waters forming a wire to the central lysine on TMH8 (K263). Figure adapted from Parey et al. (2021). For clarity, residues in all panels have been labelled with the equivalent *P. denitrificans* numbering. All residues are conserved with *Y. lipolytica* apart from the gating Leu residue in Nqo14/ND2, which is replaced with a Thr in *P. denitrificans*.

6.2. Aims of this chapter

- To create single point mutations in the membrane domain of complex I to assess the energy-coupling and proton-translocation mechanisms.
- To investigate the role of key conserved charge residues in the Nqo13 subunit in lateral energy transduction.
- To evaluate the coordination of the lateral helix of Nqo12 to the Nqo13 subunit and its role in proton translocation at Nqo13.

- To investigate the proposed gated proton import channel in the Nqo13 subunit.

6.3. Design of complex I variants

Residues were chosen for site-directed mutagenesis according to the three separate strands of investigation discussed above. Unless noted, all mutations were made in the Nqo13 subunit and are numbered according to the *P. denitrificans* enzyme. All mutations are single point mutations and were not created in combination.

6.3.1. Investigating the residues involved in lateral energy transduction

The first set of mutations was designed to assess the importance of the charge and polarity of the chain of conserved charge residues that span the central horizonal axis of the Nqo13 subunit (**Figure 6.4**, set 1). To remove the charge in the conserved Lys and Glu residues, while preserving their polarity and similar size of side chain, each residue was mutated to a Gln (E141Q, K232Q, K263Q and E405Q). These mutants were designed to investigate whether protonation/deprotonation events of these residues are essential during turnover. In addition, a pair of conserved His residues (H320 and H346) complete the chain of charge residues in the Nqo13 subunit. These His residues probably have similar roles to each other and so were considered equivalent. Two differing roles for them were investigated by substituting each with a different side chain. One was mutated to a Gln (H346Q) to investigate the requirement for protonation/deprotonation, but without removing its polarity so as to maintain possible hydrogen-bonding networks. The other was mutated to a Leu (H320L), a more severe mutation, where the aliphatic substitution may disrupt the establishment of an ordered network of water molecules.

6.3.2. Investigating the role of the lateral helix and its coordination at Nqo13

The second set of mutations was designed to weaken the coordination of the Nqo12 lateral helix to the Nqo13 subunit to clarify the role of the lateral helix in proton pumping and assess reported reductions in the proton-pumping stoichiometry when point mutants were created in this region (Steimle et al., 2012). The $D648^{Nqo12}$ residue on Nqo12 coordinates to H239 and Y315 in the Nqo13 subunit (**Figure 6.4**, set 2). Structures from various species show varied distances for the coordination of Asp to the Tyr and His residues (between ~2.7–4.9 Å and ~2.4–4.6 Å, respectively) and so the precise nature of this coordination is unclear (hydrogen bonding vs ionic bonding vs coordination via bridging waters). The $D648N^{Nqo12}$ mutant was created to replace the carboxylate group with an amide side chain to weaken the coordination to both Y315 and H239 via any ionic bonding. In separate point mutants, the Y315F variant

was generated, designed to remove its hydrogen/ionic bonding capabilities, and a H239Q mutant was designed to weaken the charge interaction with $D648^{Nqo12}$. In addition, an Nqo13 subunit knockout was also designed to investigate whether the enzyme was still able to catalyse Q-reduction and/or proton pumping, or whether the enzyme was still assembled after the Nqo13 subunit (and probably also the Nqo12 subunit) was removed.

6.3.3. Investigating the proposed gated proton import/hydration channel

Finally, a set of mutations were designed to probe the proposed Leu-gating mechanism, which may control channel hydration in the Nqo13 subunit, and, subsequently, proton import/uptake from the N-phase (**Figure 6.4**, set 3). The residues of the gating Leu-His-Trp triad were altered to disrupt its mechanism. First, an L242A substitution was created to assess the effect of shortening this proposed gating Leu residue, reducing its steric bulk and preventing it from blocking the hydration channel. This may result in an enzyme with a permanently open, hydrated channel to the N-side. Residue W241 was also seen to be shifted in the hydrated Nqo14/ND2 subunit relative to the other antiporters, which were dehydrated in *Y. lipolytica* cryo-EM structures. The W241F mutant was created to reduce the size of this bulky residue, while maintaining its hydrophobicity. This may lead to perturbations in its coordination with other surrounding residues, altering its position. If the coordination/positioning of the Trp is important for controlling the correct orientation of the adjacent proposed gating Leu, altering this residue may lead to problems controlling channel hydration in the Nqo13 subunit. As part of the triad, H239, which is backbone bonding with the L242 gating residue, may also help position the Leu correctly. Creation of the H239Q variant, designed to weaken coordination to the lateral helix of Nqo12, may disrupt its conformation and subsequently how the backbone coordinates to the Leu.

Two additional variants were generated, which were linked with the same hydration channel. A conserved, nearby Ala on TMH10, which protrudes into the proposed channel and forms a contact to the gating L242, was mutated to a larger Leu residue (A314L) with the aim of permanently blocking the hydration channel, as this residue does not appear to move in different hydration states of the antiporters. On TMH7, residue H246 was modified to a Phe (H246F) so it was no longer able to transport a proton or able to form hydrogen bonds, so assessing whether this residue was a crucial link for proton import during channel hydration, as previously proposed (Di Luca et al., 2017; Kampjut and Sazanov, 2020). Finally, sitting at the top of the proposed channel is the clinically relevant residue, R367, modified in Leber's hereditary optic neuropathy (LHON), which has been seen to coordinate a water at the top of the channel (Grba and Hirst, 2020). The clinical relevance of the LHON mutant (R367H), which leads to vision loss in patients, suggests there is a functional defect linked with this residue,

which should be investigated. Here, the LHON mutant was replicated and included in this strand of investigation as part of the hydration channel.

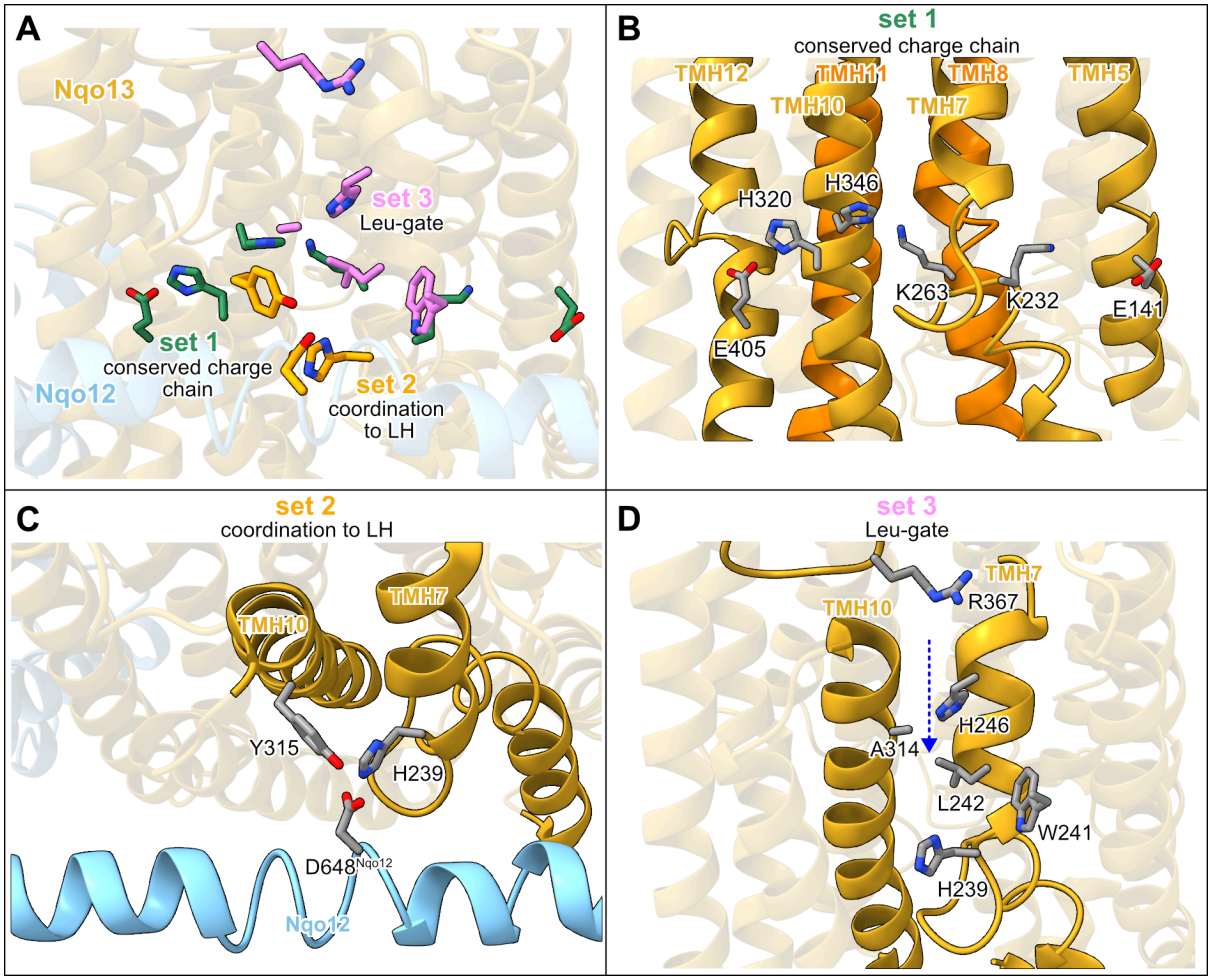

Figure 6.4. Overview of mutations created. (A) Residues mutated in the Nqo13 subunit separated into three groups. Conserved charged wire (set 1, green), coordination to the lateral helix (set 2, orange) and Leu-gating residues (set 3, pink). (B) Conserved charge residues along the central axis of Nqo13. (C) Coordination of the lateral helix (LH) to Nqo13 via $D648^{Nqo12}$ on the LH, and Y315 and H239 on TMH10 and TMH7 of Nqo13, respectively. (D) Residues involved in the proposed Leu-gating mechanism. The conserved Leu-His-Trp triad is shown along with an Ala on TMH10 and a His on TMH7. The residue mutated in LHON diseases is also highlighted at the top of the proposed channel (R367). Arrow shows channel hydration route. All images were created using the active mouse model (PDB: 6ZR2), which matches the *P. denitrificans* structure best, and where all residues shown are conserved with *P. denitrificans*. All residues are labelled according to *P. denitrificans* numbering for clarity. The numbering for equivalent residues from different species are shown in **Table 6.1**.

Table 6.1. List of complex I residues mutated in this chapter. All residues are in the Nqo13 (ND4) subunit unless otherwise indicated. The numbering for equivalent residues in other key model organisms is shown. The mutations are separated into three groups to investigate different features of the membrane domain. The final column shows the amino acid substituted.

Set	*P. denitrificans*	*M. musculus*	*E. coli*	*Y. lipolytica*	*T. thermophilus*	Mutation
Set 1	E141	E123	E144	E142	E123	Q
	K232	K206	K234	K221	K204	Q
	K263	K237	K265	K252	K235	Q
	E405	E378	E407	E395	E377	Q
	H320	H293	H322	H309	H292	L
	H346	H319	H348	H335	*S318*	Q
Set 2	D648^{Nqo12}	D554	D563	D580	D557	N
	Y315	Y288	Y317	Y304	Y287	F
	H239	H213	H241	H228	H211	Q
Set 3	L242	L216	L244	L231	L214	A
	H246	H220	H248	H235	H218	F
	A314	A287	A316	A303	A286	L
	W241	W215	W243	W230	W213	F
	R367	R340	R369	R357	L339	H

6.4. Creation of complex I variants

A DNA construct was designed for site-directed mutagenesis based on the approach described in Chapters 3 and 4. A stretch of DNA was synthesised by GENEWIZ that contained *nqo13* (Pden_2232) flanked by 1000 base pairs on either side (**Figure 6.5**). The flanking regions encompassed a section of each of the *nqo14* (Pden_2231) and *nqo12* genes (Pden_2233). A kanamycin resistance gene was added to the end of the second flanking region. *Eco*RI sites were added at both ends of the DNA construct, and internal *Eco*RI restriction sites were edited out. The construct was used to generate all the mutations studied, in both the Nqo13 subunit and in the C-terminus of the Nqo12 subunit, as the required part of the Nqo12 was contained in the F2 flanking region. Site-directed mutagenesis of the construct was performed using the primers given in **Table 2.1**. To generate the ΔNqo13 strain, a STOP codon was introduced 50 amino acids into the Nqo13 sequence.

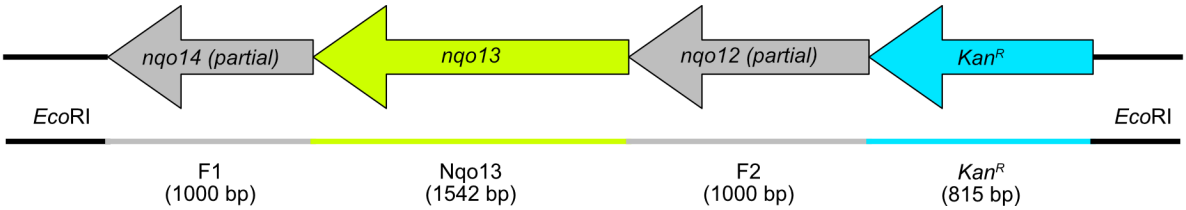

Figure 6.5. DNA construct designed for the creation of Nqo13 (and Nqo12) complex I variants. The arrow direction shows the open reading frame direction in the *P. denitrificans* genome. In the construct, the entire *nqo13* sequence is flanked by 1000 bp regions, which contain parts of the *nqo12* and *nqo14* genes. The lengths of each section of DNA in the construct are shown. *Eco*RI sites were added to both ends of the construct.

Table 6.2. List of primers used to generate and screen complex I variants. The base pairs that have been altered from the wild-type sequence are highlighted in red. The reverse (Rev) strand primer and the forward (Fwd) primer used to generate the mutations are shown. To sequence colonies for successful mutagenesis, primers bF_ND4 and bR_ND4 were used to amplify the *nqo13* and surrounding genes creating an ~3500 bp PCR product. The primers a1 to a4 were used to sequence the ~3500 bp PCR product and identify successful genomic substitutions.

Mutation	Primer (5'–3')	Original codon	Variant codon	Primer for sequencing
E141Q Fwd	GGAAGAACAGGTAGAACAGCACCAG	GAG	CAG	a2
E141Q Rev	AGGCGGGGCTGATCCCGATG			
K232Q Fwd	GGACCGCGAAGCTGGCAAAG	AAG	CAG	a2
K232Q Rev	AGATGCCGATGTGGCCGGTC			
K263Q Fwd	GCAGCAGCACCGCGGCCAGCAG	AAG	CAG	a2
K263Q Rev	AGATGGGCGGCTACGGCTTC			
E405Q Fwd	GGCCCACGAAACCCGAGGTG	GAG	CAG	a1
E405Q Rev	AGTTCCTGACGCTGATGGGG			
H320L Fwd	CGTAGCCCATCAGGGCGACCGAG	CAT	CTG	a2
H320L Rev	TGACCATGGGCGTCTTTGCC			
H346Q Fwd	GAGATAAAGCCCTGCGACAGCATC	CAC	CAG	a1
H346Q Rev	GGGCGCGCTGTTCCTGTGCG			
D648N^{Nqo12} Fwd	TGCCGCCCTTCCACAGCACG	GAC	AAC	a3
D648N^{Nqo13} Rev	ACGGCGCCGTCATCGACGGC			
Y315F Fwd	GAAGGCGATGACCTTCTTCATG	TAT	TTC	a2
Y315F Rev	TCCTCGGTCGCCCATATGGG			
H239Q Fwd	CTGGACCGGCCACATCGGC	CAT	CAG	a2
H239Q Rev	ACCTGGCTGCCCGACGCGC			
L242A Fwd	GCGCGTCGGGCGCCCAGGTATGG	CTG	GCG	a2
L242A Rev	ACGTCCAGGCGCCGACCGCC			
H246F Fwd	GCGCCTGGACGAACGCGTCGGGC	CAC	TTC	a2
H246F Rev	CGACCGCCGGCTCGGTCCTG			
W241F Fwd	CGTCGGGCAGGAAGGTATGGACC	TGG	TTC	a2
W241F Rev	CGCACGTCCAGGCGCCGACC			
A314L Fwd	CCGAGGAATACAGGATGACCTTC	GCC	CTG	a2
A314L Rev	TCGCCCATATGGGCTACGTG			
R367H Fwd	CGTCGATCTCGTGCGTGTGCATG	CGC	CAC	a1
R367H Rev	CCTATGGCGGGTTGGTGAAC			

ΔNqo13 Fwd	GAACAGCACGAACTACGAGATCACG	CTT	TAG	a4
ΔNqo13 Rev	CGCTTCGACCCGGCGAACAC			
a1	TAATCGGCGCTCATCGCCAG	–	–	–
a2	AGCCGTGCGACAGCATCTGG	–	–	–
a3	GAACAGCGCCATGATGATGG	–	–	–
a4	ACAGCACCGAGATGCCGTCC	–	–	–
bF_ND4	GCAGCATGTTCTGCACGCCG	–	–	–
bR_ND4	CGGAACTATGGCGGGCTGCG	–	–	–

To create genomic single point substitutions in *P. denitrificans*, the homologous recombination protocol described in Chapter 4 for the creation of the *Pd*-Nqo5^{His6} strain was followed. Imperative for all complex I mutagenesis, NDH-2 expression was induced by the presence of 10 mM taurine in all media during creation of the mutants. To facilitate the purification of all variants, mutants were created in the *Pd*-Nqo5^{His6} strain. Recombined colonies for each variant were screened by colony PCR across the *nqo12* and *nqo13* genes, followed by sequencing of the products. The number of colonies screened for each mutant and the number of successful genomic substitutions are shown in **Table 6.3**. No colonies were identified for creation of the ΔNqo13 variant. Attempts to generate this mutant using an alternative construct, where the entire Nqo13 gene was deleted from the genome instead, also failed.

Table 6.3. List of complex I variants identified by colony PCR and sequencing. The number of correctly recombined complex I variants is shown versus the number of colonies sequenced.

Mutation	Variants identified/colonies screened		Mutation	Variants identified/colonies screened
E141Q	8/24		H239Q	7/15
K232Q	1/24		L242A	1/24
K263Q	5/24		H246F	1/128
E405Q	2/24		W241F	1/24
H320L	1/12		A314L	8/24
H346Q	6/24		R367H	3/12
D648N^{Nqo12}	7/32		ΔNqo13	0/158
Y315F	4/15			

6.5. Catalytic activity of the complex I variants in membranes

To investigate the effect of each point mutation on enzyme function, the catalytic activities in membranes were measured (**Figure 6.6**). Three samples of membranes from individual cell culture experiments were prepared for each variant ($n \geq 3$ biological replicates), supplementing cell growth with NDH-2 expression in cultures that either did not grow without expression or where the OD_{600} of overnight cultures was significantly lower than wild type. Mutants that required NDH-2 expression for cell growth were E141Q, K232Q, K263Q, E405Q, L242A and H246F. The growth of the H320L mutant also benefited from the expression of NDH-2, allowing a sufficient mass of cells to be harvested. The flavin site (dNADH:$APAD^+$) and Q-reductase (dNADH:O_2) activities were measured for each variant using the complex I-specific substrate dNADH (Matsushita et al., 1987). The complex I-specific activities were also measured when complex III and IV were inhibited with antimycin A and KCN, respectively, with supplementation of 20 μg mL^{-1} AOX (dNADH:AOX) allowing reoxidation of the ubiquinol. The trend in dNADH:O_2 activity was nearly identical to the dNADH:AOX activity, showing that complex I turnover was not limited by complex III and IV catalysis. To compare activities between variants, and account for differences in complex I content between individual membrane preparations, the Q-reductase activity was normalised to the dNADH:$APAD^+$ activity. This normalisation assumed that the flavin site activity was unaffected by all the mutations, being distant from the flavin site. The dNADH:$APAD^+$ activity varied slightly between membrane preparations and variants. The data showed that the Q-reductase activities were significantly diminished relative to wild type for mutants E141Q, K232Q, K263Q, E405Q, L242A and H246F, with ≤18% of wild-type activity (**Figure 6.6D**). The H320L variant showed an intermediate effect on catalysis with a statistically significant reduced activity compared to wild type (57%). All other variants showed similar (or slightly reduced activities) that were not significantly changed relative to wild type.

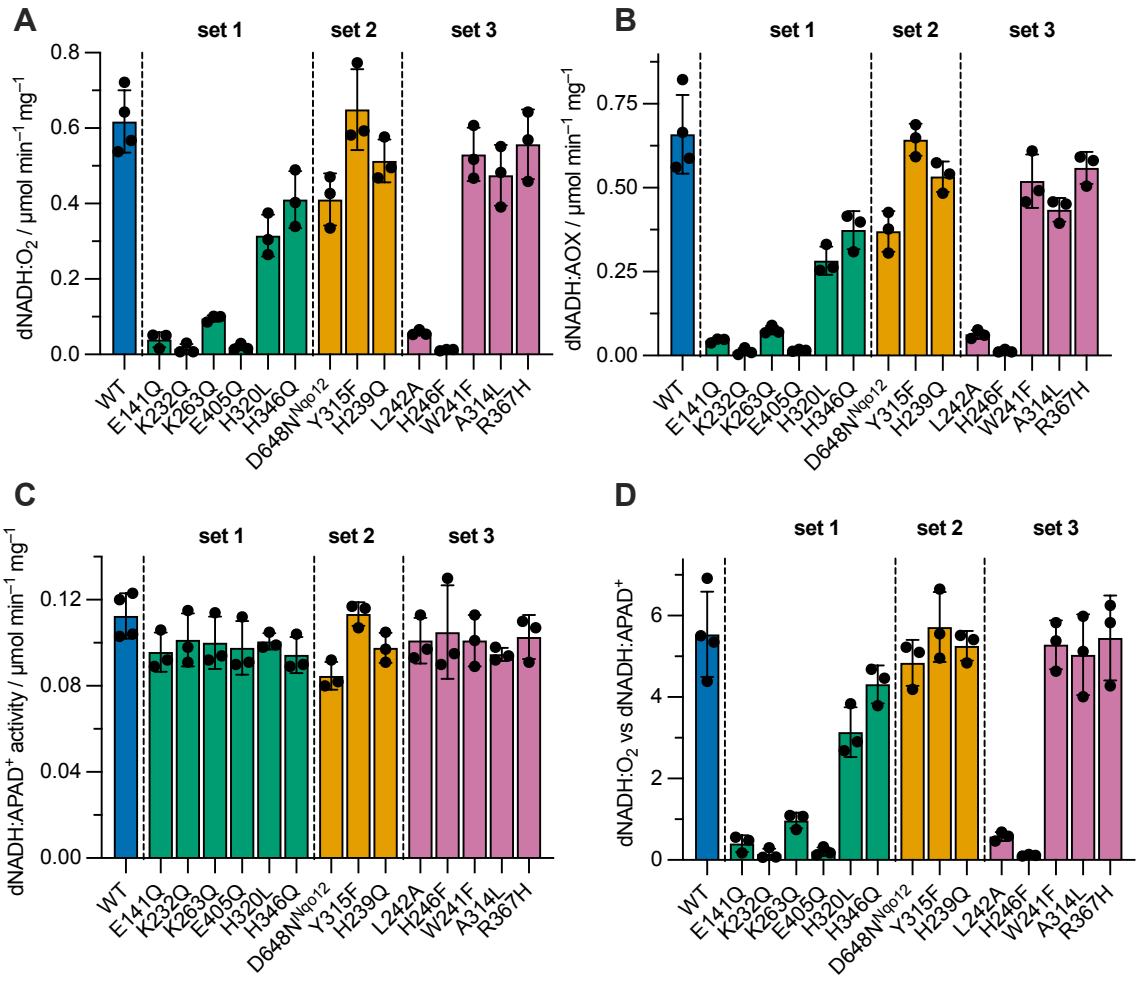

Figure 6.6. Catalytic activities in membranes for wild type and variants. Membranes were prepared in biological replicates ($n \geq 3$) for each variant and the catalytic activities (dNADH:O_2, dNADH:APAD$^+$ and dNADH:AOX) were measured. The average of three technical replicates for each biological replicate are shown as individual points. The piericidin-insensitive background rate was subtracted from the dNADH:O_2 and dNADH:AOX rates. The bar represents the average of the three biological replicates and the error bar the S.D. (A) dNADH:O_2 activity of membranes. (B) dNADH:AOX activity of membranes, which were supplemented with 20 µg mL^{-1} AOX and where complexes III and IV were inhibited with 1 mM antimycin A and 400 µM KCN, respectively. (C) dNADH:APAD$^+$ activity of membranes. (D) Normalisation of dNADH:O_2 vs dNADH:APAD$^+$. Each point represents the dNADH:O_2/dNADH:APAD$^+$ ratio of an individual membrane preparation. All assays were performed with 10 µg mL^{-1} membranes in buffer containing 10 mM MES pH 6.5 at 32 ˚C, 25 mM NaCl, 2 mM $CaCl_2$ and 20 µg mL^{-1} alamethicin. Statistical significance in panel D was calculated by one-way ANOVA between all strains followed by Dunnett's test comparing each variant to wild type. E141Q, K232Q, K263Q, E405Q, H246F and L242A mutants record a p value <0.0001. Residue H320L recorded a p value <0.001. All other variants were not statistically significant compared to wild type.

6.6. Assembly and structural integrity of complex I variants

6.6.1. Size-exclusion chromatography and SDS-PAGE

To assess their structural stability, each variant was purified as described in the Materials and Methods (Section 2.3.3), and their size-exclusion chromatography absorbance profiles (recorded at 280 nm) were compared to that of wild type (**Figure 6.7**). Nearly all variants eluted at a similar volume to wild type (1.17 mL), indicating the complexes were of matching size and thus the point mutations had not significantly disrupted the enzyme assembly and caused loss of subunits. Only the D648N^{Nqo12} variant showed a slight delay in elution (1.22 mL), possibly suggesting structural perturbations or instability in the purified enzyme. Each purified variant was then analysed by SDS-PAGE (**Figure 6.8**). All variants, including the D648N^{Nqo12} variant, displayed a near-identical band pattern to that of wild type, and thus had retained the full complement of complex I subunits. There was also no obvious evidence of NDH-2 contamination in purified samples, as no additional band at ~47 kDa was seen for compromised mutants expressing NDH-2 (E141Q, K232Q, K263Q, E405Q, H320L, L242A and H246F) compared to wild type.

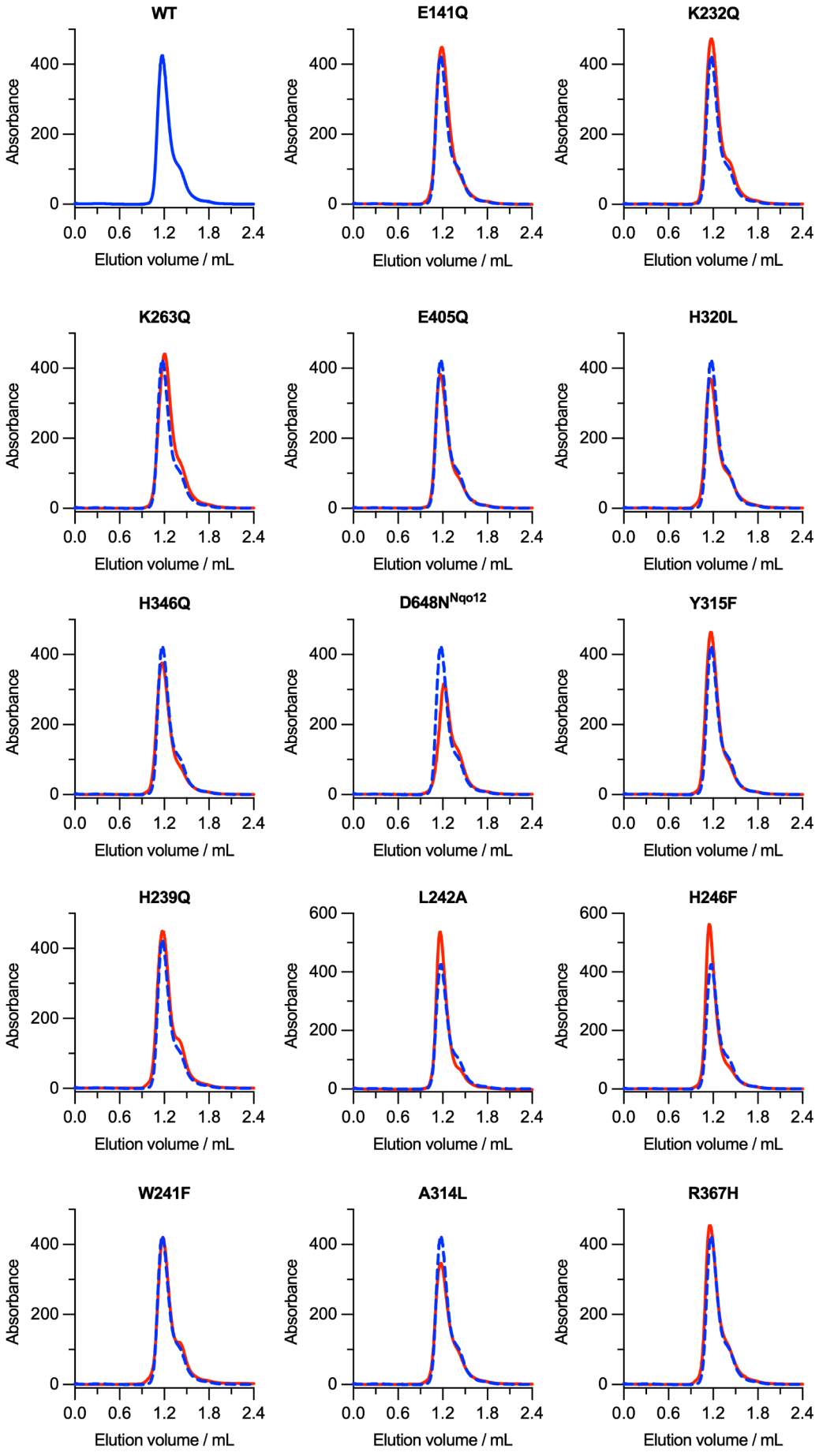
WT
E141Q
K232Q
K263Q
E405Q
H320L
H346Q
D648N^Nqo12
Y315F
H239Q
L242A
H246F
W241F
A314L
R367H
Absorbance
Elution volume / mL
0.0 0.6 1.2 1.8 2.4
0 200 400 600

Figure 6.7. Elution profile of wild type and variants analysed by size-exclusion chromatography. Complex I from each variant was first isolated as described in Chapter 4. The purified samples were subsequently diluted in gel filtration buffer (20 mM MES pH 6.5 at 4 ˚C, 150 mM NaCl, 10 mM $CaCl_2$, 10% glycerol, 0.05% DDM) and loaded onto a Superdex 200 increase 5/150 GL size-exclusion column (~200 µg of complex I) at a flow rate of 0.15 mL min^{-1}. The absorbance at 280 nm is shown for each sample and for comparison, the wild-type elution profile is shown as blue dashed lines overlayed onto each variant shown in red.

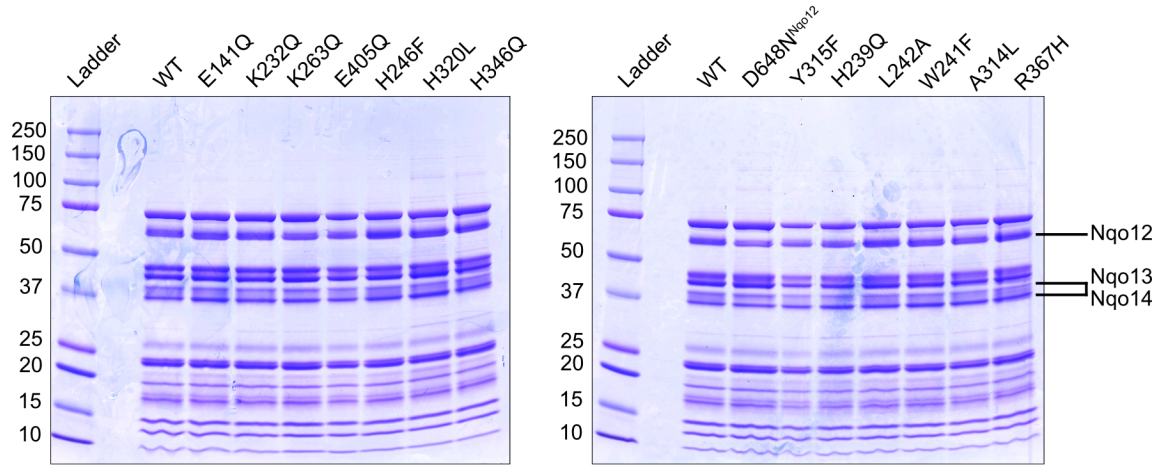

Figure 6.8. SDS-PAGE analyses of purified complex I in wild type and variants. The same band pattern is present in all variants, with no obvious missing subunit bands. Highlighted on the gel are the expected bands for the three antiporter subunits, as identified by mass spectrometry analyses of the wild-type enzyme performed in Chapter 4.

6.6.2. Nanoscale differential scanning fluorimetry (nanoDSF)

In a further assessment of the structural integrity of the complex I variants, nanoscale differential scanning fluorimetry (nanoDSF) was performed on DDM-solubilised, purified complexes. NanoDSF measures the intrinsic fluorescence of tryptophan residues as they are exposed to the solvent as the protein unfolds during heating. The more unstable the protein, the lower the temperature at which this unfolding will occur. For each mutant, the first derivate of the 330/350 nm ratio is shown relative to wild type (**Figure 6.9**). Two peaks are seen in complex I nanoDSF measurements, which probably correlate to the unfolding of the hydrophilic and hydrophobic domain at different temperatures, making it difficult to interpret the nanoDSF data. The second peak at 66.3 ± 0.1 ˚C in wild type is similar in value to the temperature at which the *E. coli* FMN dissociates (67–68 ˚C), measured by ThermoFAD (Hoeser et al., 2018), suggesting that this peak in the *P. denitrificans* enzyme could tentatively be assigned to unfolding of the hydrophilic domain, and so the first peak would be unfolding of the detergent-solubilised membrane domain. Notably, changes in stability of one domain may also affect the rate of unfolding in nearby regions of the protein or in other domains, complicating

interpretation of the data for such a large complex. Here, the nanoDSF traces for each variant were compared visually with respect to wild type to highlight any significant changes that had influenced the enzyme stability, both a shift in temperatures of the peaks and the general shape of the peak. In most cases, the single point mutations appeared to alter the peak shape and lower the peak melting temperatures, suggesting that the structural stability of the enzymes was slightly compromised. Variants E141Q, E405Q and R367H appeared to be the least affected and were nearly identical to wild type. All other variants showed larger changes, suggesting that there is localised destabilisation in the membrane domain, which can be propagated to other domains during sample heating. In particular, the stability of the purified mutants H246F and D648N^{Nqo12} appear to be significantly affected. In the H246F variant, the first peak (attributed to membrane domain unfolding) is shifted to a higher temperature relative to wild type, possibly suggesting a stabilisation of the membrane domain. The D648N^{Nqo12} variant appears to be significantly destabilised, with both fluorescence peaks shifted to lower temperatures relative to wild type. In addition, the first peak was more intense than the second peak, suggesting that exposure of tryptophan residues contained within the hydrophilic domain was also occurring at this lower temperature. The Y315F and H239Q variants, which coordinate D648N^{Nqo12}, are also affected, with the second peak (the hydrophilic domain) unfolding at lower temperatures, but less severely than in D648N^{Nqo12}. Despite changes in the enzyme stability, all variants were fully assembled and intact during purification. Cryo-EM analyses would be required to assess potential localised changes and rearrangements that may have perturbed the local structure, such as in the D648N^{Nqo12} variant, which appears to be the most significantly disturbed.

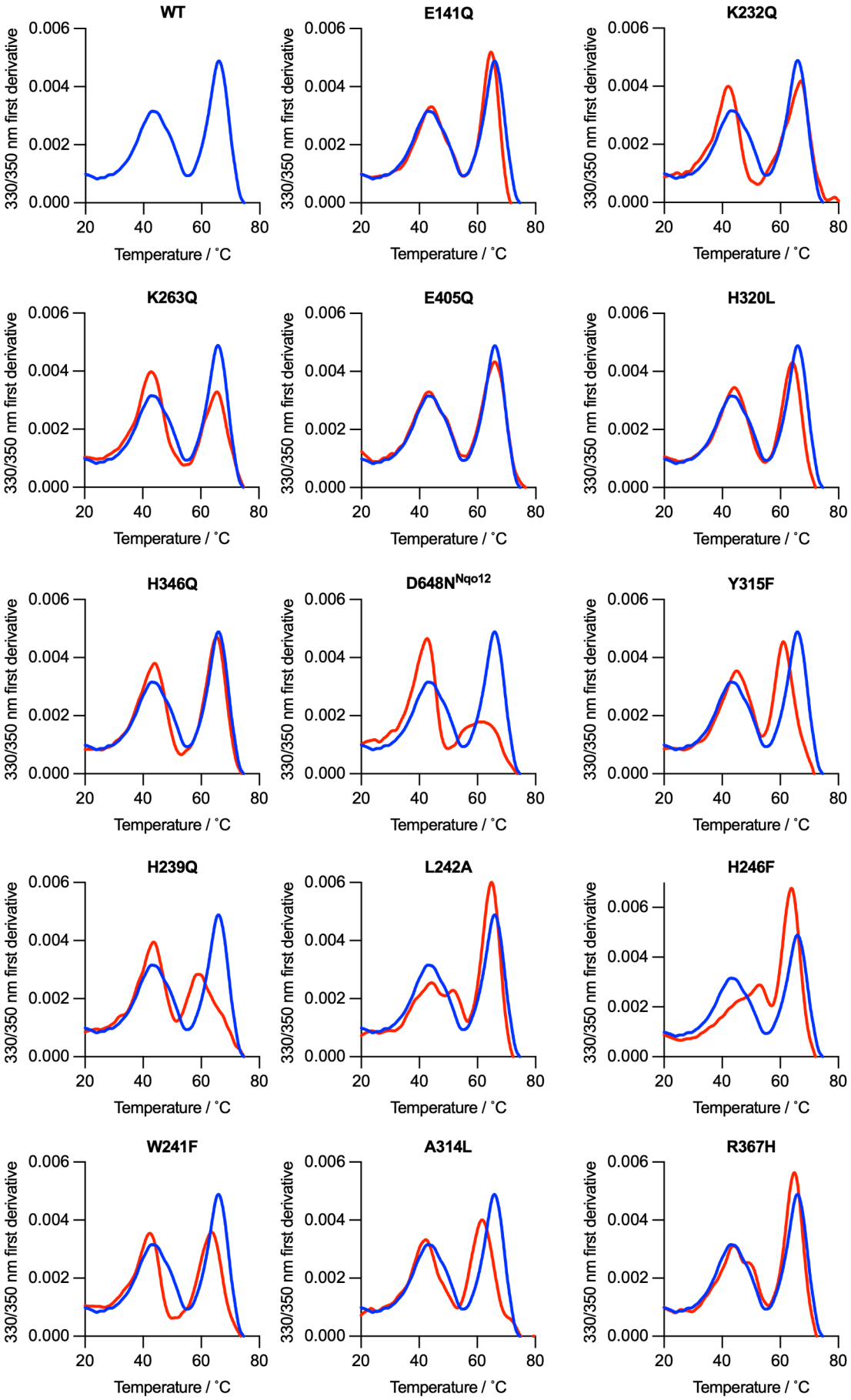
WT
E141Q
K232Q
K263Q
E405Q
H320L
H346Q
D648N^Nqo12
Y315F
H239Q
L242A
H246F
W241F
A314L
R367H
330/350 nm first derivative
0.006
0.004
0.002
0.000
20
40
60
80
Temperature / ˚C

Figure 6.9. NanoDSF fluorescence traces for wild-type and variant complex I. Each isolated complex I variant was diluted to 0.3 mg mL^{-1} and loaded into a capillary in triplicate (10 µL). The fluorescence at 330 nm and 350 nm was recorded in a Prometheus NT.48 (NanoTemper Technologies) as the temperature was increased from 20 ˚C to 80 ˚C at a rate of 4.5 ˚C min^{-1}. The first derivative of the 330/350 nm ratio is shown for each variant in red and is overlayed with the wild type in blue. The trace shown is the average reading for three samples.

6.6.3. Activity measurements on isolated complex I

The catalytic activity of each DDM-purified variant was also measured (**Figure 6.10**). The dNADH:$APAD^+$ activities for all variants were compared, showing that all variants had retained flavin site activity after purification. The Q-reductase rates were not normalised to dNADH:$APAD^+$ activities as it cannot be assumed that all flavin site rates will be the same between variants once purified, either due to intrinsic changes or due to differences in purity/stability issues of the isolated enzyme. Mirroring the membrane activities, mutants E141Q, K232Q, K263Q, E405Q, L242A and H246F were unable to catalyse Q reduction once purified. Strikingly, the Q-reductase activity of the purified $D648N^{Nqo12}$ variant was also abolished despite near-wild-type activities in membranes. Insertion of $D648N^{Nqo12}$ into proteoliposomes did not rescue complex I activity, despite the reconstitution of a lipid membrane around the protein and the removal of DDM from the enzyme, showing that the loss of activity was not reversible (**Figure 6.11**). This links with the significant decrease in the stability of the enzyme measured by nanoDSF (**Figure 6.9**). The purified variants H320L, H346Q, Y315F, H329Q, W241F and A314L all had intermediate activities (35–79% of wild type), suggesting solubilisation in DDM was problematic for the mutants as, in membranes, most of these mutants possessed a similar activity to wild type. However, independent purification would be required to confirm this. Differences in activities of the purified enzyme versus membranes are probably an artefact of purification with DDM and the increased destabilisation in the variants, agreeing with the observations in nanoDSF. Finally, the R367H mutant retained similar rates of Q reduction to the wild type, and so it appeared DDM binding had not destabilised this variant.

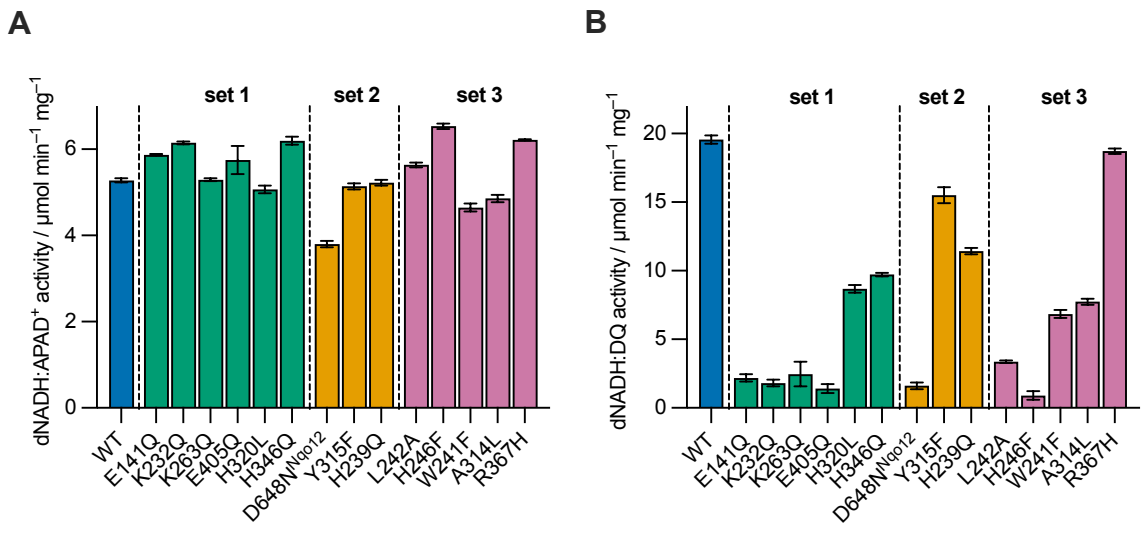

Figure 6.10. Catalytic activities for purified complex I for wild type and variants. The activities for each variant were measured in technical triplicate and the S.E.M is shown. All activities were measured in buffer containing 0.15% asolectin-CHAPS. (A) dNADH:APAD$^+$ activities for each purified variant. (B) dNADH:DQ activities for each purified variant minus the piericidin-insensitive background rate. Statistical significance in panel B was calculated by one-way ANOVA followed by Dunnett's test comparing each variant to wild type. All variants recorded a *p* value <0.0001, apart from R367H, which was not statistically significant compared to wild type.

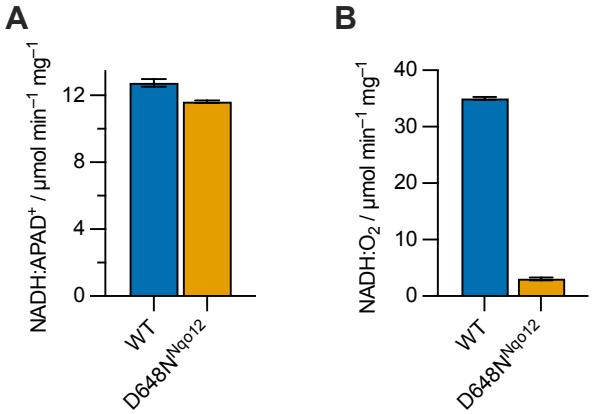

Figure 6.11. Catalytic activities for complex I reconstituted into proteoliposomes for wild type and D648N^{Nqo12}. The activities are shown per mg of outward-facing complex I and the average of three technical replicates are shown ± S.E.M. All activities were measured in proteoliposome buffer containing 10 mM MES pH 6.5 at 32 ˚C, 50 mM KCl and 250 mM sucrose. (A) NADH:APAD$^+$ activity of wild-type and D648N^{Nqo12} strains. (B) NADH:O_2 activity of wild-type and D648N^{Nqo12} strains in proteoliposomes supplemented with 20 µg mL^{-1} AOX and membranes uncoupled with 0.5 µg mL^{-1} gramicidin A, allowing maximum complex I rates to be compared where catalysis was unimpeded by a Δp.

6.7. Complex I proton-pumping stoichiometry

The number of protons translocated by complex I per NADH oxidised (the proton-pumping stoichiometry) was measured for each variant. A protocol has been established previously to quantitatively determine the *n*H$^+$/2*e*$^-$ stoichiometry of complex I in both bovine SMPs and wild-

type SBPs from *P. denitrificans* (Jones et al., 2017). The theory behind it is described in more detail in the Materials and Methods (Section 2.5.5). The system calculates the $H^+/2e^-$ stoichiometry by internal comparison of different oxidoreduction pathways in the same batch of SMPs/SBPs. This confers several advantages compared to proton-pumping measurements based on fluorescence signals from pH/Ψ-sensitive dyes, which compare proton pumping qualitatively by comparison to wild type standards (Dröse et al., 2011; Steimle et al., 2012). Dye-based measurements can be influenced by many different factors, such as enzyme activity/concentration, lipid content, protein/lipid ratio and coupling of the membranes, which makes comparisons between different preparations of variants and wild type complicated. The quantitative method designed by Jones et al. (2017) involved matching the rates of ATP synthesis for three separate pathways (CI/CIII/CIV, CII/CIII/CIV and CI/Q_1 oxidoreduction) and then assuming that, for the same rate of ATP synthesis, the rate of proton pumping would be the same. By comparing the rates of oxidoreduction the proton-pumping stoichiometry of complex I (n^{CI}) can be calculated. In the CI/Q_1 pathway, complexes III and IV were fully inhibited with myxothiazol and KCN, respectively, and the SMPs/SBPs supplemented with Q_1. To match the rates of ATP synthesis between pathways, small amounts of the complex I flavin site inhibitor, ADP-ribose, and the complex II inhibitor, atpenin A5, were added to CI-driven and CII-driven pathways, respectively. An example of the data for matched ATP synthesis rates is shown in **Figure 6.12A**.

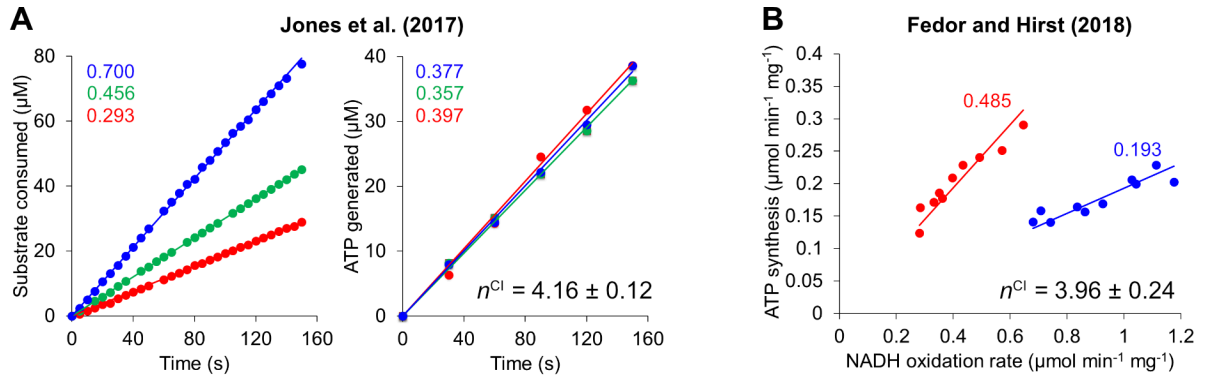

Figure 6.12. Example data for calculating complex I stoichiometry. (A) Method based on Jones et al. (2017) showing raw substrate oxidation traces for each pathway on the left and the matched ATP synthesis rates on the right. Pathways shown are CI/CIII/CIV (red), CI/Q_1 (blue) and CII/CIII/CIV (green). Comparison of the pathways yielded a $H^+/2e^-$ stoichiometry of 4.16 ± 0.2. (B) Method based on Fedor and Hirst (2018) showing ATP synthesis rates plotted versus substrate oxidation rates for CI/CIII/CIV (red) and CI/AOX (blue) pathways. The slopes of the data fitted through the origin are shown with the $H^+/2e^-$ stoichiometry calculated at 3.96 ± 0.24.

More recently, this method was adapted and improved for SMPs to avoid the technical requirement to exactly match the rates of ATP synthesis and to broaden the experiment

beyond the comparison of single data points from each pathway (Fedor and Hirst, 2018). In this method a range of ATP synthesis rates for each pathway was measured by modulating complex I catalysis by increasing concentrations of the competitive flavin site inhibitor, ADP-ribose. The rate of ATP synthesis versus the rate of substrate oxidation for each pathway could be plotted and, from this, the proton-pumping stoichiometry could be calculated by comparison of the slopes between the two pathways (see Materials and Methods, Section 2.5.5) (**Figure 6.12B**). This adapted method averages more data points (by generating a slope) to calculate the stoichiometry and so (provided that the data provide a linear dependence that goes through the origin) is considered more robust than the original method established by Jones et al. (2017). In experiments performed by Fedor and Hirst (2018), only two pathways were compared (CI/CIII/CIV and CI/AOX, where CII, CIII and CIV are inhibited and SMPs are supplemented with AOX instead of Q_1). AOX addition enabled complex I turnover (when CIII and CIV were inhibited) without the addition of exogenous short chain quinone analogues, which could complicate comparisons.

6.7.1. Optimisation of proton pumping measurements for *P. denitrificans*

To improve the protocol for measuring the proton-pumping stoichiometry in *P. denitrificans* complex I, the above methods were adapted further. To limit error in the data analyses, the rates of ATP synthesis versus substrate oxidoreduction were compared in three separate pathways (CI/CIII/CIV, CII/CIII/CIV and CI/AOX), instead of just two as performed by Fedor and Hirst (2018). Second, multiple ATP synthesis measurements, over an overlapping range, were measured for each pathway by modulating complex I and complex II activity with titrations of piericidin A and atpenin A5, respectively. More potent inhibitors than ADP-ribose used in SMPs were required for *P. denitrificans* SBPs to reduce oxidoreduction rates sufficiently to match ATP synthesis rates between pathways, which was considered important to retain the assumption of equal rates of ATP synthesis from equal rates of proton pumping. A diagram of the three different pathways designed to power ATP synthesis via different numbers of protons is shown in **Figure 6.13**.

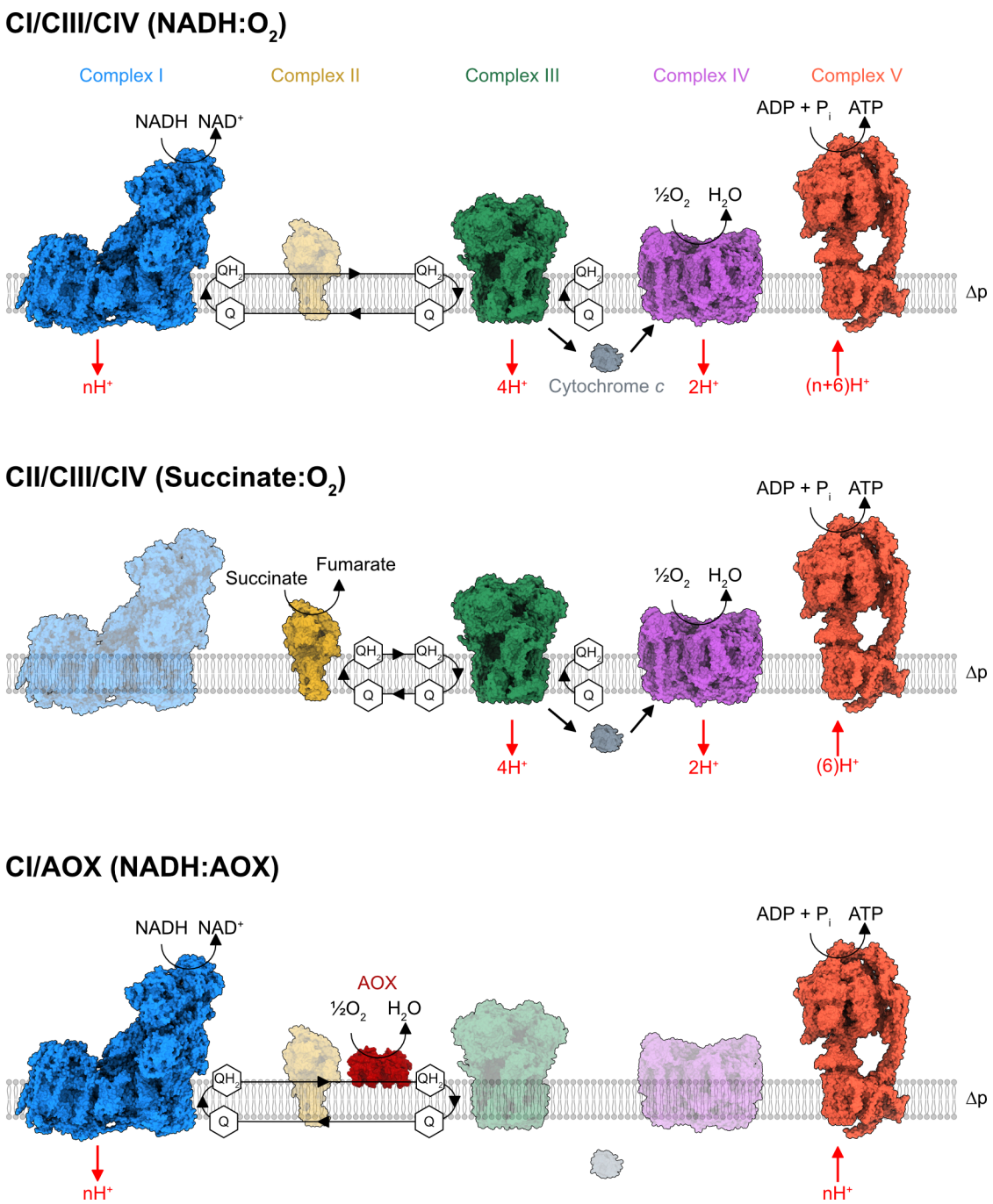

Figure 6.13. Three pathways with different numbers of protons contributing to the Δp. Shown are the enzymes of oxidative phosphorylation with fully inhibited complexes in each pathway shown as transparent. In the CI/CIII/CIV pathway, complex II catalysis is inhibited with atpenin A5 and n^{CI}+6 protons contribute to the Δp per NADH oxidised. In the CII/CIII/CIV pathway, complex I catalysis is inhibited with piericidin A and 6 protons contribute to the Δp per succinate oxidised. In the CI/AOX pathway, complexes II, III and IV are fully inhibited with atpenin A5, antimycin and KCN, respectively. In addition, AOX is supplemented into the buffer with the SBPs to drive Q reoxidation. Per NADH oxidised, n^{CI} protons contribute to the Δp.

The measurement conditions for ATP synthesis and substrate oxidation in each pathway (CI/CIII/CIV, CII/CIII/CIV and CI/AOX) were optimised for proton-pumping measurements.

Large amounts of AOX (~2.5 mg AOX mg^{-1} SBPs) were required to stimulate complex I catalysis to maximum activities in SBPs (where complex III and IV were inhibited), but at >0.5 mg AOX mg^{-1} SBPs ATP synthesis output began to decrease rapidly (**Figure 6.14**). The addition of 2 mM heptakis(2,6-di-*O*-methyl)-β-cyclodextrin (β-CD), which can sequester excess DDM present in the purified AOX enzyme, had no effect on ATP synthesis or NADH oxidation, suggesting the AOX itself at high concentrations was inhibiting ATP synthesis rather than any membrane uncoupling caused by the detergent. This could be due to membrane disruption/remodelling upon AOX binding, which disturbs the ETC complexes. Considering this, 1 mg AOX mg^{-1} SBPs was used in all proton-pumping measurements to provide a balance between securing a substantial substrate oxidation rate, while minimising the decrease in ATP synthesis observed on AOX addition (**Figure 6.14A+B**). AOX was added to all pathways to minimise differences between reaction mixtures, but was fully inhibited with 1 μM ascofuranone, an AOX inhibitor, in CI/CIII/CIV and CII/CIII/CIV pathways.

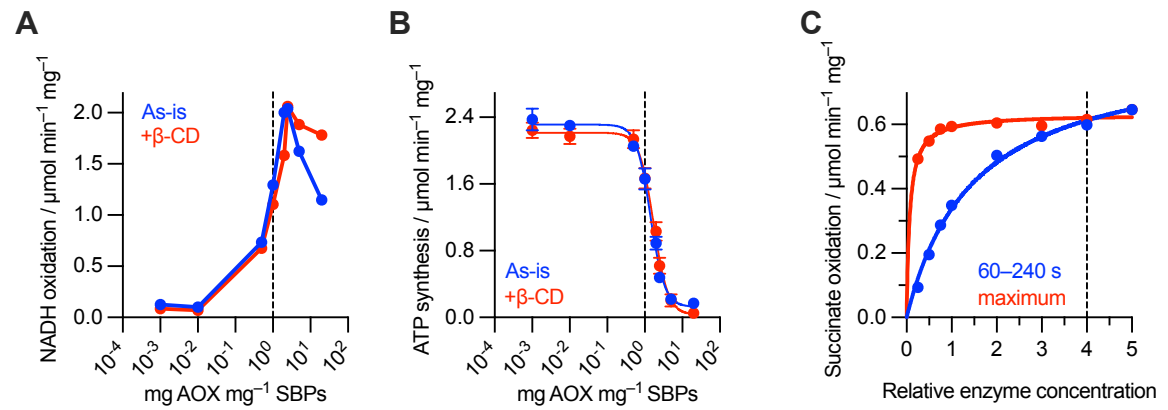

Figure 6.14. Optimisation of assay conditions for ATP synthesis stoichiometry measurements. AOX titration for SBPs grown in LB medium. (A) Rate of NADH oxidation on AOX addition. Complexes III and IV are inhibited by antimycin and KCN, respectively. The titration was performed in the presence or absence of 2 mM β-CD. (B) Effect of AOX addition on ATP synthesis driven by NADH oxidation through complex III and complex IV. AOX is inhibited with 0.5 μM ascofuranone to prevent electrons being diverted to a non-Δp-generating reaction, so any uncoupling or inhibitory effect of AOX itself could be investigated. The titration was performed in the presence or absence of β-CD. The AOX concentration used to assess complex I proton stoichiometry is shown by the dotted line. (C) Rate of succinate oxidation measured at different concentrations of FumC and MaeB. The concentration ratio of FumC to MaeB was fixed at 1:5 and the enzyme concentrations were increased or decreased relative to those found in the standard assay conditions, 60 μg mL^{-1} FumC and 300 μg mL^{-1} MaeB (Jones and Hirst, 2013). The maximum activity reached during the experiment is compared to the activity between 60 and 240 s (the time range of the ATP synthesis assays) at different relative enzyme concentrations.

The enzymatic assay detection system for the CII/CIII/CIV pathway was also optimised for proton-pumping stoichiometry measurements. Detection of succinate oxidation, which uses an enzyme-coupled assay system to detect the reduction of $NADP^+$ as fumarate is converted into

pyruvate, showed a substantial lag phase before maximum rates of detection were achieved (Jones and Hirst, 2013). ATP synthesis was recorded between 1–3 minutes in proton-pumping measurements where this lag was still prominent. To address this, the concentration of enzymes in the succinate assay detection system, oxaloacetate-decarboxylating malate dehydrogenase (MaeB) and fumarase (FumC), were increased and the succinate oxidation rates between 1–3 minutes were compared to the maximum rates reached over 40 min (**Figure 6.14C**). It was found that MaeB and FumC at four times their original assay concentrations, 1.2 mg mL^{-1} and 240 µg mL^{-1}, respectively, reduced the lag phase, allowing maximum rates of succinate oxidation to be detected during the time course of the proton-pumping measurements. These concentrations were used in all proton-pumping measurements. The final reaction conditions used are described in the Materials and Methods.

6.7.2. Proton-pumping stoichiometry of complex I variants

The number of protons pumped by complex I in all variants was measured and calculated. **Figure 6.15** shows the rate of ATP synthesis plotted versus the rate of substrate oxidation for each pathway (CI/CIII/CIV, CII/CIIII/CIV and CI/AOX) in all variants. Comparison of the slopes of best fit for each pathway produced a value for the number of protons pumped by complex I. These individual values and the average for the three pairwise comparisons are shown in **Figure 6.16A**. An alternative way to analyse the data is to globally fit the data to three slopes, which were fixed at set gradients relative to each other, calculated based on the theoretical number of protons pumped by complex I. For each simulated n^{CI} value, the sum of the squared residuals for the overall fit was calculated as shown in **Figure 6.16B**. The value where the sum of the squared residuals was minimised showed the best fit n^{CI} value for the global data. The shape of the curve indicated how the fit changed based on different simulated values of n^{CI}.

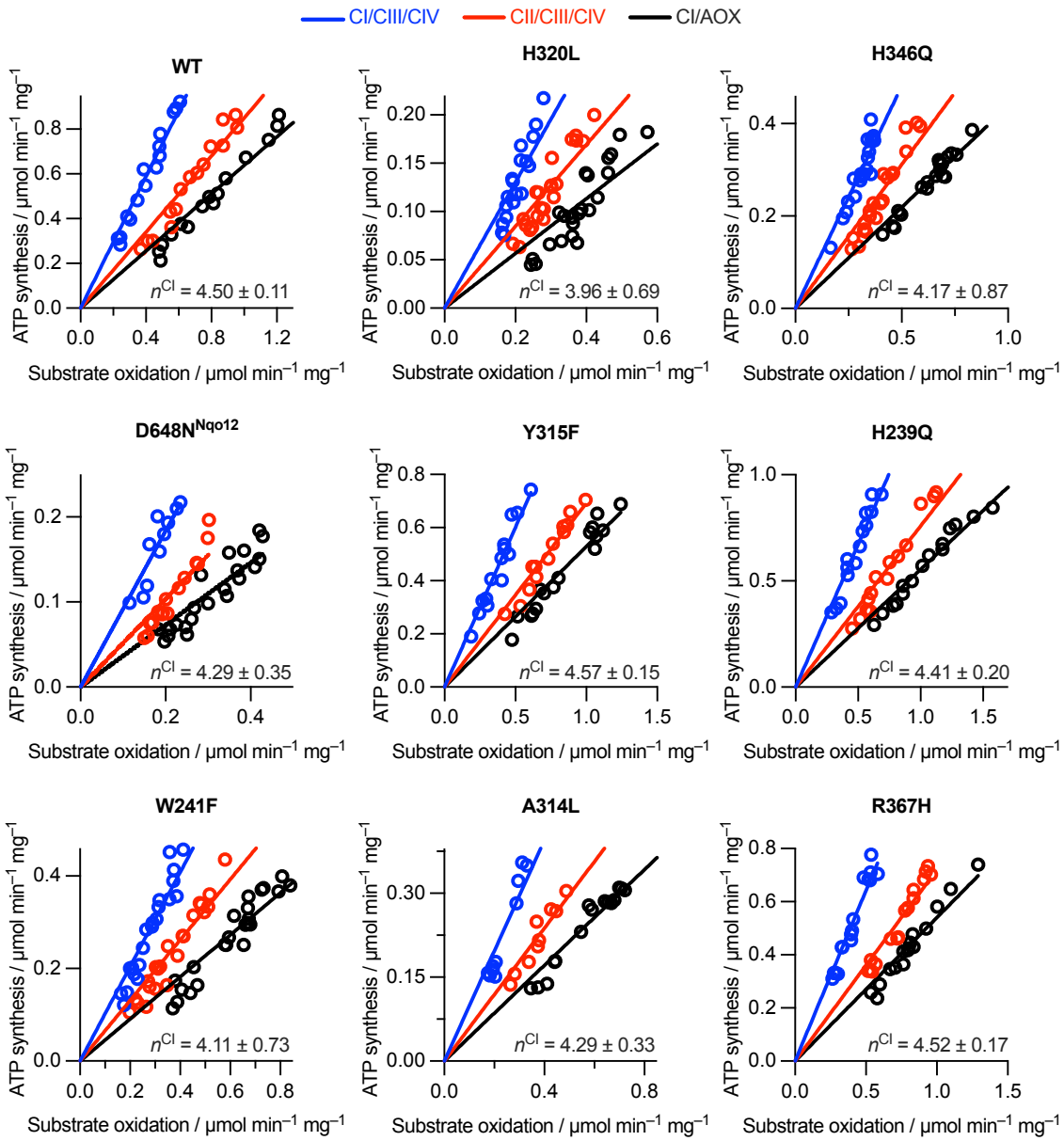

Figure 6.15. Raw data for the determination of complex I proton-pumping stoichiometry for each variant. ATP synthesis rates for three pathways are shown: CI/CIII/CIV (blue), CII/CIII/CIV (red) and CI/AOX (black). The data for each pathway were individually fit to the line of best fit, which passes through the origin. By pairwise comparison of the slopes of these lines, the complex I proton-pumping stoichiometry could be calculated. The average and standard deviation of the three pairwise comparisons for each slope are shown for each variant.

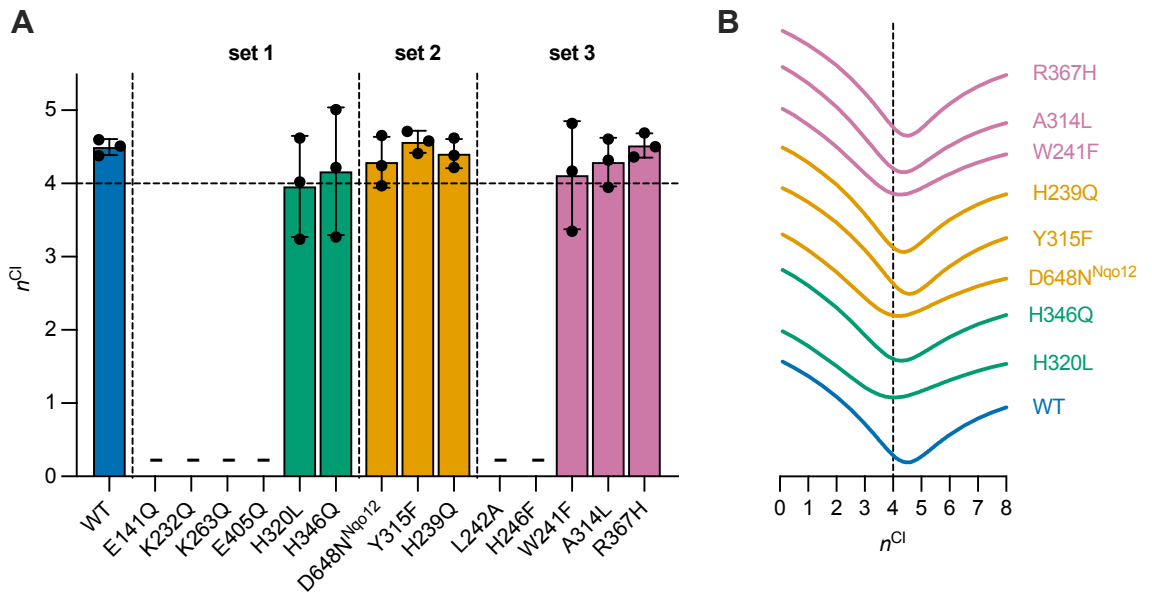

Figure 6.16. Summary of proton-pumping stoichiometries of complex I variants measured in SBPs. (A) The stoichiometry was calculated from each pairwise comparison of the individual best-fit slopes measured for CI/CIII/CIV, CII/CIII/CIV and CI/AOX pathways, and are shown as individual points on the bar chart. The average of these values is shown and the error bar showing S.D for the three pairwise comparisons. The dashed lines indicate mutants where the proton-pumping stoichiometry experiment was not performed because the complex I activity was too low. For comparison, a dotted line is shown intersecting the data where n^{CI} = 4. (B) Sum of the squared residuals for the global fitting of wild-type and variant datasets to simulated n^{CI} values. The ratio of the slopes between CI/CIII/CIV, CII/CIII/CIV and CI/AOX pathways were fixed based on values calculated for different numbers of protons pumped by complex I (using **Equations 2.8–2.10**). The simulated slopes were then fit globally to all experimental data points in each variant. The value of n^{CI} that best fits the data is shown where the sum of squares is minimised. In all cases this is between four and five protons. For clarity, the dotted line shows where n^{CI} = 4 intersects the data.

Based on the best-fit data of individual slopes, wild type and variants all returned an average proton-pumping stoichiometry value between 3.96 and 4.57. This clearly highlighted all variants pumped ≥4 protons. **Figure 6.16** shows how the data for each variant did not fit well when slopes were simulated to pump fewer than four protons. To emphasise this point, **Figure 6.17** shows the best-fit lines for each dataset when two, three and four protons pumped by complex I are simulated. Clearly, simulating the ratio between slopes for n^{CI} = 2 and 3 does not fit the data well in all cases, and only when n^{CI} = 4 did the simulated slopes begin to fit the data for all pathways, emphasising that it was not possible that any variant was pumping fewer than four protons per NADH oxidised.

It should be noted that all measurements yielded $H^+/2e^-$ values that were slightly higher than the previously determined value of $4H^+/2e^-$, suggesting a potential systematic error within all measurements (Jones et al., 2017). Why the $H^+/2e^-$ stoichiometry appears to be higher must be due to some unaccounted factors in the SBP preparations or assay system. It is possible

that other oxidases, which pump protons, are being expressed in *P. denitrificans*, which would influence the measured stoichiometry. However, the cbb_3-type oxidase is only highly expressed in low oxygen (the cells were grown aerobically) and the ba_3-type quinol oxidase is also expressed only at low levels and has a high K_M for quinol. This makes it unlikely to interfere in these pathways, where the Q-pool is predominately maintained in an oxidised state, as complexes I and II are inhibited to lower oxidoreduction rates and Q oxidation occurs rapidly, either through AOX or through CIII and CIV catalysis (Otten et al., 1999). Despite this potential systematic error, it should be emphasised that this data was more robust than previous iterations of this analysis as slopes of three different pathways were compared rather than individual points (Jones et al., 2017). Importantly, all mutants showed the same proton-pumping stoichiometry as wild type, demonstrating that all mutants still pumped a full complement of four protons per NADH oxidised.

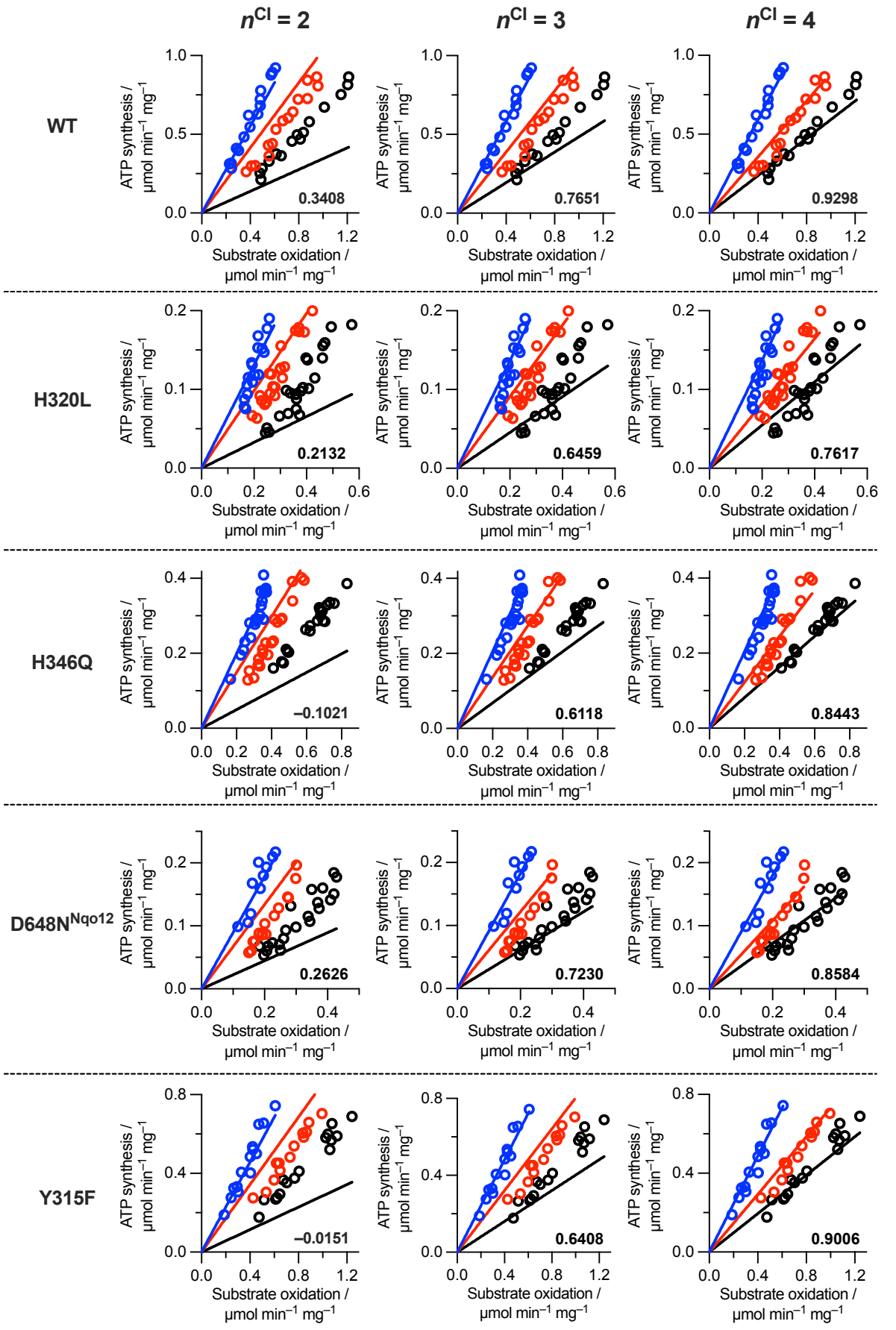
$n^{Cl} = 2$
$n^{Cl} = 3$
$n^{Cl} = 4$
WT
H320L
H346Q
D648N^{Nqo12}
Y315F
ATP synthesis / μmol min^{-1} mg^{-1}
Substrate oxidation / μmol min^{-1} mg^{-1}
0.3408
0.7651
0.9298
0.2132
0.6459
0.7617
–0.1021
0.6118
0.8443
0.2626
0.7230
0.8584
–0.0151
0.6408
0.9006

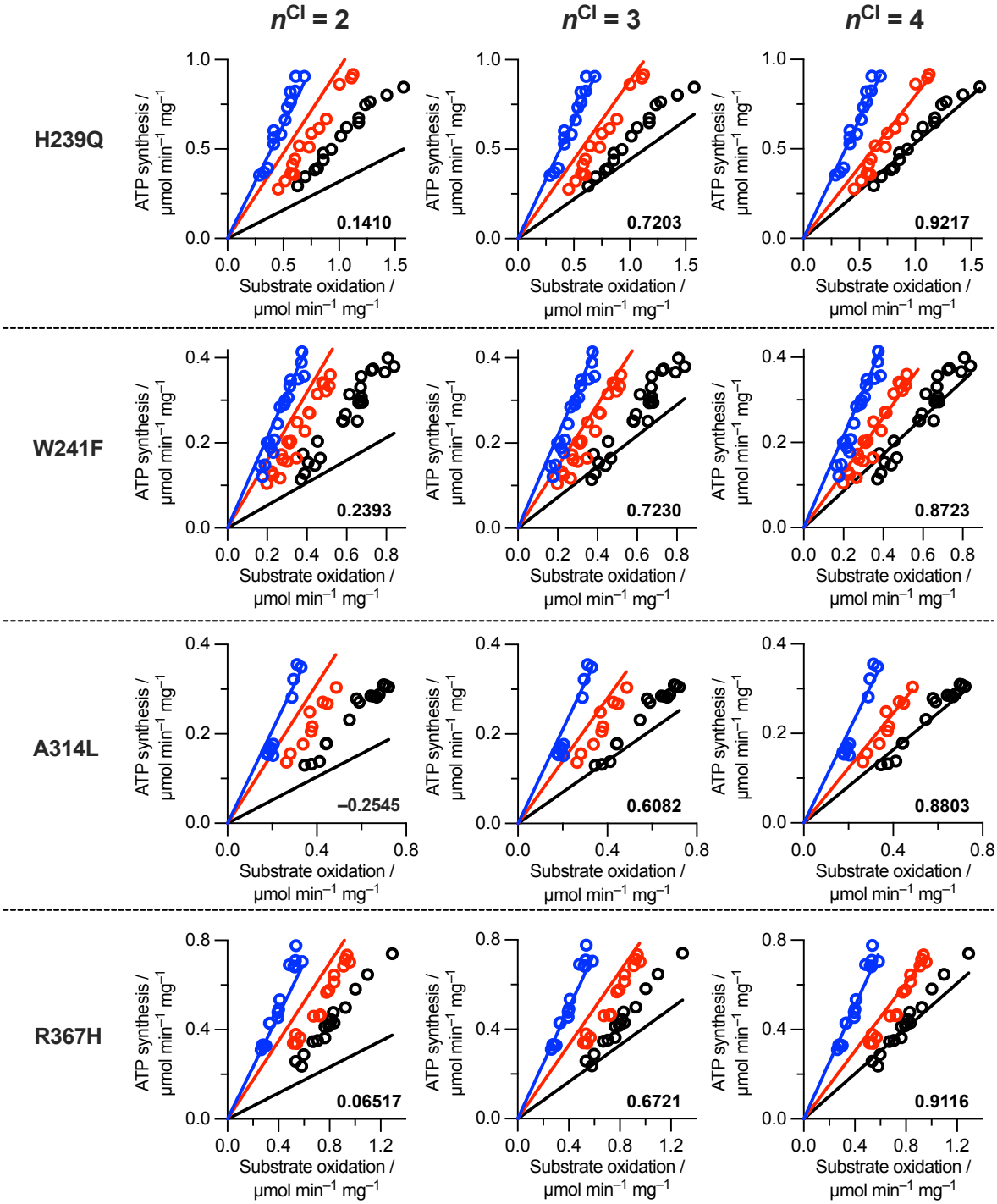

Figure 6.17. Simulations of global fits for complex I proton-pumping stoichiometry for wild type and variants for n^{CI} = 2, 3 and 4 protons. Experimental data points and the fits for CI/CIII/CIV (blue) CII/CIII/CIV (red) and CI/AOX (black) are shown. For each proton-pumping stoichiometry, the relative ratio of the slopes was calculated I (using **Equations 2.8–2.10**) and set to a fixed value. This was then globally fit to the whole dataset. The R^2 value for the global fit is shown for each simulation for each dataset. In all cases, the data fits best when four protons are simulated.

6.8. RET in complex I

Although efforts to drive complex I RET in SBPs using a ∆p generated through ATP hydrolysis were unsuccessful, as detailed in Chapter 3, past studies have measured RET in SBPs driven by succinate oxidation and complex III and IV catalysis (Kotlyar and Borovok, 2002; Kotlyar et al., 1998). Here, this method was used simply to determine whether each variant could catalyse RET.

First, the conditions for measuring RET were established (**Figure 6.18A**). The reaction was sensitive to addition of piericidin A to inhibit complex I and gramicidin A to uncouple the SBP membranes. Inhibiting complexes III and IV with antimycin A and KCN, respectively, also showed the ∆p generated by respiration was required for RET. The RET reaction appeared to plateau after a few minutes, which may be a result of the system reaching steady state, where NADH generated by RET begins to be consumed by forward catalysis through complex I, which competes with the RET reaction (Kotlyar and Borovok, 2002). This further highlights the need for a system where a ∆p can be generated independent of respiration, to prevent this competing forward reaction that proceeds via uninhibited complex III and IV catalysis. As the reaction was effectively competing with NADH oxidation, a high concentration of NAD^+ was required to achieve optimum rates of catalysis **Figure 6.18B**.

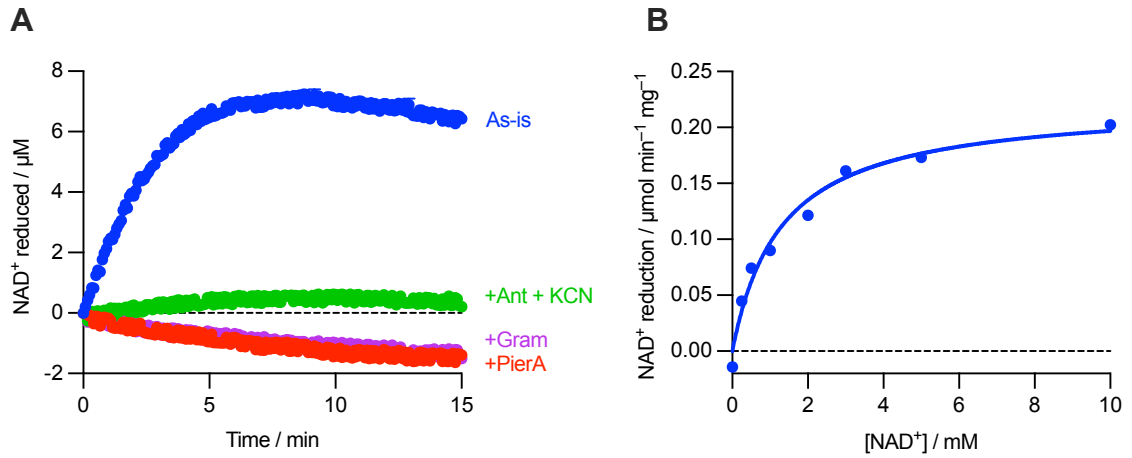

Figure 6.18. Demonstration and optimisation of RET conditions in SBPs. All measurements were performed in buffer containing 10 mM Tris-SO_4 pH 7.5 at 32 ˚C, 250 mM sucrose, 1 mM K_2SO_4 and 2 mM $MgSO_4$. (A) Demonstration of RET in SBPs showing the total concentration of NAD^+ reduced over time. The rate of RET can be determined from the initial slope, in which the rate is linear (blue). Addition of 150 ng mL^{-1} gramicidin A uncoupled the membranes and abolished RET (purple). Piericidin A addition (2 µM) also abolished activity (red). Inhibition of complexes III and IV with 1 µM antimycin and 400 µM KCN, respectively, also stopped RET (green). (B) K_M curve for NAD^+ in 20 µg mL^{-1} SBPs.

SBPs for all strains able to catalyse Q reduction (in membranes) were prepared from cells grown aerobically in a succinate minimal medium to ensure complex II content in the

membranes was sufficiently high to drive RET (Materials and Methods, Section 2.3.1). Previous RET studies also used SBPs prepared from cells grown on a succinate medium (Kotlyar and Borovok, 2002; Kotlyar et al., 1998) and other work has also shown succinate-grown SBPs were possibly better coupled relative to LB-grown SBPs (Varghese, 2016). It is unclear if LB-grown SBPs could also support RET, as these were not tested here.

First, the dNADH:O_2 activity was measured (normalised to dNADH:$APAD^+$ activity) showing the variants displayed a similar activity profile to that measured in membranes (**Figure 6.19A**). The H320L variant, which was reduced to 57% of wild type in membranes had retained a higher activity in SBPs, although it should be noted that only one preparation of SBPs was prepared here (compared to biological triplicates in membranes). The milder conditions for the preparation of SBPs versus membranes (osmolysis vs sonication) may account for these differences. Wild-type SBPs were prepared in biological triplicate to illustrate the theoretical spread in the data between all variants, which was relatively low after normalisation when comparing FET reactions. The succinate oxidation rates were also measured to show complex II catalysis was sufficiently high in all active variants to reduce the Q-pool (**Figure 6.19B**). Finally, RET for all complex I active variants was measured and normalised to the complex I content in the SBPs as measured by dNADH:$APAD^+$ (**Figure 6.19C+D**). Differences in the rates of RET were seen between variants; however, a greater spread in the RET data for biological replicates of wild-type SBPs suggests this should not be overinterpreted. While differences in complex I content between SBP preparations have been accounted for, variations in the rate of succinate oxidation and the membrane coupling (proton leak) have not. This prevented variants from being accurately compared. From this data, it was only possible to demonstrate that all variants were RET competent. Nonetheless, this was important to identify as few studies have previously shown the RET capabilities of complex I mutants, and, of those, the variants studied have been identified as unable to undergo RET (Yin et al., 2021).

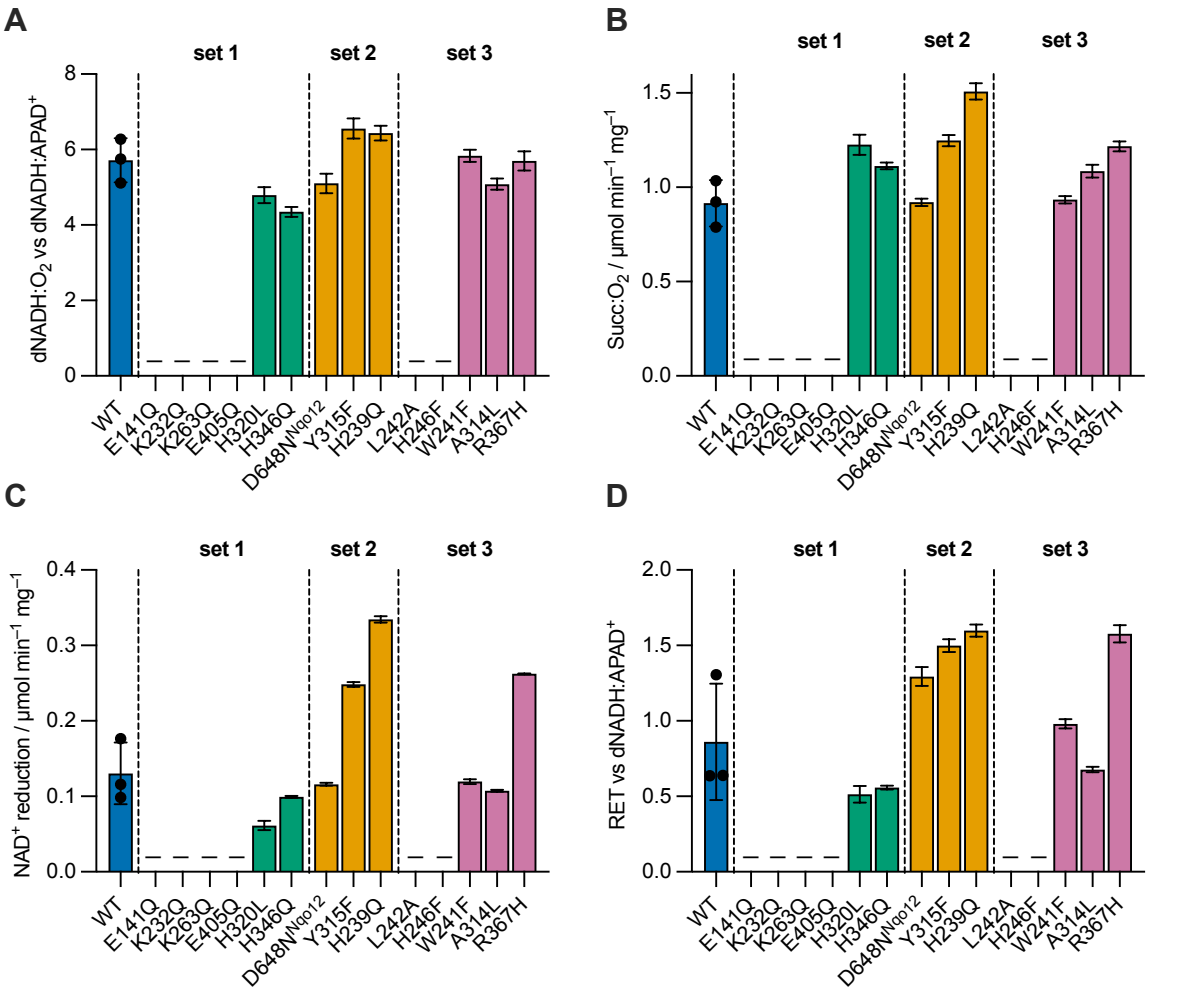

Figure 6.19. Catalytic activities of SBPs from complex I variants. SBPs were prepared only for mutants that possessed significant complex I activity in membranes. SBPs not prepared are included in the graphs for ease of comparison between other datasets and are marked by a line. All measurements are the average of three technical replicates ± S.D. Three independent SBP preparations for wild type were prepared and assayed to provide biological replicates to indicate the probable spread present in all data between SBP preparations. All assays were measured in buffer containing 10 mM Tris-SO_4 pH 7.5 at 32 ˚C, 250 mM sucrose, 1 mM K_2SO_4. $MgSO_4$ (2 mM) was added to buffers where complex II was catalysing. (A) dNADH:O_2 activity normalised to dNADH:$APAD^+$ activity. All strains were not statistically significant compared to wild type as calculated by one-way ANOVA using Dunnett's test. (B) Succinate:O_2 activity in SBPs. (C) NAD^+-reductase activity in SBPs. (D) NAD^+ reduction normalised to dNADH:$APAD^+$ activity. All strains were not statistically significant compared to wild type as calculated by one-way ANOVA followed by Dunnett's test comparing each variant to wild type.

6.9. Insights into the mechanism of complex I

A summary of the data compiled for all variants is shown in **Table 6.4**.

Table 6.4. Summary of data collected for all complex I variants. For membranes, the Q-reductase activity is shown (normalised to dNADHAPAD$^+$ rates) as a percentage relative to wild type. The purified Q-reductase activity is also shown relative to wild type. The average proton-pumping stoichiometry for each variant is shown and the capability of each variant to undergo RET is also noted.

Set	Mutation	Q-reductase activity / % (± S.E.M)		n^{CI} stoichiometry (± S.D)	RET capable?
		Membranes	Purified		
Set 1	WT	100 ± 13.4	100 ± 1.2	4.50 ± 0.11	Yes
	E141Q	7.3 ± 2.2	11.2 ± 0.8	N/A	N/A
	K232Q	2.6 ± 1.4	9.3 ± 0.8	N/A	N/A
	K263Q	17.5 ± 2.6	12.6 ± 2.7	N/A	N/A
	E405Q	3.8 ± 1.1	7.2 ± 0.9	N/A	N/A
	H320L	56.7 ± 8.3	44.4 ± 0.9	3.96 ± 0.69	Yes
	H346Q	77.9 ± 8.8	49.7 ± 0.6	4.17 ± 0.87	Yes
Set 2	D648N^{Nqo12}	87.4 ± 10.1	8.2 ± 0.7	4.29 ± 0.35	Yes
	Y315F	103.3 ± 13.2	79.2 ± 1.9	4.57 ± 0.15	Yes
	H239Q	94.9 ± 9.7	58.4 ± 0.9	4.41 ± 0.20	Yes
Set 3	L242A	10.4 ± 1.5	17.2 ± 0.3	N/A	N/A
	H246F	2.1 ± 0.3	4.6 ± 0.9	N/A	N/A
	W241F	95.4 ± 11.0	35.0 ± 0.9	4.11 ± 0.73	Yes
	A314L	90.9 ± 13.4	39.6 ± 0.7	4.29 ± 0.33	Yes
	R367H	98.4 ± 14.3	95.6 ± 1.0	4.52 ± 0.17	Yes

6.9.1. Lateral charge transfer residues in Nqo13

The importance of the charge-bearing capacity of the Lys and Glu residues, which span the central axis of Nqo13, was assessed by creating individual point mutations that replaced each with a Gln side chain (set 1). The E141Q, K232Q, K263Q and E405Q mutants showed severely reduced Q-reductase activity in both membranes and purified enzyme (**Table 6.4**, set 1). The protonation capacity of each residue is therefore essential to the enzyme mechanism and is probably involved in charge propagation through the membrane domain. The E141Q and E405Q mutants were also the least compromised structurally, based on biochemical and biophysical data, which emphasises that the loss in activity is due to the removal of the charge residues rather than structural perturbations. The critical role of the equivalent residues for E141 and K232 in *E. coli* was also highlighted by previous mutational work, where substitution with Ala or Gln resulted in complete loss of activity (Euro et al., 2008; Torres-Bacete et al., 2007). Notably, activity could be partially rescued in double point mutants, when a Glu was inserted one helical turn above or below in the E141A-equivalent variant in *E. coli*, highlighting the need for a charge residue in this location (Torres-Bacete et al., 2009). An equivalent mutation could be tested in a future iteration of this current study. In our study, we also show

that the charge on E405 on TMH12 is essential, a result that is not unexpected despite no prior mutagenesis work detailing its importance, as structures have revealed its participation in the chain of charged residues. E405 is substituted with Lys residues in the Nqo12 and Nqo14 subunits and it would be interesting to mutate the E405 to a Lys in a future study, to mirror the other antiporter subunits, and swap its charge but retain its protonatable status.

Here ~17% of the activity remained in the K263Q mutant (**Table 6.4**, set 1), yet substitution of the equivalent K263 residue in *E. coli* to an Ala showed 35–55% of the wild-type activity in membranes (Euro et al., 2008; Torres-Bacete et al., 2007). The retention of only a low amount of activity in *P. denitrificans* agrees with the proposal that protonation/deprotonation events at this residue control channel hydration (Mühlbauer et al., 2020) and are crucial for energy transduction. However, it is hard to justify why this is not also true in the *E. coli* enzyme: perhaps there are alternative proton-transfer routes in the vicinity of this residue in *E. coli* and/or mechanisms controlling channel hydration. Unfortunately, the activity of the K263Q variant in *P. denitrificans* remained too low to determine its $H^+/2e^-$ stoichiometry or its RET capabilities with any certainty.

Point mutations were also prepared for the highly conserved H320 and H346 residues, which help to connect K263 and E405 in the Nqo13 subunit. The activity of the H346Q mutant was not significantly lower than that of wild type, but H320L showed a more substantial decrease to 57% of wild type, potentially due to the more severe substitution to a non-polar residue. However, both variants are still able to catalyse with substantial rates, unlike the mutations of the Glu-Lys ion pairs. While past studies have shown no reduction in Q-reductase activity of the membranes when equivalent residues in *E. coli* were mutated to an Ala (Torres-Bacete et al., 2007), more recent investigations of the same residues in *E. coli* showed a similar decrease in activity to that observed here (Mühlbauer et al., 2020). The results may differ due to the different sample systems (membranes and proteoliposomes, respectively). It was suggested that protons may take an alternative pathway along the chain in these compromised point variants, with their lower hydrogen-bonded connectivity compared to wild type potentially modulating the proton affinity for the terminal Glu on TMH12 (E405). Importantly, it was suggested that the number of protons translocated in these mutants is reduced, based on reduced ACMA and Oxonol IV quenching, with protons only pumped in the Nqo14 and Nqo8/7/10/11 modules (Mühlbauer et al., 2020). However, our results clearly indicate that the H346Q and H320L variants still translocate a full complement of four protons (**Table 6.4**, set 1). Thus, the H346Q and H320L variants do not completely disrupt energy transduction along the membrane domain to Nqo12, unlike variants such as E141Q, K232Q and E405Q, enabling continuous turnover. Most likely these highly conserved His residues are involved in forming

optimum hydrogen-bonding networks for proton/charge transfer along the hydrophilic central axis, but amended networks are still able to form in their absence.

6.9.2. Nqo13 coordination to the transverse helix of Nqo12

The role of the transverse helix in complex I was investigated by mutations weakening the connection between it and Nqo13. The transverse helix of Nqo12 is coordinated to the Nqo13 subunit via a conserved Asp or Glu (D648^{Nqo12} in *P. denitrificans*) residue and conserved His and Tyr residues on Nqo13 (H239 and Y315F) (Agip et al., 2018; Grba and Hirst, 2020; Kampjut and Sazanov, 2020; Kolata and Efremov, 2021; Zhu et al., 2016). Here, the coordination network was disrupted by preparing D648N^{Nqo12}, H239Q and Y315F single point mutations. In membranes, all mutants showed a similar Q-reductase activity to wild type and so there was no clear indication of any disruption to the enzyme mechanism (**Table 6.4**, set 2). Further to this, all variants still pumped the full complement of four protons (**Table 6.4**, set 2). These data are at odds with previous studies suggesting the equivalent mutation in *E. coli* (D563N) only translocated three protons per NADH oxidised, based on relative comparisons of ACMA quenching signals (Steimle et al., 2012). Our results suggest the coordination site in the transverse helix is not, in fact, essential to the proton-translocation mechanism, and disconnecting the lateral helix from Nqo13 did not disengage proton pumping in this subunit.

Once purified, the D648N^{Nqo12} mutant entirely lost its Q-reductase activity and the H239Q variant also suffered relative to wild type (**Table 6.4**, set 2). In addition, the D648N^{Nqo12} variant appeared to elute later in size-exclusion chromatography, despite still showing a full complement of subunits on SDS-PAGE (**Figure 6.7** and **Figure 6.8**). It is likely that solubilisation in DDM led to more profound structural perturbations and an increase in instability of these variants, as peaks were dramatically shifted in D648N^{Nqo12}, and, to a lesser extent, in H239Q and Y315F, relative to wild type in NanoDSF. Coordination/intercalation of a DDM molecule may have caused structural perturbations and disrupted the Nqo13 subunit architecture in these compromised mutants. A structure of bovine complex I solubilised in DDM has shown that a DDM molecule can bind between the transverse helix and Nqo13, close to the Nqo13/14 interface (PDB: 7QSD, (Bridges et al., 2022)). Furthermore, complex I simulations, when embedded in a lipid membrane, have shown a POPE (1-palmitoyl-2-oleoyl-sn-glycero-3-phosphoethanolamine) bound between the transverse helix and Nqo13, coordinating to equivalent D648 and H239 residues in mouse heart complex I (Röpke et al., 2020). The mutations here, particularly D648N^{Nqo12} and H239Q, may have disrupted lipid binding at this location, and, along with DDM binding in the vicinity, have led to significant structural changes preventing Q reduction. Interestingly, reconstitution of D648N^{Nqo12} into

proteoliposomes did not rescue the complex I activity, despite the reintroduction of a stabilising membrane and expected extraction of the DDM bound at the lateral helix, which was seen to be removed in bovine complex I once reconstituted in lipid nanodiscs (Chung et al., 2022). This suggests the disruption caused by DDM in the D648N^{Nqo12} variant was irreversible, and either DDM remained bound, or the coordination of the lateral helix to Nqo13 could not be re-established. In membrane preparations, the variant may also be stabilised by the surrounding enzymes in supercomplexes, where complexes III and IV sit along the lateral helix (Milenkovic et al., 2017).

Notably, the D648N^{Nqo12} equivalent mutant from *E. coli* was also purified using DDM, but the effects observed here were not reported (Steimle et al., 2012). However, reconstitution of the *E. coli* complex I into proteoliposomes for both wild type and D563N^{Nqo12} (D648N^{Nqo12}) showed extremely low rates of catalysis for both samples (between 1.2–1.6 μmol min^{-1} mg^{-1}) compared to wild-type rates of *Pd*-CI in proteoliposomes (35.0 ± 0.2 μmol min^{-1} mg^{-1}) and more recent rates of *E. coli* complex I in proteoliposomes obtained by the same group (~36 μmol min^{-1} mg^{-1}) (Mühlbauer et al., 2020). With the results for the *E. coli* enzyme reported with very low activities, it is questionable as to how well the Q-reductase activity can be correlated to the proton-pumping stoichiometry. In fact, considering the error of these measurements, which was not reflected upon in their study, the D563N^{Nqo12} variant could pump anywhere between two and four protons (Steimle et al., 2012). Therefore, the data of Steimle and co-workers are not convincing. This observation highlights another major advantage of using an SBP system to determine the $H^+/2e^-$ stoichiometry of complex I, as enzymes do not have to be purified first, exposing them to detergents that could affect their activity/stability. Overall, our data point to a structural/stabilising role for the lateral helix in complex I, and we dispute one of the rare pieces of evidence that has supported its role as a ‘coupling rod’ (Steimle et al., 2012).

6.9.3. Hydration control mechanisms in a possible proton import channel in Nqo13

A proposed proton import channel into the Nqo13 subunit was suggested to be controlled by the movement of a Leu residue opening and closing during catalysis, and acting as a gate to channel hydration (Di Luca et al., 2018; Grba and Hirst, 2020). Strikingly, the L242A variant showed a near complete loss of complex I Q-reductase activity, lending support to this proposal (**Table 6.4**, set 3). Loss of the gating Leu may allow the channel to become permanently hydrated with water, regardless of the protonation state of K263 that has been proposed to control it (Di Luca et al., 2017, 2018), so preventing controlled and synchronised proton import and proton pumping and thereby preventing further Q reduction: with the enzyme mechanism for Q reduction being tightly coupled to proton pumping. The H239Q and W241F

mutants did not significantly affect the Q reduction and the $H^+/2e^-$ stoichiometry remained unaffected, perhaps because the backbone–backbone hydrogen-bond arrangement between H239 and L242 is not substantially perturbed by the H239Q and W241F substitutions, allowing L242 to remain correctly positioned to control channel hydration. In the MrpD subunit (Nqo13 equivalent) of the Mrp complex, the equivalent W241A mutant (W228A in MrpD) showed 86% of wild-type activity, a more significant decrease than seen here for the W241F mutant; however, the retention of the majority of the activity suggested this residue did not mediate opening and closing of the channel and was not critical in establishing the correct Leu-His backbone bonding arrangement (Di Luca et al., 2018).

The A314L mutant on TMH10, which interfaces with L242, was designed to permanently block the proton import channel; however, Q turnover was unaffected and a full complement of four protons were pumped. Perhaps a bulkier mutation to a Phe or Trp residue is required to block this channel from hydration and this should be considered in follow-up studies. Finally, the H246F mutant was created to remove the polarity of the His residue and its ability to transport a proton directly, with this residue suggested to be important for proton import into Nqo13 (Di Luca et al., 2017; Kampjut and Sazanov, 2020). Like L242A, Q-reductase activity was almost completely abolished in this variant (**Table 6.4**, set 3) suggesting it could well have a crucial role in proton import and in establishing an ordered network of water molecules for a proton to move through. Interaction of H246F with nearby F354 and L257, on TMH11 and TMH8, respectively, may create a hydrophobic pocket in the Nqo13 subunit. Along with the gating L242 residue, this may stabilise the enzyme and form an impasse for channel hydration, even if L242 were to move. It is unclear whether its essential nature is due to its inability to carry a proton (for proton pumping) or due to disruption of the water network from this potential hydrophobic blockage. Further mutations of this residue to other side chains may assist in clarifying this distinction.

Residue F354 has also been suggested as a gating residue, but it was not included in the set of mutants created here as this was proposed after completion of this work. However, mutation of the equivalent residue (F341) in the Mrp complex to an Ala only reduced the antiport activity to 64% of wild type (Morino et al., 2017; Parey et al., 2021; Steiner and Sazanov, 2020). This result suggests it is either not critical for controlling channel hydration compared to the gating Leu, or that ion pumping in this subunit may proceed independently from the other antiporter subunits. The critical role of the L242 and H246 residues in Nqo13 lends credence to the proposal that they are part of a hydration channel, important for modulating or facilitating lateral energy transduction through the enzyme or for proton pumping. Further mutations and structural characterisation of the above mutants at a sufficiently high resolution to model water

molecules will be required to further support their critical role in establishing or controlling channel hydration and linked mechanistic features.

Finally, the LHON mutant, R367H, which sits near the top of the channel, was nearly indistinguishable from wild-type complex I, so it is interesting why this mutant should cause a phenotype in patients. It has been suggested that there is an increase in ROS production in cells transfected with the LHON mutated Nqo13 subunit; however, it is hard to reason why ROS production, produced predominantly at the far-away flavin site, would be increased (Qi et al., 2007). This same LHON mutant has also been reported to have altered affinities for quinone (higher for DQ but lower for Q_2) and to be less sensitive to rotenone inhibition (Esposti et al., 1994). The decreased rotenone sensitivity may be due to structural disruptions in the third reported rotenone-binding site in Nqo13, where the rotenone is stabilised by R159, W241 and K232 (*P. denitrificans* numbering) (Kampjut and Sazanov, 2020). However, as *Pd*-CI already exhibits a decreased affinity for rotenone compared to mammalian complex I, it is not a relevant model to investigate these effects. It would be interesting to see if there is a decreased affinity for other complex I inhibitors, such as piericidin A, which are only reported to bind at the Q-site (Bridges et al., 2020). Further analyses on the R367H mutant are required to answer these questions, such as measuring the native Q_{10} affinity in proteoliposomes and possible structural studies of the mutant to reveal why this mutant, located far from the Q-binding site and the flavin site, may have increased ROS production or a changed ubiquinone affinity.

6.10. Conclusions and future directions

The complete loss of activity in single point mutants in Nqo13, including minor changes such as E405Q and L242A, suggests that the energy from Q reduction either cannot be effectively transferred into the membrane domain or back propagated to the Q-site, which may be important for further Q reduction (Kaila, 2021). The inactive mutants in the Nqo13 subunit could be considered as a closed door, preventing controlled energy propagation through this subunit in both the forward and reverse directions. Whether two protons are pumped during a first partial forward electrostatic wave is impossible to determine without continuous turnover of Q. Interestingly, the hypothesised permanent opening of the hydration channel to the N-side in the L242A variant did not show a ‘short-circuiting’ of proton pumping, suggesting that controlling the channel hydration of the antiporters is essential for energy propagation along the axis and/or for proton pumping. Future studies may be able to shed more light on these questions by performing structural characterisation of ‘stopped’ mutants. One proposal is to solve the structure of the catalytically inactive Nqo13 mutants exposed to NADH to stall

complex I turnover in an intermediate state, blocked by the impasse in Nqo13, revealing enzyme changes in preceding subunits. It is also possible that a stalled state might trap a semiquinone intermediate for study by EPR spectroscopy, which would provide evidence for whether a two-stroke mechanism exists, where the one-electron reduction of ubiquinone is sufficient to initiate proton pumping. Structures of the L242A mutant would also prove useful for identifying if its critical nature in the enzyme is due to channel hydration control or some other factor. If a flooded channel is revealed in the structure, relative to wild type, it may support its role in controlling channel hydration, and possibly even proton translocation. Creation of this mutant in silico, followed by hydration simulations of the structure may also provide an alternative route to explore this proposal.

Our data currently provide no evidence that complex I can reduce Q without translocating a full complement of protons: all mutations show either the enzyme behaves as normal; it pumps four protons even if Q reduction is slowed, or Q reduction is abolished completely. This result is supported by the observation that all functional variants could also catalyse RET (because the energy from consuming all four protons is required to reduce NAD^+). Additionally, mutations of critical components of the energy transduction and proton-pumping machinery tend to eradicate the Q-reductase activity, demonstrating an extremely tightly coupled system with even mutations very distal (>90 Å) to the site of Q chemistry having a profound impact on oxidoreductase activity. More extensive mutagenesis of the *P. denitrificans* enzyme will be required to substantiate these results and should focus on identifying whether it is possible to generate variants where Q reduction can be uncoupled from proton pumping.

In contrast to our data, a supernumerary subunit knockout in mitochondrial complex I from *Y. lipolytica*, which caused the loss of Nqo12/ND5 and Nqo13/ND4 antiporter subunits, was reported to pump only two protons per turnover (Dröse et al., 2011). This study also argues against the proposal that all four protons are ejected at Nqo12 rather than in four separate channels, which was suggested based on structural evidence where only the Nqo12 subunit had a well-defined ejection pathway for protons, composed of charge residues and resolved/simulated water molecules (Kampjut and Sazanov, 2020; Parey et al., 2021). Unfortunately, the complete loss of activity in Nqo12 and Nqo13 knockout strains in the *E. coli* enzyme has prevented further evidence supporting these observations (Belevich et al., 2011; Torres-Bacete et al., 2007). Unlike in *Y. lipolytica*, which is stabilised by numerous supernumerary subunits, these bacterial knockout strains may be too unstable to assemble a functioning enzyme. Our difficulties in generating the Nqo13 knockout strain of *P. denitrificans* are consistent with this result, as removal of the Nqo13 subunit in *Pd*-CI may have produced partially folded/assembled intermediates that are toxic to the cell, preventing creation of the

knockout. Of course, screening for this mutant was not exhaustive and it may be possible to identify subunit knockouts in the future. Reattempts to generate these antiporter subunit knockouts in *P. denitrificans* should thus be considered in future investigations as they are the most direct method for creating a variant where proton-pumping stoichiometry is potentially reduced, provided the enzyme is still able to catalyse Q reduction. This could then be measured accurately using the quantitative proton-pumping stoichiometry assay system described in Section 6.7 and would provide critical evidence for the mechanism and pathways of proton translocation.

Overall, the lack of a *Pd*-CI variant that pumped fewer protons per NADH oxidised is intriguing and should be considered as a possible mechanistic constraint. Whether it is conceivable that complex I can function at a reduced proton pumping stoichiometry will remain a key question for mechanistic studies. It is possible that proton translocation can be uncoupled from Q reduction, or Q reduction can still progress when coupled to the translocation of fewer protons in the mitochondrial enzyme, but not in the bacterial enzyme. However, this would probably involve a significant deviation in the coupling mechanism between species, an unlikely proposal based on their highly similar structures and conservation of key residues in the core subunits. A key difference may be the essential roles the supernumerary subunits play in mitochondrial complex I (Galemou Yoga et al., 2020; Steger et al., 2014). Further investigations using the *Pd*-CI model system developed in this thesis will be invaluable for investigating mechanistic questions such as this by combining genetic, biochemical and structural characterisation of complex I variants all in one experimental system.

7. References

Abele, U., and Schulz, G. E. (1995). High-resolution structures of adenylate kinase from yeast ligated with inhibitor Ap5A, showing the pathway of phosphoryl transfer. *Protein Science*, **4**, 1262–1271.

Abrahams, J. P., Leslie, A. G. W., Lutter, R., and Walker, J. E. (1994). Structure at 2.8 Å resolution of F_1-ATPase from bovine heart mitochondria. *Nature*, **370**, 621–628.

Adrian, M., Dubochet, J., Lepault, J., Mcdowall, A. W. (1984). Cryo-electron microscopy of viruses. *Nature*, **308**, 32–36.

Agip, A.-N. A., Blaza, J. N., Bridges, H. R., Viscomi, C., Rawson, S., Muench, S. P., and Hirst, J. (2018). Cryo-EM structures of complex I from mouse heart mitochondria in two biochemically defined states. *Nature Structural & Molecular Biology*, **25**, 548–556.

Agip, A.-N. A., Blaza, J. N., Fedor, J. G., and Hirst, J. (2019). Mammalian respiratory complex I through the lens of cryo-EM. *Annual Review of Biophysics*, **48**, 165–184.

Al-Shawi, M. K., Ketchum, C. J., and Nakamoto, R. K. (1997). The *Escherichia coli* F_OF_1 γM23K uncoupling mutant has a higher $K_{0.5}$ for P_i. Transition state analysis of this mutant and others reveals that synthesis and hydrolysis utilize the same kinetic pathway. *Biochemistry*, **36**, 12961–12969.

Albracht, S. P. J., Van Verseveld, H. W., Hagen, W. R., and Kalkman, M. L. (1980). A comparison of the respiratory chain in particles from *Paracoccus denitrificans* and bovine heart mitochondria by EPR spectroscopy. *Biochemica et Biophysica Acta - Bioenergetics*, **593**, 173–186.

Amano, T., Matsui, T., Muneyuki, E., Noji, H., Hara, K., Yoshida, M., and Hisabori, T. (1999). $\alpha_3\beta_3\gamma$ complex of F_1-ATPase from thermophilic *Bacillus* PS3 can maintain steady-state ATP hydrolysis activity depending on the number of non-catalytic sites. *Biochemical Journal*, **343**, 135–138.

Amarneh, B., and Vik, S. B. (2003). Mutagenesis of subunit N of the *Escherichia coli* complex I. Identification of the initiation codon and the sensitivity of mutants to decylubiquinone. *Biochemistry*, **42**, 4800–4808.

Anraku, Y., and Gennis, R. B. (1987). The aerobic respiratory chain of *Escherichia coli*. *Trends in Biochemical Sciences*, **12**, 262–266.

Armstrong, F. A., and Hirst, J. (2011). Reversibility and efficiency in electrocatalytic energy conversion and lessons from enzymes. *Proceedings of the National Academy of Sciences*, **108**, 14049–14054.

Baker, S. C., Ferguson, S. J., Ludwig, B., Page, M. D., Richter, O.-M. H., and Van Spanning, R. J. M. (1998). Molecular genetics of the genus *Paracoccus*: metabolically versatile bacteria with bioenergetic flexibility. *Microbiology and Molecular Biology Reviews*, **62**, 1046–1078.

Baradaran, R., Berrisford, J. M., Minhas, G. S., and Sazanov, L. A. (2013). Crystal structure of the entire respiratory complex I. *Nature*, **494**, 443–448.

Barker, C. D., Reda, T., and Hirst, J. (2007). The flavoprotein subcomplex of complex I (NADH:ubiquinone oxidoreductase) from bovine heart mitochondria: insights into the mechanisms of NADH oxidation and NAD^+ reduction from protein film voltammetry. *Biochemistry*, **46**, 3454–3464.

Bason, J. V., Runswick, M. J., Fearnley, I. M., and Walker, J. E. (2011). Binding of the inhibitor protein IF_1 to bovine F_1-ATPase. *Journal of Molecular Biology*, **406**, 443–453.

Bauer, M. F., Hofmann, S., Neupert, W., and Brunner, M. (2000). Protein translocation into mitochondria: the role of TIM complexes. *Trends in Cell Biology*, **10**, 25–31.

Belevich, G., Knuuti, J., Verkhovsky, M. I., Wikström, M., and Verkhovskaya, M. (2011). Probing the mechanistic role of the long α-helix in subunit L of respiratory Complex I from *Escherichia coli* by site-directed mutagenesis. *Molecular Microbiology*, **82**, 1086–1095.

Belevich, N., and Verkhovskaya, M. (2016). Resting state of respiratory complex I from *Escherichia coli*. *FEBS Letters*, **590**, 1570–1575.

Berndtsson, J., Aufschnaiter, A., Rathore, S., Marin-buera, L., Dawitz, H., Diessl, J., Kohler, V., Barrientos, A., Büttner, S., Fontanesi, F., and Ott, M. (2020). Respiratory supercomplexes enhance electron transport by decreasing cytochrome *c* diffusion distance. *EMBO Reports*, **21**, e51015.

Berrisford, J. M., and Sazanov, L. A. (2009). Structural basis for the mechanism of respiratory complex I. *Journal of Biological Chemistry*, **284**, 29773–29783.

Bianchi, C., Genova, M. L., Castelli, G. P., and Lenaz, G. (2004). The mitochondrial respiratory chain is partially organized in a supercomplex assembly. *Journal of Biological Chemistry*, **279**, 36562–36569.

Biner, O., Fedor, J. G., Yin, Z., and Hirst, J. (2020). Bottom-up construction of a minimal system for cellular respiration and energy regeneration. *ACS Synthetic Biology*, **9**, 1450–1459.

Birrell, J. A., Morina, K., Bridges, H. R., Friedrich, T., and Hirst, J. (2013). Investigating the function of [2Fe–2S] cluster N1a, the off-pathway cluster in complex I, by manipulating its reduction potential. *Biochemical Journal*, **456**, 139–146.

Birrell, J. A., Yakovlev, G., and Hirst, J. (2009). Reactions of the flavin mononucleotide in complex I: a combined mechanism describes NADH oxidation coupled to the reduction of $APAD^+$, ferricyanide, or molecular oxygen. *Biochemistry*, **48**, 12005–12013.

Blaza, J. N., Serreli, R., Jones, A. J. Y., Mohammed, K., and Hirst, J. (2014). Kinetic evidence against partitioning of the ubiquinone pool and the catalytic relevance of respiratory-chain supercomplexes. *Proceedings of the National Academy of Sciences*, **111**, 15735–15740.

Blaza, J. N., Vinothkumar, K. R., and Hirst, J. (2018). Structure of the deactive state of mammalian respiratory complex I. *Structure*, **26**, 312–319.

Bologna, F. P., Andreo, C. S., and Drincovich, M. F. (2007). *Escherichia coli* malic enzymes: two isoforms with substantial differences in kinetic properties, metabolic regulation, and structure. *Journal of Bacteriology*, **189**, 5937–5946.

Bowler, M. W., Montgomery, M. G., Leslie, A. G. W., and Walker, J. E. (2006). How azide inhibits ATP hydrolysis by the F-ATPases. *Proceedings of the National Academy of Sciences*, **103**, 8646–8649.

Bridges, H. R., Bill, E., and Hirst, J. (2012). Mössbauer spectroscopy on respiratory complex I: the iron-sulfur cluster ensemble in the NADH-reduced enzyme is partially oxidized. *Biochemistry*, **51**, 149–158.

Bridges, H. R., Blaza, J. N., Yin, Z., Chung, I., and Hirst, J. (2022). Bovine complex I in the active state at 3.1 Å. doi:10.2210/pdb7QSD/pdb.

Bridges, H. R., Fedor, J. G., Blaza, J. N., Di Luca, A., Jussupow, A., Jarman, O. D., Wright, J. J., Agip, A. N. A., Gamiz-Hernandez, A. P., Roessler, M. M., Kaila, V. R. I., and Hirst, J. (2020). Structure of inhibitor-bound mammalian complex I. *Nature Communications*, **11**, 5261.

Bridges, H. R., Mohammed, K., Harbour, M. E., and Hirst, J. (2017). Subunit NDUFV3 is present in two distinct isoforms in mammalian complex I. *Biochimica et Biophysica Acta - Bioenergetics*, **1858**, 197–207.

Bridges, H. R., Sirviö, V. A., Agip, A. N. A., and Hirst, J. (2016). Molecular features of biguanides required for targeting of mitochondrial respiratory complex I and activation of AMP-kinase. *BMC Biology*, **14**, 65.

Burnell, J. N., John, P., and Whatley, F. R. (1975). The reversibility of active sulphate transport in membrane vesicles of *Paracoccus denitrificans*. *The Biochemical Journal*, **150**, 527–536.

Cabrera-Orefice, A., Yoga, E. G., Wirth, C., Siegmund, K., Zwicker, K., Guerrero-Castillo, S., Zickermann, V., Hunte, C., and Brandt, U. (2018). Locking loop movement in the ubiquinone pocket of complex I disengages the proton pumps. *Nature Communications*, **9**, 4500.

Carmeli, C., and Lifshitz, Y. (1972). Effects of P_i and ADP on ATPase activity in chloroplasts. *Biochemica et Biophysica Acta*, **267**, 86–95.

Carroll, J., Fearnley, I. M., Shannon, R. J., Hirst, J., and Walker, J. E. (2003). Analysis of the subunit composition of complex I from bovine heart mitochondria. *Molecular & Cellular Proteomics*, **2**, 117–126.

Castro, P. J., Silva, A. F., Marreiros, B. C., Batista, A. P., and Pereira, M. M. (2016). Respiratory complex I: A dual relation with H^+ and Na^+? *Biochimica et Biophysica Acta - Bioenergetics*, **1857**, 928–937.

Cecchini, G. (2003). Function and structure of complex II of the respiratory chain. *Annual Review of Biochemistry*, **72**, 77–109.

Chan, P. P., Holmes, A. D., Smith, A. M., Tran, D., and Lowe, T. M. (2012). The UCSC Archaeal Genome Browser: 2012 update. *Nucleic Acids Research*, **40**, 646–652.

Chance, B., and Hollunger, G. (1960). Energy-linked reduction of mitochondrial pyridine nucleotide. *Nature*, **185**, 666–672.

Chandel, N. S. (2014). Mitochondria as signaling organelles. *BMC Biology*, **12**, 34.

Chouchani, E. T., Pell, V. R., James, A. M., Work, L. M., Saeb-Parsy, K., Frezza, C., Krieg, T., and Murphy, M. P. (2016). A unifying mechanism for mitochondrial superoxide production during ischemia-reperfusion injury. *Cell Metabolism*, **23**, 254–263.

Chung, I., Serreli, R., Cross, J. B., Di Francesco, M. E., Marszalek, J. R., and Hirst, J. (2021). Cork-in-bottle mechanism of inhibitor binding to mammalian complex I. *Science Advances*, **7**, eabg4000.

Chung, I., Wright, J. J., Bridges, H. R., Ivanov, B. S., Biner, O., Pereira, C. S., Arantes, G. M., and Hirst, J. (2022). Cryo-EM structures reveal ubiquinone-10 binding to mitochondrial complex I and conformational transitions associated with Q-site occupancy. *BioRxiv*, 2022.02.11.480065.

Cingolani, G., and Duncan, T. M. (2011). Structure of the ATP synthase catalytic complex (F_1) from *Escherichia coli* in an autoinhibited conformation. *Nature Structural and Molecular Biology*, **18**, 701–707.

Cipriano, D. J., and Dunn, S. D. (2006). The role of the ε subunit in the *Escherichia coli* ATP synthase. The C-terminal domain is required for efficient energy coupling. *Journal of Biological Chemistry*, **281**, 501–507.

Crofts, A. R., Meinhardt, S. W., Jones, K. R., and Snozzi, M. (1983). The role of the quinone pool in the cyclic electron-transfer chain of *Rhodopseudomonas sphaeroides*: a modified Q-cycle mechanism. *Biochimica et Biophysica Acta (BBA) - Bioenergetics*, **723**, 202–218.

D'Alessandro, M., Turina, P., Melandri, B. A., and Dunn, S. D. (2017). Modulation of coupling in the *Escherichia coli* ATP synthase by ADP and P_i: role of the ε subunit C-terminal domain. *Biochimica et Biophysica Acta - Bioenergetics*, **1858**, 34–44.

De Gier, J.-W. L., Lübben, M., Reijnders, W. N. M., Tipker, C. A., Slotboom, D., Van Spanning, R. J. M., Stouthamer, A. H., and Van Der Oost, J. (1994). The terminal oxidases of *Paracoccus*. *Molecular Microbiology*, **13**, 183–196.

De Gier, J.-W. L., Schepper, M., Reijnders, W. N. M., Van Dyck, S. J., Slotboom, D. J., Warne, A., Saraste, M., Krab, K., Finel, M., Stouthamer, A. H., Van Spanning, R. J. M., and Van Der Oost, J. (1996). Structural and functional analysis of *aa*$_3$-type and *cbb*$_3$-type cytochrome *c* oxidases of *Paracoccus denitrificans* reveals significant differences in proton-pump design. *Molecular Microbiology*, **20**, 1247–1260.

De Vries, G. E., Harms, N., Hoogendijk, J., and Stouthamer, A. H. (1989). Isolation and characterization of *Paracoccus denitrificans* mutants with increased conjugation frequencies and pleiotropic loss of a (nGATCn) DNA-modifying property. *Archives of Microbiology*, **152**, 52–57.

De Vries, S., Dörner, K., Strampraad, M. J. F., and Friedrich, T. (2015). Electron tunneling rates in respiratory complex I are tuned for efficient energy conversion. *Angewandte Chemie - International Edition*, **54**, 2844–2848.

Di Luca, A., Gamiz-Hernandez, A. P., and Kaila, V. R. I. (2017). Symmetry-related proton transfer pathways in respiratory complex I. *Proceedings of the National Academy of Sciences*, **114**, E6314–E6321.

Di Luca, A., Mühlbauer, M. E., Saura, P., and Kaila, V. R. I. (2018). How inter-subunit contacts in the membrane domain of complex I affect proton transfer energetics. *Biochimica et Biophysica Acta - Bioenergetics*, **1859**, 734–741.

Djafarzadeh, R., Kerscher, S., Zwicker, K., Radermacher, M., Lindahl, M., Schägger, H., and Brandt, U. (2000). Biophysical and structural characterization of proton-translocating NADH-dehydrogenase (complex I) from the strictly aerobic yeast *Yarrowia lipolytica*. *Biochimica et Biophysica Acta - Bioenergetics*, **1459**, 230–238.

Dou, C., Fortes, P. A. G., and Allison, W. S. (1998). The $\alpha_3(\beta Y_{341}W)_3\gamma$ subcomplex of the F_1-ATPase from the thermophilic *Bacillus* PS3 fails to dissociate ADP when MgATP is hydrolyzed at a single catalytic site and attains maximal velocity when three catalytic sites are saturated with MgATP. *Biochemistry*, **37**, 16757–16764.

Dröse, S., Galkin, A., and Brandt, U. (2005). Proton pumping by complex I (NADH:ubiquinone oxidoreductase) from *Yarrowia lipolytica* reconstituted into proteoliposomes. *Biochimica et Biophysica Acta - Bioenergetics*, **1710**, 87–95.

Dröse, S., Krack, S., Sokolova, L., Zwicker, K., Barth, H. D., Morgner, N., Heide, H., Steger, M., Nübel, E., Zickermann, V., Kerscher, S., Brutschy, B., Radermacher, M., and Brandt, U. (2011). Functional dissection of the proton pumping modules of mitochondrial complex I. *PLoS Biology*, **9**, e1001128.

Drozdetskiy, A., Cole, C., Procter, J., and Barton, G. J. (2015). JPred4: a protein secondary structure prediction server. *Nucleic Acids Research*, **43**, W389–W394.

Du, Z., and Boyer, P. D. (1990). On the mechanism of sulfite activation of chloroplast thylakoid ATPase and the relation of ADP tightly bound at a catalytic site to the binding change mechanism. *Biochemistry*, **29**, 402–407.

Dubochet, J., Adrian, M., Chang, J.-J., Homo, J.-C., Lepault, J., McDowall, A. W., and Schultz, P. (1988). Cryo-electron microscopy of vitrified specimens. *Quarterly Reviews of Biophysics*, **21**, 129–228.

Dufour, J. P., Goffeau, A., and Tsong, T. Y. (1982). Active proton uptake in lipid vesicles reconstituted with the purified yeast plasma membrane ATPase. Fluorescence quenching of 9-amino-6-chloro-2-methoxyacridine. *Journal of Biological Chemistry*, **257**, 9365–9371.

Dunn, S. D., Tozer, R. G., and Zadorozny, V. D. (1990). Activation of *Escherichia coli* F_1-ATPase by lauryldimethylamine oxide and ethylene glycol: relationship of ATPase activity to the interaction of the ε and β subunits. *Biochemistry*, **29**, 4335–4340.

Efremov, R. G., Baradaran, R., and Sazanov, L. A. (2010). The architecture of respiratory complex I. *Nature*, **465**, 441–445.

Efremov, R. G., and Sazanov, L. A. (2011). Structure of the membrane domain of respiratory complex I. *Nature*, **476**, 414–421.

Esposti, M. D., Carelli, V., Ghelli, A., Ratta, M., Crimi, M., Sangiorgi, S., Montagna, P., Lenaz, G., Lugaresi, E., and Cortelli, P. (1994). Functional alterations of the mitochondrially encoded ND4 subunit associated with Leber's hereditary optic neuropathy. *FEBS Letters*, **352**, 375–397.

Euro, L., Belevich, G., Verkhovsky, M. I., Wikström, M., and Verkhovskaya, M. (2008). Conserved lysine residues of the membrane subunit NuoM are involved in energy conversion by the proton-pumping NADH:ubiquinone oxidoreductase (complex I). *Biochimica et Biophysica Acta - Bioenergetics*, **1777**, 1166–1172.

Fang, P., Li, X., Wang, J., Xing, L., Gao, Y., Niu, L., and Teng, M. (2010). Crystal structure of the protein L-isoaspartyl methyltransferase from *Escherichia coli*. *Cell Biochemistry and Biophysics*, **58**, 163–167.

Fassone, E., and Rahman, S. (2012). Complex I deficiency: clinical features, biochemistry and molecular genetics. *Journal of Medical Genetics*, **49**, 578–590.

Fedor, J. G., and Hirst, J. (2018). Mitochondrial supercomplexes do not enhance catalysis by quinone channeling. *Cell Metabolism*, **28**, 525-531.e4.

Fedor, J. G., Jones, A. J. Y., Di Luca, A., Kaila, V. R. I., Hirst, J. (2017). Correlating kinetic and structural data on ubiquinone binding and reduction by respiratory complex I. *Proceedings of the National Academy of Sciences*, **114**, 12737–12742.

Feniouk, B. A., Suzuki, T., and Yoshida, M. (2006). The role of subunit epsilon in the catalysis and regulation of F_OF_1-ATP synthase. *Biochimica et Biophysica Acta*, **1757**, 326–338.

Feniouk, B. A., Suzuki, T., and Yoshida, M. (2007). Regulatory interplay between proton motive force, ADP, phosphate, and subunit ε in bacterial ATP synthase. *Journal of Biological Chemistry*, **282**, 764–772.

Ferguson, S. A., Cook, G. M., Montgomery, M. G., Leslie, A. G. W., and Walker, J. E. (2016). Regulation of the thermoalkaliphilic F_1-ATPase from *Caldalkalibacillus thermarum*. *Proceedings of the National Academy of Sciences*, **113**, 10860–10865.

Ferguson, S. J., John, P., Lloyd, W. J., Radda, G. K., and Whatley, F. R. (1976). The ATPase as an irreversible component in electron transport linked ATP synthesis. *FEBS Letters*, **62**, 272–275.

Fernández-Agüera, M. C., Gao, L., González-Rodríguez, P., Pintado, C. O., Arias-Mayenco, I., García-Flores, P., García-Pergañeda, A., Pascual, A., Ortega-Sáenz, P., and López-Barneo, J. (2015). Oxygen sensing by arterial chemoreceptors depends on mitochondrial complex I signaling. *Cell Metabolism*, **22**, 825–837.

Fernandez-Leiro, R., and Scheres, S. H. W. (2016). Unravelling biological macromolecules with cryo-electron microscopy. *Nature*, **537**, 339–346.

Fernandez-Leiro, R., and Scheres, S. H. W. (2017). A pipeline approach to single-particle processing in RELION. *Acta Crystallographica Section D: Structural Biology*, **73**, 496–502.

Ferrándiz, M. J., and De La Campa, A. G. (2002). The membrane-associated F_OF_1 ATPase is essential for the viability of *Streptococcus pneumoniae*. *FEMS Microbiology Letters*, **212**, 133–138.

Ferrières, L., Hémery, G., Nham, T., Guérout, A. M., Mazel, D., Beloin, C., and Ghigo, J. M. (2010). Silent mischief: bacteriophage Mu insertions contaminate products of *Escherichia coli* random mutagenesis performed using suicidal transposon delivery plasmids mobilized by broad-host-range RP4 conjugative machinery. *Journal of Bacteriology*, **192**, 6418–6427.

Fiedorczuk, K., Letts, J. A., Degliesposti, G., Kaszuba, K., Skehel, M., and Sazanov, L. A. (2016). Atomic structure of the entire mammalian mitochondrial complex i. *Nature*, **538**, 406–410.

Fiedorczuk, K., and Sazanov, L. A. (2018). Mammalian mitochondrial complex I structure and disease-causing mutations. *Trends in Cell Biology*, **28**, 835–867.

Finel, M. (1996). Genetic inactivation of the H^+-translocating NADH:ubiquinone oxidoreductase of *Paracoccus denitrificans* is facilitated by insertion of the *ndh* gene from *Escherichia coli*. *FEBS Letters*, **393**, 81–85.

Galemou Yoga, E., Parey, K., Djurabekova, A., Haapanen, O., Siegmund, K., Zwicker, K., Sharma, V., Zickermann, V., and Angerer, H. (2020). Essential role of accessory subunit LYRM6 in the mechanism of mitochondrial complex I. *Nature Communications*, **11**, 6008.

Galkin, A., Meyer, B., Wittig, I., Karas, M., Schägger, H., Vinogradov, A., and Brandt, U. (2008). Identification of the mitochondrial ND3 subunit as a structural component involved in the active/deactive enzyme transition of respiratory complex I. *Journal of Biological Chemistry*, **283**, 20907–20913.

Galkin, A., and Moncada, S. (2017). Modulation of the conformational state of mitochondrial complex I as a target for therapeutic intervention. *Interface Focus*, **7**, 20160104.

Galkin, A. S., Grivennikova, V. G., and Vinogradov, A. D. (1999). H^+/ $2e^-$ stoichiometry in NADH-quinone reductase reactions catalyzed by bovine heart submitochondrial particles. *FEBS Letters*, **451**, 157–161.

Galkin, M. A., and Vinogradov, A. D. (1999). Energy-dependent transformation of the catalytic activities of the mitochondrial F_OF_1-ATP synthase. *FEBS Letters*, **448**, 123–126.

Gamiz-Hernandez, A. P., Jussupow, A., Johansson, M. P., and Kaila, V. R. I. (2017). Terminal electron-proton transfer dynamics in the quinone reduction of respiratory complex I. *Journal of the American Chemical Society*, **139**, 16282–16288.

García-Trejo, J. J., Zarco-Zavala, M., Mendoza-Hoffmann, F., Hernández-Luna, E., Ortega, R., and Mendoza-Hernández, G. (2016). The inhibitory mechanism of the ζ subunit of the F_1F_O-ATPase nanomotor of *Paracoccus denitrificans* and related α-proteobacteria. *Journal of Biological Chemistry*, **291**, 538–546.

Gavrikova, E. V., and Vinogradov, A. D. (1999). Active/de-active state transition of the mitochondrial complex I as revealed by specific sulfhydryl group labeling. *FEBS Letters*, **455**, 36–40.

Giorgi, C., Marchi, S., and Pinton, P. (2018). The machineries, regulation and cellular functions of mitochondrial calcium. *Nature Reviews Molecular Cell Biology*, **19**, 713–730.

Gledhill, J. R., Montgomery, M. G., Leslie, A. G. W., and Walker, J. E. (2007). How the regulatory protein, IF_1, inhibits F_1-ATPase from bovine mitochondria. *Proceedings of the National Academy of Sciences*, **104**, 15671–15676.

Gorenkova, N., Robinson, E., Grieve, D. J., and Galkin, A. (2013). Conformational change of mitochondrial complex I increases ROS sensitivity during ischemia. *Antioxidants and Redox Signaling*, **19**, 1459–1468.

Grba, D. N., and Hirst, J. (2020). Mitochondrial complex I structure reveals ordered water molecules for catalysis and proton translocation. *Nature Structural & Molecular Biology*, **27**, 892–900.

Griffith, S. C., Sawaya, M. R., Boutz, D. R., Thapar, N., Katz, J. E., Clarke, S., and Yeates, T. O. (2001). Crystal structure of a protein repair methyltransferase from *Pyrococcus furiosus* with its L-isoaspartyl peptide substrate. *Journal of Molecular Biology*, **313**, 1103–1116.

Grivennikova, V. G., Serebryanaya, D. V, Isakova, E. P., Belozerskaya, T. A., and Vinogradov, A. D. (2003). The transition between active and de-activated forms of NADH:ubiquinone oxidoreductase (complex I) in the mitochondrial membrane of *Neurospora crassa*. *Biochem. J.*, **369**, 619–626.

Gu, J., Liu, T., Guo, R., Zhang, L., and Yang, M. (2022). The coupling mechanism of mammalian mitochondrial complex I. *Nature Structural & Molecular Biology*, **29**, 172–182.

Gu, J., Wu, M., Guo, R., Yan, K., Lei, J., Gao, N., and Yang, M. (2016). The architecture of the mammalian respirasome. *Nature Publishing Group*, **537**, 639–643.

Guo, H., Courbon, G. M., Bueler, S. A., Mai, J., Liu, J., and Rubinstein, J. L. (2021). Structure of mycobacterial ATP synthase bound to the tuberculosis drug bedaquiline. *Nature*, **589**, 143–147.

Guo, H., Suzuki, T., and Rubinstein, J. L. (2019). Structure of a bacterial ATP synthase. *eLife*, **8**, e43128.

Guo, R., Zong, S., Wu, M., Gu, J., and Yang, M. (2017). Architecture of human mitochondrial respiratory megacomplex $I_2III_2IV_2$. *Cell*, **170**, 1247–1257.

Gutiérrez-Fernández, J., Kaszuba, K., Minhas, G. S., Baradaran, R., Tambalo, M., Gallagher, D. T., and Sazanov, L. A. (2020). Key role of quinone in the mechanism of respiratory complex I. *Nature Communications*, **11**, 4135.

Haapanen, O., Djurabekova, A., and Sharma, V. (2019). Role of second quinone binding site in proton pumping by respiratory complex I. *Frontiers in Chemistry*, **7**, 221.

Hahn, A., Vonck, J., Mills, D. J., Meier, T., and Kühlbrandt, W. (2018). Structure, mechanism, and regulation of the chloroplast ATP synthase. *Science*, **360**, eaat4318.

Hahnke, S. M., Moosmann, P., Erb, T. J., and Strous, M. (2014). An improved medium for the anaerobic growth of *Paracoccus denitrificans* Pd1222. *Frontiers in Microbiology*, **5**, 18.

Hameedi, M. A., Grba, D. N., Richardson, K. H., Jones, A. J. Y., Song, W., Roessler, M. M., Wright, J. J., and Hirst, J. (2021). A conserved arginine residue is critical for stabilizing the N2 FeS cluster in mitochondrial complex I. *Journal of Biological Chemistry*, **296**, 100474.

Hanahan, D. (1983). Studies on transformation of *Escherichia coli* with plasmids. *Journal of Molecular Biology*, **166**, 557–580.

Haruyama, T., Hirono-Hara, Y., and Kato-Yamada, Y. (2010). Inhibition of thermophilic F_1-ATPase by the ε subunit takes different path from the ADP-Mg inhibition. *Biophysics*, **6**, 59–65.

Henderson, R., Baldwin, J. M., Ceska, T. A., Zemlin, F., Beckmann, E., Downing, K. H., Road, H., Zemlin, F., and Division, M. B. (1990). Model for the structure of bacteriorhodopsin based on high-resolution electron cryo-microscopy. *Journal of Molecular Biology*, **213**, 899–929.

Hirono-Hara, Y., Ishizuka, K., Kinosita, K., Yoshida, M., and Noji, H. (2005). Activation of pausing F_1 motor by external force. *Proceedings of the National Academy of Sciences*, **102**, 4288–4293.

Hirst, J. (2010). Towards the molecular mechanism of respiratory complex I. *Biochemical Journal*, **425**, 327–339.

Hirst, J. (2011). Why does mitochondrial complex I have so many subunits? *Biochemical Journal*, **437**, e1–e3.

Hirst, J. (2013). Mitochondrial complex I. *Annual Review of Biochemistry*, **82**, 551–575.
Hirst, J., and Roessler, M. M. (2016). Energy conversion, redox catalysis and generation of reactive oxygen species by respiratory complex I. *Biochimica et Biophysica Acta - Bioenergetics*, **1857**, 872–883.

Hoeser, J., Gnandt, E., and Friedrich, T. (2018). Low cost, microcontroller based heating device for multi-wavelength differential scanning fluorimetry. *Scientific Reports*, **8**, 1457.

Holt, P. J., Morgan, D. J., and Sazanov, L. A. (2003). The location of NuoL and NuoM subunits in the membrane domain of the *Escherichia coli* complex I. Implications for the mechanism of proton pumping. *Journal of Biological Chemistry*, **278**, 43114–43120.

Huang, C. S., Kopacz, S. J., and Lee, C. P. (1983). Mechanistic differences in the energy-linked fluorescence decreases of 9-aminoacridine dyes associated with bovine heart submitochondrial membranes. *Biochimica et Biophysica Acta - Bioenergetics*, **722**, 107–115.

Ind, A. C., Porter, S. L., Brown, M. T., Byles, E. D., De Beyer, J. A., Godfrey, S. A., and Armitage, J. P. (2009). Inducible-expression plasmid for *Rhodobacter sphaeroides* and *Paracoccus denitrificans*. *Applied and Environmental Microbiology*, **75**, 6613–6615.

Iwata, S., Ostermeier, C., Ludwig, B., and Michel, H. (1995). Structure at 2.8 Å resolution of cytochrome *c* oxidase from *Paracoccus denitrificans*. *Nature*, **376**, 660–669.

Jault, J. M., and Allison, W. S. (1994). Hysteretic inhibition of the bovine heart mitochondrial F_1-ATPase is due to saturation of noncatalytic sites with ADP which blocks activation of the enzyme by ATP. *Journal of Biological Chemistry*, **269**, 319–325.

Jault, J. M., Matsui, T., Jault, F. M., Kaibara, C., Muneyuki, E., Yoshida, M., Kagawa, Y., and Allison, W. S. (1995). The $\alpha_3\beta_3\gamma$ complex of the F_1-ATPase from thermophilic *Bacillus* PS3 containing the $\alpha D_{261}N$ substitution fails to dissociate inhibitory MgADP from a catalytic site when ATP binds to noncatalytic sites. *Biochemistry*, **34**, 16412–16418.

John, P., and Whatley, F. R. (1975). *Paracoccus denitrificans* and the evolutionary origin of the mitochondrion. *Nature*, **254**, 495–498.

John, P., and Whatley, F. R. (1977). The bioenergetics of *Paracoccus denitrificans*. *Biochemica et Biophysica Acta*, **463**, 129–153.

Jones, A. J. Y., Blaza, J. N., Bridges, H. R., May, B., Moore, A. L., and Hirst, J. (2016). A self-assembled respiratory chain that catalyzes NADH oxidation by ubiquinone-10 cycling between complex I and the alternative oxidase. *Angewandte Chemie - International Edition*, **55**, 728–731.

Jones, A. J. Y., Blaza, J. N., Varghese, F., and Hirst, J. (2017). Respiratory complex I in *Bos taurus* and *Paracoccus denitrificans* pumps four protons across the membrane for every NADH oxidized. *Journal of Biological Chemistry*, **292**, 4987–4995.

Jones, A. J. Y., and Hirst, J. (2013). A spectrophotometric coupled enzyme assay to measure the activity of succinate dehydrogenase. *Analytical Biochemistry*, **442**, 19–23.

Junesch, U., and Gräber, P. (1985). The rate of ATP synthesis as a function of ΔpH in normal and dithiothreitol-modified chloroplasts. *Biochemica et Biophysica Acta*, **809**, 429–434.

Kaczmarczyk, A., Vorholt, J. A., and Francez-Charlot, A. (2013). Cumate-inducible gene expression system for sphingomonads and other *Alphaproteobacteria*. *Applied and Environmental Microbiology*, **79**, 6795–6802.

Kaila, V. R. I., Verkhovsky, M. I. and Wikström, M. (2010). Proton-coupled electron transfer in cytochrome oxidase. *Chemical reviews*, **110**, 7062–7081

Kaila, V. R. I. (2018). Long-range proton-coupled electron transfer in biological energy conversion: towards mechanistic understanding of respiratory complex I. *Journal of the Royal Society Interface*, **15**, 20170916.

Kaila, V. R. I. (2021). Resolving chemical dynamics in biological energy conversion: long-range proton-coupled electron transfer in respiratory complex I. *Accounts of Chemical Research*, **54**, 4462–4473.

Kamiya, K., Boero, M., Tateno, M., Shiraishi, K., and Oshiyama, A. (2007). Possible mechanism of proton transfer through peptide groups in the H-pathway of the bovine cytochrome *c* oxidase. *Journal of the American Chemical Society*, **129**, 9663–9673.

Kampjut, D., and Sazanov, L. A. (2020). The coupling mechanism of mammalian respiratory complex I. *Science*, **370**.

Kao, M. C., Di Bernardo, S., Nakamaru-Ogiso, E., Miyoshi, H., Matsuno-Yagi, A., and Yagi, T. (2005). Characterization of the membrane domain subimit NuoJ (ND6) of the NADH-quinone oxidoreductase from *Escherichia coli* by chromosomal DNA manipulation. *Biochemistry*, **44**, 3562–3571.

Kashani-Poor, N., Kerscher, S., Zickermann, V., and Brandt, U. (2001). Efficient large scale purification of his-tagged proton translocating NADH:ubiquinone oxidoreductase (complex I) from the strictly aerobic yeast *Yarrowia lipolytica*. *Biochemica et Biophysica Acta - Bioenergetics*, **1504**, 363–370.

Kato-Yamada, Y., Bald, D., Koike, M., Motohashi, K., Hisabori, T., and Yoshida, M. (1999). ε subunit, an endogenous inhibitor of bacterial F_1-ATPase, also inhibits F_OF_1-ATPase. *Journal of Biological Chemistry*, **274**, 33991–33994.

Keis, S., Stocker, A., Dimroth, P., and Cook, G. M. (2006). Inhibition of ATP hydrolysis by thermoalkaliphilic F_1F_O-ATP synthase is controlled by the C terminus of the ε subunit. *Journal of Bacteriology*, **188**, 3796–3804.

Kerscher, S., Dröse, S., Zwicker, K., Zickermann, V., and Brandt, U. (2002). *Yarrowia lipolytica*, a yeast genetic system to study mitochondrial complex I. *Biochimica et Biophysica Acta - Bioenergetics*, **1555**, 83–91.

Kerscher, S. J., Eschemann, A., Okun, P. M., and Brandt, U. (2001). External alternative NADH:ubiquinone oxidoreductase redirected to the internal face of the mitochondrial inner membrane rescues complex I deficiency in *Yarrowia lipolytica*. *Journal of Cell Science*, **114**, 3915–3921.

Kim, H. J., Khalimonchuk, O., Smith, P. M., and Winge, D. R. (2012). Structure, function, and assembly of heme centers in mitochondrial respiratory complexes. *Biochimica et Biophysica Acta - Molecular Cell Research*, **1823**, 1604–1616.

Klusch, N., Senkler, J., Yildiz, Ö., Kühlbrandt, W., and Braun, H. P. (2021). A ferredoxin bridge connects the two arms of plant mitochondrial complex I. *Plant Cell*, **33**, 2072–2091.

Kmita, K., and Zickermann, V. (2013). Accessory subunits of mitochondrial complex I. *Biochemical Society Transactions*, **41**, 1272–1279.

Kolata, P., and Efremov, R. G. (2021). Structure of *Escherichia coli* respiratory complex I reconstituted into lipid nanodiscs reveals an uncoupled conformation. *eLife*, **10**, e68710.

Konno, H., Isu, A., Kim, Y., Murakami-Fuse, T., Sugano, Y., and Hisabori, T. (2011). Characterization of the relationship between ADP- and ε-induced inhibition in cyanobacterial F_1-ATPase. *Journal of Biological Chemistry*, **286**, 13423–13429.

Kotlyar, A. B., Albracht, S. P. J., and Van Spanning, R. J. M. (1998). Comparison of energization of complex I in membrane particles from *Paracoccus denitrificans* and bovine heart mitochondria. *Journal of Bioenergetics and Biomembranes*, **1365**, 53–59.

Kotlyar, A. B., and Borovok, N. (2002). NADH oxidation and NAD^+ reduction catalysed by tightly coupled inside-out vesicles from *Paracoccus denitrificans*. *European Journal of Biochemistry*, **269**, 4020–4024.

Kotlyar, A. B., Sled, V. D., and Vinogradov, A. D. (1992). Effect of Ca^{2+} ions on the slow active/inactive transition of the mitochondrial NADH-ubiquinone reductase. *Biochimica et Biophysica Acta - Bioenergetics*, **1098**, 144–150.

Kotlyar, A. B., and Vinogradov, A. D. (1990). Slow active/inactive transition of the mitochondrial NADH-ubiquinone reductase. *Biochimica et Biophysica Acta - Bioenergetics*, **1019**, 151–158.

Krah, A., Zarco-Zavala, M., and McMillan, D. G. G. (2018). Insights into the mechanistic features of the ε subunit from bacterial ATP synthases: a comparison of structural, biochemical and biophysical data. *Open Biology*, **8**, 170275.

Kühlbrandt, W. (2019). Structure and mechanisms of F-type ATP synthases. *Annual Review of Biochemistry*, **88**, 515–549.

Kuki, M., Noumi, T., Maeda, M., Amemura, A., and Futai, M. (1988). Functional domains of ε subunit of *Escherichia coli* H^+-ATPase (F_OF_1). *Journal of Biological Chemistry*, **263**, 17437–17442.

Kunji, E. R. S. (2004). The role and structure of mitochondrial carriers. *FEBS Letters*, **564**, 239–244.

Kurki, S., Zickermann, V., Kervinen, M., Hassinen, I., and Finel, M. (2000). Mutagenesis of three conserved Glu residues in a bacterial homologue of the ND1 subunit of complex I affects ubiquinone reduction kinetics but not inhibition by dicyclohexylcarbodiimide. *Biochemistry*, **39**, 13496–13502.

Kussmaul, L., and Hirst, J. (2006). The mechanism of superoxide production by NADH:ubiquinone oxidoreductase (complex I) from bovine heart mitochondria. *Proceedings of the National Academy of Sciences*, **103**, 7607–7612.

Lanyi, J. K., Schobert, B. (2004). Local–global conformational coupling in a heptahelical membrane protein: transport mechanism from crystal structures of the nine states in the bacteriorhodopsin photocycle. *Biochemistry*, **43**, 3–8.

Lapashina, A. S., and Feniouk, B. A. (2018). ADP-inhibition of H^+-F_OF_1-ATP synthase. *Biochemistry (Moscow)*, **83**, 1141–1160.

Lass, A., Agarwal, S., and Sohal, R. S. (1997). Mitochondrial ubiquinone homologues, superoxide radical generation, and longevity in different mammalian species. *Journal of Biological Chemistry*, **272**, 19199–19204.

Lee, S., Tak, E., Lee, J., Rashid, M., Murphy, M. P., Ha, J., and Kim, S. S. (2011). Mitochondrial H_2O_2 generated from electron transport chain complex I stimulates muscle differentiation. *Cell Research*, **21**, 817–834.

Letts, J. A., Fiedorczuk, K., and Sazanov, L. A. (2016). The architecture of respiratory supercomplexes. *Nature*, **537**, 644–648.

Lill, R., and Stehling, O. (2013). The role of mitochondria in cellular iron-sulfur protein biogenesis: mechanisms, connected processes, and diseases. *Cold Spring Harbour Perspectives in Biology*, **5**, a011312.

Lin, P. C., Puhar, A., and Steuber, J. (2008). NADH oxidation drives respiratory Na^+ transport in mitochondria from *Yarrowia lipolytica*. *Archives of Microbiology*, **190**, 471–480.

Lötscher, H.-R., deJong, C., and Capaldi, R. A. (1984). Interconversion of high and low adenosinetriphosphatase activity forms of *Escherichia coli* F_1 by the detergent lauryldimethylamine oxide. *Biochemistry*, **23**, 4140–4143.

Luria, S. E., Adams, J. N., and Ting, R. C. (1960). Transduction of lactose-utilizing ability among strains of *E. coli* and *S. dysenteriae* and the properties of the transducing phage particles. *Virology*, **12**, 348–390.

Madeira, F., Park, Y. M., Lee, J., Buso, N., Gur, T., Madhusoodanan, N., Basutkar, P., Tivey, A. R. N., Potter, S. C., Finn, R. D., and Lopez, R. (2019). The EMBL-EBI search and sequence analysis tools APIs in 2019. *Nucleic Acids Research*, **47**, W636—W641.

Magnitsky, S., Toulokhonova, L., Yano, T., Sled, V. D., Hägerhäll, C., Grivennikova, V. G., Burbaev, D. S., Vinogradov, A. D., and Ohnishi, T. (2002). EPR characterization of ubisemiquinones and iron-sulfur cluster N2, central components of the energy coupling in the NADH-ubiquinone oxidoreductase (complex I) in situ. *Journal of Bioenergetics and Biomembranes*, **34**, 193–208.

Maklashina, E., Kotlyar, A. B., and Cecchini, G. (2003). Active/de-active transition of respiratory complex I in bacteria, fungi, and animals. *Biochimica et Biophysica Acta - Bioenergetics*, **1606**, 95–103.

Margulis, L. (1967). On the origin of mitosing cells. *Journal of Theoretical Biology*, **14**, 255–274.

Matsui, T., Muneyuki, E., Honda, M., Allison, W. S., Dou, C., and Yoshida, M. (1997). Catalytic activity of the $\alpha_3\beta_3\gamma$ complex of F_1-ATPase without noncatalytic nucleotide binding site. *Journal of Biological Chemistry*, **272**, 8215–8221.

Matsuno-Yagi, A., and Hatefi, Y. (1988). Estimation of the turnover number of bovine heart F_OF_1 complexes for ATP synthesis. *Biochemistry*, **27**, 335–340.

Matsushita, K., Ohnishi, T., and Kaback, H. R. (1987). NADH-ubiquinone oxidoreductases of the *Escherichia coli* aerobic respiratory chain. *Biochemistry*, **26**, 7732–7737.

Meinhardt, S. W., Kula, T., Yagi, T., Lillich, T., and Ohnishi, T. (1987). EPR characterization of the iron-sulfur clusters in the NADH:ubiquinone oxidoreductase segment of the respiratory chain in *Paracoccus denitrificans*. *Journal of Biological Chemistry*, **262**, 9147–9153.

Mendoza-Hoffmann, F., Pérez-Oseguera, Á., Cevallos, M. Á., Zarco-Zavala, M., Ortega, R., Peña-Segura, C., Espinoza-Simón, E., Uribe-Carvajal, S., and García-Trejo, J. J. (2018). The biological role of the ζ subunit as unidirectional inhibitor of the F_1F_O-ATPase of *Paracoccus denitrificans*. *Cell Reports*, **22**, 1067–1078.

Meyerson, J. R., Rao, P., Kumar, J., Chittori, S., Banerjee, S., Pierson, J., Mayer, M. L., and Subramaniam, S. (2014). Self-assembled monolayers improve protein distribution on holey carbon cryo-EM supports. *Scientific Reports*, **4**, 7084.

Meyrat, A., and Von Ballmoos, C. (2019). ATP synthesis at physiological nucleotide concentrations. *Scientific Reports*, **9**, 3070.

Milenkovic, D., Blaza, J. N., Larsson, N.-G., and Hirst, J. (2017). The enigma of the respiratory chain supercomplex. *Cell Metabolism*, **25**, 765–776.

Mileykovskaya, E., and Dowhan, W. (2009). Cardiolipin membrane domains in prokaryotes and eukaryotes. *Biochimica et Biophysica Acta - Biomembranes*, **1788**, 2084–2091.

Milgrom, Y. M., and Cross, R. L. (1993). Nucleotide binding sites on beef heart mitochondrial F_1-ATPase. Cooperative interactions between sites and specificity of noncatalytic sites. *Journal of Biological Chemistry*, **268**, 23179–23185.

Milgrom, Y. M., and Duncan, T. M. (2020). F-ATP-ase of *Escherichia coli* membranes: the ubiquitous MgADP-inhibited state and the inhibited state induced by the ε-subunit's C-terminal domain are mutually exclusive. *Biochimica et Biophysica Acta - Bioenergetics*, **1861**, 148189.

Mimaki, M., Wang, X., McKenzie, M., Thorburn, D. R., and Ryan, M. T. (2012). Understanding mitochondrial complex I assembly in health and disease. *Biochimica et Biophysica Acta - Bioenergetics*, **1817**, 851–862.

Mitchell, P. (1961). Coupling of phosphorylation to electron and hydrogen transfer by a chemi-osmotic type of mechanism. *Nature*, **191**, 144–148.

Mizumoto, J., Kikuchi, Y., Nakanishi, Y. H., Mouri, N., Cai, A., Ohta, T., Haruyama, T., and Kato-Yamada, Y. (2013). ε subunit of *Bacillus subtilis* F_1-ATPase relieves MgADP inhibition. *PLoS ONE*, **8**, e73888.

Moir, J. W. B., and Ferguson, S. J. (1994). Properties of a *Paracoccus denitrificans* mutant deleted in cytochrome c_{550} indicate that a copper protein can substitute for this cytochrome in electron transport to nitrite, nitric oxide and nitrous oxide. *Microbiology*, **140**, 389–397.

Montgomery, M. G., Gahura, O., Leslie, A. G. W., Zíková, A., and Walker, J. E. (2018). ATP synthase from *Trypanosoma brucei* has an elaborated canonical F_1-domain and conventional catalytic sites. *Proceedings of the National Academy of Sciences*, **115**, 2102–2107.

Morales-Ríos, E., de la Rosa-Morales, F., Mendoza-Hernández, G., Rodríguez-Zavala, J. S., Celis, H., Zarco-Zavala, M., and García-Trejo, J. J. (2010). A novel 11-kDa inhibitory subunit in the F_1F_O ATP synthase of *Paracoccus denitrificans* and related α-proteobacteria. *FASEB Journal*, **24**, 599–608.
Morales-Ríos, E., Montgomery, M. G., Leslie, A. G. W., and Walker, J. E. (2015). Structure of ATP synthase from Paracoccus denitrificans determined by X-ray crystallography at 4.0 Å resolution. *Proceedings of the National Academy of Sciences*, **112**, 13231–13236.

Morgner, N., Zickermann, V., Kerscher, S., Wittig, I., Abdrakhmanova, A., Barth, H. D., Brutschy, B., and Brandt, U. (2008). Subunit mass fingerprinting of mitochondrial complex I. *Biochimica et Biophysica Acta - Bioenergetics*, **1777**, 1384–1391.

Morino, M., Natsui, S., Ono, T., Swartz, T. H., Krulwich, T. A., and Ito, M. (2010). Single site mutations in the hetero-oligomeric Mrp antiporter from alkaliphilic *Bacillus pseudofirmus* OF4 that affect Na^+/H^+ antiport activity, sodium exclusion, individual Mrp protein levels, or Mrp complex formation. *Journal of Biological Chemistry*, **285**, 30942–30950.

Morino, M., Ogoda, S., Krulwich, T. A., and Ito, M. (2017). Differences in the phenotypic effects of mutations in homologous MrpA and MrpD subunits of the multi-subunit Mrp-type Na^+/H^+ antiporter. *Extremophiles*, **21**, 51–64.

Moser, C. C., Farid, T. A., Chobot, S. E., and Dutton, P. L. (2006). Electron tunneling chains of mitochondria. *Biochimica et Biophysica Acta - Bioenergetics*, **1757**, 1096–1109.

Mühlbauer, M. E., Saura, P., Nuber, F., Di Luca, A., Friedrich, T., and Kaila, V. R. I. (2020). Water-gated proton transfer dynamics in respiratory complex I. *Journal of the American Chemical Society*, **142**, 13718–13728.

Nakamaru-Ogiso, E., Kao, M. C., Chen, H., Sinha, S. C., Yagi, T., and Ohnishi, T. (2010). The membrane subunit NuoL (ND5) is involved in the indirect proton pumping mechanism of *Escherichia coli* complex I. *Journal of Biological Chemistry*, **285**, 39070–39078.

Nakanishi-Matsui, M., Sekiya, M., and Futai, M. (2016). ATP synthase from *Escherichia coli*: mechanism of rotational catalysis, and inhibition with the ε subunit and phytopolyphenols. *Biochimica et Biophysica Acta - Bioenergetics*, **1857**, 129–140.

Nalin, C. M., and McCarty, R. E. (1984). Role of a disulfide bond in the γ subunit in activation of the ATPase of chloroplast coupling factor 1. *Journal of Biological Chemistry*, **259**, 7275–7280.

Narayanan, M., Leung, S. A., Inaba, Y., Elguindy, M. M., and Nakamaru-Ogiso, E. (2015). Semiquinone intermediates are involved in the energy coupling mechanism of *E. coli* complex I. *Biochimica et Biophysica Acta - Bioenergetics*, **1847**, 681–689.

Navon, G., Ogawa, S., Shulman, R. G., and Yamane, T. (1977). High resolution ^{31}P nuclear magnetic resonance studies of metabolism in aerobic *Escherichia coli* cells. *Proceedings of the National Academy of Sciences*, **74**, 888–891.

Niatsetskaya, Z. V., Sosunov, S. A., Matsiukevich, D., Utkina-Sosunova, I. V., Ratner, V. I., Starkov, A. A., and Ten, V. S. (2012). The oxygen free radicals originating from mitochondrial complex I contribute to oxidative brain injury following hypoxia-ischemia in neonatal mice. *Journal of Neuroscience*, **32**, 3235–3244.

Nogales, E., and Scheres, S. H. W. W. (2015). Cryo-EM: a unique tool for the visualization of macromolecular complexity. *Molecular Cell*, **58**, 677–689.

Nuber, F., Mérono, L., Oppermann, S., Schimpf, J., Wohlwend, D., and Friedrich, T. (2021). A quinol anion as catalytic intermediate coupling proton translocation with electron transfer in *E. coli* respiratory complex I. *Frontiers in Chemistry*, **9**, 672969.

Nuber, F., Schimpf, J., Di Rago, J.-P., Tribouillard-Tanvier, D., Procaccio, V., Martin-Negrier, M. L., Trimouille, A., Biner, O., Von Ballmoos, C., and Friedrich, T. (2021). Biochemical consequences of two clinically relevant ND-gene mutations in *Escherichia coli* respiratory complex I. *Scientific Reports*, **11**, 12641.

Ohnishi, T. (1998). Iron-sulfer clusters/semiquinones in complex I. *Biochemica et Biophysica Acta - Bioenergetics*, **1364**, 186–206.

Olgun, A., Akman, S., Tezcan, S., and Kutluay, T. (2003). The effect of isoprenoid side chain length of ubiquinone on life span. *Medical Hypotheses*, **60**, 325–327.

Onukwufor, J. O., Berry, B. J., and Wojtovich, A. P. (2019). Physiologic implications of reactive oxygen species production by mitochondrial complex I reverse electron transport. *Antioxidants*, **8**, 20–24.

Otten, M. F., Reijnders, W. N. M., Bedaux, J. J. M., Westerhoff, H. V., Krab, K., and Van Spanning, R. J. M. (1999). The reduction state of the Q-pool regulates the electron flux through the branched respiratory network of *Paracoccus denitrificans*. *European Journal of Biochemistry*, **261**, 767–774.

Pacheco-Moisés, F., García, J. J., Rodríguez-Zavala, J. S., and Moreno-Sánchez, R. (2000). Sulfite and membrane energization induce two different active states of the *Paracoccus denitrificans* F_OF_1-ATPase. *European Journal of Biochemistry*, **267**, 993–1000.

Pacheco-Moisés, F., Minauro-Sanmiguel, F., Bravo, C., and García, J. J. (2002). Sulfite inhibits the F_1F_O-ATP synthase and activates the F_1F_O-ATPase of *Paracoccus denitrificans*. *Journal of Bioenergetics and Biomembranes*, **34**, 269–278.

Padavannil, A., Ayala-Hernandez, M. G., Castellanos-Silva, E. A., and Letts, J. A. (2022). The mysterious multitude: structural perspective on the accessory subunits of respiratory complex I. *Frontiers in Molecular Biosciences*, **8**, 798353.

Page, C. C., Moser, C. C., Chen, X., and Dutton, P. L. (1999). Natural engineering principles of electron tunnelling in biological oxidation-reduction. *Nature*, **402**, 47–52.

Parey, K., Brandt, U., Xie, H., Mills, D. J., Siegmund, K., Vonck, J., Kühlbrandt, W., and Zickermann, V. (2018). Cryo-EM structure of respiratory complex I at work. *eLife*, **7**, e39213.

Parey, K., Haapanen, O., Sharma, V., Köfeler, H., Züllig, T., Prinz, S., Siegmund, K., Wittig, I., Mills, D. J., Vonck, J., Kühlbrandt, W., and Zickermann, V. (2019). High-resolution cryo-EM structures of respiratory complex I: mechanism, assembly, and disease. *Science Advances*, **5**, eaax9484.

Parey, K., Lasham, J., Mills, D. J., Djurabekova, A., Haapanen, O., Yoga, E. G., Xie, H., Kühlbrandt, W., Sharma, V., Vonck, J., and Zickermann, V. (2021). High-resolution structure and dynamics of mitochondrial complex I–insights into the proton pumping mechanism. *Science Advances*, **3221**, eabj3221.

Pfitzner, U., Hoffmeier, K., Harrenga, A., Kannt, A., Michel, H., Bamberg, E., Richter, O.-M. H., and Ludwig, B. (2000). Tracing the D-pathway in reconstituted site-directed mutants of cytochrome *c* oxidase from *Paracoccus denitrificans*. *Biochemistry*, **39**, 6756–6762.

Pryde, K. R., and Hirst, J. (2011). Superoxide is produced by the reduced flavin in mitochondrial complex I: A single, unified mechanism that applies during both forward and reverse electron transfer. *Journal of Biological Chemistry*, **286**, 18056–18065.

Qi, X., Sun, L., Lewin, A. S., Hauswirth, W. W., and Guy, J. (2007). The mutant human ND4 subunit of complex I induces optic neuropathy in the mouse. *Investigative Ophthalmology and Visual Science*, **48**, 1–10.

Quandt, J. J., and Hynes, M. F. (1993). Versatile suicide vectors which allow direct selection for gene replacement in Gram-negative bacteria. *Gene*, **127**, 15–21.

Raitio, M., and Wikström, M. (1994). An alternative cytochrome oxidase of *Paracoccus denitrificans* functions as a proton pump. *Biochimica et Biophysica Acta - Bioenergetics*, **1186**, 100–106.

Recktenwald, D., and Hess, B. (1977). Allosteric influence of anions on mitochondrial ATPase of yeast. *FEBS Letters*, **76**, 25–28.

Reda, T., Barker, C. D., and Hirst, J. (2008). Reduction of the iron-sulfur clusters in mitochondrial NADH:ubiquinone oxidoreductase (complex I) by Eu^{II}-DTPA, a very low potential reductant. *Biochemistry*, **47**, 8885–8893.

Rich, P. R., and Maréchal, A. (2013). Functions of the hydrophilic channels in protonmotive cytochrome *c* oxidase. *Journal of the Royal Society Interface*, **10**, 20130183.

Rich, P. R., (2017). Mitochondrial cytochrome *c* oxidase: catalysis, coupling and controversies. *Biochemical Society Transactions*, **45**, 813–829.

Robb, E. L., Hall, A. R., Prime, T. A., Eaton, S., Szibor, M., Viscomi, C., James, A. M., and Murphy, M. P. (2018). Control of mitochondrial superoxide production by reverse electron transport at complex I. *Journal of Biological Chemistry*, **293**, 9869–9879.

Roessler, M. M., King, M. S., Robinson, A. J., Armstrong, F. A., Harmer, J., and Hirst, J. (2010). Direct assignment of EPR spectra to structurally defined iron-sulfur clusters in complex I by double electron-electron resonance. *Proceedings of the National Academy of Sciences*, **107**, 1930–1935.

Ronneberger, O., Tunyasuvunakool, K., Bates, R., Žídek, A., Ballard, A. J., … Hassabis, D. (2021). Highly accurate protein structure prediction with AlphaFold. *Nature*, **596**, 583–589.

Röpke, M., Saura, P., Riepl, D., Pöverlein, M. C., Kaila, V. R. I. (2020). Functional water wires catalyze long-range proton pumping in the mammalian respiratory complex I. *Journal of the American Chemical Society*, **142**, 21758–21766.

Rosenthal, P. B., and Henderson, R. (2003). Optimal determination of particle orientation, absolute hand, and contrast loss in single-particle electron cryomicroscopy. *Journal of Molecular Biology*, **333**, 721–745.

Ruprecht, J. J., and Kunji, E. R. S. S. (2020). The SLC25 mitochondrial carrier family: structure and mechanism. *Trends in Biochemical Sciences*, **45**, 244–258.

Russo, C. J., and Passmore, L. A. (2014). Ultrastable gold substrates for electron microscopy. *Science*, **346**, 1377–1381.

Sarewicz, M., Pintscher, S., Pietras, R., Borek, A., Bujnowicz, Ł., Hanke, G., Cramer, W. A., Finazzi, G., and Osyczka, A. (2021). Catalytic reactions and energy conservation in the cytochrome bc_1 and b_6f complexes of energy-transducing membranes. *Chemical Reviews*, **121**, 2020–2108.

Sato, M., Sinha, P. K., Torres-bacete, J., Matsuno-Yagi, A., and Yagi, T. (2013). Energy transducing roles of antiporter-like subunits in *Escherichia coli* NDH-1 with main focus on subunit NuoN. *The Journal of Biological Chemistry*, **288**, 24705–24716.

Sato, M., Torres-Bacete, J., Sinha, P. K., Matsuno-Yagi, A., and Yagi, T. (2014). Essential regions in the membrane domain of bacterial complex I (NDH-1): the machinery for proton translocation. *Journal of Bioenergetics and Biomembranes*, **46**, 279–287.

Sazanov, L. A., Carroll, J., Holt, P., Toime, L., and Fearnley, I. M. (2003). A role for native lipids in the stabilization and two-dimensional crystallization of the *Escherichia coli* NADH-ubiquinone oxidoreductase (complex I). *Journal of Biological Chemistry*, **278**, 19483–19491.

Schägger, H., and Von Jagow, G. (1991). Blue native electrophoresis for isolation of membrane protein complexes in enzymatically active form. *Analytical Biochemistry*, **199**, 223–231.

Scheres, S. H. W. (2016). Processing of structurally heterogeneous cryo-EM data in RELION. *Methods in Enzymology*, **579**, 125–157.

Schimpf, J., Oppermann, S., Gerasimova, T., Santos Seica, A. F., Hellwig, P., Grishkovskaya, I., Wohlwend, D., Haselbach, D., and Friedrich, T. (2022). Structure of the peripheral arm of a minimalistic respiratory complex I. *Structure*, **30**, 80–94.

Schindelin, J., Arganda-carreras, I., Frise, E., Kaynig, V., Longair, M., Pietzsch, T., Preibisch, S., Rueden, C., Saalfeld, S., Schmid, B., Tinevez, J. Y., White, D. J., Hartenstein, V., Eliceiri, K., Tomancak, P., and Cardona, A. (2012). Fiji: an open-source platform for biological-image analysis. *Nature Methods*, **9**, 676–682.

Schuller, J. M., Birrell, J. A., Tanaka, H., Konuma, T., Wulfhorst, H., Cox, N., Schuller, S. K., Thiemann, J., Lubitz, W., Sétif, P., Ikegami, T., Engel, B. D., Kurisu, G. and Nowaczyk, M. M. (2019). Structural adaptations of photosynthetic complex I enable ferredoxin-dependent electron transfer. *Science*, **363**, 257–260.

Schulz, S., Iglesias-Cans, M., Krah, A., Yildiz, Ö., Leone, V., Matthies, D., Cook, G. M., Faraldo-Gómez, J. D., and Meier, T. (2013). A new type of Na^+-driven ATP synthase membrane rotor with a two-carboxylate ion-coupling motif. *PLoS Biology*, **11**, e1001596.

Sekiguchi, K., Murai, M., and Miyoshi, H. (2009). Exploring the binding site of acetogenin in the ND1 subunit of bovine mitochondrial complex I. *Biochimica et Biophysica Acta - Bioenergetics*, **1787**, 1106–1111.

Shah, N. B., and Duncan, T. M. (2015). Aerobic growth of *Escherichia coli* is reduced, and ATP synthesis is selectively inhibited when five C-terminal residues are deleted from the ε subunit of ATP synthase. *Journal of Biological Chemistry*, **290**, 21032–21041.

Shah, N. B., Hutcheon, M. L., Haarer, B. K., and Duncan, T. M. (2013). F_1-ATPase of *Escherichia coli*: the ε-inhibited state forms after ATP hydrolysis, is distinct from the ADP-inhibited state, and responds dynamically to catalytic site ligands. *Journal of Biological Chemistry*, **288**, 9383–9395.

Sharpley, M. S., Shannon, R. J., Draghi, F., and Hirst, J. (2006). Interactions between phospholipids and NADH:ubiquinone oxidoreductase (complex I) from bovine mitochondrial. *Biochemistry*, **45**, 241–248.

Shimokata, K., Katayama, Y., Murayama, H., Suematsu, M., Tsukihara, T., Muramoto, K., Aoyama, H., Yoshikawa, S., and Shimada, H. (2007). The proton pumping pathway of bovine heart cytochrome *c* oxidase. *Proceedings of the National Academy of Sciences*, **104**, 4200–4205.

Shirakihara, Y., Shiratori, A., Tanikawa, H., Nakasako, M., Yoshida, M., and Suzuki, T. (2015). Structure of a thermophilic F_1-ATPase inhibited by an ε-subunit: deeper insight into the ε-inhibition mechanism. *FEBS Journal*, **282**, 2895–2913.

Simon, R., Priefer, U., and Pühler, A. (1983). A broad host range mobilization system for in vivo genetic engineering: transposon mutagenesis in gram negative bacteria. *Biotechnology*, **1**, 784–790.

Smith, P.K., Krohn, R.I, Hermanson, G.T., Mallia, A.K., Gartner, F.H., Provenzano, M.D., Fujimoto, E.K., Goeke, N.M., Olson, B.J., Klenk, D.C. (1985). Measurment of protein using bicinchoninic acid. *Analytical Biochemistry*, **150**, 76–85.

Smith, R. A. J., Hartley, R. C., Cochemé, H. M., and Murphy, M. P. (2012). Mitochondrial pharmacology. *Trends in Pharmacological Sciences*, **33**, 341–352.

Spikes, T. E., Montgomery, M. G., and Walker, J. E. (2020). Structure of the dimeric ATP synthase from bovine mitochondria. *Proceedings of the National Academy of Sciences*, **117**, 23519–23526.

Steger, M., Zwicker, K., Heide, H., Angerer, H., Radermacher, M., Mankowska, M., Steger, M., Zwicker, K., Heide, H., Wittig, I., Brandt, U., and Zickermann, V. (2014). The LYR protein subunit NB4M/NDUFA6 of mitochondrial complex I anchors an acyl carrier protein and is essential for catalytic activity. *Proceedings of the National Academy of Sciences*, **111**, 5207–5212.

Steimle, S., Bajzath, C., Katerina, D., Schulte, M., Bothe, V., and Friedrich, T. (2011). The role of subunit NuoL for proton translocation by respiratory complex I. *Biochemistry*, **50**, 3386–3393.

Steimle, S., Willistein, M., Hegger, P., Janoschke, M., Erhardt, H., and Friedrich, T. (2012). Asp563 of the horizontal helix of subunit NuoL is involved in proton translocation by the respiratory complex I. *FEBS Letters*, **586**, 699–704.

Stein, L. R., and Imai, S. I. (2012). The dynamic regulation of NAD metabolism in mitochondria. *Trends in Endocrinology and Metabolism*, **23**, 420–428.

Steiner, J., and Sazanov, L. (2020). Structure and mechanism of the MRP complex, an ancient cation/proton antiporter. *eLife*, **9**, e59407.

Sternweis, P. C. (1978). The ε subunit of *Escherichia coli* coupling factor 1 is required for its binding to the cytoplasmic membrane. *Journal of Biological Chemistry*, **253**, 3123–3128.

Stoll, S., and Schweiger, A. (2006). EasySpin, a comprehensive software package for spectral simulation and analysis in EPR. *Journal of Magnetic Resonance*, **178**, 42–55.

Stroh, A., Anderka, O., Pfeiffer, K., Yagi, T., Finel, M., Ludwig, B., and Schägger, H. (2004). Assembly of respiratory complexes I, III, and IV into NADH oxidase supercomplex stabilizes complex I in *Paracoccus denitrificans*. *Journal of Biological Chemistry*, **279**, 5000–5007.
Sun, F., Huo, X., Zhai, Y., Wang, A., Xu, J., Su, D., Bartlam, M., and Rao, Z. (2005). Crystal structure of mitochondrial respiratory membrane protein Complex II. *Cell*, **121**, 1043–1057.

Symersky, J., Osowski, D., Walters, D. E., and Mueller, D. M. (2012). Oligomycin frames a common drug-binding site in the ATP synthase. *Proceedings of the National Academy of Sciences*, **109**, 13961–13965.

Taanman, J.-W. (1999). The mitochondrial genome: structure, transcription, translation and replication. *Biochimica et Biophysica Acta - Bioenergetics*, **1410**, 103–123.

Tett, A. J., Rudder, S. J., Bourdès, A., Karunakaran, R., and Poole, P. S. (2012). Regulatable vectors for environmental gene expression in *Alphaproteobacteria*. *Applied and Environmental Microbiology*, **78**, 7137–7140.

Torres-Bacete, J., Nakamaru-Ogiso, E., Matsuno-Yagi, A., and Yagi, T. (2007). Characterization of the NuoM (ND4) subunit in *Escherichia coli* NDH-1. Conserved charged residues essential for energy-coupled activities. *Journal of Biological Chemistry*, **282**, 36914–36922.

Torres-Bacete, J., Sinha, P. K., Castro-Guerrero, N., Matsuno-Yagi, A., and Yagi, T. (2009). Features of subunit NuoM (ND4) in *Escherichia coli* NDH-1. Topology and implication of conserved Glu^{144} for coupling site 1. *Journal of Biological Chemistry*, **284**, 33062–33069.

Torres-Bacete, J., Sinha, P. K., Matsuno-Yagi, A., and Yagi, T. (2011). Structural contribution of C-terminal segments of NuoL (ND5) and NuoM (ND4) subunits of complex I from *Escherichia coli*. *Journal of Biological Chemistry*, **286**, 34007–34014.

Torres-Bacete, J., Sinha, P. K., Sato, M., Patki, G., Kao, M. C., Matsuno-Yagi, A., and Yagi, T. (2012). Roles of subunit NuoK (ND4L) in the energy-transducing mechanism of *Escherichia coli* NDH-1 (NADH:quinone oxidoreductase). *Journal of Biological Chemistry*, **287**, 42763–42772.

Trumpower, B. L. (1991). The three-subunit cytochrome bc_1 complex of *Paracoccus denitrificans*. Its physiological function, structure, and mechanism of electron transfer and energy transduction. *Journal of Bioenergetics and Biomembranes*, **23**, 241–255.

Tsukihara, T., Aoyama, H., Yamashita, E., Tomizaki, T., Yamaguchi, H., Shinzawa-Itoh, K., Nakashima, R., Yaono, R., and Yoshikawa, S. (1996). The whole structure of the 13-subunit oxidized cytochrome *c* oxidase at 2.8 Å. *Science*, **272**, 1136–1144.

Tsunoda, S. P., Rodgers, A. J. W., Aggeler, R., Wilce, M. C. J., Yoshida, M., and Capaldi, R. A. (2001). Large conformational changes of the ε subunit in the bacterial F_1F_O ATP synthase provide a ratchet action to regulate this rotary motor enzyme. *Proceedings of the National Academy of Sciences*, **98**, 6560–6564.

Ugurbil, K., Rottenberg, H., Glynn, P., and Shulman, R. G. (1978). ^{31}P nuclear magnetic resonance studies of bioenergetics and glycolysis in anaerobic *Escherichia coli* cells. *Proceedings of the National Academy of Sciences*, **75**, 2244–2248.

Uno, S., Masuya, T., Shinzawa-Itoh, K., Lasham, J., Haapanen, O., Shiba, T., Inaoka, D. K., Sharma, V., Murai, M., Miyoshi, H. (2020). Oversized ubiquinones as molecular probes for structural dynamics of the ubiquinone reaction site in mitochondrial respiratory complex I. *Journal of Biological Chemistry*, **295**, 2449–2463.

Van Spanning, R. J. M., De Boer, A. P. N., Reijnders, W. N. M., De Gier, J. W. L., Delorme, C. O., Stouthamer, A. H., Westerhoff, H. V, Harms, N., and Van Der Oost, J. (1995). Regulation of oxidative phophorylation: the flexible respiratory network of *Paracoccus denitrificans*. *Journal of Bioenergetics and Biomembranes*, **27**, 499–512.

Van Spanning, R. J. M., Wansell, C. W., Reijnders, W. N. M., Harms, N., Ras, J., Oltmann, L. F., and Stouthamer, A. H. (1991). A method for introduction of unmarked mutations in the genome of *Paracoccus denitrificans*: construction of strains with multiple mutations in the genes encoding periplasmic cytochromes c_{550}, c_{551i}, and c_{553i}. *Journal of Bacteriology*, **173**, 6962–6970.

Varghese, F. (2016). Development of yeast and bacterial model systems for studying mutations in respiratory complex I. *Ph.D. thesis*. University of Cambridge.

Varghese, F., Atcheson, E., Bridges, H. R., and Hirst, J. (2015). Characterization of clinically identified mutations in NDUFV1, the flavin-binding subunit of respiratory complex I, using a yeast model system. *Human Molecular Genetics*, **24**, 6350–6360.

Varghese, F., Blaza, J. N., Jones, A. J. Y., Jarman, O. D., and Hirst, J. (2018). Deleting the IF_1-like ζ subunit from *Paracoccus denitrificans* ATP synthase is not sufficient to activate ATP hydrolysis. *Open Biology*, **8**, 170206–170215.

Verkhovskaya, M. L., Belevich, N., Euro, L., Wikström, M., and Verkhovsky, M. I. (2008). Real-time electron transfer in respiratory complex I. *Proceedings of the National Academy of Sciences*, **105**, 3763–3767.

Verkhovsky, M., Bloch, D. A., and Verkhovskaya, M. (2012). Tightly-bound ubiquinone in the *Escherichia coli* respiratory complex I. *Biochimica et Biophysica Acta - Bioenergetics*, **1817**, 1550–1556.

Vinothkumar, K. R., Zhu, J., and Hirst, J. (2014). Architecture of mammalian respiratory complex I. *Nature*, **515**, 80–84.

Von Ballmoos, C., Biner, O., Nilsson, T., and Brzezinski, P. (2016). Mimicking respiratory phosphorylation using purified enzymes. *Biochimica et Biophysica Acta*, **1857**, 321–331.

Walker, J. E. (2013). The ATP synthase: the understood, the uncertain and the unknown. *Biochemical Society Transactions*, **41**, 1–16.

Wang, C., and Youle, R. J. (2009). The role of mitochondria in apoptosis. *Annual Review of Genetics*, **43**, 95–118.

Watt, I. N., Montgomery, M. G., Runswick, M. J., Leslie, A. G. W., and Walker, J. E. (2010). Bioenergetic cost of making an adenosine triphosphate molecule in animal mitochondria. *Proceedings of the National Academy of Sciences*, **107**, 16823–16827.

Weaver, T. M., Levitt, D. G., Donnelly, M. I., Wilkens Stevens, P. P., and Banaszak, L. J. (1995). The multisubunit active site of fumarase C from *Escherichia coli*. *Nature Structural Biology*, **2**, 654–662.

Wikström, M. K. F. (1977). Proton pump coupled to cytochrome *c* oxidase in mitochondria. *Nature*, **266**, 271–273.

Wilkinson, B. J., Morman, M. R., and White, D. C. (1972). Phospholipid composition and metabolism of *Micrococcus denitrificans*. *Journal of Bacteriology*, **112**, 1288–1294.

Wright, J. J., Fedor, J. G., Hirst, J., and Roessler, M. M. (2020). Using a chimeric respiratory chain and EPR spectroscopy to determine the origin of semiquinone species previously assigned to mitochondrial complex I. *BMC Biology*, **18**, 54.

Yagi, H., Kajiwara, N., Tanaka, H., Tsukihara, T., Kato-Yamada, Y., Yoshida, M., and Akutsu, H. (2007). Structures of the thermophilic F_1-ATPase ε subunit suggesting ATP-regulated arm motion of its C-terminal domain in F_1. *Proceedings of the National Academy of Sciences*, **104**, 11233–11238.

Yagi, T. (1991). Bacterial NADH-quinone oxidoreductases. *Journal of Bioenergetics and Biomembranes*, **23**, 211–225.

Yano, T., Dunham, W. R., and Ohnishi, T. (2005). Characterization of the $\Delta\mu_{H^+}$-sensitive ubisemiquinone species (SQ_{Nf}) and the interaction with cluster N2: new insight into the energy-coupled electron transfer in complex I. *Biochemistry*, **44**, 1744–1754.

Yano, T., Sklar, J., Nakamaru-Ogiso, E., Takahashi, Y., Yagi, T., and Ohnishi, T. (2003). Characterization of cluster N5 as a fast-relaxing [4Fe-4S] cluster in the Nqo3 subunit of the proton-translocating NADH-ubiquinone oxidoreductase from *Paracoccus denitrificans*. *Journal of Biological Chemistry*, **278**, 15514–15522.

Yin, Z., Burger, N., Kula-Alwar, D., Aksentijević, D., Bridges, H. R., Prag, H. A., Grba, D. N., Viscomi, C., James, A. M., Mottahedin, A., Krieg, T., Murphy, M. P., and Hirst, J. (2021). Structural basis for a complex I mutation that blocks pathological ROS production. *Nature Communications*, **12**, 707.

Yip, C.-Y., Harbour, M. E., Jayawardena, K., Fearnley, I. M., and Sazanov, L. A. (2011). Evolution of respiratory complex I "supernumerary" subunits are present in the α-proteobacterial enzyme. *Journal of Biological Chemistry*, **286**, 5023–5033.

Ylikallio, E., and Suomalainen, A. (2012). Mechanisms of mitochondrial diseases. *Annals of Medicine*, **44**, 41–59.

Yu, H., Wu, C.H., Schut, G. J., Haja, D. K., Zhao, G., Peters, J. W., Adams, M. W. W and Li, H. (2018). Structure of an ancient respiratory system. *Cell*, **173**, 1636–1649.

Yu, H., Schut, G. J., Haja, D. K., Adams, M. W. W., and Li, H. (2021). Evolution of complex I–like respiratory complexes. *Journal of Biological Chemistry*, **296**, 100740.

Zarco-Zavala, M., Mendoza-Hoffmann, F., and García-Trejo, J. J. (2018). Unidirectional regulation of the F_1F_O-ATP synthase nanomotor by the ζ pawl-ratchet inhibitor protein of *Paracoccus denitrificans* and related α-proteobacteria. *Biochimica et Biophysica Acta - Bioenergetics*, **1859**, 762–774.

Zarco-Zavala, M., Morales-Ríos, E., Mendoza-Hernández, G., Ramírez-Silva, L., Pérez-Hernández, G., and García-Trejo, J. J. (2014). The ζ subunit of the F_1F_O-ATP synthase of α-proteobacteria controls rotation of the nanomotor with a different structure. *FASEB Journal*, **28**, 2146–2157.

Zerbetto, E., Vergani, L., and Dabbeni-Sala, F. (1997). Quantification of muscle mitochondrial oxidative phosphorylation enzymes via histochemical staining of blue native polyacrylamide gels. *Electrophoresis*, **18**, 2059–2064.

Zeth, K., and Thein, M. (2010). Porins in prokaryotes and eukaryotes: common themes and variations. *Biochemical Journal*, **431**, 13–22.

Zhang, A. T., Montgomery, M. G., Leslie, A. G. W., Cook, G. M., and Walker, J. E. (2019). The structure of the catalytic domain of the ATP synthase from *Mycobacterium smegmatis* is a target for developing antitubercular drugs. *Proceedings of the National Academy of Sciences*, **116**, 4206–4211.

Zhang, K. (2016). Gctf: real-time CTF determination and correction. *Journal of Structural Biology*, **193**, 1–12.

Zharova, T. V., and Vinogradov, A. D. (2004). Energy-dependent transformation of $F_O \cdot F_1$-ATPase in *Paracoccus denitrificans* plasma membranes. *Journal of Biological Chemistry*, **279**, 12319–12324.

Zharova, T. V, and Vinogradov, A. D. (2003). Proton-translocating ATP-synthase of *Paracoccus denitrificans*: ATP-hydrolytic activity. *Biochemistry (Moscow)*, **68**, 1101–1108.

Zheng, S. Q., Palovcak, E., Armache, J. P., Verba, K. A., Cheng, Y., and Agard, D. A. (2017). MotionCor2: anisotropic correction of beam-induced motion for improved cryo-electron microscopy. *Nature Methods*, **14**, 331–332.

Zhou, A., Rohou, A., Schep, D. G., Bason, J. V., Montgomery, M. G., Walker, J. E., Grigorieffniko, N., and Rubinstein, J. L. (2015). Structure and conformational states of the bovine mitochondrial ATP synthase by cryo-EM. *eLife*, **4**, e10180.

Zhu, J., Han, H., Pawate, A., and Gennis, R. B. (2010). Decoupling mutations in the D-Channel of the aa_3-type cytochrome *c* oxidase from *Rhodobacter sphaeroides* suggest that a continuous hydrogen-bonded chain of waters is essential for proton pumping. *Biochemistry*, **49**, 4476–4482.

Zhu, J., Vinothkumar, K. R., and Hirst, J. (2016). Structure of mammalian respiratory complex I. *Nature*, **536**, 354–358.

Zhu, S., and Vik, S. B. (2015). Constraining the lateral helix of respiratory complex I by cross-linking does not impair enzyme activity or proton translocation. *Journal of Biological Chemistry*, **290**, 20761–20773.

Zickermann, V., Barquera, B., Wikström, M., and Finel, M. (1998). Analysis of the pathogenic human mitochondrial mutation ND1/3460, and mutations of strictly conserved residues in its vicinity, using the bacterium *Paracoccus denitrificans*. *Biochemistry*, **37**, 11792–11796.

Zickermann, V., Wirth, C., Nasiri, H., Siegmund, K., Schwalbe, H., Hunte, C., and Brandt, U. (2015). Mechanistic insight from the crystal structure of mitochondrial complex I. *Science*, **347**, 44–49.

Zíková, A., Schnaufer, A., Dalley, R. A., Panigrahi, A. K., and Stuart, K. D. (2009). The F_OF_1-ATP synthase complex contains novel subunits and is essential for procyclic *Trypanosoma brucei*. *PLoS Pathogens*, **5**, e1000436.

Zivanov, J., Nakane, T., Forsberg, B. O., Kimanius, D., Hagen, W. J. H., Lindahl, E., and Scheres, S. H. W. (2018). New tools for automated high-resolution cryo-EM structure determination in RELION-3. *eLife*, **7**, e42166.

Zivanov, J., Nakane, T., and Scheres, S. H. W. W. (2019). A Bayesian approach to beam-induced motion correction in cryo-EM single-particle analysis. *IUCrJ*, **6**, 5–17.

Zu, Y., Di Bernardo, S., Yagi, T., and Hirst, J. (2002). Redox properties of the [2Fe-2S] center in the 24 kDa (NQO2) subunit of NADH:ubiquinone oxidoreductase (complex I). *Biochemistry*, **41**, 10056–10069.